Faculty of Science and Engineering
Department of Chemistry

Structural Studies of Titanyl and Zirconyl Sulphate Hydrates

Phillip Martin English

This thesis is presented for the Degree of
Doctor of Philosophy
of
Curtin University of Technology

June 2011

To the best of my knowledge and belief this thesis contains no material previously published by any other person except where due acknowledgement has been made. This thesis contains no material which has been accepted for the award of any other degree or diploma in any university.

Signed: _____

Date: _____

"The electron is not as simple as it looks."

Sir William Lawrence Bragg

CURTIN UNIVERSITY OF TECHNOLOGY

Abstract

Faculty of Science and Engineering
Department of Applied Chemistry

Doctor of Philosophy

Structural Studies of Titanyl and Zirconyl Sulphate Hydrates

by Phillip Martin English

The aim of this thesis was to use a combination of computer simulations and experimental methods to gain insight into the unknown structure of the material titanyl sulphate dihydrate, $TiOSO_4 \cdot 2H_2O$.

Samples of $TiOSO_4 \cdot 2H_2O$, along with $TiOSO_4 \cdot H_2O$, were produced and analysed using X-ray and neutron diffraction at both laboratory and synchrotron facilities. Both *ex-situ* and *in-situ* experiments were performed in order to analyse both the structure and growth of the crystals. The diffraction data resulting from these experiments was then used in various structure determination programs. A unit cell was able to be determined from the synchrotron X-ray diffraction patterns, and the first neutron diffraction pattern of a $TiOSO_4 \cdot 2D_2O$ sample was produced. *In-situ* synchrotron X-ray diffraction studies showed that the formation of the crystals followed a single step process, and indicated the possibility of meta-stable phases being present in the sample.

In parallel with the experimental studies, computer modelling was used to develop and create candidate $TiOSO_4 \cdot 2H_2O$ structures. Initially both forcefield and first principles techniques were validated against a series of test cases. These included the first such calculations for the $TiOSO_4$ and $TiOSO_4 \cdot H_2O$ structures. The candidate structures of $TiOSO_4 \cdot 2H_2O$ thus produced were then used as input into the structural determination step.

Structure determination was attempted with multiple approaches, using the determined unit cell and a variety of space group settings. Despite a thorough treatment and validation of the method using the diffraction data and known structure of $TiOSO_4 \cdot H_2O$, the structure was unable to be solved. However, structural motifs consistent with a layered, needle-like morphology, as observed in experimental studies, were commonly found to be present in solutions offered by these approaches. Future use of techniques such as the substitution of isotopic titanium in neutron diffraction may provide enough information to more accurately determine atomic positions.

Acknowledgements

I would first like to thank my two primary project supervisors, Prof. Julian Gale and Dr. Bill Richmond, for providing me with outstanding guidance. I've learned a huge amount and experienced a great deal during the time spent completing this project, none of which would have happened without their help. I would also like to acknowledge Dr. Glenn Bryant and Dr. Alan Stuart, both formerly of the BHP Billiton Newcastle Technology Centre, for their support and expert advice as adjunct supervisors.

Dr. Maxim Avdeev at the ANSTO OPAL research reactor and Dr. Kareena Chapman of the Advanced Photon Source at Argonne National Laboratory were both incredibly helpful and professional, going far beyond their official capacity as beamline scientists to offer assistance wherever they could. Similarly, the structure determination from powder diffraction newsgroup has demonstrated to me how a scientific community should operate, in particular the tremendous efforts of Prof. Armel Le Bail and Dr. Holger Putz, as will be shown within the pages of this thesis.

I would also like to thank the Australian Government, BHP Billiton, and Curtin University for funding my project through the Australian Postgraduate Awards (Industry) scholarship, as well as the iVEC supercomputing facility for computer time.

To all my friends from the terminal room/computational lab, a huge thanks for putting up with me. I don't think anyone could have asked for a more friendly, encouraging environment to work in.

To my family, thanks for being there with me through thick and thin, and providing the motivation to get past the finish line. Especially my mother, who is solely responsible for my education and has never wavered in her support for me achieving whatever it was I set out to achieve. There is no way I'd have arrived at where I am today without her amazing willpower. Thanks, Mum.

Last, but by no means least, thanks to my beautiful, wonderful girlfriend Louise. I can't wait to see where our journey takes us next.

Contents

Dedicated to Joe.

Chapter 1

Introduction

1.1 Background

Australia is one of the highest producers of the world's mineral rutile (TiO_2) accounting for 53% of the total titanium dioxide produced in 2009 [1]. Titanium dioxide is well known for its many uses as a pigment due to its white colour, non-toxicity, and relative inexpense. This has resulted in it being the main pigment in a variety of products: paints and coatings, paper, plastic, ink, foods, and medicines. It also finds special application in sunscreens due to its high refractive index, coupled with a strong ultraviolet (UV) light absorption and resistance to discoloration under UV light. A more recent application has been as a photocatalyst under UV light. This phenomenon was observed in 1972, when Fujishima and Honda reported the photocatalytic splitting of water on TiO_2 electrodes [2]. Since then, a similar technique has been adapted to produce dye-sensitised solar cells [3] that offer a commercially viable alternative to traditional photovoltaic devices.

As a result of all these applications, TiO_2 is a highly sought after material, and the industries that surround its recovery, and the recovery of Ti metal, from the earth are worth many millions of dollars to the Australian economy. While titanium dioxide occurs in nature in various mineral polymorphs, such as rutile, anatase, and brookite, the most commerically viable forms of titanium compounds for industrial uses are that of rutile and the complex oxide ilmenite [4] due to their availability . Ilmenite is a titanium-iron oxide mineral with formula $FeTiO_3$, and is found in Australia in concentrations and purities that allow it to be readily treated to form synthetic rutile using the Western Australian developed Becher process [5].

There are two main processes that produce high purity titanium dioxide pigment from a raw stock of ilmenite or rutile ores: the sulphate process and the chloride process [6] (see

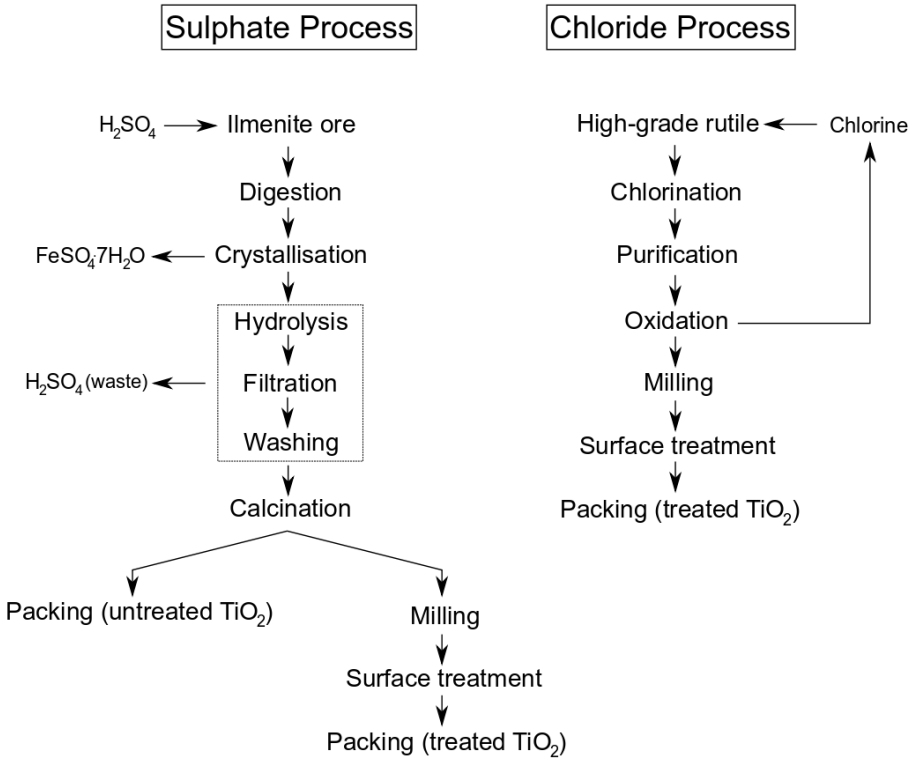

FIGURE 1.1: The production schemes of the sulphate and chloride processes.

Figure 1.1) . Both processes consist of two broad steps; the first being the production of the pigment particles, and the second being the surface treatment, drying, and milling of the final product. There are advantages and disadvantages to both processes, but the one strong advantage the chloride process has over the sulphate process is its ability to recycle the chlorine used, leading to less waste and a more economic use of reactants. With the increased focus on environmental considerations within industries, this has led to the widespread adoption of the chloride process. However, the chloride process requires feedstock of high purity TiO_2, while the sulphate process can take in ilmenite ore and lower purity rutile [7].

While plants that use the sulphate process still exist, the tighter environmental constraints have led them to introduce new steps to neutralise or convert waste sulphuric acid, and sell on the iron sulphate as a product [8]. It is therefore obvious that any improvement to the sulphate process would be an environmental and economic boon. Recently, a new process has been developed by BHP Billiton that makes use of sulphuric acid while leading to a reduction in waste products [9, 10]. This new process involves a stage after the ilmenite ore is digested in highly concentrated sulphuric acid to remove

the iron impurities as crystalline $FeSO_4 \cdot 7H_2O$. A further digestion is carried out once the iron is removed that crystallises out $TiOSO_4 \cdot 2H_2O$ at higher concentrations of sulphuric acid. However, the $TiOSO_4 \cdot 2H_2O$ crystallises in the form of fibrous, needle-like crystals that are difficult to filter and cause blockages in pumping systems. Unfortunately, despite numerous attempts to find a work-around – including alterations to filtration apparatus, solution chemistry, and reactor parameters such as stirring speed and stirrer geometry [11] – the problem still remains. Therefore, a more fundamental approach to understanding the production of the $TiOSO_4 \cdot 2H_2O$ needles is required in the hope that this will lead to some way of modifying their growth.

The ultimate objective on the completion of this project is the complete structural characterisation of the unknown structure of $TiOSO_4 \cdot 2H_2O$. In doing so, it is hoped that insight will be obtained into the growth mechanisms of this substance, and a method of retarding the problematic fibrous characteristics of the crystals will be developed. In aiming to achieve this, it is useful to investigate the structure of the other titanyl sulphate hydrates and their respective growth mechanisms, along with that of the related zirconyl sulphate hydrates in order to provide analogues.

1.2 Previous work

1.2.1 The structures of $TiOSO_4$ and $TiOSO_4 \cdot H_2O$

The structures of both $TiOSO_4$ and $TiOSO_4 \cdot H_2O$ have been known for quite some time. The structure of the anhydrate was first studied by Naka *et al.* [12] by growing single crystals in hydrothermal conditions and using X-ray diffraction to determine a unit cell and space group. An atomic structure solution was only completed much later by Gatehouse *et al.* [13] using single crystal X-ray diffraction, complemented by high resolution transmission electron microscopy (TEM) techniques when the initial X-ray diffraction results – collected using the unit cell of Naka *et al.* – failed to produce a high quality determination. The TEM results gave a complex diffraction pattern, the complexity of which led to a data set being collected with a quadrupled c axis. This data set encompassed distortions across the four included sub-lattices that enabled a more satisfactory structure determination to be completed.

Figures 1.2a)-c) show the resultant structure of the anhydrate. It can be described as an infinite array of corner-shared titanium oxide octahedra and sulphate tetrahedra parallel to the **b** direction. These ribbons result in four- and five-sided voids in the same direction, which are substantially distorted when compared to the similar structure of WPO_5 [14]. The source of the distortion was proposed as being the high variability in

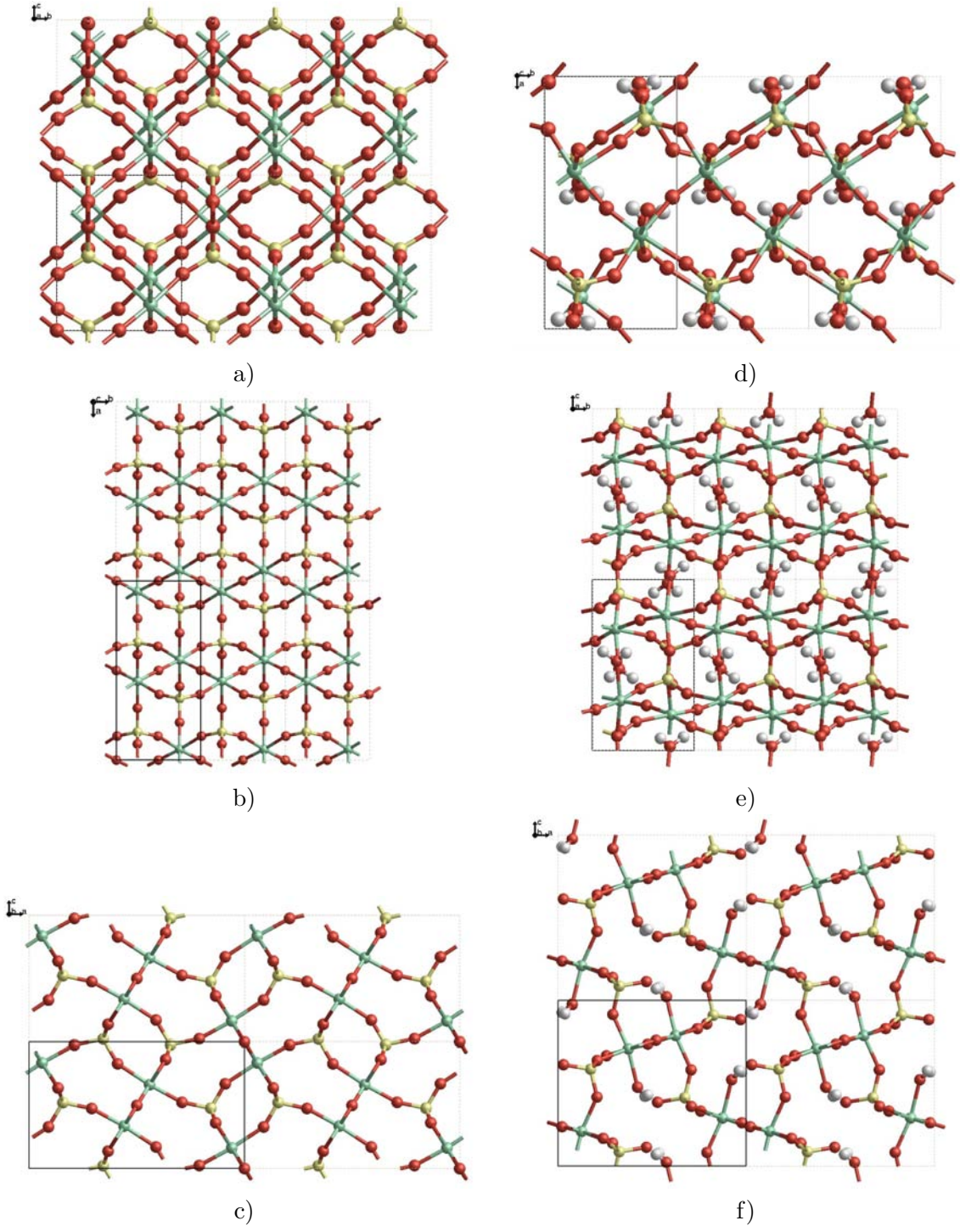

FIGURE 1.2: The structure of $TiOSO_4$ viewed down the a) **a**, b) **c**, and c) **b** axes; and the structure of $TiOSO_4 \cdot H_2O$ viewed down the d) **c**, e) **a**, and f) **b** axes. Titanium atoms are green, sulfur atoms are yellow, oxygen atoms are red, and hydrogen atoms are white.

TABLE 1.1: Literature values of $TiOSO_4$ and $TiOSO_4{\cdot}H_2O$ orthorhombic cell parameters.

Structure	a (Å)	b (Å)	c (Å)	Spacegroup
$TiOSO_4$ [12]	10.936(5)	5.150(5)	6.340(5)	$Pmn2_1$
$TiOSO_4$ [13]	10.942(1)	5.158(1)	25.726(2)	$P2_1ma$
$TiOSO_4$ [15]	10.953(3)	5.152(1)	6.426(1)	Pnma
$TiOSO_4{\cdot}H_2O$ [16]	9.788	5.120	8.598	Pnma
$TiOSO_4{\cdot}H_2O$ [13]	9.818(1)	5.133(1)	8.614(2)	$P2_12_12_1$
$TiOSO_4{\cdot}H_2O$ [15]	9.828(1)	5.134(1)	8.613(1)	Pnma

the Ti–O bond distances in the titanium octahedra, which range from 1.70 Åto 2.05 Å. These variations were proposed to underly the supercell structure presented. A subsequent powder X-ray diffraction study by Ahmed *et al.* [15] confirmed a more ordered atomic structure with a unit cell very similar to Naka *et al.*, but with the caveat that '...the reaction mechanism which rules the syntheses of these compounds makes it quite likely that there exists some disorder between sulphate groups in $TiOSO_4$ as well as between sulphate and/or water groups in $TiOSO_4{\cdot}H_2O$.'

The structure of the monohydrate was initially examined by Lundgren using single crystal X-ray diffraction [16]. However, the report by Lundgren contained the statement that '...the experimental intensity material was too poor to allow a complete structure determination'. A complete structure determination and refinement was only achieved much later by single crystal X-ray diffraction and refinement of the atom positions using the configuration offered by Lundgren as a starting point [13]. This resulted in a full determination of the atomic positions and structure of the monohydrate, as shown in Figures 1.2d)-f). The structure is very similar to the anhydrate, consisting of the same ribbons of corner-shared titanium octahedra and sulphate tetrahedra and voids, but the latter no longer take on the regular four- and five-sided shapes. With the addition of the water molecule, each titanium is now coordinated to two bridging oxide ions, three linking sulphate oxygens, and one water oxygen. The remaining oxygen on the sulphate group is directed into the void, where it hydrogen bonds to the water molecule. In a subsequent redetermination of the structure by Ahmed *et al.* [15], the structure was suggested to follow a more symmetrical space group, but with a concession towards disorder being made by introducing anisotropic atomic displacement parameters for two of the oxygens.

The various structural parameters of $TiOSO_4$ and $TiOSO_4{\cdot}H_2O$ proposed by different papers are shown in Table 1.1. The similarity of the structures of the anyhydrate and monohydrate is most obviously seen in Figures 1.3 and 1.4, which provide side-on views of the infinite ribbons in the **b** direction. From these figures it is possible to see that

the introduction of water into the chains results in an alteration in the way that the chains stack with each other. In the anhydrate the chains run parallel, requiring only a translation in the plane to repeat the structure, whereas in the monohydrate the different cross-linking between the sulphate groups and titanium octahedra results in the chains being related by a mirror plane.

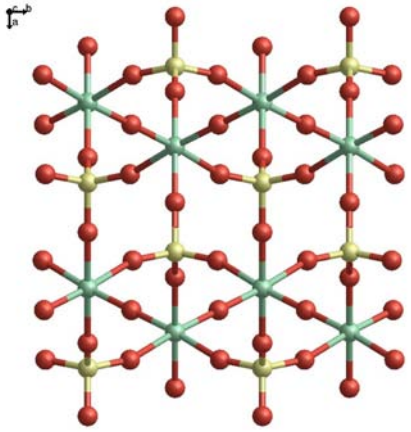

FIGURE 1.3: $TiOSO_4$ viewed down the **c** axis. Green atoms are Ti, yellow atoms are S, and red atoms are O.

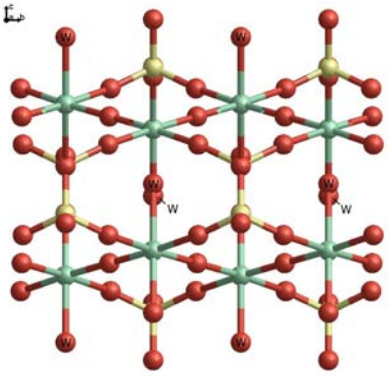

FIGURE 1.4: $TiOSO_4 \cdot H_2O$ viewed down the **a** axis. Green atoms are Ti, yellow atoms are S, and red atoms are O. Hydrogen atoms have been removed for clarity, but water oxygens are labelled with a 'W'.

In light of these structural similarities, it might be assumed that the transition from the monohydrate to the anhydrate could be achieved by heating the monohydrate to remove the water molecules. While this does remove the water of crystallization, the crystal structure is so disordered by the process that XRD experiments produce broad amorphous humps (see Figure 1.5) rather than its characteristic crystalline diffraction pattern. Similarly, going from the crystalline anhydrate to the monohydrate by way of reflux with concentrated sulphuric acid does not yield the desired structure. This is not particularly surprising given the rearrangement that would be required in the

anhydrate in order to allow the water to enter the structure; namely the breaking of a Ti–O bond and introduction of some disorder. The standard syntheses of the anhydrate and monohydrate support this, in that both are started 'from scratch' using a solution of TiO_2 in boiling concentrated (60 - 95 wt%) H_2SO_4 [15]. Using this process, $TiOSO_4{\cdot}H_2O$ is formed at lower concentrations, between 60 - 80 wt% H_2SO_4, while $TiOSO_4$ is formed at concentrations greater than 80 wt% H_2SO_4. It is supposed that the mechanism of formation is a competition between water and sulphate in solution, therefore any increase in sulphuric acid concentration favours the linkage of titanium and sulphate groups.

An alternate means for production of $TiOSO_4{\cdot}H_2O$ is described in the report by Richmond *et al.* [10] which uses amorphous $TiOSO_4$ produced by furnacing $TiOSO_4{\cdot}2H_2O$ at 300°C. The amorphous $TiOSO_4$ is then reacted with H_2SO_4 to produce $TiOSO_4{\cdot}H_2O$. While repeating these experiments, it was found that it is also possible to produce crystalline $TiOSO_4{\cdot}2H_2O$ using this method. More detailed results are discussed in chapter 5.

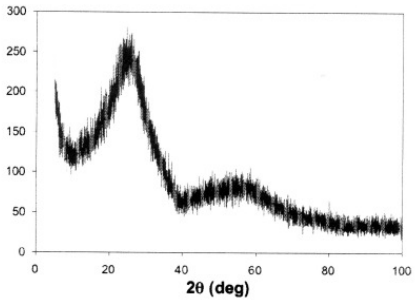

FIGURE 1.5: An XRD pattern of amorphous $TiOSO_4$ produced by heating $TiOSO_4{\cdot}2H_2O$ in a furnace, reprinted from Richmond et. al [10].

1.2.2 The structure of $TiOSO_4{\cdot}2H_2O$

Unfortunately, while single crystals of $TiOSO_4$ and $TiOSO_4{\cdot}H_2O$ are able to be grown and used to determine structures with a high degree of accuracy, the same cannot be said for $TiOSO_4{\cdot}2H_2O$. The crystals that are able to be grown have been described as 'acicular, light in weight, and soft to the touch, closely resembling asbestos' [17]. Powder X-ray diffraction and electron microscope studies of $TiOSO_4{\cdot}2H_2O$ have been performed which describe the decomposition of the crystals in air to form bundles of fibres that remain oriented about the needle axis [18]. This inability to grow single crystals, combined with the complications associated with their morphology has evidently made it very difficult to ascertain the structure of titanyl sulphate dihydrate; in fact, no structural determination has been reported from powder diffraction patterns. This may

be because structure determinations resulting purely from powder diffraction experiment data were not common until the last decade or so, when software dealing with the implicit complications of powder data were made more commonly available.

There does exist a study by Johnsson *et al.* [19] on the thermal decomposition of $TiOSO_4 \cdot 2H_2O$ to anatase TiO_2 which mentions a unit cell for $TiOSO_4 \cdot 2H_2O$ for the first time in the literature, referencing an International Centre for Diffraction Data Powder Diffraction File (PDF) #14-0503. The unit cell is quoted as being orthorhombic with a=16.6509 Å, b=9.3509 Å, and c=3.5022 Å. Curiously, while a search of the most current Inorganic Crystal Structure Database (ICSD) returned the referenced PDF, it made no mention of any unit cell calculated from the diffraction lines it contained, nor the experiment from which it was submitted. It is therefore assumed that this unit cell was included by mistake.

Even though there has been no complete structural determination, there are still some comments on the structure that have been made from the results of various experiments. The most compelling of these comments were based on the IR studies performed on both the monohydrate and the dihydrate [18]. The spectra of the monohydrate shows two bands of Ti-O-Ti chain vibrations at 825 cm^{-1} and 938 cm^{-1}, whereas the dihydrate only shows one band at 868 cm^{-1}. In addition to this the water bending bands are observed at different frequencies (1605 cm^{-1} and 1645 cm^{-1} for the monohydrate and the dihydrate, respectively), and intensity measurements of these vibrations are said to indicate that '...the dihydrate contains only one molecule of water as such, and may be considered a basic sulphate $Ti(OH)_2SO_4 \cdot H_2O$, rather similar to $Zr(OH)_2SO_4$, with each Ti atom bonded to four hydroxyl groups' [18]. The vibrations involving sulphate were found to be too complex to interpret with regards to the coordination of the titanium by the sulphate ion. These arguments seem to suggest that the structure of the dihydrate contains some degree of disorder, possibly a higher degree than that of the monohydrate.

Thermal gravimetric analysis (TGA) has also been used to examine the relationship between the hydrates. A TGA curve published by Johnsson *et al.* [19] is shown in Figure 1.6. While the paper's focus was on the conversion to TiO_2 after 580°C, some comment on the weight losses prior to this have been made in previous studies. In the study conducted by Hanrahan *et al.* [20] it was reported that '...an endothermic reaction observed at 135°C which does not correspond to any observable volatilization, melting, or chemical reaction.' This was followed by the formation of an amorphous material after dehydration at 225°C. This step and the amorphous material were unexplained at the time. Reynolds [18] interpreted the unknown step at 135°C as being the loss of three-dimensional periodicity in the crystals and the '...transition to an X-ray amorphous material [is] the solution of the dihydrate in its more labile water of crystallization.' The

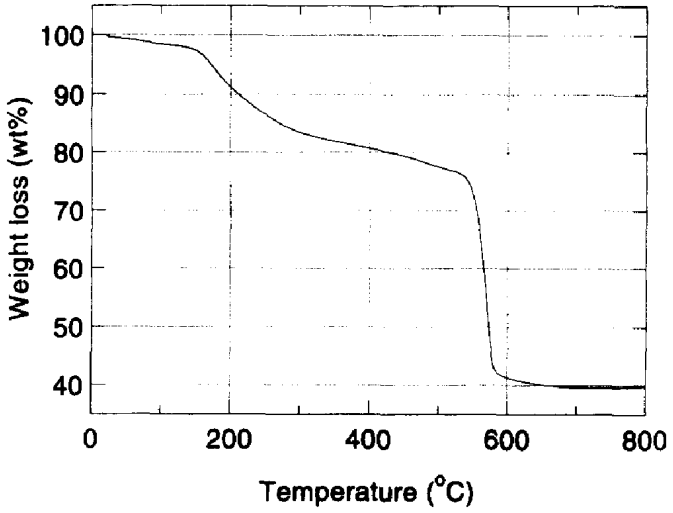

FIGURE 1.6: The TGA curve of $TiOSO_4 \cdot 2H_2O$ reproduced from Johnsson *et al.* [19].

term 'water of crystallization' is used here to describe water molecules that are present in the crystal structure but are not directly bound to the metal ion. So it is thought that upon heating $TiOSO_4 \cdot 2H_2O$ an amorphous material is formed by the water molecules escaping the crystal and redissolving the dihydrate, before further heating evaporates these waters and leaves the anhydrous $TiOSO_4$.

1.2.3 Solution chemistry

A fundamental question regarding the Ti-SO_4-H_2O system is, in what form does the titanium(IV) ion exist in solution? The question arises as a result of the supposition of a titanyl ion, TiO^{2+}, based on the existence of similar oxycations in the higher transition metals and actinide series [21]. In particular, the well-known vanadyl ion, VO^{2+}, is often cited as a good example why a titanyl ion is not an impossibility [22, 23]. However, in general the existence of a titanyl ion is still described as being unproven in most recent literature, and even the number of solid Ti(IV) complexes that have been proven to have a true titanyl core are few. Among these are; TiO(porphyrin) where the Ti-O bond is very short (1.619 Å) [24]; TiO(phtha1ocyanine) [25]; $TiO(acac)_2$, a dimer with a $Ti(\mu\text{-}O)_2Ti$ ring; and $(NH_4)_2TiO(C_2O_4)_2 \cdot H_2O$ which contains cyclic tetrameric anions with a central eight-ring $(\text{-Ti-O-})_4$, although the existence of this last structure has been contested [26].

Beukenkamp [27] was amongst the first to tackle the question of the existence of a titanyl species. Ion-exchange elution techniques were employed to determine that in sulphuric acid, up to around 2.0 M, Ti(IV) exists in solution in equilibirum between hydroxyl species and sulphated hydroxyl species as per the reactions:

$$\mathrm{Ti(OH)_3^+ + H^+ \longleftrightarrow Ti(OH)_2^{2+} + H_2O}$$
$$\mathrm{Ti(OH)_3^+ + HSO_4^- \longleftrightarrow Ti(OH)_3HSO_4}$$
$$\mathrm{Ti(OH)_2^{2+} + HSO_4^- \longleftrightarrow Ti(OH)_2HSO_4^+}$$

These reaction pathways led Beukenkamp to calculate a phase diagram illustrating the degree of complexation of the sulphuric acid with the titanium species. This relationship is shown in Figure 1.7. It should be noted that this diagram has been calculated with the assumption that the concentration of titanium in solution is not large enough to appreciably affect the acidity of the solution.

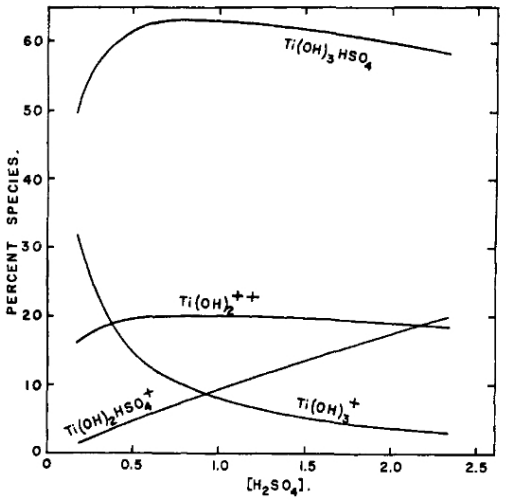

FIGURE 1.7: Relative percentages of different species in H_2SO_4, reproduced from Beukenkamp [27].

Pourbaix [28] produced a phase diagram of the soluble species in the Ti-H_2O system at 25°C that included a domain for $Ti(OH)_2^{2+}$ formation in non-oxidising, strong acids. This diagram is shown in Figure 1.8.

Ellis *et al.* [29] conducted experiments investigating the reduction of Ti(IV) by Cr^{2+} according to the reaction:

$$\mathrm{Cr(II) + Ti(IV) \longrightarrow Cr(III) + Ti(III)}$$

By examining the results of reaction kinetics, obtained *via* stopped-flow spectrophotometry, Ellis was able to surmise that the rate law contained no dependence on the concentration of $[H^+]$ in solution, a feature shared by the reduction of V(IV) by Cr^{2+}. To substantiate this claim, an experiment was carried out to determine the products of the reduction in the presence of Cl^- and compare them to the products of the reduction of V(IV). There was no evidence found for the presence of $Ti(OH)_2^{2+}$,

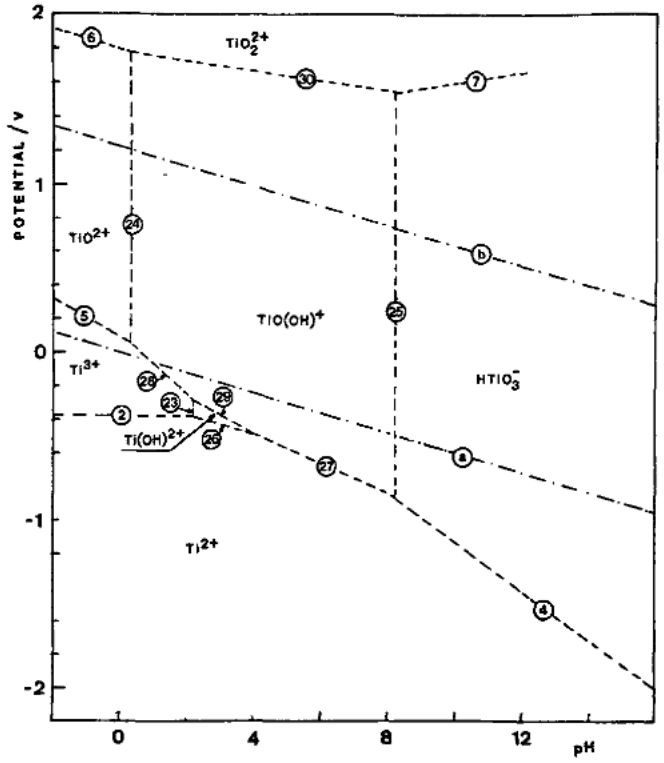

FIGURE 1.8: Domains of thermodynamic stability of soluble species in the system Ti-H_2O at 25°C, reproduced from Pourbaix [28].

therefore the experiment was considered to support the evidence for a TiO^{2+} species. Ellis and Thompson [30] then went on to determine the kinetics of reactions between the TiO^{2+} ion with thiocyanate, pyrophosphate, and hydrogen fluoride.

Gratzel [31] performed a Raman spectroscopic study of the existence of the titanyl ion that was mentioned as being unable to be completed in a previous paper by Ellis *et al.* [30] In this study, a band was found at $\tilde{\nu}$=975 cm^{-1}. This band did not correspond to a hypothetical $\tilde{\nu}$(Ti-OH) band expected at around 500 cm^{-1}. On the basis of the location of $\tilde{\nu}$(Ti=O) bands in the spectra of solids containing a titanyl moiety, it was determined to correspond to that of a Ti=O bond in solution.

Comba [23] addresses the question of the existence of a titanyl ion directly, performing ^{17}O nuclear magnetic resonance (NMR) spectroscopy, Raman spectroscopy, UV-Vis spectroscopy, and Fourier transform infrared (FTIR) spectroscopy on acidic aqueous solutions of dilute hydrolyzed Ti(IV). By performing ^{17}O NMR spectroscopy on a lower temperature solution, a spectral feature at 1028 ppm was recorded which corresponds to a typical region in which titanyl-type oxygens occur. However, studies of the exchange rate determined that the titanyl oxygen thus confirmed was relatively easily protonated and existed in equilibrium with other monomeric species such as $Ti(OH)_2^{2+}$ and Ti^{4+}.

1.2.4 Other studies

Other than the studies shown in section 1.2.2, there are very few recent experiments that make comment on the nature of $TiOSO_4 \cdot 2H_2O$. Instead, they choose to focus on its use in the production of nanoparticles of TiO_2 polymorphs from various starting materials and using different methods. Some examples of these studies include:

- Nanoparticles of anatase TiO_2 with a size distribution of 25-50 nm have been synthesized by the sol-gel route from an aqueous solution of titanyl sulphate [32];
- The effect of temperature [33] on the production of nanoparticles of anatase TiO_2 synthesized *via* an alternative thermal hydrolysis route;
- The effect of alcohol content in solution [34] and starting reagents [35] on the production of nanoparticulate anatase *via* the thermal hydrolysis route; and
- The effect of stirrer speed [36] and seeding volume [37] have been investigated using a batch production method designed to mimic industrial conditions.

However, the main focus of these experiments addresses the nature of the TiO_2 produced with their chosen method, rather than the behaviour of the titanyl sulphate as a reagent.

As part of a previous initiative between BHP Billiton, the Nanochemistry Research Institute, and Curtin University of Technology there have been studies on the effects of temperature, sulphuric acid concentration, titanium solid content, additives, seeding, supersaturation and starting material on the crystal morphology of titanyl sulphate dihydrate [10, 38]. There were no discernible changes reported in the morphology as a result of the variation of these conditions within the range explored. However, the opinion was formed that '...the sulphuric acid and/or water content in solution plays an important role in controlling the phase composition and subsequently the morphology of titanyl sulphate (dihydrate)' [10].

1.2.5 Basic zirconium sulphates

When attempting to solve an unknown structure, it is often instructive to analyse materials that might be considered analogous. In the case of the titanyl sulphates, the most obvious group of materials are the basic zirconium sulphates. There are four known basic zirconium sulphates; zirconium sulphate anhydrate ($Zr(OH)_2SO_4$), zirconium sulphate monohydrate ($Zr(OH)_2SO_4 \cdot H_2O$), zironium sulphate trihydrate ($Zr(OH)_2SO_4 \cdot 3H_2O$), and zirconium sulphate quadhydrate ($Zr_2(OH)_2(SO_4)_3 \cdot 4H_2O$). Their unit cell parameters and space groups are shown in Table 1.2.

TABLE 1.2: Literature values of basic zirconium sulphate cell parameters and space groups.

Structure	a (Å)	b (Å)	c (Å)	Space group
$Zr(OH)_2SO_4$ [39]	11.0921	5.5484	6.7051	P n m a
$Zr(OH)_2SO_4 \cdot H_2O$ [40]	6.4571	11.4517	6.6749	C 1 2/c 1
$Zr(OH)_2SO_4 \cdot 3H_2O$ [41]	7.6467	14.3704	5.4904	P 1 2_1/c 1
$Zr_2(OH)_2(SO_4)_3 \cdot 4H_2O$ [42]	12.7312	6.4030	14.3716	C 1 2/c 1

A brief discussion of each basic zirconium sulphate and their relation to the titanyl sulphate hydrate series follows.

$Zr(OH)_2SO_4$

The crystal structure of $Zr(OH)_2SO_4$ was first determined by El Brahimi *et al.* in 1988, and its structure is shown in Figure 1.9 [39]. It can be seen to be quite similar to that of the structure of titanyl sulphate anhydrate (previously shown in Figure 1.3), with its chains along the **b**-axis being related by a translation in the **a**-axis. The higher coordination number of 8 of zirconium is what allows it to form the double hydroxyl bridges between zirconium atoms. One can imagine that if a formula unit of water were lost from these double hydroxyl bridges, and the remaining oxygen moved to become a single bridging oxygen, this would essentially leave the titanyl sulphate anhydrate structure.

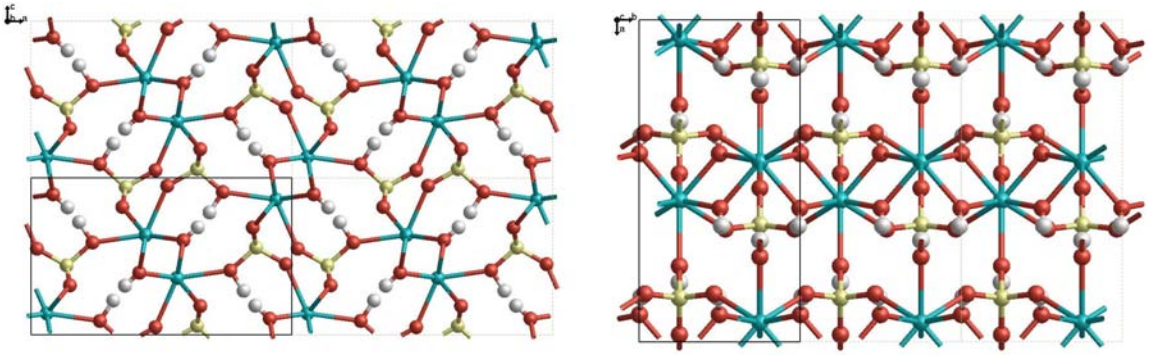

FIGURE 1.9: The structure of $Zr(OH)_2SO_4$ viewed down the **b** (left) and **c** (right) axes. Zr, S, O, and H atoms are coloured turqoise, yellow, red, and white respectively.

$Zr(OH)_2SO_4 \cdot H_2O$

The crystal structure of the second basic zirconium sulphate in the series, $Zr(OH)_2SO_4 \cdot H_2O$, was determined by Hansson in 1973 using single crystal X-ray diffraction data [40] and is shown in Figure 1.10. The addition of a water molecule to the zirconium coordination replaces one of the bonds with the sulphate tetrahedra, and results in a layered chain structure in the **b** direction. Chains of double hydroxyl

bridged zirconium run in the **c** direction, while the zirconia octahedra are linked by sulphate tetrahedra in the **a** direction in an almost planar fashion. The layers in the **b** direction are held together only by hydrogen bonds. In the case of $Zr(OH)_2SO_4{\cdot}H_2O$, the analogy to $TiOSO_4{\cdot}H_2O$ is not as strongly present as that of $Zr(OH)_2SO_4$ to $TiOSO_4$. $TiOSO_4{\cdot}H_2O$ does not form a layered structure in any direction, as a result of its extra sulphate cross-linkages between titania octahedra; each titania octahedra contains bonds to three sulphate tetrahedra, as opposed to two in $Zr(OH)_2SO_4{\cdot}H_2O$.

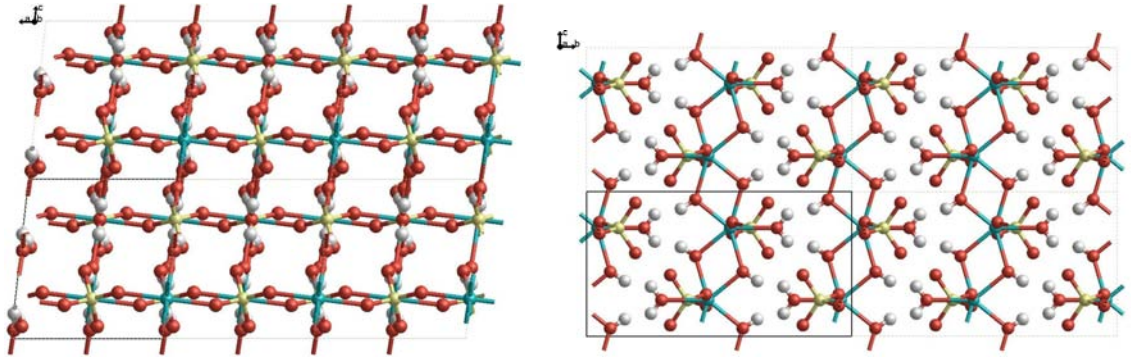

FIGURE 1.10: The structure of $Zr(OH)_2SO_4{\cdot}H_2O$ viewed down the **b** (left) and **a** (right) axes.

$Zr(OH)_2SO_4{\cdot}3H_2O$

The crystal structure of $Zr(OH)_2SO_4{\cdot}3H_2O$ was determined by Gascoigne *et al.* using conventional powder X-ray diffraction [41]. Its structure is shown in Figure 1.11. It too has a layered structure, with the layering now occurring in two directions–that of **a** and **b**–due to the addition of extra water molecules occupying the coordination of zirconium and preventing cross-linkages with sulphate tetrahedra. The chains are stabilised by hydrogen bonding in both layered directions. The double bridging hydroxyls are present once more, forming chains between zirconium polyhedra in the **c** direction.

It is noteworthy that there is no equivalent analogous structure to that of the unknown $TiOSO_4{\cdot}2H_2O$; the basic zirconyl sulphate $Zr(OH)_2SO_4{\cdot}2H_2O$ is not reported as having been produced or analysed in the literature.

$Zr_2(OH)_2(SO_4)_3{\cdot}4H_2O$

The structure of $Zr_2(OH)_2(SO_4)_3{\cdot}4H_2O$ is shown in Figure 1.12, as determined by McWhan *et al.* [42]. There are suggestions of a layered structure in the **a**–**c** plane, with diagonal chains of zirconia octahedra linked with sulphate tetrahedra; these chains cross-linked only by double bridging hydroxyls between zirconia polyhedra. Cross-linking between zirconia polyhedra and sulphate tetrahedra extends into the **b** direction in a translational fashion. From its formula unit, it is obvious that this basic sulphate exists

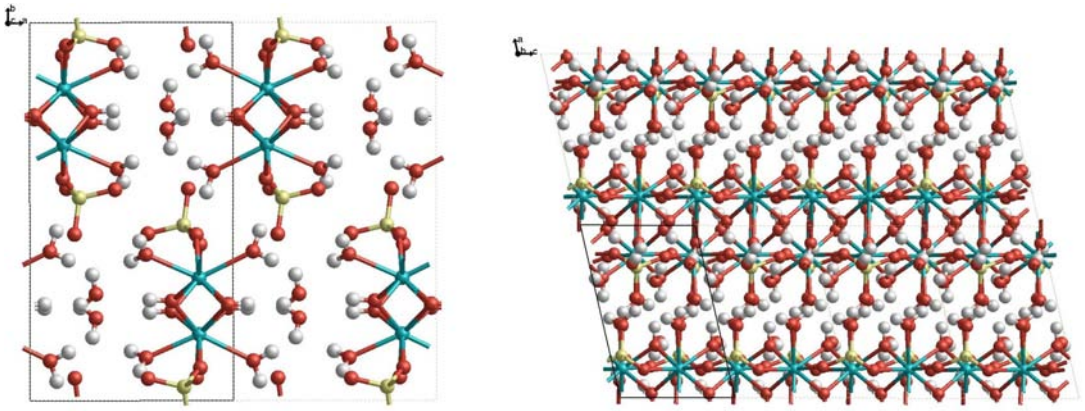

FIGURE 1.11: The structure of $Zr(OH)_2SO_4{\cdot}3H_2O$ viewed down the **c** (left) and **b** (right) axes.

somewhat outside the series of the previous basic zirconium sulphates, and therefore the lack of a layered structure is not too surprising.

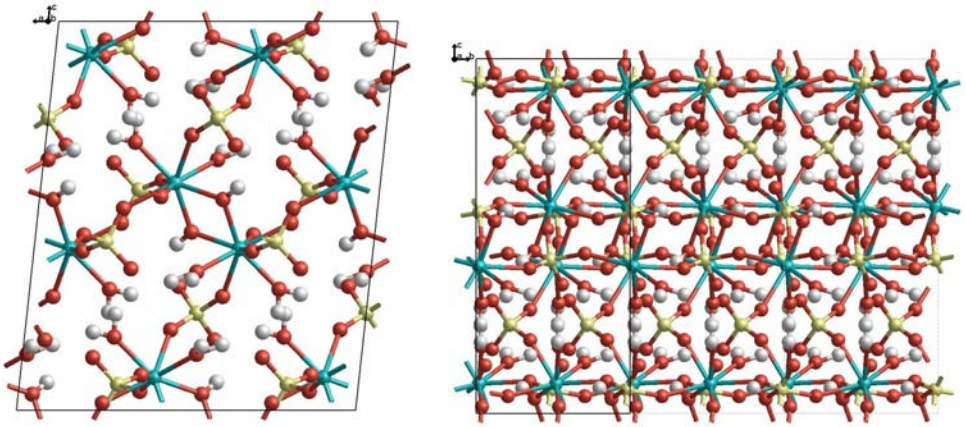

FIGURE 1.12: The structure of $Zr_2(OH)_2(SO_4)_3{\cdot}4H_2O$ viewed down the **b** (left) and **a** (right) axes.

1.2.6 Conclusions

The lack of detailed structural information in the literature for a material such as $TiOSO_4{\cdot}2H_2O$ that has been known about and used in synthesis for such a long time is indicative of a certain degree of difficulty in its determination. The prevailing reason behind this seems difficulty seems to lie in the fact that it does not precipitate as single crystals, instead forming needle-like crystals that are in turn made up of overlapping sub-units that align along the needle axis. The fact that single crystals cannot be grown means that powder diffraction methods need to be called on, which are not nearly as straight-forward as single crystal determinations.

From looking at the basic zirconium sulphates, it is obvious that similarities exist between them and the series of titanyl sulphate hydrates. The repeated formation of chains and cross-linking of titanium/zirconium polyhedra and sulphate tetrahedra suggests that these features will almost certainly be present in any structure of $TiOSO_4 \cdot 2H_2O$. The fact that there is no equivalent analogous structure to that of the unknown $TiOSO_4 \cdot 2H_2O$ in the series of basic zirconium sulphates is somewhat disappointing, in that there is no structure to draw immediate parallels to. However, the limited ways in which to rearrange the structures shown by the higher zirconium sulphates means that there is some hope for producing candidate $TiOSO_4 \cdot 2H_2O$ structures for use in computer simulations and, ultimately, structure refinements.

This thesis will present the experimental and computational work performed in the pursuit of a structural determination of $TiOSO_4 \cdot 2H_2O$. However, before results can be discussed, some time must be taken to provide some background in the form of the theory behind the experimental techniques and computer simulations. These will be discussed in chapter 2 and chapter 3, respectively.

Chapter 2

Experimental techniques

2.1 Crystallography principles

Before discussing the results of the diffraction experiments that have been performed during the project, it is important to provide the theoretical foundation underlying the operation of the equipment associated with various diffraction techniques. This theoretical framework is especially important given the context of structural solution, as so much of the procedure of obtaining structural information from diffraction patterns is governed by how well the variables introduced by instrumentation are understood.

This chapter will provide a brief overview of the theories governing X-ray and neutron diffraction, the practical applications of diffraction experiments, and finally the basic tenets behind the practise of structure solution from powder diffraction.

2.1.1 X-ray diffraction and Bragg's Law

When attempting to solve a crystal structure it is important to choose techniques that provide insight into atom positions, bond lengths, and bond angles. One such technique that has been used reliably for a broad range of materials is X-ray diffraction (XRD) [43]. The basic principle of XRD lies in the fact that atoms in a crystal can act as a grating through which X-rays diffract in very specific directions that are dependent on the spacings between said atoms [44]. This idea can be extended to describe the crystal as being made up of layers of atoms which 'reflect' the X-ray beam under certain conditions; these conditions being when the path differences between reflections from successive planes are equal to an integer number of wavelengths. While this description may not accurately represent the physical reality of the diffraction of X-rays from atoms in a crystal, it does provide a geometrical framework with which to formulate an expression

for the conditions under which it occurs. This formulation is known as Bragg's Law [45, 46];

$$n\lambda = 2d_{hkl}sin\theta \tag{2.1}$$

where λ is the wavelength, n is the order of reflection, d_{hkl} is the lattice plane spacing and θ is the angle of incidence/reflection to the plane. Figure 2.1 shows a schematic illustrating the derivation of Bragg's Law.

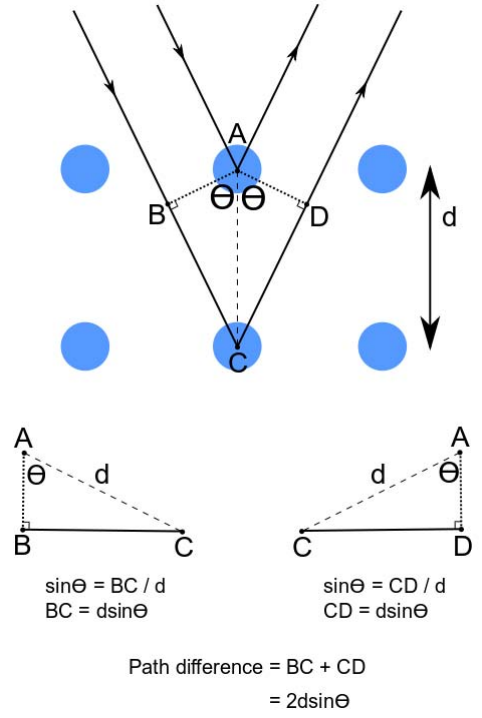

FIGURE 2.1: Schematic illustrating the derivation of Bragg's Law from the path difference of two incident X-rays. If $n\lambda$ is equal to $2d\sin\theta$ they will constructively interfere and diffraction will occur.

2.1.2 Ewald sphere construction

A common method of expressing Bragg's Law that leads more naturally to the experimental techniques which are to be discussed in later sections is Ewald's reflecting sphere construction [47]. An Ewald sphere is a geometrically based construction that uses the reciprocal lattice to show which planes in a crystal will result in a diffraction event. Consider a hypothetical crystal that has just one plane of atoms. To build an Ewald sphere, first we place the crystal such that this plane satisfies the Bragg condition.

We then trace a sphere (or, in the two-dimensional case shown here, a circle) of radius $1/\lambda$, where λ is the incident X-ray wavelength, and place the crystal at its centre. The incident beam is then drawn to pass through both the crystal and the origin of reciprocal space. Wherever the circle intersects with a reciprocal lattice point, i.e. at point B, a diffracted beam results. This construction can be seen in Figure 2.2.

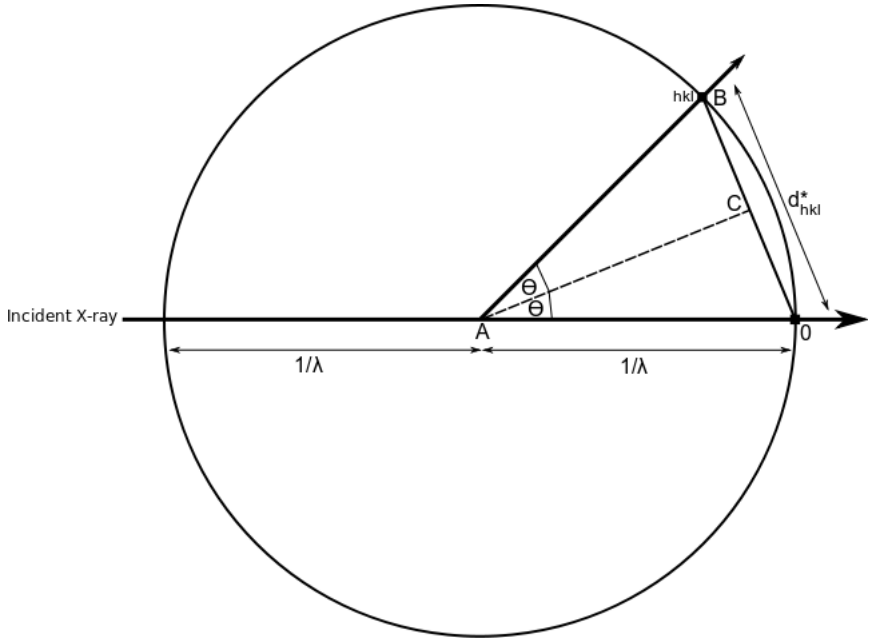

FIGURE 2.2: Schematic showing the construction of an Ewald sphere in two-dimensions. Point A is the crystal location, while O is the origin of reciprocal space. Point B represents the reciprocal lattice point resulting from the single plane of atoms. As point B is located on the Ewald circle, the plane of atoms is known to diffract.

In the above there is only one reflecting plane of atoms and therefore one reciprocal lattice point (at B) which we have made satisfy the Bragg condition for ease of example. However, in real crystals there are many more lattice points and it is a relatively simple matter to extend the Ewald sphere construction to include all the reciprocal lattice points in a crystal. This can be seen in Figure 2.3. While there are still only two lattice points that are fulfilling the Bragg condition, we can imagine that if we rotated the crystal, the plane of points would also rotate. Referring again to Figure 2.3, we can see that if we rotated the crystal around the (00l) direction, we would be rotating the reciprocal lattice of points around the red line. In this way, different points would, at some stage, be situated on the Ewald sphere. It should be noted that this representation is a two-dimensional slice of an Ewald sphere constructed in three-dimensional space, and as a result would need to be projected 'above' and 'below' the page in order to consider different slices of the sphere–i.e. to determine whether different sets of lattice points satisfy the Bragg condition.

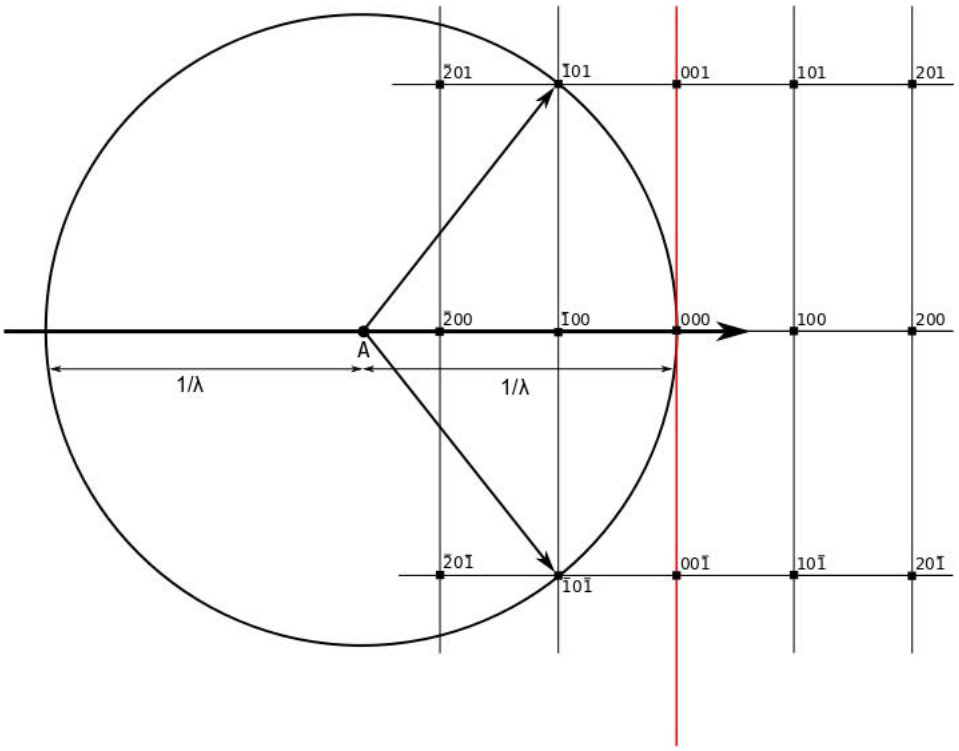

FIGURE 2.3: The Ewald sphere construction in two dimensions for multiple lattice points. The red line represents the (00l) axis about which the lattice would rotate if the crystal were rotated in the same direction, in order for more points to intersect the Ewald sphere.

2.1.3 Structure factor and phase

Thus far, the formulations discussed have been based on point atoms situated at each lattice point with no difference in how much or how little they scatter. However, in order to fully understand the way X-ray diffraction patterns are produced, we now need to consider two additional facts:

- X-ray diffraction occurs as a result of interactions with electrons, and thus we must account both for the fact that electrons have a distribution around nuclei, and that different elements will have different contributions to the overall scattering intensity; and
- The complexity of atomic distributions in samples results in multiple diffraction events at any one scattering angle.

These points are addressed in the calculation of the atomic scattering factor and the structure factor. The atomic scattering factor, f, is described by the equation:

$$f(\mathbf{S}) = \int \rho(\mathbf{r}) e^{i(\mathbf{S}\cdot\mathbf{r})} d^3\mathbf{r} \tag{2.2}$$

where $\rho(\mathbf{r})$ is the electron charge density about the centre of mass ($\mathbf{r}$=0) of the atom, and $\mathbf{S}$ is the vector difference between the incident and diffracted X-rays, known as the diffraction vector. This equation takes into account the fact that atoms are not point charges; they possess an electronic distribution which will be different for each atom. It should be noted that the subtle effects of electrons interacting with other atoms through bonding are ignored in this formulation.

Previously, Figure 2.1 showed diffraction occurring from one set of atoms at each lattice point. But if we add another set of atoms parallel to these first ones but displaced by some distance, as shown in Figure 2.4, we can see that there will be some interference between the scattered X-ray beams as a result of the phase difference between them [48].

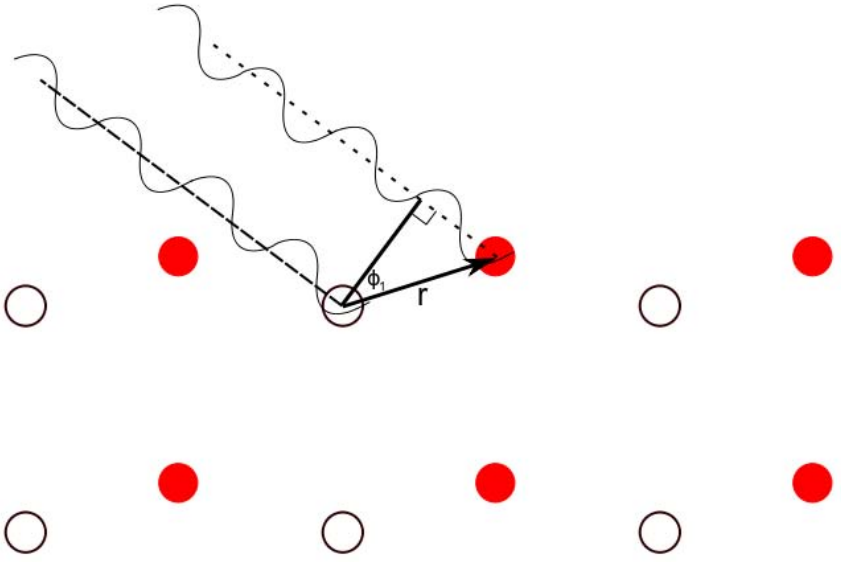

FIGURE 2.4: Illustration showing the phase difference of scattered beams due to multiple planes of atoms.

The total wave resultant from this interference can be calculated as a linear addition of wave vectors of magnitude $\mathbf{f}_1$ and $\mathbf{f}_2$ with a phase difference of ϕ, as shown in Figure 2.5. The structure factor, F_{hkl}, can then be used to describe how an X-ray interacts with the unit cell of a crystal, and is written as:

$$F_{hkl}(\mathbf{S}) = \sum_j f_j e^{-i\Delta\mathbf{S}\cdot\mathbf{r}_j} \tag{2.3}$$

where $\mathbf{r}_j$ is the position of the j^{th} atom in the unit cell. Note that the summation includes an imaginary term in the exponential that allows for interference between waves, as shown in Figures 2.4 and 2.5. It should also be mentioned that f_j is also generally convoluted with a function known as the temperature factor which takes into account the thermal vibrations of atoms.

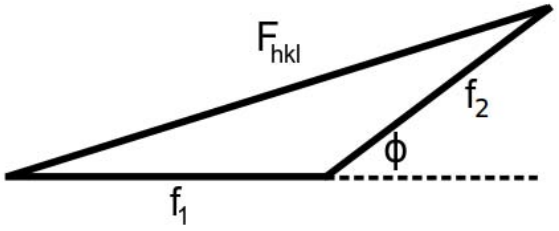

FIGURE 2.5: The structure factor resulting from the phase difference of the two diffraction events resulting from the vector addition of $\mathbf{f}_1$ and $\mathbf{f}_2$.

The structure factor becomes important when we consider the intensities recorded by diffractometers. These intensities are proportional to the magnitude of the complex conjugate of the structure factor, meaning that this will always be real. Therefore when we measure the intensities of diffraction events, we are only getting the scalar quantity, $|\mathbf{F}|$, not the vector quantity. In other words, we are losing the phase information. This loss is referred to in the literature as the 'phase problem' and forms one of the most problematic issues in crystal structure determination; how do we recover this phase information? The higher resolution data of single crystal diffraction is able to overcome this loss through techniques such as direct methods, using the full three-dimensional reciprocal space afforded by being able to rotate the crystal. Unfortunately, the equal distribution of random crystal orientations as produced by a crystalline powder sample causes this three-dimensional reciprocal space to be projected onto one dimension. This causes a large loss of information as reflections overlap, a problem that is often exacerbated by line broadening resulting from the microstructural size and strain effects that are present in crystalline powder samples [49]. The challenges faced in addressing this loss of information in the process of structural determination from powder diffraction will be explained in more detail later in this chapter.

2.2 X-ray diffraction geometry

The preparation of single crystals of sufficient size for single crystal diffraction experiments is often difficult, or in many cases completely impossible. As the latter case applies to the system that is being examined in this thesis, focus will be given to the problems involved in the execution of powder X-ray diffraction experiments. A brief discussion of single-crystal geometries is presented, but while there may be some overlap in the applicability of the topics covered between the two techniques, they are not interchangeable and unique challenges and concepts arise in each.

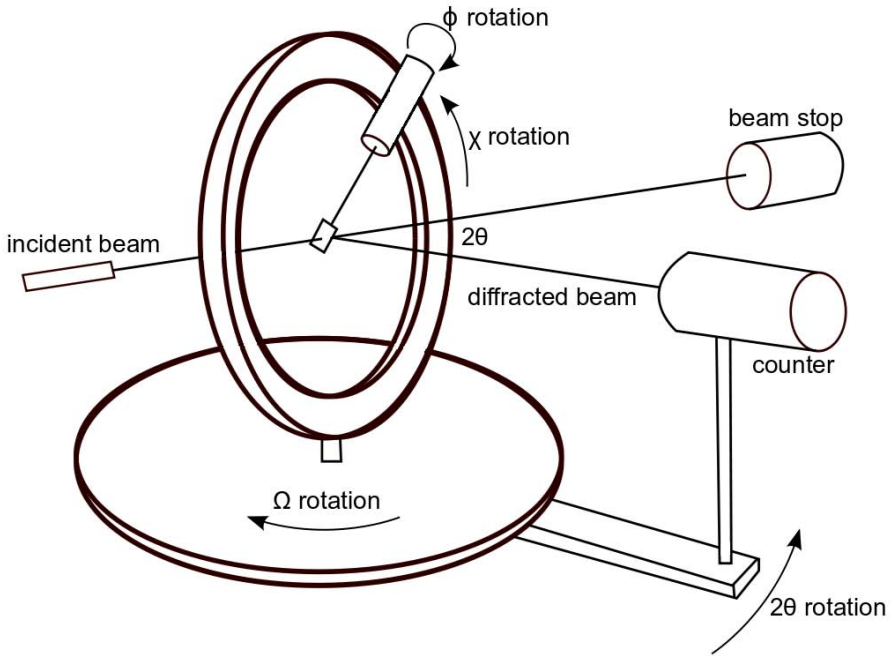

FIGURE 2.6: An example geometry of a single crystal diffraction experiment [50].

From the previously discussed example of a single crystal in a monochromatic beam of X-rays, it can be seen that there are two variables that dictate whether a lattice point intersects with the Ewald sphere and satisfies Bragg's law; these being θ and λ. In order to explore reciprocal space experimentally, either one of these can be chosen to vary while the other remains static. Generally speaking, variable θ geometries predominate in modern experimental setups, and so they will be focussed on. Figure 2.6 shows that in the case of single crystal diffraction experiments, the incident X-rays are filtered by monochromators (not shown) to a constant wavelength, while variable θ (and Ω, χ, and ϕ) is achieved by rotating the crystal and altering the geometry of the incident X-rays and the detector. In this way one can imagine that all possible orientations of lattice planes are able to be explored, resulting in a full set of signals from the lattice planes that have fulfilled the Bragg condition. These signals are recorded and converted into an intensity by the detector for later interpretation.

Diffraction using powder samples relies on a different concept in order to achieve variable θ. The detector is still rotated, but the sample need not be, as a result of the random orientation of crystals throughout the powder. At any value of θ, some proportion of the *hkl* planes in some of the crystals will be oriented in such a way as to satisfy the Bragg condition for reflection. The assumption here is that the crystals in a powder sample are oriented randomly around the axis of the incident X-rays, so that no single *hkl* plane is given an artificially overestimated relative intensity.

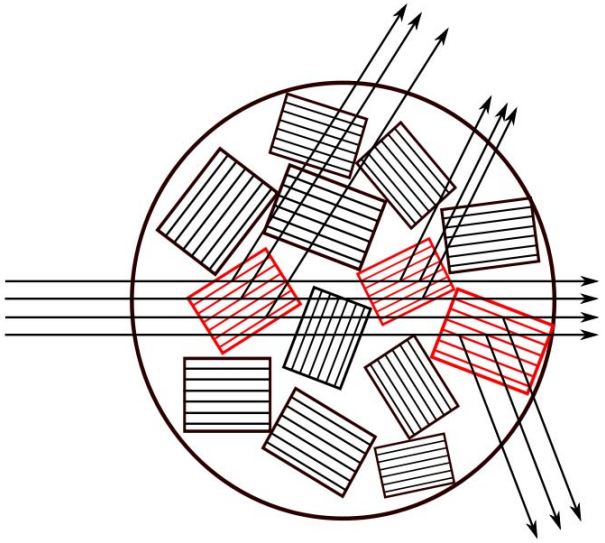

FIGURE 2.7: The occurence of diffracting domains in a powder sample.

There are two main experimental geometries used for powder diffraction experiments; Bragg-Brentano flat plate geometry, and Debye-Scherrer transmission geometry. Laboratory X-ray sources usually employ the former, whereby monochromated X-rays are fired at a flat specimen holder from a source that is at an equal distance and angle to the sample as the receiving detector. The θ angle is varied by tracking the detector and source through an arc of a circle, at the centre of which the sample lies. Debye-Scherrer transmission geometry is similar in its setup, but rather than a flat specimen holder, a thin capillary is used to hold the sample. The X-rays are then directed through the capillary and the diffracted beam is collected on a curved strip of film, or in more modern machines a microstrip sensor or array of detector modules. These detectors produce signals which can be interpreted by software to produce diffraction patterns.

2.3 Applications of polycrystalline (powder) X-ray diffraction

X-ray diffraction is primarily used to gain information related to structural parameters. Phase identification, crystal size, crystal strain, and texture are all able to be determined from X-ray diffraction patterns produced by powder samples. In this section we will discuss the experimental basis for the determination of each of these structural features.

2.3.1 Phase identification

When collecting powder diffraction patterns, the particular peak positions and intensities of any one sample act as a unique identifier when compared to any other sample. It is therefore easy to imagine that the ability to search and compare the peak positions and intensities of a large database of diffraction patterns would be of great use in determining the phase or phases present within an unknown sample. Such information is available through the International Centre for Diffraction Data and the database of powder diffraction files (PDFs) that they maintain. Over 200,000 inorganic materials are represented in the PDF-2 database alone. Each entry includes the chemical formula, name, experimental conditions, diffraction parameters, a set of d-spacings and their corresponding *hkl* values and relative intensities.

Searching a database as large as this is impossible without employing a system to narrow down potential candidates. In a similar manner to automatic indexing, computers are used to speed up this process with 'search/match' software that can scan the huge number of entries and provide candidates for the identification of phases in the user-provided diffraction pattern (a review of the methods used in searching databases in this way can be found in 'Data Mining in Crystallography' [51]). Often it is not as simple as merely clicking a button. Phase purity, for example, can alter the order of relative intensities and therefore lead to anomalous characterisation. On top of this, the enormous range of results can mean that there are multiple datasets that match a provided sample, varying only slightly by way of experimental conditions or instrumental error [52]. More complex algorithms than the initial, influential Hanawalt search method [53] have been developed to deal with these possible pitfalls and provide ranked matches, but it is still important to be wary when the sample is not known to be absolutely pure.

2.3.2 Crystal size and strain

The profile, or shape, of a diffraction peak depends on many different factors including, but not limited to; instrumental factors such as detector slit width or the cross-sectional area of the sample irradiated, defects in the crystal lattice, crystallite size, and crystallite strain. Crystallite size effects result from the fact that there is a limit in the size of the crystal domains that are able to produce coherent diffraction. If we were to take perfect crystal–one that extends infinitely in all directions–it would contain no line broadening from the sample. The deviation of powders from this ideal crystal gives the effect of line broadening.

The crystal size and strain cannot simply be calculated from the observed broadening of the peak. Instead, the broadening from instrumental factors must be subtracted from the overall observed breadth. This is usually achieved by determining the instrumental broadening by the peak shape of a large-grained material in which the crystallite size broadening is assumed to be negligible. It is then possible to simply subtract this measured instrumental broadening from the observed broadening to give the size broadening. Similarly, to obtain the strain broadening on its own, a stress-free material must be used to calculate the instrumental contribution.

Whether by this or other methods, once the size and strain broadening are obtained they can be used in the Hall-Williamson method to determine size and strain [54];

$$\beta \cdot cos(\theta) = \frac{k\lambda}{D} + \eta \cdot sin(\theta) \tag{2.4}$$

where β is the combined size/strain broadening, θ is the angle of incidence, η is the strain in the crystals, D is the size of the crystals, and the parameter k ranges between 0.8-1.4. Using this equation, a plot of $\beta \cdot cos(\theta)$ on the y-axis versus $sin(\theta)$ on the x-axis will give a straight line with a y-intercept of $\frac{k\lambda}{D}$ and slope of η.

2.3.3 Texture

In order for the intensities in a diffraction pattern to accurately represent the reciprocal lattice, the crystallites within a powder must be randomly oriented around the beam. Texture, also known as 'preferred orientation' or 'fabric', is the name given to the situation where the crystallites in a powder do not have this random orientation. If the statistics are skewed by crystals orienting in a particular direction, then this will

result in systematic errors in the intensities and structure factors. Crystallites that have plate-like, or acicular (needle-like) morphologies are prone to this behaviour. Unless they are perfectly spherical, all crystallites will show some degree of texture. Crystallographic texture can be determined by the use of pole figures that are produced by using a specific geometry of diffractometer known as a texture goniometer.

There are a number of methods to eliminate preferred orientation from a sample [55–57]:

- Change sample holder geometry: Back-loading the sample rather than front-mounting it can reduce the preferred orientation associated with packing the sample into the holder, as long as the crystals are very finely ground. Also, capillary geometries give much less preferred orientation as they do not need to be packed as firmly.
- Reducing crystallite size: If the material is subjected to grinding techniques, it can have its crystallite size significantly reduced, therefore increasing the chances of individual crystallites being randomly oriented.
- Spinning the sample: Spinning the sample while recording a diffraction pattern averages out the contributions from crystallites and can result in a larger number of crystals being surveyed.
- Suspension media: Mixing and suspending the sample in a solid dilutent can help to randomise the crystallite orientation, but can have some detrimental effects, such as reduced diffraction intensities and an increase in background from amorphous scattering.

2.4 Structure determination from powder diffraction

One of the main uses of X-ray diffraction patterns is in the exploration and classification of unknown materials and their structures. Included in this usage is the complete determination of unknown structures. As previously stated, structural determination from single crystals has long been a standard practise, with many well-developed methods that have been adapted into software and refined to a point where the solving of a single crystal structure is almost guaranteed when adequate care is taken to prevent obvious errors within the sample and the instrument. This is made possible by the preservation of three-dimensional reciprocal space that can be analysed to atomic resolution.

However, there are times where, for one reason or another, a single crystal is unable to be prepared. In these cases, powder diffraction is often the only way to gain

structural information about the material. Unfortunately, structure solution from powder diffraction is made much more difficult than that of single crystal diffraction as a result of the collapse of the three-dimensional reciprocal space into the one-dimensional representation of a diffraction pattern. Nevertheless, the steady improvement of powder diffraction instruments, coupled with the development of more complex algorithms capable of taking advantage of increasing computer power, have resulted in the process of structure solution from powder diffraction becoming–if not straightforward–at least capable of being described in a step-by-step manner [58].

The structure determination process can be broken up into a number of steps, each vital to the success of the final result [59]:

- Sample preparation and instrument choice
- Indexing
- Space group determination
- Integrated intensity extraction
- Structure determination
- Rietveld refinement

In the following sections, each of these steps will be discussed.

2.4.1 Sample preparation, instrument choice, and data collection

Preparation of the sample is an often underappreciated first step in the process of structure determination. While there do exist corrections that account for instrumental and sample specific abberations, these corrections are approximations and do not fully eliminate the errors. There are two main objectives that need to be considered when preparing samples; providing an adequate number of crystallites to be surveyed by the incoming beam, and ensuring that the crystallites thus surveyed are randomly oriented.

Grinding is a frequently cited method of achieving both of these aims. Grinding the sample, whether by hand using a mortar and pestle or using machinery such as a micronising mill, breaks up and reduces the size of crystallites, thus increasing the number of crystallites that are in a unit volume. There are still considerations that need to be kept in mind, for example the degree of grinding is important as too much may result in size and strain effects, or induce phase transitions [60]. Instrumentally, widening the beam is another obvious choice, though it should be noted that this will reduce the

resolution and should be used with caution. Rotating the sample is another commonly used technique, as this allows more of the sample to be analysed and averages volumes of crystallites within the sample. If there is enough of the sample, multiple datasets can be taken and either re-analysed for improvement or averaged together to give better statistics.

The flat-plate geometry found in most laboratories has a tendency to produce preferred orientation in a sample as a result of the sample preparation requiring the sample to be packed into the holder. If a flat-plate geometry is to be used, a spinner can be used as described above: Side-loading and back-pressed sample holders can also help eliminate orientation effects. With regards to the sample, it can be mounted in an epoxy glue or gum, though it must be noted that this will obviously influence counting statistics and the level of background present in the pattern. Transmission capillary (Debye-Scherrer) geometry does not suffer nearly as much from preferred orientation as it does not need to be pressed into the capillary as tightly, and is the better choice when it is available. Unfortunately very few laboratory diffractometers feature this geometry, which is more commonly found at synchrotron sources. Particle statistics may become an issue in capillaries due to much less sample being subjected to the beam. In this case, grinding to a fine enough extent becomes paramount to obtaining quality data.

Instrumental decisions are often made as a result of availability, making laboratory X-ray diffraction a very common choice as most universities will have at least one diffractometer available for use. X-ray diffraction is frequently quoted as having the best prospects for structure solution compared to neutron diffraction, the relatively constant nuclear scattering lengths of which correspond to a higher number of visible atoms and less success in determining heavy atom positions within the structure. Neutron diffraction remains more important in the latter stages of structure refinement, and in determining positions of lighter elements [57]. The choice of wavelength with any instrument is important, though often it is dictated by the established setup of the laboratory. In general, wavelengths that cause atoms in the sample to fluoresce should be avoided. Some geometries, such as transmission, require a shorter wavelength to overcome absorption in the sample and the beam path.

Wavelength choice is important when considering the number of independent observations in a diffraction pattern, and hence how 'possible' it is to solve the structure from the information available. Powder diffraction has a greatly reduced amount of information present in the diffraction pattern when compared to single crystal data because the intensities of overlapping reflections need to be deconvoluted before they can be assigned. The greater the separation of overlapping reflections – i.e. the longer

the wavelength – the greater the confidence in the deconvolution process, and the more accurately intensities can be assigned and used for structure solution.

Thus, when collecting data, it is important to optimise the number of intensity counts that are accumulated at each step, and the number of angular points that are measured across the width of the peak; the step time and step width, respectively. These two variables define the integrated intensities that are the basis for structure solution, and therefore getting them right is highly important. However, while one could easily just increase the step time and narrow the step width to their limits to ensure that the counting statistics are as precise as possible, often in modern laboratories some limit is placed on the amount of time available to the user. Thus if the sample is somehow misaligned or contaminated, then a lot of time has been wasted for no result. Instead, the step time and width should be optimised according to how much peak overlap is expected and how broad the peaks are expected to be, in order to allow for rerunning of the sample should anything go wrong.

Once data has been collected and corrected for instrumental error, the task of analysing the data and extracting information from it can begin. The first step in doing so is the indexing of the pattern.

2.4.2 Indexing

In the process of structure determination from powder diffraction, the determination of the lattice parameters–that is, the dimensions of the unit-cell–is a necessary first step. In the early days of structure determination, indexing was a process completed manually by the use of peak positions and equations that related the peak positions and X-ray wavelength to reciprocal space vectors. Nowadays it is more common to rely on computational methods that are based on the same equations but are able to test thousands of possible unit cells automatically. In this section a brief explanation of the mathematical basis of these methods will be presented.

The first step in indexing is usually to take the dot product of a reciprocal lattice vector with itself;

$$\mathbf{r}^*_{hkl} \cdot \mathbf{r}^*_{hkl} = (h\mathbf{a}^* + k\mathbf{b}^* + l\mathbf{c}^*) \cdot (h\mathbf{a}^* + k\mathbf{b}^* + l\mathbf{c}^*) \tag{2.5}$$

which, when the dot product is expanded, results in:

$$(\mathbf{r}^*_{hkl})^2 = h^2a^{*^2}+k^2b^{*^2}+l^2c^{*^2}+2hka^*b^*cos\gamma^*+2klb^*c^*cos\alpha^*+2hla^*c^*cos\beta^* = \frac{1}{d^2_{hkl}} \quad (2.6)$$

For convenience we introduce the term Q_{hkl}, where:

$$Q_{hkl} = \frac{1}{d^2_{hkl}} \quad (2.7)$$

We then use (2.6) and (2.7) to define six parameters, a_{ij}, that are directly related to the reciprocal cell and therefore the real space cell parameters;

$$Q_{hkl} = h^2a_{11} + k^2a_{22} + l^2a_{33} + hka_{12} + kla_{23} + hla_{13} \quad (2.8)$$

where $a_{11} = a^{*^2}$; $a_{22} = b^{*^2}$; $a_{33} = c^{*^2}$; $a_{12} = 2a^*b^*cos\gamma^*$; $a_{23} = 2b^*c^*cos\alpha^*$; $a_{13} = 2a^*c^*cos\beta^*$. Determination of all six a_{ij} values is not necessary for every symmetry. For the generalised case we need to find the three crystallographic indexes (h, k, and l) such that;

$$Q_{obs} - \Delta < h^2a_{11} + k^2a_{22} + l^2a_{33} + hka_{12} + kla_{23} + hla_{13} < Q_{obs} + \Delta \quad (2.9)$$

where Δ is usually given as an input parameter from the measured data. Automatic indexing programs, such as ITO [61] and DICVOL04 [62, 63], utilise this equation in various methods in order to produce trial indexing solutions. However, in all these methods there needs to be a criterion for the physical plausibility of each solution. Otherwise it would be all too easy to end up with results that meet the inequality illustrated in (2.9), but consist of huge cell parameters and volumes. These criteria are usually referred to as figure of merit (FoM) tests, and they are used as checks to rank results that are obtained from automatic indexing.

The de Wolff figure of merit is usually written as M_{20} and can be defined as;

$$M_{20} = \frac{Q_{20}}{2 \cdot \langle Q \rangle \cdot N_{20}} \tag{2.10}$$

where N is the number of calculated Q values (20), Q_{20} is the Q value for the 20^{th} indexed line, and $\langle Q \rangle$ is the average discrepancy in Q for the 20 indexed lines [64]. When applied to an indexing result, an M_{20} of greater than 10 is generally thought to indicate a physically reliable result. There are a small number of situations where indexing can achieve this result without being physically plausible, but as a general rule the de Wolff figure of merit is very robust as a test. Geometrical ambiguities within automatic indexing programs are not uncommon, but can be investigated in a fairly systematic manner [65].

From indexing a diffraction pattern, we obtain a set of unit cell parameters, a, b, c, α, β, and γ. Each peak present in the pattern is also given a hkl value based on the indexing, corresponding to the lattice plane in the unit cell that has produced that particular reflection. This becomes important in the later step of space group determination of the system.

2.4.3 Integrated intensity extraction

The extraction of integrated intensities from a powder diffraction pattern is the process that most obviously shows the disparity in available information between structure determination from single crystal diffraction patterns and structure determination from powder diffraction patterns. As previously stated, powder diffraction patterns suffer greatly from the overlap in peaks that occurs when collapsing the three-dimensional reciprocal space of a single crystal into the one-dimensional representation of a powder diffraction pattern. While this can be compensated to a certain extent by the increased resolution of synchrotron X-ray sources, at higher $sin(\theta)/\lambda$ the overlap between peaks is inevitable since, generally speaking, the number of diffraction peaks increases with $(2sin(\theta)/\lambda)^3$ [60]. It is therefore highly desirable to have a method with which the overlapping peaks can be modelled and deconvoluted such that the integrated intensities can be accurately estimated and incorporated into any subsequent structure solution methodology.

The major step in the extraction of integrated intensities was made by Hugo Rietveld [66]. Before Rietveld, a crystallographer might manually integrate intensities, discarding any peaks that appeared to be overlapped. If a model had been developed, they could generate a powder diffraction pattern and visually compare it with experimental

data to verify the model through similarities. If they were able to program, they also might alter a piece of single crystal software in order to take into account overlapping reflections [67]. For example, while single crystal software might make the assumption that every reflection is independent, a crystallographer with the appropriate knowledge could rewrite the software such that a particular reflection was a sum of two reflections (for example, the Cheetham group at Oxford [68]). This was, understandably, a tedious process.

Rietveld contributed two major steps in making the extraction of intensities from powder diffraction data a tractable problem. The first of these was the realisation that if an experimentally produced pattern could be modelled, it could be compared to a pattern computed from a model and the fit between the two could be optimised. This was similar to the process that was already being undertaken by single crystal programs, except experimentally dependent parameters were now required to be fitted. These included background functions, peak broadening due to size/strain, and lattice constants. A list of reflections and their corresponding structure factors, F_{hkl} would be produced, and from these peak heights would be generated. These peaks would then be convoluted with the experimental parameters and their fit with experimental data could be optimised by least-squares regression. However, peaks that overlapped were still unable to be included in the fit, which resulted in a much-reduced dataset and therefore less confidence in any model.

This problem was addressed in the second part of Rietveld's contribution. When trying to solve a structure, what we really would like to have is the observed structure factors of each peak, for use in techniques such as Patterson and Fourier map analysis (discussed in more detail later). Unfortunately, due to the loss of phase information in the collapse of the three-dimensional lattice into a one-dimensional diffraction pattern, this is not possible. Instead, the next best thing we can do is use structure factors calculated from a model to make an estimate as to how to apportion intensity between overlapping peaks. So in the case of two overlapping peaks:

$$A_1(obs) = \sum_i \frac{A_1(calc) \times q_1(i)}{A_1(calc) \times q_1(i) + A_2(calc) \times q_2(i)} (obs(i) - back(i)) \tag{2.11}$$

$$A_2(obs) = \sum_i \frac{A_2(calc) \times q_2(i)}{A_1(calc) \times q_1(i) + A_2(calc) \times q_2(i)} (obs(i) - back(i)) \tag{2.12}$$

where:

- $A_k(calc) = j_k|F_k|^2$ is the integrated intensity of the peaks;
- j_k is the reflection multiplicity of the peaks;
- $|F_k|^2$ is the structure factor magnitude of the peaks;
- $q_k(i) = c_k(i)H_k(i)$ is the product of $c_k(i)$ (which is in turn made up of polarisation, absorption, and extinction terms) and $H_k(i)$ (which is the normalised peak shapes);
- $obs(i) - back(i)$ is the observed peak at the ith point in the diffraction pattern with the background subtracted.

If we sum the two formulae, we end up with a very simple expression;

$$A_1(obs) + A_2(obs) = \sum_i (obs(i) - back(i)) \tag{2.13}$$

which shows that the sum of the observed peak areas are always equal to the background-subtracted area of the peaks in a diffraction pattern.

Rietveld's contributions greatly increased the feasibility of obtaining structural determinations from powder diffraction data. However, Rietveld's method still relied on the knowledge of structure factors beforehand, which, within the confines of structure solution, is certainly not always the case. Fortunately, there exist two methods for integrated intensity extraction without prior knowledge of structure factors which are employed in computer software packages today. The first of these is known as the iterative Le Bail method [69] after its formulator, Armel Le Bail. Le Bail's method extends Rietveld's method to a situation where no structural information is known beforehand and therefore no structure factors can be calculated. Rather than setting the calculated structure factors, $F_{hkl}(calculated)$, from the structural model, the Le Bail method instead sets them all to be equal to some initial value. We then use Rietveld's method for extracting approximations of $F_{hkl}(observed)$ from independent and overlapping peaks. Once this is done, we reset the $F_{hkl}(calculated)$ to the extracted $F_{hkl}(observed)$ values, and iterate. With each iteration, the estimations of the peak areas converge to give the values of the integrated intensities of peaks; even of those overlapping to a significant extent. The resulting list of integrated intensities can then be used to calculate the structure factors, and from there Fourier map analysis that might lead to placement of atoms in the structure. The popularity of the Le Bail method can be attributed to the fact that it only requires a small modification to the Rietveld method.

The other well-known method of extracting integrated intensities is the Pawley method [70]. The Pawley method uses the same least-squares fit to the peak shape as the Rietveld and Le Bail methods. However, rather than setting the values of parameters relying on atomic position from a structural model, all parameters that relied on atomic coordinates (i.e. the peak areas and intensities) are set to be variables. In other words, while parameters such as the unit cell, zero-point shift, and peak shape (e.g. Gaussian character, Pseudo-Voigt character) which determine peak position and peak shape are still able to be set from experimental data, the parameters that give the peak areas (determined by the atomic positions) are set to be the peak areas themselves and refined.

Present in both methods is a caveat with regards to extracting peak profiles at high angles. When the Bragg peak overlap is so extreme that no features can be made out against the background, it is obviously impossible for any method to reliably provide extraction. Where this point occurs in any one pattern is variable and often down to the judgement of the user, but caution must be taken when trying to extract too much data from the higher angles of a diffraction pattern.

2.4.4 Space group determination

Space group determination is one of the more difficult steps in the process of structure determination from powder diffraction, traditionally involving a manual inspection of the presence or absence of indexed peaks. Each space group has a set of systematic absences such that certain indexed peaks will not be present in the diffraction pattern. For example, the $P2_1$ space group will have systematic absences of $k = 2n + 1$ for the $0k0$ peaks.

Unfortunately, the loss of three-dimensional reciprocal space means that a lot of the peaks with high Miller indices that might have been used to more specifically determine the space group possess a high degree of overlap. This peak overlap often occurs such that at high angles a peak absence overlaps with a peak that is present for all space groups, and therefore the absence is not counted. While the well-separated peaks at low-angles can usually be used to make a rudimentary estimate of the space group, quite often there will be a number of space groups that match the limited number of absences counted after overlap has resulted in the discarding of high-index peaks. In fact, some space groups even share the exact same absences; in these cases, intensity statistics might, in theory, be used to differentiate between them. Thus it is almost inevitable that a range of space groups will be suggested for any one diffraction pattern.

In order to make the problem of peak overlap in space group determination less reliant on visual determination of what is and isn't an absence, the whole-pattern fitting methods

of Le Bail and Pawley described above can be employed to give a ranking to each possible space group. As in profile fitting, a goodness-of-fit value can be assigned to each space group tested; a space group that predicts a peak where there isn't one gets a penalty to its goodness of fit, while one that correctly shows an absence receives a bonus. In this way, differentiation between space groups that may not have been able to be accomplished by eye is now enabled by statistical means.

2.4.5 Structural determination and Fourier analysis

Once the unit cell, space group, and integrated intensities have been determined or calculated, structure solution can proceed. The method used is usually dependent on how much prior chemical knowledge is available regarding the structure to be solved. Broadly speaking, direct methods extract individual intensities and attempt to solve the phase problem directly from them, while direct-space methods avoid extracting intensities and instead make use of prior chemical information to generate models and compare their calculated diffraction patterns to experimental ones.

2.4.5.1 Direct methods

Direct methods in structure determination by powder diffraction (SDPD) are adapted from their basis in single crystal structure determination [67] and thus rely on the diffraction pattern containing a high number of single crystal quality intensities. Returning to the phase problem, the electron density is related to the structure factors and phase of a reflection by the equation;

$$\rho(\mathbf{r}) = \frac{1}{V}\sum_{\mathbf{S}}|F(\mathbf{S})|e^{i\phi-2\pi i\mathbf{S}\cdot\mathbf{r}} \tag{2.14}$$

where, again, $\rho(\mathbf{r})$ is the electron density, $\mathbf{S}$ is the diffraction vector (reflection) with amplitude $|F(\mathbf{S})|$ and phase angle ϕ, and V is the volume of the unit cell. As mentioned earlier, if both $|F(\mathbf{S})|$ and ϕ were known, we could produce a crystal structure exactly from the resulting electron density map. Unfortunately, while we do measure $|F(\mathbf{S})|$, ϕ cannot be determined from the diffraction pattern, and thus we need some way of estimating it if we are to find a crystal structure solution. This is the approach that direct methods take, using statistical analysis to make assumptions about the phase angles in order to find some starting point–usually a well-defined group of reflections that gives the positions of a few atoms–for the determination of the structure.

As the level of quality required for direct methods is often difficult to obtain using X-ray powder diffraction, they are generally very limited in their application to SDPD. While direct methods were not used in our explorations of structure, there are numerous review articles and books available that explain them and their application [67, 71, 72].

2.4.5.2 Patterson methods

Patterson methods are named after Patterson [73] who derived a formula similar to that of (2.14), but without the dependence on the phase angle:

$$P(\mathbf{r}) = \frac{1}{V}\sum_{\mathbf{S}}|F(\mathbf{S})|^2 e^{-2\pi i \mathbf{S}\cdot\mathbf{r}} \tag{2.15}$$

where $P(\mathbf{r})$ is referred to as the Patterson function, and produces a map similar to that of the electron density map produced from (2.14). This map contains peaks that correspond to the interatomic vectors (r_i-r_j) in the unit cell, the heights of which will increase as a function of the scattering powers of the two atoms [74]. Thus, heavy atoms will produce larger peaks, and this is the basis for the Patterson method (which is also sometimes referred to as the 'heavy atom' method). However, its ability to highlight the positions of a few heavy atoms is also its weakness: if there are no outstandingly heavy scatterers in the unit cell, then the Patterson map will appear as a uniform collection of peaks of very similar intensity, indistinguishable from each other within the bounds of the error associated with powder X-ray diffraction experiments.

However, while structures with no outstandingly heavy atoms may not be able to be determined in this way, they can still benefit from the Patterson method. If fragments of the structure are known to exist, then the interatomic vectors associated with that fragment can be searched for using rotation and translation of the fragment: much like the placing of a jigsaw piece in a puzzle. Patterson methods in general do not require as many, or as high quality, intensity measurements as direct methods, substituting in at least a small amount of prior knowledge of the structure being examined.

2.4.5.3 Direct-space methods

Despite the similarity in name, the direct-space methodology relies a lot less on attaining a diffraction pattern of the quality of a single crystal experiment, and more on the incorporation of prior chemical knowledge into the structure determination process. The

essential difference between direct-space methods and direct methods is that rather than extracting the intensities, we propose candidate structures completely independently of the diffraction data and compare the calculated diffraction pattern of these candidate structures with the experimental pattern. Before the advent of powerful computer-based methods, the typical direct-space structure determination would require the manual construction and testing of a model using all information available. Obviously this placed a great deal of emphasis on making sure as many pieces of the puzzle were present as possible before attempting to build the model, in order to reduce the amount of time spent advancing iterations of the model. All manner of experiments might be used to elucidate the chemical information of the structure to be solved: infra-red spectroscopy, thermogravimetric analysis, electron microscopy, Raman spectroscopy, etc.

With the development of more powerful (and affordable) computers, the need to have a comprehensive idea of the structure before employing direct-space methods has become less of a limiting factor. While investing time obtaining a greater range of data can result in a more expedient determination of the structure, the ability for algorithms driven by computer software to generate and test a vast array of possible structures using only small fragments of chemical information has greatly reduced the need for a comprehensive experimental study before attempting SDPD, and many such algorithms have been developed recently [75–81].

Direct-space methods are also referred to as global optimisation methods, and this describes one of the main challenges in the technique. When generating structures whose calculated diffraction patterns are to be compared to the experimental one, we need some way of guiding subsequent structures so that we get progressively closer to reaching the true structure, otherwise we would be trialling random positions for atoms and the chances of determining the structure this way are incredibly small [57]. The aforementioned algorithms work by exploring a chosen cost function in search of a global minima that corresponds to the atomic coordinates of the true structure. However, they must also be designed so that they can avoid the local minima in the function that correspond to incorrect or physically unreasonable structures [59]. A schematic illustrating the general strategy for a global minimisation using direct-space methods is shown in Figure 2.8.

Experiments other than good quality X-ray diffraction data are sometimes not needed at all. For example, a material may have analogues whose structures have already been determined. Thus any connectivity information could be used as a starting point for the determination of the unknown structure; polyhedra, bond distances and angles, or the possiblity of distortions might all be gained just by examining at similar materials. Of course, how this information is used to generate candidate structures is also important.

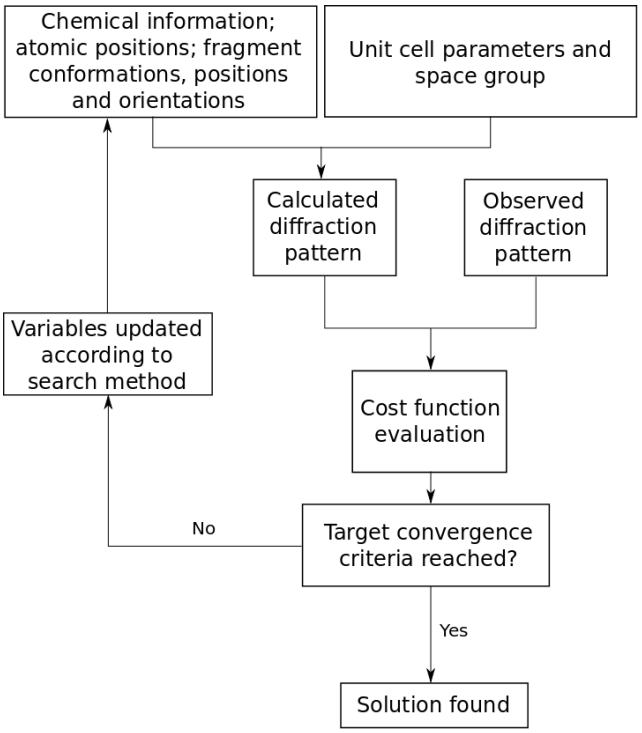

FIGURE 2.8: General flow chart for a global optimisation approach to crystal structure solution. Reproduced from David *et al.* [57].

If only composition and not connectivity is known, one can take an approach such as that of the FOX software [81], which uses reverse Monte Carlo–a method of stepping through random configurations. If some connectivity is known, such as the typical bond distances for an SO_4 tetrahedron, this can be incorporated into the generation of trial structures such that the number of variables is greatly reduced. Current software is sufficiently advanced that a combination of single atoms, molecule fragments, and polyhedra can be used in combination to reduce the sample space of any one structure. This is the case for zeolites, whose general cage structure can be used in a predictive way for new zeolite-like structures [82, 83].

2.4.6 Rietveld refinement

While structure determination can be considered complete once the atoms have been reasonably placed, structure *solution* is only considered complete when the structure has been refined. Refinement in this case means the determination of atomic displacement parameters and the more precise estimation of atomic coordinates, including standard errors. This is achieved by the least-squares refinement of parameters such as the Gaussian/Lorentzian/pseudo-Voigt character of the peak shapes, scale factors, zero-point detector shift, peak asymmetry, texture and preferred orientation parameters

(if present), etc. of the calculated line profile against the experimental one. Often other diffraction patterns can be brought in at this point to help determine the positions of lighter elements. For example, neutron diffraction patterns can more accurately determine oxygen atom positions, and even the positions of hydrogen atoms with the use of a deuterated sample.

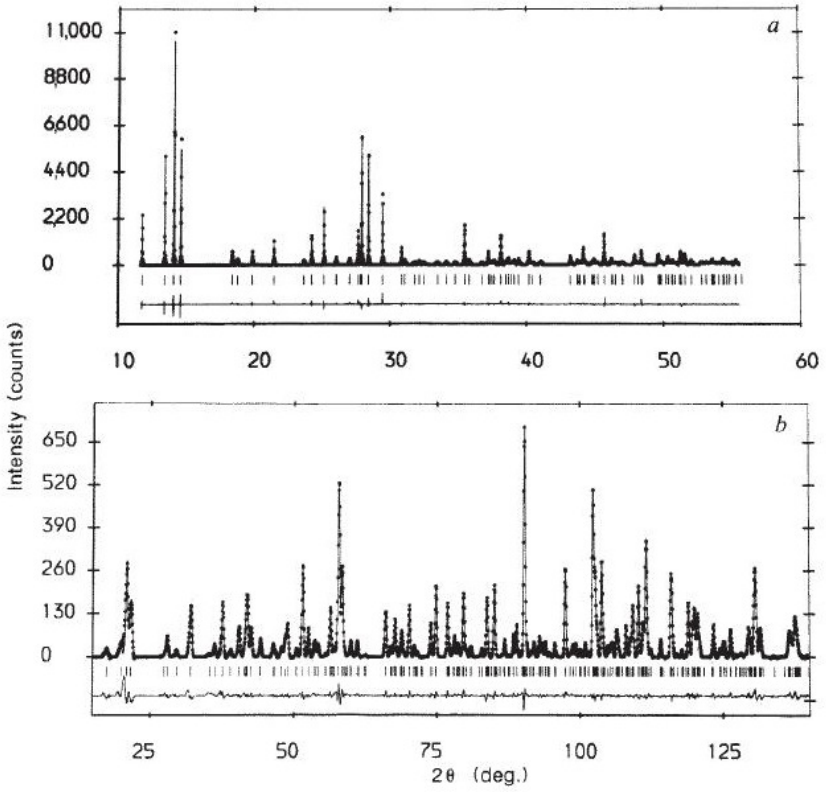

FIGURE 2.9: Figure showing the representation of Rietveld refinement results. The difference profile is shown underneath the comparison of observed (points) and calculated (lines) diffraction patterns. The top graph shows a synchrotron X-ray diffraction pattern, while the bottom is a neutron diffraction pattern. This image was reproduced from the paper by Attfield *et al.* which showed the first structure determination by synchrotron powder X-ray diffraction [84].

Once a structure has been refined, it is usually presented as a graph of the experimental diffraction pattern overlayed with the calculated diffraction pattern, with the difference between the two shown underneath. Figure 2.9 shows an example of this using the results from Attfield *et al.* [84].

2.4.7 Noteable examples of SDPD

As noted in Le Bail's review [85], four of the top five cited articles in the area of SDPD are that of software announcements for FULLPROF [86], WPPF [87], RIETAN [88], and EXTRA [89] (which was then incorporated into the EXPO package [90]). This points

to a large user group of such software, as well as a healthy community of developers looking to optimise past implementations of SDPD code for more modern computers.

As previously mentioned, the first structure solved from synchrotron X-ray powder diffraction was that of α-$CrPO_4$ by Attfield *et al.* [84], but the works of Lightfoot *et al.* on the structures of $MnPO_4{\cdot}H_2O$ [91] and $BaBiO_{2.5}$ [92] are often given as a representative of *ab initio* structure determination from synchrotron X-ray powder diffraction. Cheetham *et al.* [68] reported one of the first determinations of a high-temperature structure that wasn't quenched, instead using a modified vacuum furnace to record *in-situ* neutron diffraction patterns.

Laboratory diffractometers have become more common and increasingly powerful, resulting in a large amount of structures solved from in-house instruments. Gascoigne *et al.* [41] solved the structure of $Zr(OH)_2SO_4{\cdot}3H_2O$ using a laboratory diffractometer with Bragg-Brentano geometry. However, transmission (Debye-Scherrer) geometry is also available for use with laboratory diffractometers, as evidenced by the solution of $LiB_2O_3(OH){\cdot}H_2O$ by Louer *et al.* [93].

Chapter 3

Computational techniques

In chapter 2 the case was made for experimental studies in which diffraction experiments can provide a great deal of insight into the structures of any crystalline material. However, if it is the case that very little information is known about the structure, diffraction experiments can be difficult to interpret and attempts at structure solution from them, particularly in the case of powder diffraction, can be greatly prolonged compared to those where some chemical connectivity is known. Traditionally, analogues from the literature may provide some clues, but if the material is truly unique or behaves unusually, thereby excluding precedent, there is little to be gained from such a search.

In the above particular instances, where there is seen to be very little information pertaining to atom positions, connectivities or general motifs, computer simulation is a potentially useful tool that can be used to provide insight into possible conformations. The goal of computer simulation in this context is both the prediction of hypothetical structures and the validation of proposed structures. In order to achieve these dual objectives, the computer technique must possess some key qualities:

- Be computationally feasible, i.e. able to be performed in a timely fashion;
- Calculate energies and forces in order to explore the potential energy landscape of any proposed structure for local and global minima;
- Provide an accurate determination of atomic positions.

Quantum mechanical methods of simulation fulfill most of these requirements. *Ab initio* quantum mechanical methods require no data beyond that of the atomic number of each atom considered. They are also able to provide both energies and forces, giving the potential energy landscape of a system. However, the balance of accuracy

and computational feasibility have resulted in a need for compromise. The degree of complexity of quantum mechanical equations means that, for all but the simplest of systems, approximations must be employed to avoid making the computational processing power required to solve them intractable. For example, techniques such as full configuration interaction (Full CI) are able to give exact answers to these equations, but their nature is such that the processing power required to do so increases factorially with the complexity of the system [94]. As such, it is only possible to solve the equations with this level of accuracy for very small systems of atoms or molecules.

Numerous methods have been developed in order to navigate the issue of accuracy versus computational expense. This chapter will first provide a general background in quantum mechanical theory necessary to present the development of density functional theory (DFT). A more detailed explanation of DFT will then be undertaken. Following this will be a concise overview of empirical forcefield methods.

3.1 Quantum Mechanics

3.1.1 The Schrödinger Wave Equation

When discussing the *ab initio* calculation of many-body systems, it is usual to start by recalling the time-independent Schrödinger wave equation [95]:

$$\hat{H}\Psi_i = E_i\Psi_i \tag{3.1}$$

For a system of N electrons in a field of M nuclei with mass M_A and charge Z, the Hamiltonian, $\hat{H}$, has the form;

$$\hat{H} = -\frac{1}{2}\sum_{i=1}^{N}\nabla_i^2 - \frac{1}{2}\sum_{A=1}^{M}\frac{1}{M_A}\nabla_A^2 - \sum_{i=1}^{N}\sum_{A=1}^{M}\frac{Z_A}{r_{iA}} + \sum_{A=1}^{M}\sum_{B>A}^{M}\frac{Z_A Z_B}{R_{AB}} + \sum_{i=1}^{N}\sum_{j>i}^{N}\frac{1}{r_{ij}} \tag{3.2}$$

where the first term is the kinetic energy of the electrons, the second term is the kinetic energy of the nuclei, the third term is the electrostatic attraction between the electrons and the nuclei, the fourth term is the electrostatic repulsion between nuclei, and the fifth term is the electrostatic repulsion between electrons. In this equation, atomic units are being used to simplify the expression. Equation (3.2) can be represented in a form of convenience as:

$$\hat{H} = \hat{T}_e + \hat{T}_n + \hat{V}_{e-n} + \hat{V}_{n-n} + \hat{V}_{e-e} \tag{3.3}$$

Unfortunately, there exists an intrinsic feature of the wave equation, the correlation of electrons, that result in it being unable to be solved analytically for all but a few specific cases. The reasons behind the insoluble nature of the problem, along with methods to overcome it, will be discussed throughout the rest of this chapter.

3.1.2 The Born-Oppenheimer Approximation

The Born-Oppenheimer approximation states that due to the electrons being much lighter than the nucleus of any atom (excepting hydrogen and, to a certain degree, helium), they are able to explore configurations very rapidly as the system evolves and can thus be considered to be in their ground state configuration at any position that the nuclei assume during their motion [96]. Therefore the total wavefunction is assumed to be separable and can be written as the product of two functions describing the positions of the nuclei and the electrons;

$$\Psi_i(\mathbf{R}, \mathbf{r}) = \Psi_{nuc}(\mathbf{R})\Psi_{elec}(\mathbf{r}, \mathbf{R}) \tag{3.4}$$

where $\mathbf{R} = R_I$ is the set of all nuclear coordinates, and $\mathbf{r} = r_i$ is the set of all electronic coordinates. As a result of this, we can assume that when studying the electronic structure of a system the nuclei can be accounted for using classical motion, and separated from the electronic wavefunction. Considering only the electronic Schrödinger equation, (3.2) can be reduced to:

$$\hat{H}_{elec} = -\frac{1}{2}\sum_{i=1}^{N}\nabla_i^2 - \sum_{i=1}^{N}\sum_{A=1}^{M}\frac{Z_A}{r_{iA}} + \sum_{i=1}^{N}\sum_{j>i}^{N}\frac{1}{r_{ij}} \tag{3.5}$$

Solving the Schrödinger wave equation with this electronic Hamiltonian gives the electronic wavefunction, Ψ_{elec}, and the electronic energy, E_{elec}:

$$\hat{H}_{elec}\Psi_{elec}(\mathbf{r}) = E_{elec}\Psi_{elec}(\mathbf{r}) \tag{3.6}$$

It is important to note that the nuclear coordinates enter the electronic wavefunction only parameterically, as the electrons move in a static potential generated by the nuclei. This means that the total energy, E_{total}, can be written as a sum of E_{elec} and the nuclear repulsion term in equation (3.2):

$$E_{total} = E_{elec} + \sum_{A=1}^{M} \sum_{B>A}^{M} \frac{Z_A Z_B}{R_{AB}} \tag{3.7}$$

In this way, we are only solving the wave equation for electrons in the system, while the movements of the nuclei are handled classically. The classical movement of the nuclei is a good approximation in all cases except those such as the hydrogen atom where the nucleus exhibits significant quantum behaviour. It should be noted that solving this simplified Schrödinger wave equation does not give us the motion and position of the electrons in the classical sense. Rather, it gives us the wavefunction of the electrons, $\Psi_{elec}(\mathbf{r})$, which we can multiply by its complex conjugate in order to give the probability of finding an electron at any point, $\mathbf{r}$.

3.1.3 The variational principle

Looking at (3.6) it might seem a simple matter of setting up the Hamiltonian, $\hat{H}_{elec}$, finding the eigenvalues, Ψ_{elec}, and determining the eigenfunctions, E_{elec}. Unfortunately, with the exception of hydrogen and some other examples, no method exists to solve the Schrödinger wave equation analytically. Despite this, there does exist a systematic approach to approximating the ground state wave function in the form of the variational principle. The variational principle states that if a Hamiltonian is known for a system, then the energy expectation value of the Hamiltonian for any trial wavefunction must be greater than or equal to the actual ground state energy. This is expressed (in Dirac's *bra-ket* notation) with the equation:

$$\langle \Psi_{trial} | \hat{H} | \Psi_{trial} \rangle = E_{trial} \geq E_{ground} = \langle \Psi_{ground} | \hat{H} | \Psi_{ground} \rangle \tag{3.8}$$

To state it more plainly, by varying the trial wavefunction and finding solutions of lower and lower energy, we are going to get closer and closer to the ground state for the system. Eventually, the solution will vary so little in subsequent iterations that we can say that the limit has been achieved and, to within a specified threshold and the space of Ψ_{trial}, the ground state energy of the system has been calculated.

Expressed with the focus on the electronic Schrödinger wave equation, the variational principle can be written as:

$$E_0 = minE[\Psi] = min\langle \Psi_{trial} | \hat{T} + \hat{V}_{Ne} + \hat{V}_{ee} | \Psi_{trial} \rangle \tag{3.9}$$

3.1.4 Hartree-Fock theory

Quantum mechanical theory states that along a given direction, the spin of an electron can be one of two values, $\pm\frac{1}{2}$. The nomenclature given to this result is that the spin can only be 'up' or 'down'. This introduces a new condition for the determination of electronic wavefunctions, in that the wavefunction for any individual electron should also depend on the spin variable. Therefore the probability of finding an electron at point $\mathbf{r}$ can be written as $|\psi\uparrow(\mathbf{r})|^2$ or $|\psi\downarrow(\mathbf{r})|^2$ given up or down spin, respectively.

The second consideration is that no Fermion–the class of particle to which the electron belongs to–can be differentiated from any other, i.e. they are indistinguishable. While this has many consequences in the field of quantum mechanics in general, the important result relating to Hartree theory is that the wavefunction for a system of electrons will change its sign when any two electrons are interchanged. This alters the product of electronic wavefunctions so that, if considering a system of two electrons, it becomes:

$$\Psi(\mathbf{r}_1,\mathbf{r}_2)=\frac{1}{\sqrt{2}}\left[\Psi_a(\mathbf{r}_1)\Psi_b(\mathbf{r}_2)-\Psi_a(\mathbf{r}_2)\Psi_b(\mathbf{r}_1)\right] \tag{3.10}$$

This requirement is referred to as 'exchange symmetry' and forms the basis of the Pauli exclusion principle which states that no two electrons can occupy the same quantum state at the same time. In the context of equation (3.10) we can see that if $\mathbf{r_1}$ was made to be equal to $\mathbf{r_2}$, the resultant total wavefunction would be zero, i.e. there is zero chance that two electrons with the same spin can be found in the same position. By introducing this exchange symmetry we are lowering the energy of the system, since electrons will have a greater probability of staying away from each other and thus feel less of a repulsive force. This lowering in energy is referred to as the exchange energy. By introducing this exchange symmetry compliant product of the wavefunctions and its resultant reduction in system energy, we have the essential features of Hartree-Fock (HF) theory.

The derivation of the Hartree-Fock method is an important precursor to the discussion of density functional theory methods [97, 98]. While the two methods differ in their use of wavefunctions and electron density as a means of determining the energy of a system, the derivation of HF theory presents concepts which will be revisited in later discussions of Kohn-Sham density functional theory.

HF theory uses the antisymmetric product of N one-electron wave functions, or 'spin orbitals', $(\chi_i(x_i))$, commonly known as the Slater determinant, combined with the Aufbau principle, to build up an approximation to the wavefunction:

$$\Phi_{SD} = \frac{1}{\sqrt{N!}} \begin{vmatrix} \chi_1(\mathbf{x}_1) & \chi_2(\mathbf{x}_1) & \cdots & \chi_N(\mathbf{x}_1) \\ \chi_1(\mathbf{x}_2) & \chi_2(\mathbf{x}_2) & \cdots & \chi_N(\mathbf{x}_2) \\ \vdots & \vdots & & \vdots \\ \chi_1(\mathbf{x}_N) & \chi_2(\mathbf{x}_N) & \cdots & \chi_N(\mathbf{x}_N) \end{vmatrix} \tag{3.11}$$

The problem now is to find the set of $\chi_i(x_i)$ in equation (3.11) that gives the lowest energy of the system, and therefore the best estimate of the ground state energy. Due to the non-linearity of this process it is usually carried out by a iterative calculation, which is referred to as the self-consistent field (SCF) method. While this Slater determinant is obviously not a solution of N interacting electrons, what it does provide is the exact wavefunction of N independent electrons moving in the HF effective potential, V_{HF}. V_{HF} is the average repulsive potential experienced by an electron due to all the other electrons in the system. By minimising the energy associated with these wavefunctions, we arrive at the HF energy:

$$E_{HF} = minE\left[\Phi_{SD}\right] \tag{3.12}$$

The energy of a system of independent electrons, E_{HF}, will always be larger than the exact ground state energy, E_0. Physically this makes sense: if the instantaneous repulsion between electrons is only treated in an average sense, then they will tend to be closer to each other and therefore experience a greater repulsive force, resulting in a more energetic system. The difference between the HF energy and the exact ground state energy is known as the correlation energy:

$$E_{corr} = E_0 - E_{HF} \tag{3.13}$$

There are two components of the correlation energy; the dynamical and non-dynamical correlation. The dynamical correlation is that which governs the instantaneous repulsion between electrons. The non-dynamical correlation (sometimes called the static correlation) is related to the fact that in certain circumstances (i.e. the system has multi-determinant character) the ground-state Slater determinant is not a good approximation to the ground state wavefunction.

3.1.4.1 Post-Hartree-Fock methods

Post-Hartree-Fock methods aim to improve upon the Hartree-Fock method by the addition of varying levels of electron correlation into the calculation. This section will

briefly explain some of the more common methods for achieving this.

Møller-Plesset perturbation theory:

Correlation can be added as a perturbation from the Hartree-Fock solution, and this forms the basis of Møller-Plesset (MP) perturbation theory [99]. MP theory assumes that the true energy, including the unknown correlation energy, of a system is a small perturbation away from the Hartree-Fock energy. This perturbative potential can be used to describe complex systems in a more precise fashion:

$$\hat{H} = \hat{H}_0 + \lambda\hat{V} \tag{3.14}$$

where λ is an arbitrary real parameter varying between 0 and 1. When $\lambda = 0$, then $\hat{H}$ is equal to its unperturbed, zeroth-order state, i.e. the Hartree-Fock Hamiltonian. But when $\lambda = 1$, then $\hat{H}$ equals its true value. The pertubation, $\hat{V}$, is the correlation potential. Using equation (3.14), the wavefunctions and energies of the system are expressed in powers of λ:

$$\Psi_i = \Psi_i^{(0)} + \lambda\Psi_i^{(1)} + \lambda^2\Psi_i^{(2)} + ... = \sum_{n=0}\lambda^n\Psi_i^{(n)} \tag{3.15}$$

$$E_i = E_i^{(0)} + \lambda E_i^{(1)} + \lambda^2 E_i^{(2)} + ... = \sum_{n=0}\lambda^n E_i^{(n)} \tag{3.16}$$

The different orders of MP calculations (MP2, MP3, MP4, etc.) are based on the truncation of the energy term. For example, MP2 involves using the perturbation to second order, i.e.:

$$E_i^{(2)} = \int \Psi_i^{(0)}\hat{v}\Psi_i^{(1)} \tag{3.17}$$

Configuration Interaction:

Electron correlation can be accounted for if we introduce a mechanism by which electrons are allowed to stay away from each other, the main consequence of electron correlation. Configuration interaction (CI) does this by introducing virtual orbitals into the wavefunction that are ordinarily unoccupied in the HF calculation, producing new determinants [100]. This leads to the variational optimisation of a wavefunction composed of a linear combination of Slater determinants;

$$\Psi = c_0\Psi_0 + \sum_{i=1}^{N}\sum_{a=N+1}^{K} c_i^a\Psi_i^a + \sum_{i>j=1}^{N}\sum_{a>b=N+1}^{K} c_{ij}^{ab}\Psi_{ij}^{ab} + \sum_{i>j>k=1}^{N}\sum_{a>b>c=N+1}^{K} c_{ijk}^{abc}\Psi_{ijk}^{abc} + \dots \tag{3.18}$$

where c_i are the weighting factors to be optimised variationally in the calculation. The point at which equation (3.18) is truncated determines the accuracy of the calculation. For example, truncating at $c_0\Psi_0$ would result in the ground-state Hartree-Fock wavefunction. Truncating at $c_i^a\Psi_i^a$ corresponds to including Slater determinants of electrons singly excited from the ith occupied orbital to the ath unoccupied orbital. $c_{ij}^{ab}\Psi_{ij}^{ab}$ is the inclusion of the Slater determinants of all doubly excited states, and so on. Full configuration interaction (full CI) would give the exact ground energy, but would necessarily require the inclusion of all possible excited electrons. The computational cost of introducing these virtual orbitals is quite high but the energies calculated in this way can be very accurate, and the increasing power of computer processors means that larger and larger systems are becoming accessible to study by CI [99].

3.2 Density Functional Theory

While methods such as configuration interaction and coupled cluster theory are able to include correlation in an accurate fashion, they do so at a high computational cost. In order to perform calculations with large, complex systems, a method that is both reasonably accurate and computationally less exhausting is required. Density functional theory (DFT) is one method that can achieve this. Given the larger role that DFT occupied in this project, a greater amount of time will be devoted to going through its formulation.

3.2.1 Hohenberg-Kohn theorems

The fundamental argument that DFT makes is that the complex, N-electron wave function that we have seen approximated using the Hartree-Fock scheme can, in fact, be replaced by a simpler quantity. In DFT, this quantity is the electron density. Following on from the early efforts of Thomas and Fermi [101], Hohenberg and Kohn were the first to provide a fundamental proof that this was possible [102].

Returning to the electronic Hamiltonian (reproduced here for clarity);

$$\hat{H}_{elec} = \hat{T} + \hat{V}_{Ne} + \hat{V}_{ee} \tag{3.19}$$

their proof was based around the idea that there cannot be two different V_{Ne}, or external potentials in general, which result in the same ground state electron density, i.e. the ground state electron density is uniquely determined by V_{Ne}. Since the two other terms $\hat{T}$ and $\hat{V}_{ee}$ are obviously dependent on the ground state electron density, this means that all terms of the Hamiltonian are reliant on the electron density, and therefore the ground state energy can be determined as a function of the electron density:

$$E_0[\rho_0] = T[\rho_0] + E_{ee}[\rho_0] + E_{Ne}[\rho_0] \tag{3.20}$$

The first two terms can be grouped together into a new expression, the Hohenberg-Kohn functional, $F_{HK}[\rho]$, due to their independence of which system is being considered (i.e. no dependence on the presence or number of nuclei):

$$F_{HK}[\rho] = T[\rho] + E_{ee}[\rho] \tag{3.21}$$

This equation has a very significant meaning; by inputting an electron density into $F_{HK}[\rho]$, we obtain the sum of the ground state kinetic and electron-electron repulsion operators corresponding to that density. In other words, if we knew the exact form of the $F_{HK}[\rho]$ functional and the V_{Ne} to integrate to E_{Ne}, we would be able to calculate the ground state energy for any electron density, ρ, and any system, thanks to the universal nature of the functional. Unfortunately, the form of the $F_{HK}[\rho]$ functional remains unknown.

This leads us to the second main component of the Hohenberg-Kohn scheme; the variational principle as applied to the determination of the ground state electron density, and therefore the ground state energy. This can be expressed in much the same form as has been previously mentioned:

$$E_0 \leq E[\rho_t] = T[\rho_t] + E_{Ne}[\rho_t] + E_{ee}[\rho_t] \tag{3.22}$$

In other words, the functional $F_{HK}[\rho] + E_{Ne}[\rho]$ only results in the true ground state energy if the trial input electron density, ρ_t, is the ground state electron density, ρ_0.

3.2.2 The Kohn-Sham method

While the Hohenberg-Kohn theorems show how the electron density of a system can be directly mapped to its ground state energy, and therefore used to determine all its

properties, there is a stumbling block in the form of the unknown $\mathrm{F_{HK}}[\rho]$ functional that may never be found. The Kohn-Sham method attempts to work around this barrier [103].

The first step in the Kohn-Sham approach was to construct a non-interacting reference system of N particles whose ground state is a single Slater determinant, and whose density is the same as the target real, interacting system. This construction is very similar to that of H-F theory, but with K-S orbitals replacing H-F orbitals in the Slater determinant and subsequent operators. So we have:

$$\Theta_{SD} = \frac{1}{\sqrt{N!}} \begin{vmatrix} \varphi_1(\mathbf{x}_1) & \varphi_2(\mathbf{x}_1) & \cdots & \varphi_N(\mathbf{x}_1) \\ \varphi_1(\mathbf{x}_2) & \varphi_2(\mathbf{x}_2) & \cdots & \varphi_N(\mathbf{x}_2) \\ \vdots & \vdots & & \vdots \\ \varphi_1(\mathbf{x}_N) & \varphi_2(\mathbf{x}_N) & \cdots & \varphi_N(\mathbf{x}_N) \end{vmatrix} \tag{3.23}$$

where the spin orbitals, φ are determined by;

$$\hat{f}^{KS}\varphi_i = \varepsilon_i\varphi_i \tag{3.24}$$

and the one-electron, non-interacting Kohn-Sham operator, $\hat{f}^{KS}$ being defined as;

$$\hat{f}^{KS} = -\frac{1}{2}\nabla^2 + V_S(\mathbf{r}) \tag{3.25}$$

where the choice of V_S must be made such that the density resulting from the spin orbitals, φ_i, is equal to the ground state density of the real, interacting system of electrons. Having defined the reference system, the total energy of the real system can then be expressed as a function of the electron density;

$$E[\rho] = T_S[\rho] + J[\rho] + E_{XC}[\rho] + E_{Ne}[\rho] \tag{3.26}$$

where $\mathrm{T}_S[\rho]$ is the kinetic energy of the non-interacting reference system, $\mathrm{J}[\rho]$ is the known mean field interaction between electrons, $\mathrm{E}_{Ne}[\rho]$ is the energy due to nuclei-electron interaction, and $\mathrm{E}_{XC}[\rho]$ is a catch-all term including the correlation, and exchange energies, plus the part of the interacting system's kinetic energy not accounted for by $\mathrm{T}_S[\rho]$. Each of these terms can be expressed in terms of the electron density of the system, and therefore the K-S orbitals, φ, with the exception of $\mathrm{E}_{XC}[\rho]$.

We now apply the variational principle with respect to the independent variables on the K-S orbitals to determine the set of K-S orbitals that minimise the energy of the system. This results in the so-called Kohn-Sham equations [104]:

$$\left[-\frac{1}{2}\nabla^2 + V_{ext} + \int \frac{n(r^{'})}{|r - r^{'}|}dr^{'} + V_{XC}\right]\varphi_i = \epsilon_i\varphi_i \tag{3.27}$$

where:

$$V_{XC} = \frac{\delta E_{XC}|n(r)|}{\delta n(r)} \tag{3.28}$$

and

$$n(r) = \sum_{i=1}^{N}|\varphi_i(r)|^2 \tag{3.29}$$

If the exact forms of V_{XC} and E_{XC} were known, the K-S method would lead to the exact energy of the system. Unfortunately they remain unknown, and the exploration of appropriate functionals to describe them is an activity that takes up a great deal of the modern work in DFT [105–108].

3.2.3 Functionals

As stated in the previous section, the search for functionals to approximate E_{XC} is of the utmost importance; assuming converged basis sets, the quality of any density functional theory calculation depends almost exclusively on the quality of the functional used. Unfortunately the explicit form of the exact exchange-correlation functional is not only unknown, but it is unable to be reached by means of any systematic improvement scheme. In this section, various approximations used in producing exchange-correlation functions will be presented.

3.2.3.1 Local density approximation

The local density approximation (LDA) uses the model system of a uniform electron gas, also known as jellium, as its foundation [109, 110]. The uniform electron gas is a system of electrons with constant density, ρ, everywhere. While this kind of system is obviously at a disadvantage in representing atoms and molecules, which undergo rapid

electronic density changes around the nuclei, it does have the unique advantage that the exchange functionals for all densities are able to be exactly calculated.

The LDA XC energy is written as;

$$E_{XC}^{LDA}[\rho] = \int \rho(\mathbf{r})\varepsilon_{XC}(\rho(\mathbf{r}))d\mathbf{r} \tag{3.30}$$

where $\varepsilon_{XC}(\rho(\mathbf{r}))$ is the E_{XC} per electron of a uniform electron gas of density $\rho(\mathbf{r})$. This energy can be split up into its exchange and correlation parts;

$$\varepsilon_{XC}(\rho(\mathbf{r})) = \varepsilon_X(\rho(\mathbf{r})) + \varepsilon_C(\rho(\mathbf{r})) \tag{3.31}$$

where $\varepsilon_X(\rho(\mathbf{r}))$ can be defined explicitly as:

$$\varepsilon_X = -\frac{3}{4}\left(\frac{3\rho(\mathbf{r})}{\pi}\right)^{\frac{1}{3}} \tag{3.32}$$

While the correlation part has no such explicit form, the use of highly accurate Quantum Monte Carlo numerical simulations has resulted in various numerical tabulations of ε_C being developed [111]. These accurate values of the correlation energy are then interpolated in order to provide the LDA functional, examples being those of Perdew-Zunger [108] and Perdew-Wang [106]. As previously stated, the drastic approximation of any system's E_{XC} being equal to that of a uniform electron gas wouldn't appear to be very realistic. However, the performance of the LDA in solid state systems has been comparable to Hartree-Fock calculations, though with a tendency to overbind.

One other modification to the LDA is the LSDA, the local spin density approximation (as exemplified in the Vosko-Wilk-Nusair functional [112]). This is the form of the LDA when the spins of the electrons are taken into account, and can be written:

$$E_{XC}^{LSDA}[\rho_\uparrow, \rho_\downarrow] = \int \rho(\mathbf{r})\varepsilon_{XC}(\rho_\uparrow(\mathbf{r}), \rho_\downarrow(\mathbf{r}))d\mathbf{r} \tag{3.33}$$

3.2.3.2 Generalized Gradient Approximation

The generalized gradient approximation (GGA) extended the work of the LDA. The idea of the GGA was to take the local density information present in the LDA, that is, the information given about the electronic density at one point, and incorporate the

information about the gradient of the electronic density at that point. In this way, we can interpret the LDA as the first term in a Taylor expansion of the density, and the GGA as extending the series to the next term [103]:

$$E_{XC}^{GGA}[\rho_\uparrow, \rho_\downarrow] = \int f(\rho_\uparrow(\mathbf{r}), \rho_\downarrow(\mathbf{r}), \nabla\rho_\uparrow(\mathbf{r}), \nabla\rho_\downarrow(\mathbf{r}))d\mathbf{r} \tag{3.34}$$

The derivations of different f functions require a huge amount of attention to detail and so won't be reproduced here for brevity. A paper by Perdew, Burke, and Ernzerhof shows a derivation of their PBE GGA functional in relatively simple terms and is recommended for an introduction to the derivation of GGA functionals [113]. The practical consequence of the GGA is that, contrary to the LDA, it has a tendency to underbind in the solid state, resulting in longer unit cell parameters.

Beyond GGA functionals, there are also schemes such as the meta-GGA and hybrid functionals. The former have been derived to expand the series further in order to include the higher derivatives of the density at any point in the calculation, an example of which is the Tao-Perdew-Staroverov-Scuseria (TPSS) meta-GGA functional [114]. The latter use combinations of Hartree-Fock exchange with varying numbers of weighted exchange and correlation functional terms [115–117].

3.2.4 Basis Sets

Applying Hartree-Fock or Kohn-Sham DFT theory in practise, we require a way to methodically explore the infinite number of trial wavefunctions we could substitute into equation (3.8). Basis functions are essentially the numerical method through which a computer is able to make use of the variational principle to approach a ground state. Practically speaking, in order to do this a computer must be able to interpret a wavefunction as a set of numbers it can manipulate. There are a number of ways in which this is achieved, but they all use basis functions as a mechanism for the variation of wavefunctions.

One particular way of using basis functions is to make the assumption that the wavefunctions of electrons in assemblies of atoms are similar to the wavefunctions of electrons in isolated atoms. So in order to represent the total wavefunction of the system, we sum the atomic wavefunctions. To do so, we make use of an expansion of the orbitals:

$$\varphi_i(\mathbf{r}) = \sum_\alpha c_{i\alpha}\phi_\alpha(\mathbf{r}) \tag{3.35}$$

where the basis functions are the atomic wavefunctions, $\phi_\alpha(\mathbf{r})$, and $c_{i\alpha}$ are the coefficients to be varied in order to reach a ground state *via* the variational principle. This method is known as the linear combination of atomic orbitals (LCAO). The LCAO method takes the approach that the atomic orbital acts as a basis function, while the total wavefunction is a molecular orbital. The expansion of equation (3.35) is ordinarily truncated at a point where satisfactory precision is balanced with a feasible computational cost for the basis functions being used.

The question then becomes one of what form the basis functions should take. The most accurate way of describing atomic orbitals is through the use of Slater orbitals (shown as the solid line in Figure 3.1) [118].

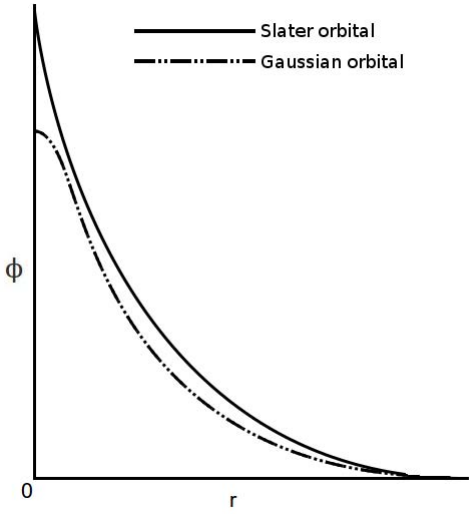

FIGURE 3.1: The 1s atomic orbital as described by Slater and Gaussian orbitals.

A Slater s-orbital is defined by the function:

$$\phi_i(\mathbf{r}) = N\mathbf{r}^{n-1}e^{-\zeta\mathbf{r}} \tag{3.36}$$

where n is a natural number that plays the role of principal quantum number, N is a normalization constant, r is the distance of the electron from the nucleus, and ζ is a constant involving the effective charge of the nucleus. Slater orbitals have the advantage that they exhibit a realistic shape, accurately describing the area around the nuclear cusp. This is because Slater orbitals are in fact the analytical solutions of the hydrogen atom. Unfortunately, integrals over Slater orbitals are not all known analytically for 3- and 4-centred terms. This has led to the adoption of other basis functions. The most commonly used treatment for molecules is that of Gaussian functions [119]:

$$\phi_i(\mathbf{r}) = Nx^l y^m z^n e^{-\zeta \mathbf{r}^2} \tag{3.37}$$

The main difference between the Slater orbitals and the Gaussian functions is that the r in the exponential function is squared, leading to a vanishing slope at the origin which does not describe the nuclear cusp as accurately as a Slater orbital (as can be seen in Figure 3.1), and decays too quickly at large radii compared to the Slater orbital's exponential decay. In order to counter this, several Gaussian functions can be summed into one contracted Gaussian function by utilising different values of ζ in order to give an approximation to a Slater orbital:

$$\phi_i^{Slater}(\mathbf{r}) \approx \sum_{j=1}^{n} c_j \phi_j^{Gaussian} \tag{3.38}$$

Thus, as n increases the approximation is more accurate. It is generally thought that 3-6 Gaussian functions are required to approximate a Slater orbital to a good degree of accuracy while still enjoying the saving in computational expenditure achieved by the easier integration of Gaussian functions. This combination of multiple basis functions is referred to as a Slater-type orbital basis set, written STO-#G, where # is the number of Gaussian orbitals used to approximate the Slater orbital [120, 121].

A third type of basis function is the numerical basis function which, as can be inferred by its name, uses numerical rather than analytical methods to describe the basis functions [122]. This entails representing the basis functions on atom-centred grids with interpolation between mesh points. The numerical nature of these basis functions means that they can not be systematically improved like Slater-type orbitals but to a certain extent they do not need to be as their shape is already reasonable, if well chosen.

Finally, we will mention one more type of basis function that does not strictly follow the linear combination of atomic orbitals method, referred to as plane waves. Plane waves are not centred on the nuclei like STOs, instead extending throughout space within periodic boundary conditions. This means that equation (3.35) becomes:

$$\Phi_i(\mathbf{r}) = \sum_{\mathbf{k}} c_{i\mathbf{k}} e^{i\mathbf{k}\cdot\mathbf{r}} \tag{3.39}$$

where $\mathbf{k}$ is the wavevector of the basis function, related to the electron's momentum. The nature of plane waves means that a huge number of plane waves would be required to accurately represent the core electron region and its rapidly varying wavefunction. The use of pseudopotentials to describe the core electrons means that plane waves are

typically only used to describe the valence electrons, reducing the number of plane waves to a manageable level. The pseudopotential is also smoothed, eliminating nodes in the wavefunction, again resulting in a less expensive calculation. Plane waves have the advantage of not giving rise to basis set superposition error, and their integral is a lot easier to compute than for Gaussian functions. They are also able to reliably converge towards the target wavefunction simply by the addition of more plane waves (increasing the kinetic energy cut-off), something that is harder for the orbitals used in the LCAO method.

3.2.5 Periodic boundary conditions

It is often the case that we wish to simulate a system of bulk solid. We could create a large system of this solid, but we would soon see that at the edges of the bulk the atoms have far fewer neighbours than those in the centre. In other words, the atoms at the edge of the solid act as though they are a surface. To remedy this situation, we could simply enlarge the size of the system. However, this would require an infinitely large system to reduce the effects of the 'surface' atoms to zero and obtain a simulation that truly represented a bulk solid.

Instead, we can use periodic boundary conditions. Periodic boundary conditions replace the infinite system of bulk solid with a repeating box of solid where the box is usually taken to be the unit cell [123]. We can then replicate the box in all directions by translation. So when we consider an atom inside a unit cell at position $\mathbf{r}$, invoking periodic boundary conditions means that atom will also represent all atoms at

$$\mathbf{r}' = \mathbf{r} + x\mathbf{a} + y\mathbf{b} + z\mathbf{c} \tag{3.40}$$

where x, y, and z can take any integer value from -inf to +inf, and $\mathbf{a}$, $\mathbf{b}$, and $\mathbf{c}$ are lattice vectors of the unit cell. In using periodic boundary conditions, we choose to simulate a select number of atoms and surround this arrangement with images of itself which are periodically repeated such that each atom acts as if it were part of an infinite system. Figure 3.2 shows the placement of repeating boxes around a system.

Bloch's theorem:

By introducing periodic boundary conditions we have created an infinite system with an infinite number of electrons, and therefore require an infinite set of basis functions to describe the wavefunctions. However, in a periodic system every box has the same total set of orbitals and therefore the same set of wavefunctions, just shifted by some

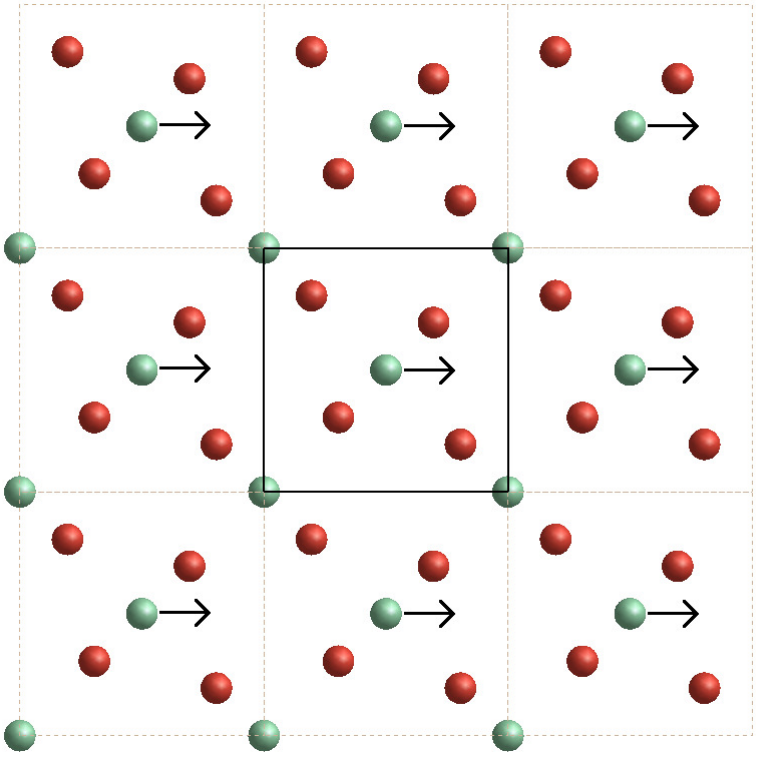

FIGURE 3.2: A two-dimensional representation of periodic boundary conditions, showing the repeated unit cell and the translation of an atom in each.

phase. Bloch's theorem takes advantage of this fact by introducing periodicity into the wavefunctions [124]. In order to introduce periodicity into the orbitals, we must have:

$$\varphi(r_1 + r_2) = \varphi(r_1)e^{ik \cdot r_2} \tag{3.41}$$

which is Bloch's theorem. By introducing Bloch's theorem we are mapping the problem of calculating the wavefunctions of an infinite number of electrons to one of expressing that wavefunction with an infinite number of reciprocal space, so-called k vectors, in order to account for all possible phase shifts. This problem then becomes one of sampling k space such that the electronic structure is able to be calculated accurately.

When sampling k space, we usually choose each k-point to lie within the first Brillouin zone. The Brillouin zone is the unique primitive cell in k-space; in other words, the minimum volume of k-space that can be repeated using periodic boundary conditions to represent the infinite system. The k-points are usually chosen to be dispersed evenly across the Brillouin zone on a fine enough grid as to integrate smoothly the electronic structure. This is but one way of distributing the k-points, known as the Monkhorst-Pack method [125], but there are others such as the tetrahedron method [126].

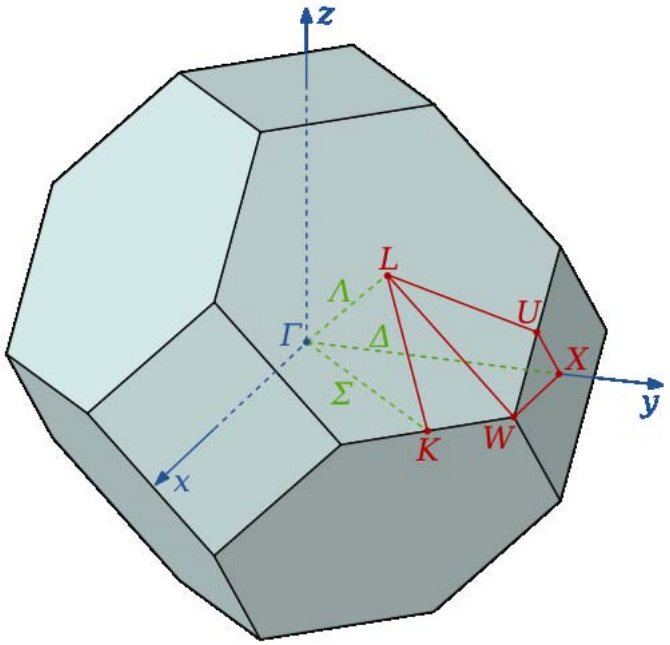

FIGURE 3.3: The first Brillouin zone for a FCC lattice showing symmetry labels for high symmetry lines and points [127].

3.2.5.1 Basis set extensions

Multiple-zeta and split-valence orbitals

Minimal basis sets are not designed with inherent transferability between systems. It is therefore necessary to add modifications to basis sets in order to allow them to deal with a changing molecular environment. In order to deal with multiple environments and therefore achieve a degree of transferability, the minimal basis sets are often modified by representing each atomic orbital by more than one basis function. Each of these basis functions can in turn be made up of a different combination of Gaussian-type orbitals, for example. As a result of this, the size of the orbital can vary between the spatial extents of the basis functions, therefore enabling it to accommodate changes in molecular environment. Multiple-zeta basis sets can also be referred to as 'split-valence'. This means that more flexible basis functions have been assigned to the valence electrons than to the core electrons. This is done in recognition of the fact that valence electrons are the principal influence in the bonding process and should therefore have a greater degree of freedom. This can be seen in Figure 3.4.

Diffuse functions

Diffuse functions are commonly required in anions due to the greater spatial extent of the electron density from the nuclei. Diffuse functions are those with very small ζ

FIGURE 3.4: A p orbital showing the extra spatial flexibility offered by introducing a split-valence basis set, with the two separate zeta functions shown by the white and orange orbitals.

values that describe the tail of the orbital more accurately. At the level of double-zeta basis sets the addition of diffuse functions has been shown to be of greater benefit than regular functions (i.e. a triple-zeta basis set) when calculating reaction energies and conformational energies [128].

Polarisation orbitals

While multiple-zeta orbitals and diffuse functions offer additional radial flexibility, angular flexibility can be added by including a polarisation orbital to the basis set. A polarisation orbital is typically an atomic orbital that is of one angular quantum number higher than the highest occupied state. For example, if adding a polarisation function to an oxygen basis set, we would add a 3d polarisation function, as oxygen has the ground state configuration of $1s^2 2s^2 2p^4$. The purpose of this is to allow the outermost occupied 2p orbitals the ability to distort by mixing with the unoccupied 3d polarisation orbitals.

Basis set notation

The notation for Gaussian basis sets usually follows that established by Pople et al. [129]. The notation is generally in the form of $\mathbf{X} - \mathbf{YZG}$, where $\mathbf{X}$ is the number of Gaussian orbitals that are used to describe each core atomic orbital, and the presence of $\mathbf{Y}$ and $\mathbf{Z}$ indicates that there are two basis functions for each valence orbital; the first one composed of $\mathbf{Y}$ and the other of $\mathbf{Z}$ Gaussian-type orbitals. The addition of a "+" or "$*$" indicates that diffuse or polarisation functions have been added, respectively.

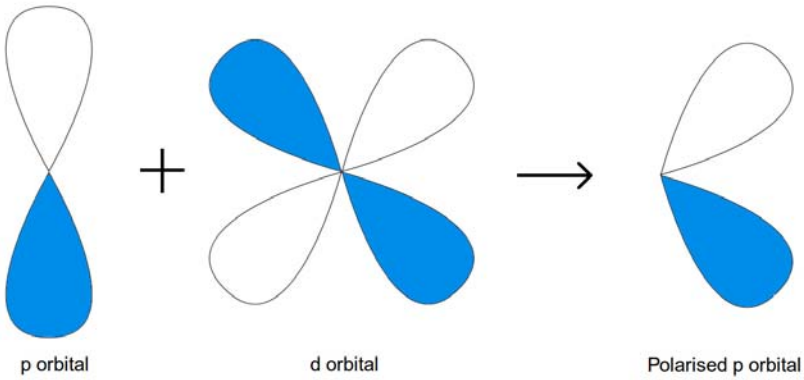

FIGURE 3.5: Illustration showing the distortion of a p orbital by mixing with a d orbital to give a polarised p orbital.

3.2.5.2 Basis set superposition error

The basis set superposition error (BSSE) is an error in the sum of the total energy of a system as a result of finite-sized basis sets [130]. It arises in systems when atoms approach each other, causing their basis sets to overlap. This interaction leads to the interacting atoms expanding their basis sets by borrowing the functions of each other, resulting in an improved calculation using these expanded basis sets. When the energies of the atoms which have interacted in this fashion and the atoms which have not are compared, there exists a spurious lowering of the energy of the former. This error is especially important to consider if the total energy is being minimised as a function of the structural geometry of the system.

The BSSE is usually handled in one of two ways: the first is known as the chemical Hamiltonian approach [131], and essentially removes the ability for basis sets to mix. Alternatively the counterpoise (CP) method [132] repeats all the energy calculations with or without the presence of neighbouring basis functions, and then subtracts the error from the uncorrected energy [133].

3.2.6 Pseudopotential approximation

It is often the case that most of the physical properties of solids are dependent on the valence electrons to a much greater degree than the core electrons. The pseudopotential approximation exploits this by removing the core electrons and nucleus, replacing the strong ionic potential with a weaker pseudopotential [134]. In this way, the core electrons are assumed to be in exactly the same states as they would be in an isolated atom.

Even with this much weaker potential acting on the valence electrons, it has been found that a reasonable description of the system is able to be calculated. This means that only the atomic orbitals for the valence electrons are required to be calculated, reducing the complexity of the total calculation and therefore the computational cost. As a consequence of the reduction in complexity, the numerics of the calculation actually become more precise, as we are now taking the difference of two smaller numbers; the occasion can arise where the pseudopotential calculation gives a much more precise answer than the all-electron calculation. The pseudopotential approximation was responsible for making the plane wave method of defining basis sets a practical alternative to the localized basis set approximation.

Properties of a pseudopotential

The main parameters of a pseudopotential are the cut-off radii of each angular momentum channel, i.e. the point up to which the real potential is replaced by the pseudopotential. A pseudopotential is constructed such that outside the cut-off radius, r_c, the pseudo wavefunction exactly matches the all-electron wavefunction. Inside r_c the nodal form of the true wavefunction is approximated to a nodeless, smooth pseudo wavefunction. The choice of a cut-off radius determines the trade-off between how transferable/accurate and smooth the pseudopotential is.

An assumption made in the pseudopotential approximation is that the core and valence orbitals do not overlap to any appreciable degree, allowing the exchange-correlation potential to be separated out into two terms; one for the core and one for the valence. If this assumption is not accurate, as is the case in some transition metals, the overlapping orbitals are known as 'semi-core' states. These can be dealt with in a couple of ways, the most common being to simply include them in the valence so that they are considered explicitly. The other is through the use of a non-linear core correction [135].

Norm-conserving pseudopotentials

Norm-conserving pseudopotentials are essentially defined by their name: pseudopotentials that conserve the 'norm'–that is, the integrated square of the amplitude–of the all-electron wavefunction for the valence states [136, 137] inside the cut-off radius. A typical comparison of a norm-conserving pseudopotential and an all-electron potential can be seen in Figure 3.6 below.

A pseudopotential with a large radial cut-off is referred to as a 'soft' pseudopotential, due to its smoother form. Soft pseudopotentials have the advantage that they require smaller plane wave basis sets to represent them, having accounted for a larger majority of the wavefunction with the effective pseudopotential. Unfortunately this makes them less transferable to other systems as they have lost a large amount of the realistic features

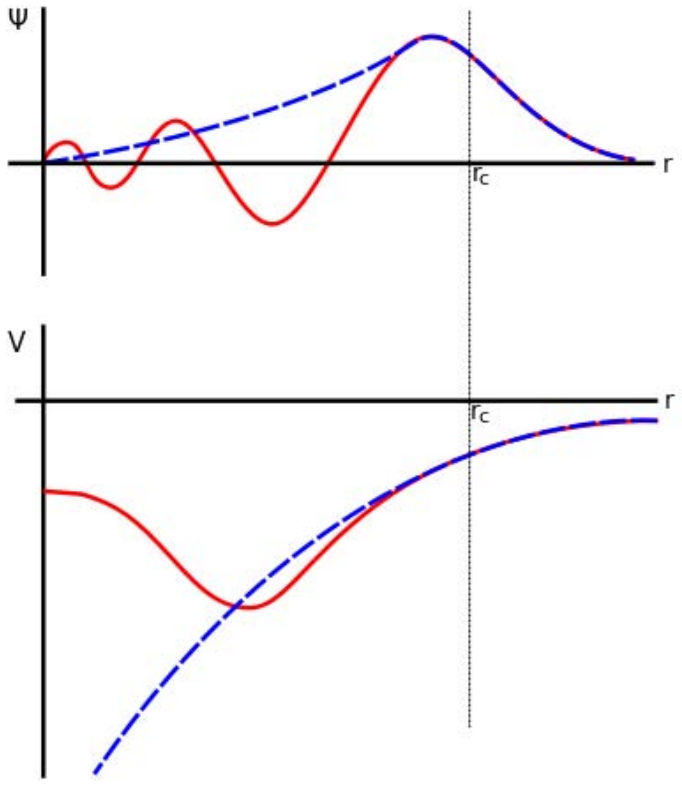

FIGURE 3.6: Norm-conserving pseudopotential (dashed blue line) versus the all-electron (red line) wavefunction and potential. Cut-off radius indicated by a dotted line.

that characterise that orbital. Conversely, a 'hard' pseudopotential is one that has a smaller cut-off radius, giving it a greater transferability as it retains more of the all-electron character.

Ultrasoft pseudopotentials

Ultrasoft pseudopotentials were developed in an effort to attain calculations of similar accuracy to, say, norm-conserving pseudopotentials, but with a greatly reduced number of plane wave basis functions [138]. As per the naming convention of 'soft' versus 'hard' pseudopotentials, an ultrasoft pseudopotential is one that offers a very smooth function that can be described with even fewer basis functions. This ultrasoft nature is achieved by relaxing the condition of norm-conservation used in norm-conserving pseudopotentials and compensating for this by adding back an auxillary charge density.

3.3 Potential models

While quantum mechanical methods, such as density functional theory, can provide us with precise and consistent determinations of the energy and forces of a system, they do

so at great computational expense. The consideration of electrons in the system–even when some of those electrons are considered in an average sense–introduces a high level of complexity into the simulations. This complexity means that there is an upper limit on the size of a system and the timescale that it can be simulated for.

Potential models extend that upper bound by ignoring electronic motions and instead calculating the energy and forces of a system using the positions of the nuclei only. This approximation drastically reduces the cost of calculations performed, resulting in an ability to simulate systems with numbers of atoms orders of magnitude larger than quantum mechanical methods. In addition, as long as the properties being calculated are not overly dependent on the explicit electronic distribution in the system (e.g. distortions arising from the Jahn-Teller effect [139]), potential models often can be 'trained' to give values that are in agreement with more costly methods. The main advantage of potential models, as pertaining to this thesis, is their ability to simulate long timescales in a process known as molecular dynamics, or a large number of configurations in Monte Carlo calculations. This is useful for exploring energy landscapes in search of new candidate structures to be used in structure determination.

3.3.1 Born model of ionic solids

When considering modelling using empirical potentials, we generally frame the system in terms of long-range and short-range interactions. The most basic description of these interactions comes from the Born model of ionic solids [140]. He proposed a simple summation over long-range Coulombic terms and short-range repulsive forces, based on the assumption that the solid is composed of spherically symmetric positive and negative ions:

$$U(r_{ij}) = \sum_{i=1}^{N}\sum_{j\neq i}^{N}\left(\frac{q_i q_j}{4\pi\varepsilon_0 r_{ij}} + \phi_{ij}(r_{ij})\right) \tag{3.42}$$

The Born model of ionic solids makes a few important approximations: it is restricted to only two-body (pairwise) interactions, the repulsive potential only acts on nearest neighbours, and the charges q_i and q_j are said to be equal to the oxidation states of the atoms. Obviously some modifications can be made to this model to make it more appropriate for a wider variety of systems.

3.3.2 Ewald summation

We can rewrite the Coulombic term present in the Born model to include the consideration of a periodic system;

$$U(r_{ij}) = \frac{1}{2} \sum_{|\mathbf{n}|=0} {}' \sum_{i=1}^{N} \sum_{j=1}^{N} \frac{q_i q_j}{4\pi\varepsilon_0 |\mathbf{r}_{ij} + \mathbf{n}|} \tag{3.43}$$

where q_i and q_j are the charges on the ions i and j, r_{ij} is the displacement of ion i from ion j, and $\mathbf{n}$ is the set of lattice vectors describing the periodic crystal lattice. The problem with equation (3.43) is that the summation converges very slowly, and is in fact conditionally convergent in real space. This means that the series has a mixture of positive and negative terms such that the positive terms by themselves do not converge, and the negative terms by themselves do not converge. This means that the solution to a conditionally convergent series is contingent on the order in which the terms are considered.

This convergence problem was the basis for the development of the Ewald summation, a method for computing the long-range interaction energies of periodic systems [141]. The derivation of the Ewald summation utilises reciprocal space to describe the long-range interactions between atoms, ensuring their rapid convergence. While the full derivation is too long to be included here, a conceptual explanation can be given.

The problem with convergence encountered in the Coulombic expansion can be avoided by utilising a mathematical identity to split the potential into two parts. The first part is made to be the point charges of each ion, surrounded by a Gaussian charge distribution of equal magnitude but opposite sign, effectively neutralising the long range effects of the charge. This construction means that this part converges rapidly in real space. The second part is composed of Gaussian distributions of charge of equal magnitude and the same sign as the ions, situated at each ionic site. This part converges rapidly in reciprocal space. The two calculations are summed such that the Gaussian functions cancel each other out, leaving the point charges. In this way we have avoided the conditional convergence problems of equation 3.43.

As well as the real and reciprocal Gaussian charge distribution functions, there is also a third function that must be subtracted from the summation in order to account for the self interaction of the Gaussian functions. Taking into account all these terms, the final Ewald sum can be written;

$$U(r_{ij}) = \frac{1}{2}\sum_{i=1}^{N}\sum_{j=1}^{N}\left\{ \begin{array}{l} \sum_{|\mathbf{n}|=0}^{\infty}{}' \frac{q_i q_j}{4\pi\varepsilon_0}\frac{\mathrm{erfc}(\alpha|\mathbf{r_{ij}}+\mathbf{n}|)}{|\mathbf{r_{ij}}+\mathbf{n}|} \\ +\sum_{k\neq 0}\frac{1}{\pi V}\frac{q_i q_j}{4\pi\varepsilon_0}\frac{4\pi^2}{k^2}\exp\left(-\frac{k^2}{4\alpha^2}\right) cos(\mathbf{k}\cdot\mathbf{r_{ij}}) \end{array} \right\} - \frac{\alpha}{\sqrt{\pi}}\sum_{k=1}^{N}\frac{q_k^2}{4\pi\varepsilon_0}$$

where erfc is the complementary error function, α is the exponent of the Gaussian functions, $\mathbf{k}$ are the reciprocal vectors, and V is the volume of the periodic unit cell. This expression assumes a system is charge neutral and has zero net dipole.

3.3.3 Examples of short range potentials

While the Ewald summation represents one of the better methods of calculating long-range electrostatic interactions, the short-range interactions can be modelled using a variety of approximations. A short discussion of some of the more common examples follows.

The Lennard-Jones potential

The Lennard-Jones potential [142] describes the nuclear and electronic repulsions, plus Van der Waals attraction, using a two term equation:

$$U_{LJ}(r_{ij}) = 4\epsilon_{ij}\left[\left(\frac{\sigma_{ij}}{r_{ij}}\right)^{12} - \left(\frac{\sigma_{ij}}{r_{ij}}\right)^{6}\right] \tag{3.44}$$

where ϵ is the depth of the potential well, σ is the distance at which the potential is zero, and r is the interatomic distance. The first term in the L-J potential is modelled after the repulsion experienced by ions when their electron clouds are brought close together, while the second term describes the attractive dispersion forces that take over at longer distances. The 12^{th} power on the repulsive first term has no theoretical justification, but it is an easy calculation, taken as the square of the 6^{th} power calculated first. The repulsion that it results in does have a physical analogue, as the energy of a system is found to increase as electrons are brought closer together due to the Pauli exclusion principle. The typical fit of a L-J potential to an argon dimer is shown below in Figure 3.7.

The Buckingham potential

The Buckingham potential [144] takes the Lennard-Jones potential model and replaces the repulsive first term with a more flexible, exponential form;

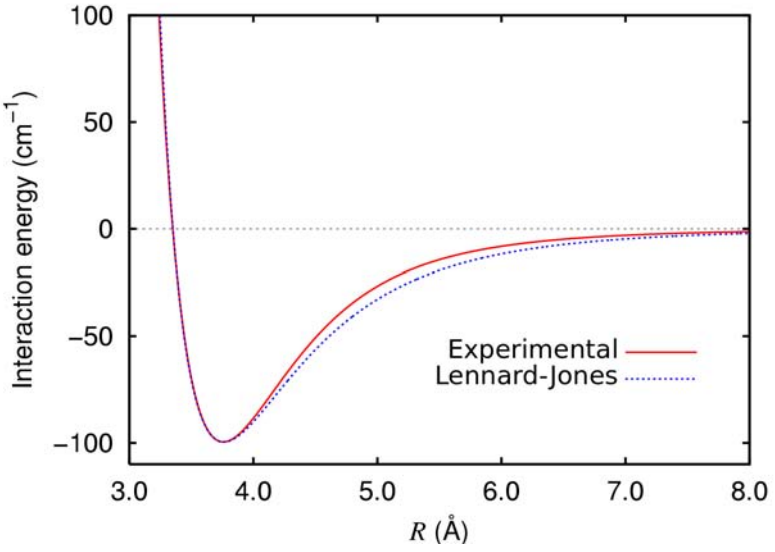

FIGURE 3.7: Interaction energy of argon dimer with L-J potential fitted to experimental results, reproduced from [143].

$$U_{Buck}(r_{ij}) = A_{ij}e^{\left(-\frac{r_{ij}}{\rho}\right)} - \frac{C}{r_{ij}^6} \tag{3.45}$$

where A, σ, and C are parameters again related to the depth and shape of the potential. The greater flexibility of the first term enables the Buckingham potential to be used for the simulation of solids containing a greater degree of polar character.

The Morse potential

For covalently bonded atoms, it is often preferable to describe the two-body interaction with either a harmonic or Morse [145] potential. The Morse potential takes the form:

$$U_{Morse}(r_{ij}) = D_e\left[(1 - e^{-a(r-r_e)})^2 - 1\right] \tag{3.46}$$

This gives the potential a physical significance, where r is the distance between the two atoms, r_e is the equilibrium bond distance, D_e is the well depth of the potential (can be used to calculate the dissociation energy), and a is related to the curvature at the minimum of the potential. When ionic Coulombic interactions are subtracted and replaced with these covalent harmonic models for bonds, the method is referred to as 'molecular mechanics'.

Three-body potential

Just as the implementation of the two-body potential comes in the different forms of Lennard-Jones, Buckingham, and Morse (and many more besides), there are also multiple forms of three-body potentials. These different forms generally have different physical interpretations. For example, if dealing with covalent bonds, the three-body potential models achieve their angular dependence by adding a penalty for deviating from an expected angle, e.g. the 109.5° bond angles of a tetrahedra. This results in a harmonic form of potential:

$$U_{ijk} = \frac{1}{2} k_2 \left(\theta - \theta_0\right)^2 \tag{3.47}$$

where k is the harmonic force constant, θ is the bond angle, and θ_0 is the equilibrium bond angle.

3.3.4 Parameterisation of potential models

All forcefields contain a series of parameters that need to be determined. Generally speaking, this parameterisation of potential models is achieved by two methods; adjustment to try and reproduce higher level theoretical calculations, or adjustment to try and reproduce experimental results. In circumstances such as those presented in this project where physical data is not available, fitting to *ab initio* results represent the next best alternative. It should be noted that the approximations inherent in such calculations need to be accounted for in the interpretation of any results, and caution should be maintained when attempting to extrapolate to systems outside the training set.

Given the patience required to manually fit parameters, a favoured approach is the use of algorithms to fit force fields to data. An example of this is the use of a least-squares fit of the desired parameters to experimental thermodynamic and vibrational data [146]. The error in the fit is defined as the sum of squares of the differences between the experimentally observed and calculated values:

$$F = \sum_{observables} w(f_{calc} - f_{observed})^2 4 \tag{3.48}$$

The objective then becomes to minimise the error, F, by varying the parameters of the force field. The weighting factor, w, can be used to give preference to properties, such as the non-bonding terms and torsional angles, that may affect the final performance of the potential to a greater extent than other properties.

Chapter 4

Sample Production and Diffraction Experiments

4.1 Introduction

In chapter 2, the theory underlying the practise of diffraction experiments as a method for gaining insight into the atomic structure of crystals was presented. In this chapter the results from preparing and executing experiments utilising those theories will be discussed. We will first detail the methods used to produce $TiOSO_4 \cdot 2H_2O$ from solution, and the laboratory X-ray diffraction that was performed on the solid samples thus produced. Following this, a set of experiments used to explore the formation of $TiOSO_4 \cdot H_2O$ and $TiOSO_4 \cdot 2H_2O$ within small capillaries will be presented within the context of preparation for *in-situ* synchrotron X-ray diffraction experiments. The results from *ex-situ* and *in-situ* synchrotron X-ray diffraction experiments will be shown. Finally, the preparation of $TiOSO_4 \cdot 2D_2O$ for a neutron diffraction experiment and subsequent results will be presented.

4.2 Production of $TiOSO_4 \cdot 2H_2O$ from anhydrous $TiOSO_4$

The motivation for these experiments was to ensure that $TiOSO_4 \cdot 2H_2O$ could be made using $TiOSO_4$ as a starting material. Confirmation of the production of $TiOSO_4 \cdot 2H_2O$ was to be made by search/match procedures against previous X-ray diffraction experiments through various crystal structure databases. To a lesser extent, these experiments would also explore the products' dependence on the source of $TiOSO_4$ used to produce it, in order to determine the influence of impurities on the formation of $TiOSO_4 \cdot 2H_2O$.

4.2.1 Equipment and reagents

All experiments were performed in a Variomag reaction block, Type 12.42, purchased from H+P Labortechnik AG. The reaction block had space for twelve test tubes and contained an internal temperature monitor, as well as a thermocouple for insertion into solution for more closely controlled temperatures. Powdered samples of $TiOSO_4{\cdot}2H_2O$ were provided by BHP Billiton, but also purchased from Sigma-Aldrich and Riedel-de Haen chemical suppliers, as previous studies [9] have shown that the BHP Billiton $TiOSO_4{\cdot}2H_2O$ is only ∼75% pure. Concentrated (98%, 1.84g/mL) H_2SO_4 was used to prepare dilutions with de-ionised water.

4.2.2 Preparation of anhydrous $TiOSO_4$

$TiOSO_4{\cdot}2H_2O$ preparation and concentration experiments were carried out using amorphous $TiOSO_4$ as a starting reagent. Amorphous $TiOSO_4$ was produced by heating a quantity of $TiOSO_4{\cdot}2H_2O$ in a standard muffle furnace at 300°C overnight, or for at least four hours. During this process, the water molecules evaporate from the solid leaving amorphous $TiOSO_4$ [19].

The reasoning behind using amorphous $TiOSO_4$ as a starting point for the production of $TiOSO_4{\cdot}2H_2O$ was consideration towards future *in-situ* experiments. Other starting materials, such as TiO_2 and $TiOSO_4{\cdot}2H_2O$ itself, can take a long time to dissolve which, in the context of a time-limited synchrotron experiment, can be very inconvenient. Anhydrous $TiOSO_4$ has the advantage of dissolving readily in solution and can be used to generate both $TiOSO_4{\cdot}H_2O$ and $TiOSO_4{\cdot}2H_2O$, something the dihydrate has been shown to be unable to do [9].

4.2.3 Formation of $TiOSO_4{\cdot}2H_2O$ from $TiOSO_4$

The production of $TiOSO_4{\cdot}2H_2O$ from amorphous $TiOSO_4$ has not been explored very widely despite the particular advantages it possesses, as described above. Therefore, a series of experiments exploring the effect of acid concentration, titanium concentration, and temperature on the production of $TiOSO_4{\cdot}2H_2O$ and $TiOSO_4{\cdot}H_2O$ from amorphous $TiOSO_4$ was needed in order to know more precisely how the reactions might proceed. A combination of optical microscopy and X-ray diffraction was used to confirm the successful production of the two titanyl sulphate products.

The very first experiments to test the production of the dihydrate within the test tubes were carried out based on calculations provided to us by BHP Billiton; specifically the

FIGURE 4.1: Photographs of the products of the reaction between 2.8g of $TiOSO_4$ produced from BHP Billiton (left), Sigma-Aldrich (middle) and Riedel-de Haen (right) $TiOSO_4{\cdot}2H_2O$ precursor and 20mL of 400 gL^{-1} H_2SO_4 at 110($\pm$5)°C after 1 hour (top), 2.5 hours (middle), and 4 hours (bottom).

work of Marco Peng [11] on what he referred to as the 'fudge window' of titanyl sulphate solutions. A stock solution of 400 gL^{-1} sulphuric acid was prepared using 220mL of concentrated (98%, 1840 gL^{-1}) sulphuric acid made up to 1 litre with de-ionised water. Previous experiments had shown that the use of 400 gL^{-1} H_2SO_4 maximised the uptake of $TiOSO_4{\cdot}2H_2O$ into solution. Maximising the uptake was a necessity as we did not want any particles remaining in solution and acting as seeds for the dihydrate to nucleate on, and therefore influence the induction time or products of the reaction. A $TiOSO_4$ concentration of approximately 140 gL^{-1} was required to achieve precipitation, which corresponded to the addition of approximately 2.8g of $TiOSO_4$ to 20mL of 400 gL^{-1} H_2SO_4. Three test tubes of such composition were prepared using the BHP Billiton, Sigma-Aldrich, and Riedel-de Haen $TiOSO_4{\cdot}2H_2O$ as a starting reagent to produce the anhydrous $TiOSO_4$.

Figure 4.1 shows the products of the reaction at 110($\pm$5)°C after 1 hour, 2.5 hours, and 4 hours. As can be seen from the figure, the solution produced from the BHP Billiton anhydrous $TiOSO_4$ sample has a greater solubility than those produced from the commercial Sigma-Aldrich and Riedel-de Haen samples. This is shown by the clarity of the BHP Billiton solution, where the other solutions are clouded with undissolved $TiOSO_4$. The greater solubility of the BHP Billiton sample is thought to be due to the inclusion of iron within the sample, as a result of it having been crystallised from an ilmenite ($FeTiO_3$) leach solution, which would also explain the green colour of the solution.

In these experiments the induction time is defined as the time after which the solution becomes cloudy, presumably with nuclei of $TiOSO_4{\cdot}2H_2O$ particles. Due to the opacity of the starting solutions of the Sigma-Aldrich and Riedel-de Haen test tubes, their induction times were unable to be determined by this measure. The BHP Billiton sample's induction time was measured to be approximately 2 hours.

The solid produced from this reaction was very wet with sulphuric acid, and required extensive vacuum filtering and washing with ethanol in order to remove this excess. Once the sample had been dried to as high an extent as was possible, an optical microscope was used to confirm, on the basis of product morphology, that $TiOSO_4{\cdot}2H_2O$ had been produced. A series of optical microscope images of the $TiOSO_4{\cdot}2H_2O$ produced from the BHP Billiton precursor can be found in Figure 4.2 and from the Sigma-Aldrich precursor in Figure 4.3.

From these microscope images, it can be seen that the product formed in both cases fits the description of a fibrous, needle-like solid, as expected for $TiOSO_4{\cdot}2H_2O$. The morphologies of the crystals are similar despite the different precursors used to

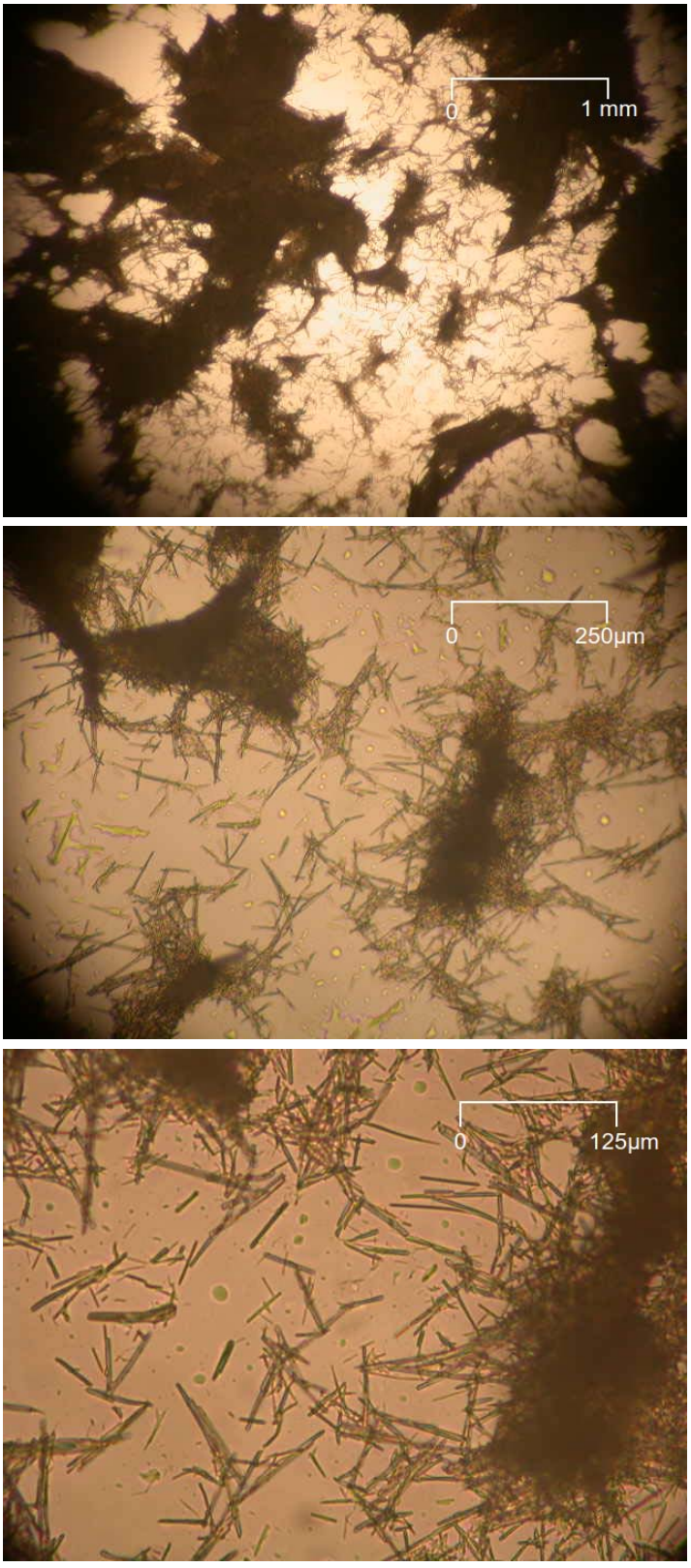

FIGURE 4.2: 100x (top), 400x (middle), and 800x (bottom) optical microscope photographs of the product formed from the reaction of 2.8g of $TiOSO_4$ produced from BHP Billiton $TiOSO_4{\cdot}2H_2O$ precursor and 20mL of 400 gL^{-1} H_2SO_4 at 130°C after 4 hours.

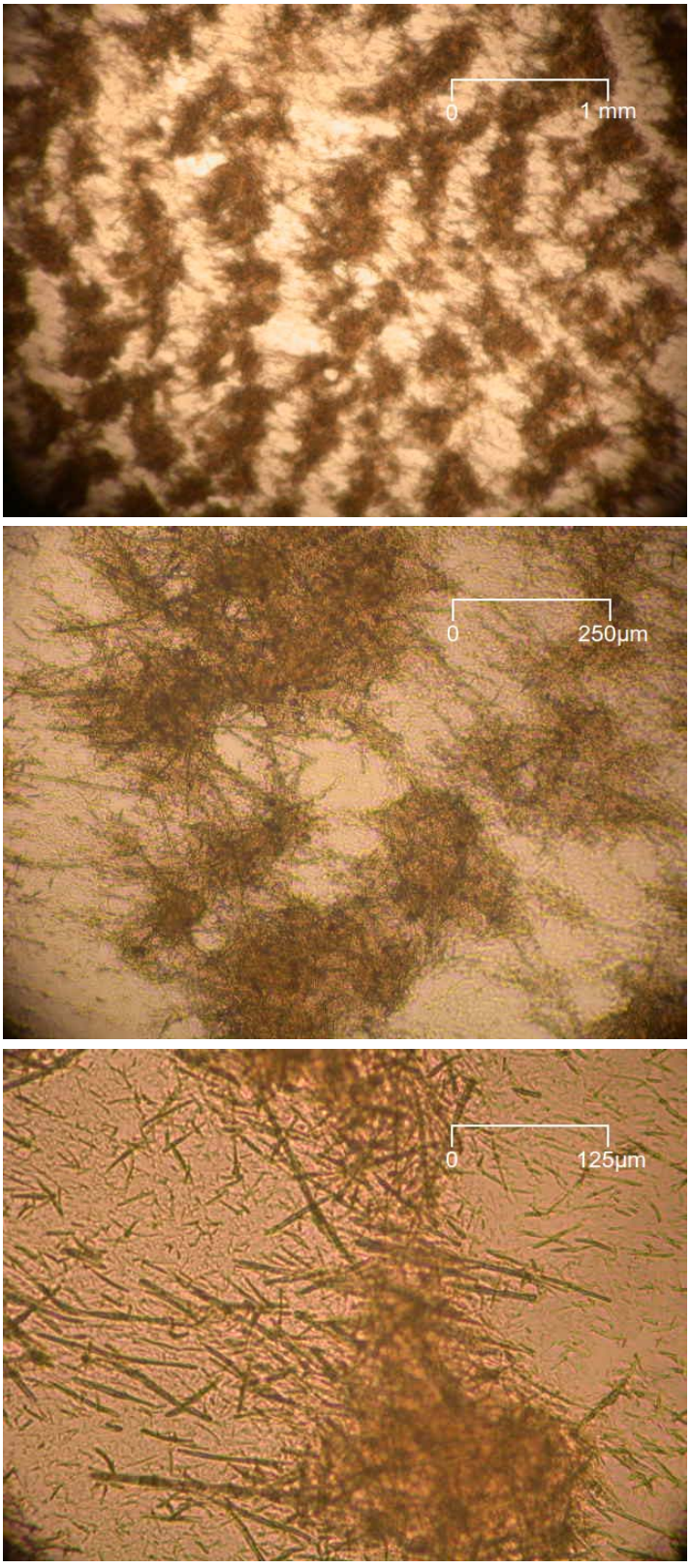

FIGURE 4.3: 100x (top), 400x (middle), and 800x (bottom) optical microscope photographs of the product formed from the reaction of 2.8g of $TiOSO_4$ produced from Sigma-Aldrich $TiOSO_4 \cdot 2H_2O$ precursor and 20mL of 400 gL^{-1} H_2SO_4 at 110($\pm$5)°C after 4 hours.

create them, which led us to believe that the supposed undissolved $TiOSO_4$ in the Sigma-Aldrich reaction had not affected the production of $TiOSO_4{\cdot}2H_2O$ crystals.

4.3 Laboratory X-ray diffraction

As a standard practise, X-ray diffraction with a laboratory diffractometer is useful for confirming the presence of phases in a sample. Laboratory X-ray diffraction was performed using the $TiOSO_4{\cdot}2H_2O$ product whose formation was described in the previous section. All laboratory X-ray diffraction experiments were performed on a Kristalloflex Siemens D500 diffractometer with Bragg-Brentano geometry, fitted with a Cu Kα X-ray tube that operated at an accelerating voltage of 20kV and beam current of 30mA. Diffraction patterns were recorded over a range of 5-65° 2θ, with a step size of 0.02° 2θ. Samples were mounted on a flat-plate sample holder and a spinner was engaged to improve counting statistics.

Figure 4.4 shows the laboratory X-ray diffraction pattern of the product produced from Sigma-Aldrich $TiOSO_4$, while Figure 4.5 shows the laboratory X-ray diffraction pattern of the product produced from BHP Billiton $TiOSO_4$. The two patterns are, to all intents and purposes, identical, proving that there is little variability introduced by the impurities present in the BHP Billiton $TiOSO_4$.

In order to confirm that the needle-like crystals were indeed indicative of the presence of $TiOSO_4{\cdot}2H_2O$ in the product, a peak search was made using both the 'Jade' software suite, which utilises the Powder Diffraction File (PDF) database maintained and distributed by the International Centre for Diffraction Data (ICDD), and also the 'FindIt' software suite, which utilises the Inorganic Crystal Structure Database (ICSD). Both programs use the peaks found in an input diffraction pattern to search the associated database of patterns, and rank the results by the number of peaks that are matched. In our case the diffraction pattern from the Sigma-Aldrich powder sample was used as representative. Obviously some filters must be applied on the type of materials from which diffraction pattern matches are returned. In our case, a chemistry filter was used to restrict the elements present in the matching patterns to that of titanium, sulfur, oxygen, and hydrogen. Titanium, sulfur, and oxygen were all required to be in the material, while hydrogen was flagged as optional. This resulted in the list of matched structures and their references shown in Table 4.1.

It should be noted that in all of the structures listed, the diffraction patterns were not available to be downloaded; instead a list of peaks was provided in the PDF. The positions and relative intensities of these peaks are calculated from the ideal XRD

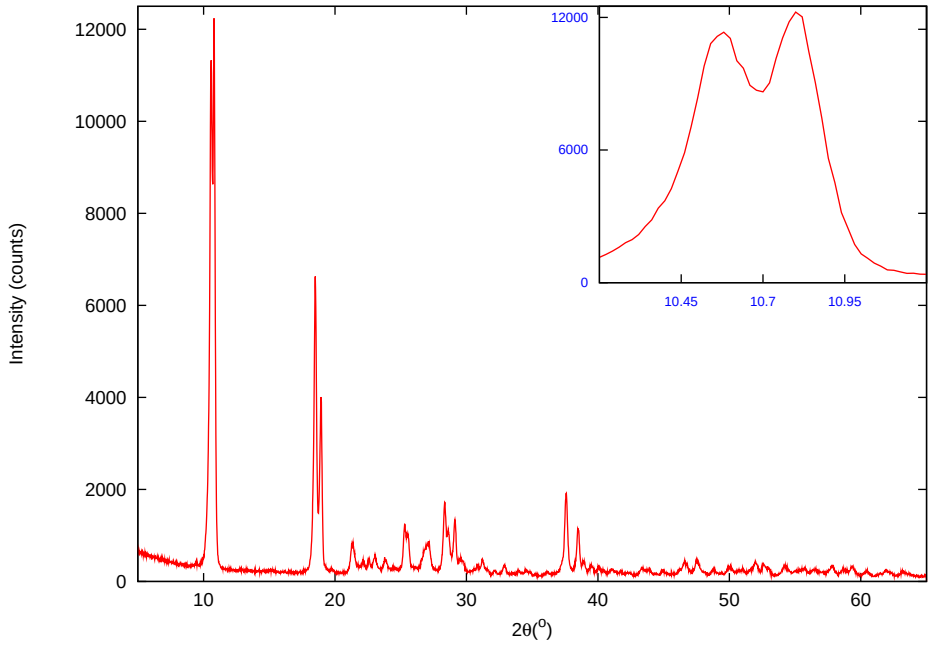

FIGURE 4.4: Laboratory X-ray diffraction pattern of Sigma-Aldrich powder sample. Inset; enlarged view of double peaks present at low angle.

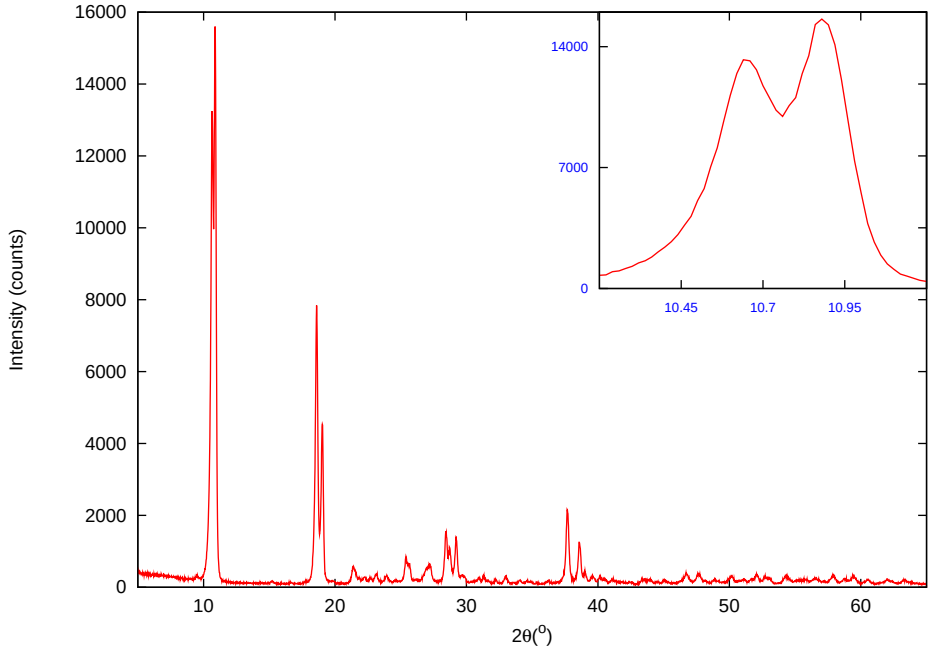

FIGURE 4.5: Laboratory X-ray diffraction pattern of BHP Billiton powder sample. Inset; enlarged view of double peaks present at low angle.

PDF number	**Structure**	**Reference**
11-0032	$TiOSO_4 \cdot H_2O$	Lundgren, G., Ark. Kemi, 10, 397 (1957)
14-0503	$TiOSO_4 \cdot 2H_2O$	Kubo, T. *et al.* The Tokyo Institute of Technology, Tokyo, Japan. ICDD Grant-in-Aid (1959)
18-1406	$Ti(SO_4)_2$	Frazer, M. J., *et al.* J. Chem. Soc. 342 (1965)
21-1240	$Ti_2(SO_4)_3 \cdot 5H_2O$	Blondel, B., *et al.* Bull. Soc. Chim. Fr. 101 (1968)
21-1241	$Ti_2(SO_4)_3 \cdot 8H_2O$	Blondel, B., *et al.* Bull. Soc. Chim. Fr. 101 (1968)
22-0947	$Ti_2(SO_4)_3$	Blondel, B., *et al.* Bull. Soc. Chim. Fr. 101 (1968)
39-0671	$TiOSO_4 \cdot H_2O$	Samoilova, G. *et al.* J. Inorg. Chem. (Engl. Transl.), 31, 801 (1986)
40-0653	$TiOSO_4$	Samoilova, G. *et al.* J. Inorg. Chem. (Engl. Transl.), 31, 801 (1986)
42-0230	$Ti_2(SO_4)_3$	Holzer, J. *et al.* North Dakota State University, Fargo, North Dakota, USA. ICDD Grant-in-Aid (1991)
42-0291	$TiOSO_4 \cdot H_2O$	Pervushin, V. *et al.* J. Inorg. Chem. (Engl. Transl.), 34, 615 (1989)
49-0467	α-$TiOSO_4$	Grey, I. *et al.* Royal Aust. J. Chem., 49, 801 (1996)

TABLE 4.1: List of structures returned from search/match procedure.

pattern of each crystal structure using the Graphical Display Interface for Structures (GDIS) software package [147]. Thus in any figure that uses the diffraction data from these structures, only impulses (i.e. single lines with varying intensities, but no peak width) will be shown rather than full diffraction profiles with peak character.

Out of all the suggestions of matched peak patterns, only one had a figure of merit of less than 1 (0 being a perfect fit of all peaks present), that being PDF #14-0503. Figure 4.6 shows the Sigma-Aldrich sample XRD pattern overlayed with the PDF #14-0503 impulses. The Sigma-Aldrich pattern has been normalised to the PDF for ease of comparison.

From this figure it is easy to see that the majority of low angle peaks are matched, with only a small cluster of peaks in the 21-25° 2θ range, and various shoulders on peaks at higher angles, remaining unaccounted for. Given the age of the PDF—first recorded in 1959—it is conceivable that the peaks which are not included in the peak list were unable to be distinguished from the background, while the shoulders were unable to be resolved using the technology current at the time. The former statement is supported by the fact that the cluster of peaks that are not accounted for are of lower intensity than

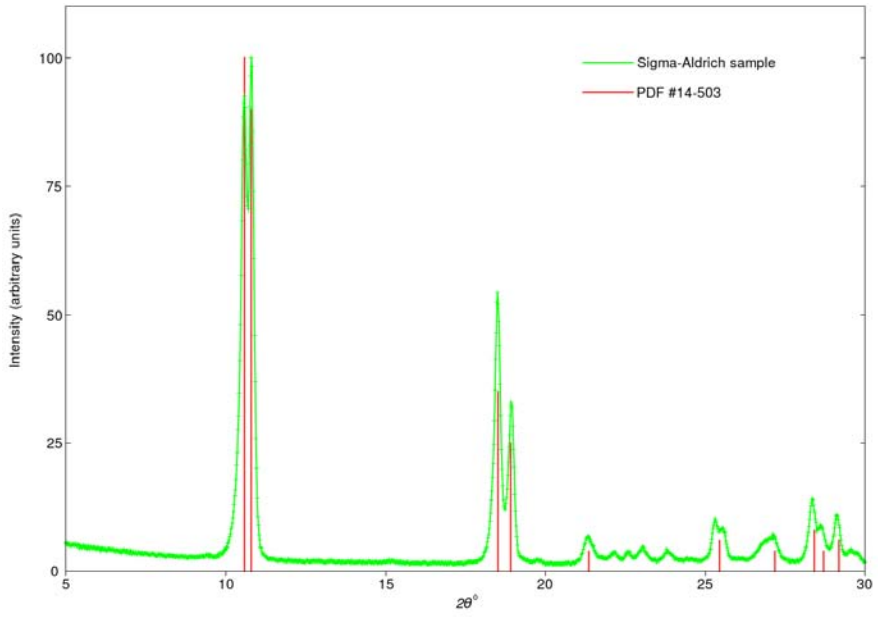

FIGURE 4.6: Diffraction pattern of Sigma-Aldrich sample with the peaks in PDF #14-503 overlayed.

any other in the range explored, and thus may have been under the threshold of the background noise. One interesting detail that comes out of this comparison is that in the PDF file, the double peak at low angles has its ratios reversed compared to the pattern we collected. Given that the rest of the pattern has correct ratios of each recorded peak, it comes as a surprise that these lower angled peaks do not. This behaviour is repeated in other diffraction experiments, and the possible origins for it will be offered in a later section.

Unfortunately, PDF #14-503 was not the result of a paper and so there is no journal article or record that details what procedure Kubo *et al.* followed to produce their $TiOSO_4 \cdot 2H_2O$ sample. The incompleteness of the accompanying data in the PDF record (for example, the density and cell parameters are missing) coupled with the lack of a resultant journal article seems to suggest that this was an isolated experiment.

The gap in fit probability between PDF #14-503 and the remaining matches was substantial. The figures of merit and other statistics relating to the fit of data are shown in Table 4.2. The reason for this is obvious; besides PDF #14-503, there were no other patterns found for $TiOSO_4 \cdot 2H_2O$. This is very unfortunate, as the incomplete nature of the record means that beyond the few matching peaks we have there is no way of confirming sample character by matching to an indexed unit cell.

To verify the method's capability of producing a phase pure sample of $TiOSO_4 \cdot H_2O$, an experiment was performed with the same technique outlined in section 4.2, but using a

PDF #	Compound	Peaks matched	Peaks not matched	Figure of merit
14-0503	$TiOSO_4{\cdot}2H_2O$	13	0	0.35
49-0467	α-$TiOSO_4$	17	11	14.79
11-0032	$TiOSO_4{\cdot}H_2O$	27	11	29.64
18-1406	$Ti(SO_4)_2$	14	5	45.62
21-1240	$Ti_2(SO_4)_3{\cdot}5H_2O$	10	5	51.55
39-0671	$TiOSO_4{\cdot}H_2O$	6	6	110.3
22-0947	$Ti_2(SO_4)_3$	13	13	125.9
21-1241	$Ti_2(SO_4)_3{\cdot}8H_2O$	9	9	149.0
42-0291	$TiOSO_4{\cdot}H_2O$	12	7	202.0
42-0230	$Ti_2(SO_4)_3$	19	16	414.6
40-0653	$TiOSO_4$	8	6	489.1

TABLE 4.2: List of structures returned from search/match procedure, with the number of peaks matched and figures of merit.

higher concentration of acid (20mL of 9M H_2SO_4) and a larger amount of $TiOSO_4$ ($\tilde{4}$g BHP Billiton $TiOSO_4$). From a solution chemistry point of view, it is believed that the increase in acidity corresponds to a 'crowding out' of the water molecules, leaving them unable to form the higher hydrate form. The product from this reaction was verified *via* morphological character as monohydrate crystals using an optical microscope. X-ray diffraction was then performed in the same manner as was described for $TiOSO_4{\cdot}2H_2O$.

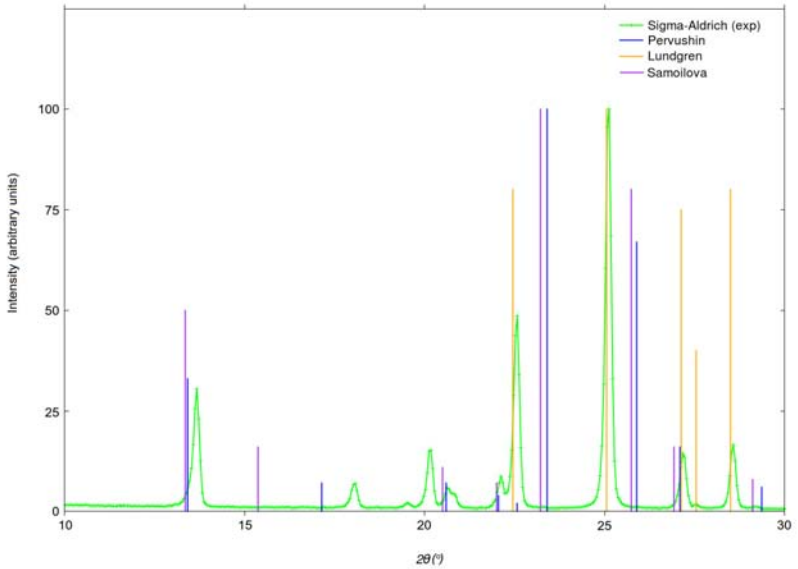

FIGURE 4.7: Figure showing a section of the diffraction pattern of Sigma-Aldrich $TiOSO_4{\cdot}H_2O$ compared to the PDFs of Pervushin [148], Lundgren [16], and Samoilova [149].

Figure 4.7 shows the comparison between the experimental pattern and the PDFs of the structures of $TiOSO_4{\cdot}H_2O$. Of some interest is the disparity between the diffraction patterns of what is supposedly the same crystal structure. In light of these

disagreements, and in order to confirm that our product was indeed $TiOSO_4 \cdot H_2O$, an ideal diffraction pattern was generated from the atomic structure presented in Gatehouse [13]. The comparison between experimental and calculated diffraction patterns is shown in Figure 4.8.

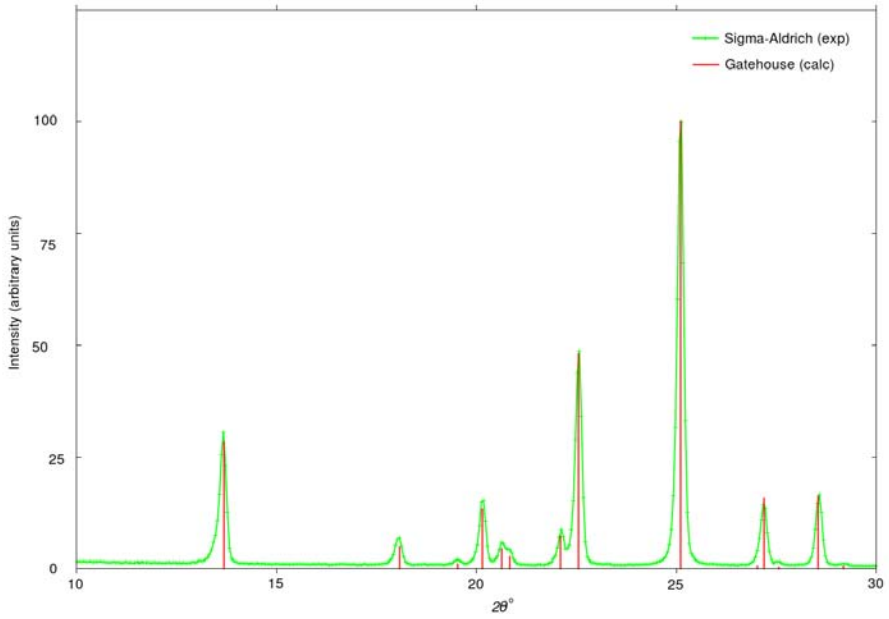

FIGURE 4.8: Figure showing the diffraction pattern of Sigma-Aldrich $TiOSO_4 \cdot H_2O$ compared to ideal diffraction pattern of $TiOSO_4 \cdot H_2O$ crystal structure of Gatehouse *et al.*[13].

From this figure it can be seen that the match between the sample and the calculated diffraction pattern is very close. There are no unmatched peaks, and the relative peak intensities are almost perfect. It is therefore relatively safe to say that the sample produced using this method is phase pure $TiOSO_4 \cdot H_2O$, despite the confusion introduced by the PDF records.

Having confirmed the purity of the $TiOSO_4 \cdot H_2O$ phase produced by reacting anhydrous $TiOSO_4$ and sulphuric acid, we could use its diffraction pattern to ensure that there was no $TiOSO_4 \cdot H_2O$ coprecipitating within the $TiOSO_4 \cdot 2H_2O$ reaction. A comparison of the two diffraction patterns is shown in Figure 4.9.

From this figure it can be seen that there are very few occasions where the two patterns overlap. In fact, the only points at which the patterns do show a definitive coincidence of peaks are the two peaks at 22.1 and 22.6° 2θ. While these two peaks are part of the group that was not characterised as $TiOSO_4 \cdot 2H_2O$ in PDF #14-503, if we were to assume that the coincidence is evidence of an additional phase of $TiOSO_4 \cdot H_2O$ present in the sample, we would expect to see some of the larger peaks being expressed as well, which we do not. Therefore it can be concluded that, on the basis of both

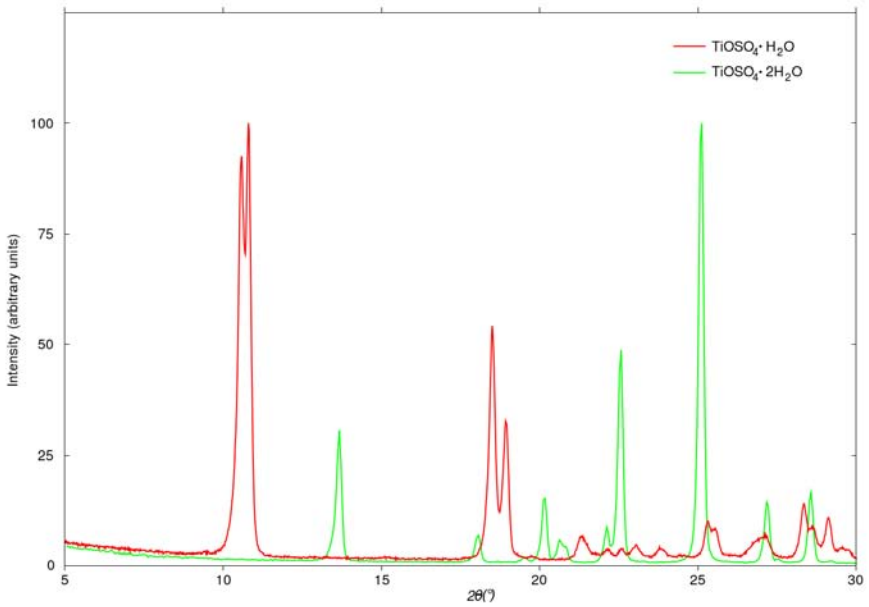

FIGURE 4.9: Comparison of the diffraction pattern of $TiOSO_4 \cdot H_2O$ with that of $TiOSO_4 \cdot 2H_2O$.

the search/match programs returning no other suitable matches and the only other expected phase remaining unexpressed in the $TiOSO_4 \cdot 2H_2O$ diffraction pattern, the $TiOSO_4 \cdot 2H_2O$ phase is pure.

Following on from these results, it was seen as no coincidence that the inability to solve the structure was coupled with a distinct lack of reported diffraction experiments in the literature. It was decided that in order to attain a more definitive diffraction pattern as a base from which structure determination could be launched, a synchrotron X-ray diffraction experiment would be an appropriate starting point given the technique's greater resolution and counting statistics. Sample preparation for synchrotron X-ray diffraction experiments possesses its own unique challenges, and these will be detailed in the following sections.

4.4 Induction time experiments

The differing ratios of the double peaks in PDF #14-503 and our sample guided us to consider *in-situ* growth experiments. Such experiments would allow us to observe how the peaks evolve over the course of precipitation, and thus give us insight into the possible mechanisms governing the phase growth. Given the need to acquire *ex-situ* synchrotron X-ray diffraction data and the absence of adequate heating equipment in the laboratory X-ray diffractometer, it was decided that *in-situ* experiments would be

best performed at a synchrotron facility. However, the limited availability of synchrotron beam time at Australian and international facilities meant that experiments needed to be feasible within a reasonable time frame (i.e. less than 24 hours). To prepare for this, a series of experiments exploring the variation of induction times as a function of acidity and reagent concentration was performed. The aim was to determine conditions that might allow us to perform an *in-situ* experiment within the limits of synchrotron beam time. The results of these experiments are shown in the following sections.

4.4.1 Effect of acid concentration on induction time

For this experiment, four solutions were prepared using the same method as that described in section 4.2.3, but maintaining a constant $TiOSO_4$ concentration of approximately $142gL^{-1}$ while varying H_2SO_4 concentrations. Solid BHP Billiton precursor was added to 20mL of $400gL^{-1}$ H_2SO_4 in quantities specified below in Table 4.3. A small volume of concentrated H_2SO_4 was then added to each solution to bring the concentration up to the desired amount.

Solution number	**m($TiOSO_4$) g**	**V(conc. H_2SO_4) mL**	**c(H_2SO_4) gL^{-1}**
1	3.08	2	527
2	3.36	4	633
3	3.50	6	752
4	3.92	8	800

TABLE 4.3: Composition of the four solutions showing the variation in acid concentration. $TiOSO_4$ concentration was kept constant at $142gL^{-1}$.

The solutions were placed in the Variomag reaction block at $110(\pm5)^{\circ}C$, and monitored to track the induction time of the intended product. Again, the induction time was determined by a visual inspection of each solution at regular intervals. Obviously a camera setup would have been preferable to this manual inspection, but the nature of the reaction block meant that the solutions were obscured during any experiments and needed to be removed to be inspected, as can be seen above in Figure 4.1. As a result of this, there was a twenty minute uncertainty imposed on the times listed in Table 4.4, which shows the induction times of the solutions during the experiment.

The presence of undissolved $TiOSO_4$ in solutions 1 and 2 effectively exclude those solutions from giving a correct induction time. Not only is it impossible to discern between the undissolved $TiOSO_4$ particles and the nucleation of $TiOSO_4{\cdot}2H_2O$ crystals with the naked eye, but the undissolved $TiOSO_4$ particles may in fact act as seeds for the $TiOSO_4{\cdot}2H_2O$ crystals to form from, driving the induction time down greatly. Figures 4.10 and 4.11 show photographs of the experiment as it proceeded.

Solution number	**Induction time (±20 mins)**
1	N/A
2	N/A
3	240 minutes
4	300 minutes

TABLE 4.4: Observations recorded during the reaction of solutions 1-4, as described in Table 4.3.

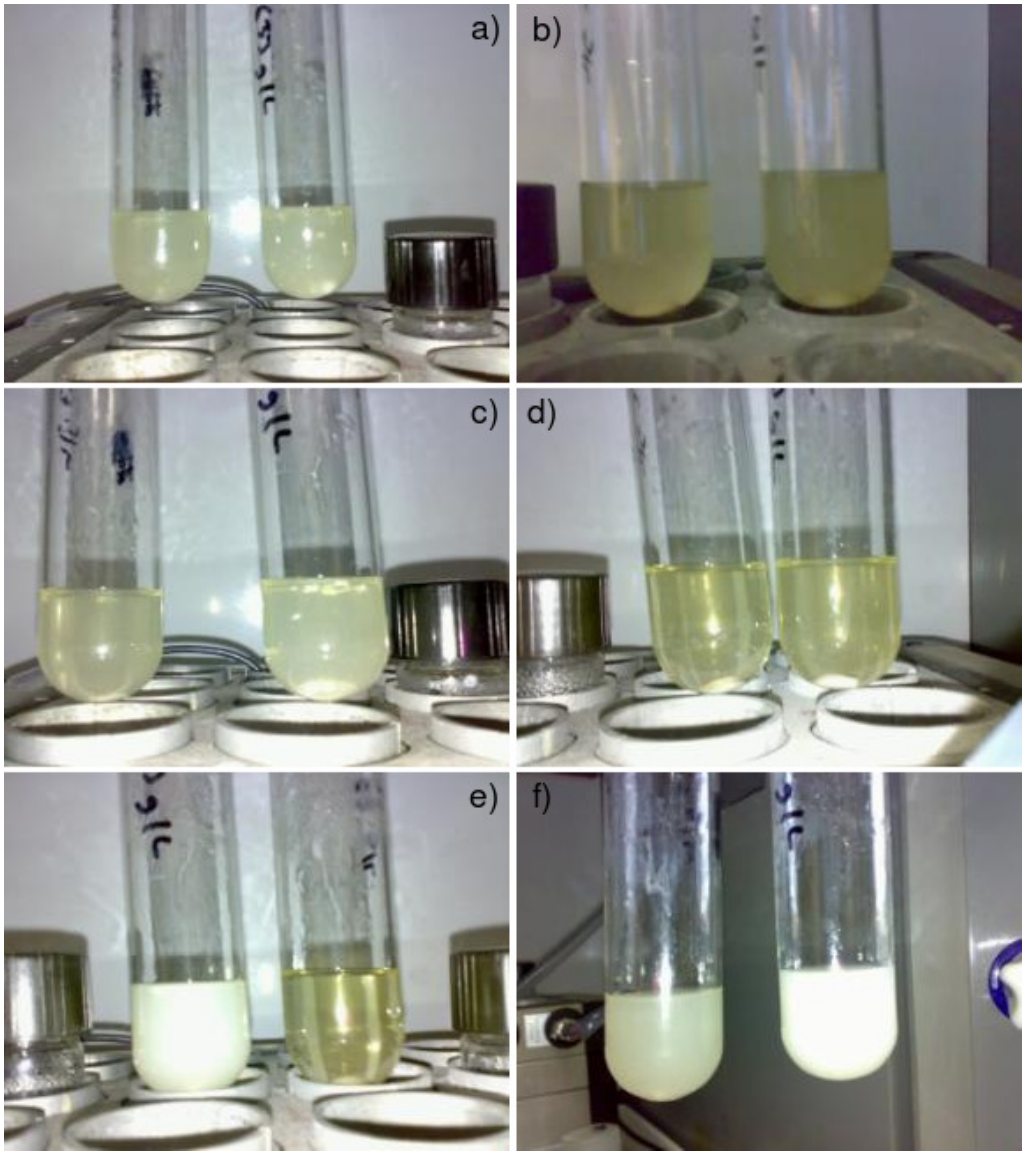

FIGURE 4.10: Photographs of solutions with concentrations shown in Table 4.3 during varying acidity experiment: a) solutions 1 and 2 at the start of the experiment; b) solutions 3 and 4 at the start of the experiment; c) solutions 1 and 2 after 10 minutes; d) solutions 3 and 4 after 10 minutes; e) solutions 2 and 3 after 20 minutes; f) solutions 1 and 2 after 40 minutes.

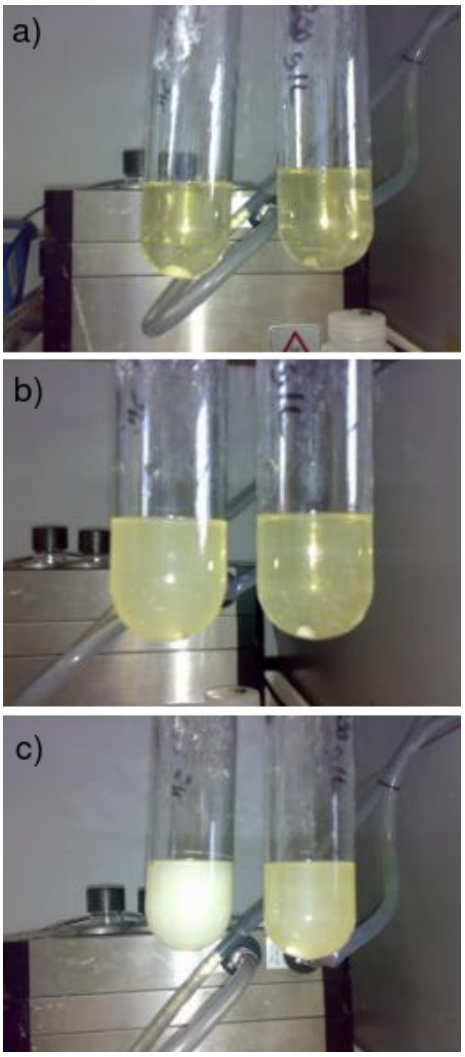

FIGURE 4.11: Continuation of photographs of solutions during varying acidity experiment: a) solutions 3 and 4 after 3 hours; b) solutions 3 and 4 after 4 hours; c) solutions 3 and 4 after 5 hours.

Solutions 3 and 4 took a lot longer to nucleate than was expected—Marco Peng's previous work on this system suggested that an increase in acidity corresponded to a decrease in fudge time and therefore, necessarily, induction time. While solutions 1 and 2 did not yield useful results, it was expected that solutions 3 and 4 would have an induction time less than that of the BHP Billiton sample.

It could be intuited from these experiments that the BHP Billiton precursor is more soluble at lower acid concentrations. In order to circumvent the problem of undissolved $TiOSO_4$ particles, a tighter range of H_2SO_4 concentrations of 400-445gL^{-1} was proposed to investigate the influence of acid concentration on induction time. The concentration of $TiOSO_4$ was kept constant at 142 gL^{-1}. The new range of concentrations and their constituents are shown in Table 4.5, while the observations from the experiment are

Solution number	**m($TiOSO_4$) g**	**V(conc. H_2SO_4) mL**	**c(H_2SO_4) gL^{-1}**
1	2.8010	0	400
2	2.8703	0.211	415
3	2.8919	0.422	430
4	2.9240	0.633	445

TABLE 4.5: Composition of the four solutions showing the tighter range of variation in acid concentration

Solution number	**Induction time (± 10 mins.)**
1	100 minutes
2	70 minutes
3	60 minutes
4	80 minutes

TABLE 4.6: Observations recorded during the reaction of solutions 1-4, as described in Table 4.5

shown in Table 4.6. From these observations, it can be seen that solution 1 had the longest induction time at 100 minutes, followed by solution 4 at 80 minutes, solution 2 at 70 minutes, and finally solution 3 achieving induction the quickest at 60 minutes; i.e. solution $1 > 4 > 2 > 3$. Based on Marco Peng's work, the expected order was solution $1 > 2 > 3 > 4$, and therefore the correlation between the experimental result and the expected result is weak.

From these experiments it is clear that the measurement of an induction time from a crystallisation reaction is difficult to achieve. Any number of influences may cause variation in solubility and induction time; as well as small amounts of impurities, residual particles, imperfections in the glassware used, etc. [150]. More specifically, in this experiment, it is thought that the erroneous solution 4 result may have been due to the small graduations of concentrated H_2SO_4 required introducing human error, or possibly a result of evaporation within the test tubes reducing the concentration of the solution.

4.4.2 Investigation of the production of $TiOSO_4{\cdot}2H_2O$ and $TiOSO_4{\cdot}H_2O$ in capillaries

The geometry of the Australian Synchrotron beam line involves the use of capillaries filled with solid sample (in the case of *ex-situ* experiments) or solutions of reactants (in the case of *in-situ* experiments). While the experiments previously performed in test tubes had been capable of producing both $TiOSO_4{\cdot}2H_2O$ and $TiOSO_4{\cdot}H_2O$, concern was raised over the vast reduction in vessel volume when moving from reactions in test tubes to capillaries. Accordingly, a new set of experiments was proposed to investigate

any risk of anomolous behaviour in the new environment, and guarantee the feasibility of crystallisation experiments.

4.4.2.1 Equipment and procedure

Initial experiments:

Due to the high cost of quartz capillaries, preliminary tests were carried out using Pasteur pipettes, which were drawn out using a handheld butane burner to form glass capillaries with a diameter similar to that of the quartz capillaries to be used for synchrotron XRD experiments. In these inital experiments, a 20mL solution of 65wt% H_2SO_4 was used to dissolve 1.59g of anhydrous $TiOSO_4$, and stirred for approximately 10 minutes to ensure that dissolution was complete. This solution corresponds to set 1 in Table 4.7. Once the solid was dissolved, a rubber bulb was used to draw up a small amount of the solution into the long section of the Pasteur pipette. Both ends of the pipette were then sealed with the burner to produce a solution within a sealed glass tube.

Three such capillaries were produced and taped to a glass stirring rod. The stirring rod was then immersed in a test tube containing Ondina heating oil, along with a thermostat. The test tube was then placed wihin the Variomag Reaction Block and heated at 110($\pm$5)°C for 24 hours. The original solution that the capillaries were filled using was placed in a separate test tube within the reaction block as a control.

Both samples from the original solution and the capillaries themselves were taken at 4 and 24 hours reaction time and analysed under an optical microscope, with images taken by a digital camera attachment. The image quality for the capillaries varies, as the curvature of the glass can cause difficulty in focussing the lens. The dimensions of the images are as follows: 100x = 4.33 mm x 3.25 mm; 400x = 1.08 mm x 0.81 mm; 800x = 0.54 mm x 0.41 mm; 1200x = 0.36 mm x 0.27 mm. Using these values, the length of $TiOSO_4 \cdot 2H_2O$ needles can be seen to vary from between 50-600 μm, with widths of only between 10-20 μm. However, the curvature of the glass and difficulty of focussing in liquids does introduce a certain amount of error, so these values should be taken as guides only.

Secondary experiments:

Once the method in the initial experiments was confirmed to work, a secondary set of capillaries were created to explore a larger range of concentrations and confirm the repeatability of the precipitation. These were sets 2-6 in Table 4.7, which records the set numbers and their corresponding compositions. Each set in these experiments consisted of two capillaries.

Set number	**m($TiOSO_4$)** (g)	**V(H_2SO_4)** (mL)	**c(H_2SO_4)** (wt%)	**$TiOSO_4$ stock**
Set 1	1.59	35	80	BHP
Set 2	5.03	20	65	BHP
Set 3	5.01	30	75	BHP
Set 4	5.01	30	75	Sigma-Aldrich
Set 5	5.01	30	75	BHP
Set 6	5.01	30	75	BHP
Set 7	5.00	20	65	BHP
Set 8	5.00	30	75	BHP
Set 9	5.00	30	87	BHP
Set 10	6.50	20	65	BHP
Set 11	6.50	30	75	BHP
Set 12	6.50	30	87	BHP

TABLE 4.7: Composition and labelling of the second set of capillaries used to investigate the precipitation of $TiOSO_4{\cdot}2H_2O$ within smaller volumes.

Tertiary experiments:

Following the results from the secondary sets of solutions, a third and final set of experiments was performed with the aim of forming monohydrate in the capillaries. These are listed as sets 7-12 in Table 4.7. The procedure to create the capillaries was the same as that undertaken with the previous experiments. Four capillaries were produced for each combination of $TiOSO_4$ and H_2SO_4 concentrations, to be reacted for 1, 4, 24, and 72 hours, respectively. After each period of time had elapsed, the capillaries were removed from the reaction block, cleaned, and examined under an optical microscope.

4.4.2.2 Results

Initial experiments–set 1:

The initial experiments were designed to replicate the conditions under which Bobby Pejcic produced $TiOSO_4{\cdot}H_2O$ during his project [9]. This was done to determine whether the reduced volume of the capillaries would alter the final product; if instead of $TiOSO_4{\cdot}H_2O$, $TiOSO_4{\cdot}2H_2O$ or a multi-phase system might be produced.

Figure 4.12 shows the optical microscope images from the original solution in the test tube after 4 and 24 hours. From these images it could be seen that the precipitate being formed in the test tube appears to be $TiOSO_4{\cdot}H_2O$, as it lacked the distinctive fibrous nature of the $TiOSO_4{\cdot}2H_2O$. Comparison to micrographs that Pejcic produced from a similar solution confirmed their character as being that of the expected $TiOSO_4{\cdot}H_2O$ product.

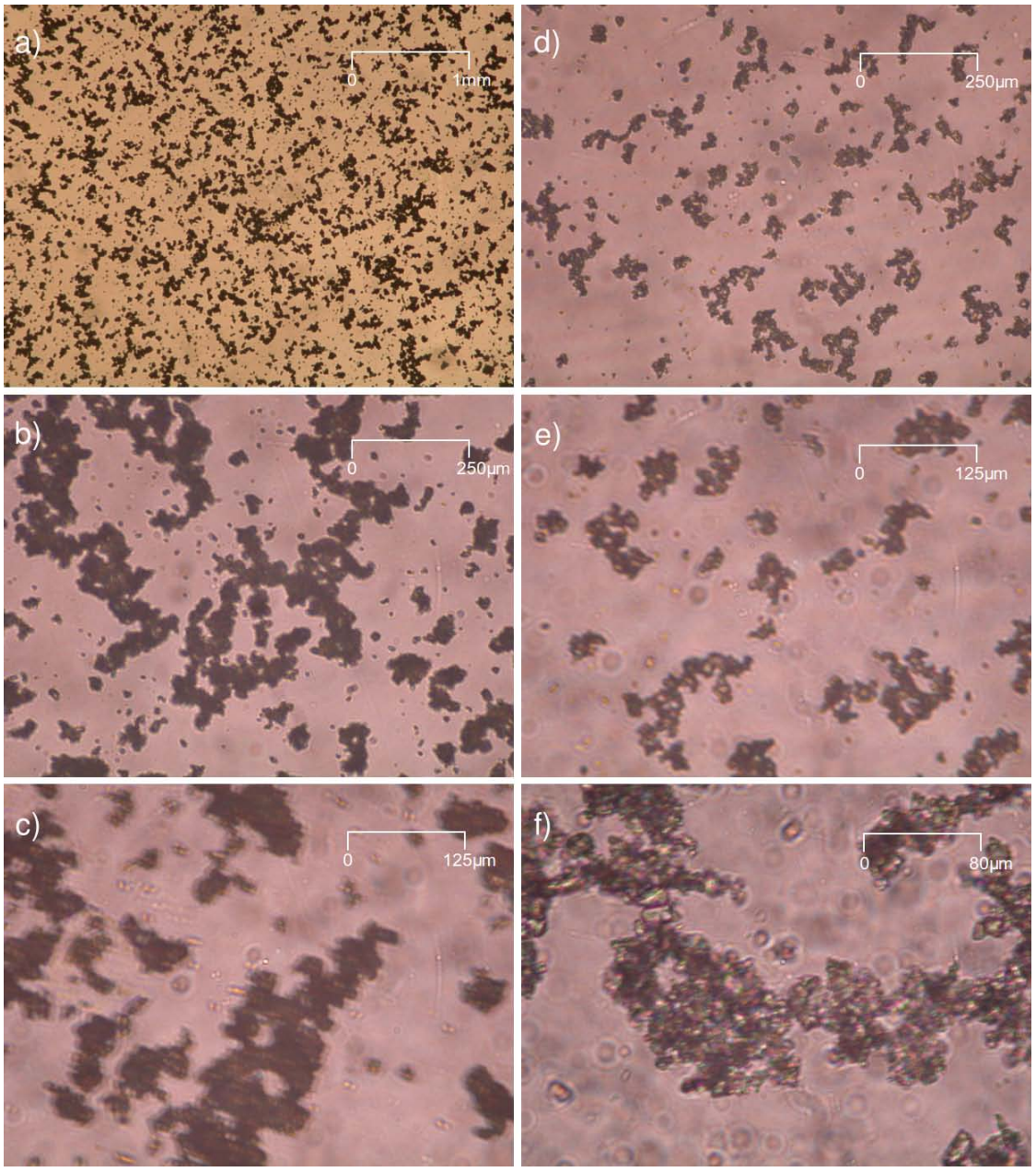

FIGURE 4.12: a) - c): 100x, 400x, and 800x optical microscope images of the particles present in the original solution after 4 hours; d) - f): 400x, 800x, and 1200x magnification images of the particles present in the original solution after 24 hours.

Figure 4.13 shows the optical microscope images of the solution in the capillary set 1 after 4 and 24 hours. It is important to remember that the solution used in the capillaries was taken from the original solution, and should therefore result in the precipitation of $TiOSO_4 \cdot H_2O$ seen in 4.12. However, it is obvious from the microscope images that after 4 hours the only phase present was the needle-like crystals of $TiOSO_4 \cdot 2H_2O$. After 24 hours, especially in Figure 4.13 f), some crystals can be seen that do not have the needle character, and it could be presumed that these crystals are small amounts of $TiOSO_4 \cdot H_2O$. To confirm this, the capillary was left for a further 72 hours and then re-examined. Figure 4.14 shows an isolated image of what appears to be $TiOSO_4 \cdot H_2O$ in the solution.

The important result from these experiments was the formation of a majority of $TiOSO_4 \cdot 2H_2O$ crystals in the capillary, when the same solution resulted in the formation of $TiOSO_4 \cdot H_2O$ crystals in the test tube. Regardless of the cause of this result—reduction in volume, a sampling anomaly, or some other mechanism—the experiment would need to be repeated and the system more thoroughly explored.

Secondary experiments–sets 2-6:

Images from capillary set 2, prepared with a higher titanium concentration than that of the other capillaries, are shown in Figure 4.15. These images were taken after 24 hours of reaction. The conditions present in the capillary resulted in $TiOSO_4 \cdot 2H_2O$ crystals of what appeared to be quite uniform length. Evident in all of the images is the appearance of what might be referred to as 'puffballs' or 'tumbleweeds' of crystals; agglomerations of needles in an asterisk-like (*) formation. It was not certain whether these formations share a common nucleation point; the 100x optical microscope image would suggest otherwise, as there appears to be unattached crystals floating in solution. It could therefore be that the formation of these 'puffballs' is the result of purely random orientation. Alternatively, it could be that there are surface effects in play. It is difficult to make a precise statement regarding this, given the nature of the crystals and the difficulty in imaging a single 'puffball' in solution. The prospect of obtaining SEM images was discussed, but in order to guarantee the presence of the 'puffballs', we would have required sampling immersion in the original sulphuric acid, which was not feasible.

Figure 4.16 shows the comparison of capillary sets containing the same, higher concentration of both titanium and acid, but with different $TiOSO_4$ precursor sources. These conditions resulted in the formation of the $TiOSO_4 \cdot H_2O$ phase with its typical prismatic crystals. From these images it could be surmised that the presence of impurities in the BHP Billiton sample did not have a significant effect on the formation of $TiOSO_4 \cdot H_2O$ crystals.

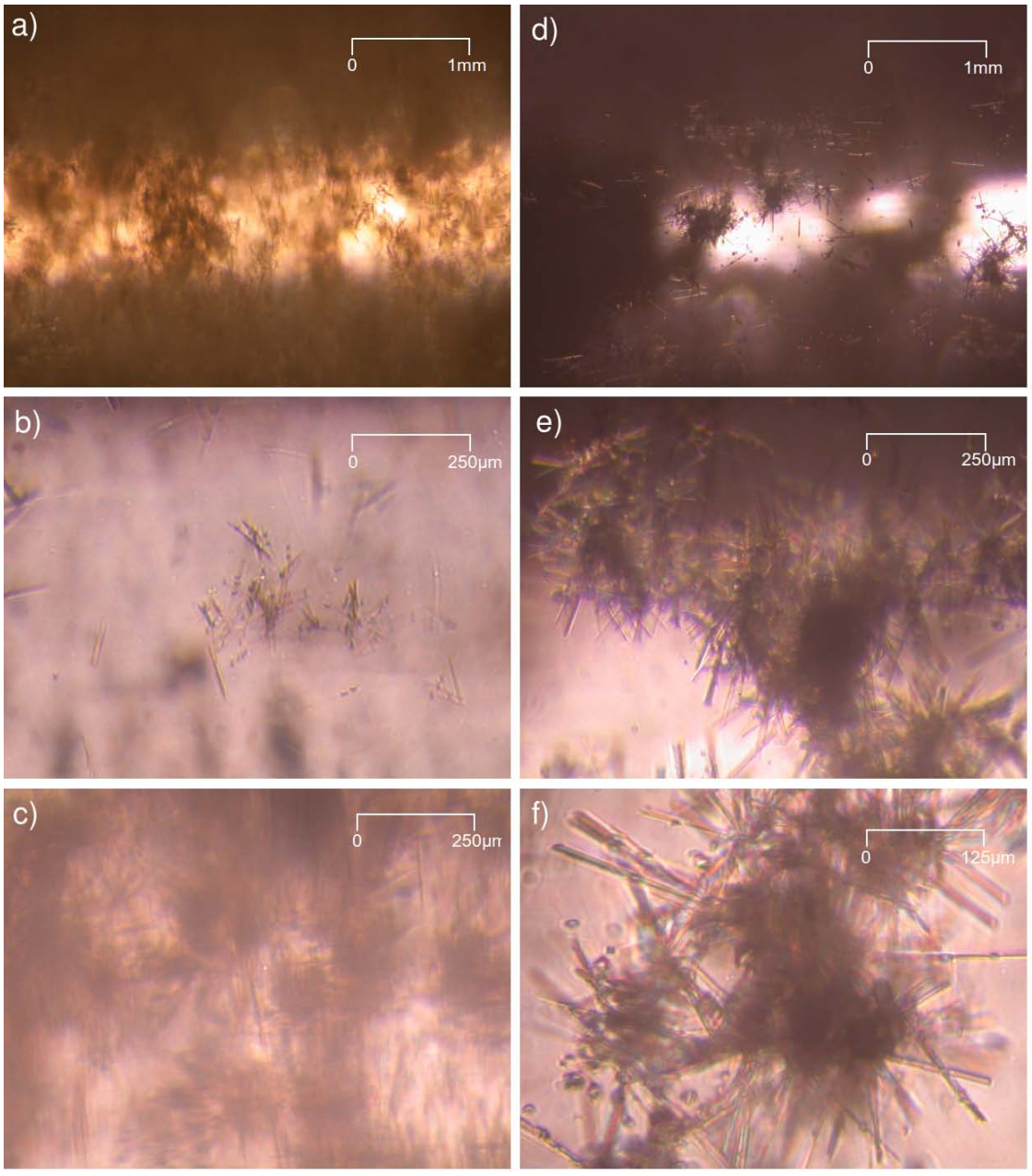

FIGURE 4.13: a) - c): 100x, 400x (in an area of sparse precipitation), and 400x (in an area of dense precipitation) optical microscope images of the particles present in the capillary solution after 4 hours; d) - f): 100x, 400x, and 800x optical microscope images of the particles present in the capillary solution after 24 hours.

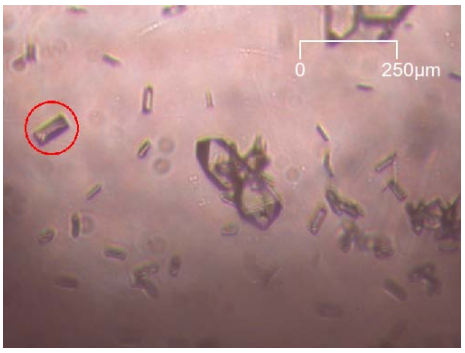

FIGURE 4.14: 400x optical microscope image showing an isolated prismatic crystal of $TiOSO_4 \cdot H_2O$ (circled in red) produced after reaction for a further 72 hours.

Capillary sets 5 and 6 were produced in an effort to test the reproducibility of the formation of phases in the capillaries. While capillary set 5 showed the same product as that of 3 and 4, Figure 4.17 shows optical microscope images of product formed in capillary 6. Clearly this can be seen to be the $TiOSO_4 \cdot 2H_2O$ phase, and therefore we once again had two different products resulting from presumably similar conditions.

The obvious conclusion from the above was that this set of capillaries did not have the assumed concentration of titanium or acid within, and there were a few ways that this could have happened. The heat sealing of the capillaries could have been imperfect, which would have allowed some water to escape and affect the concentration of the acid, or; when sampling the capillaries from the original solution, the solute may not have dissolved entirely. Over such a small scale of sampling it was difficult to determine what the cause may have been. Ultimately though, both phases were formed as more or less pure phases, and following on from this experiment it was a matter of refining the process to guarantee the production of either phase.

Tertiary experiments–sets 7-12:

Sets 7-12 were produced to explore a wider range of acidities and titanium concentrations, with an emphasis on a generally higher acidity solution than had been used previously. It should be reiterated that for each combination of concentrations there were four capillaries produced so that at the advent of 1, 4, 24, and 72 hours, one capillary from each combination could be removed. This ensured that there would be continuous heating for the capillaries over the periods specified. As a dual aim, it would also serve as a measure of reliability; if a capillary withdrawn at 4 hours produced $TiOSO_4 \cdot 2H_2O$, then the capillary with the same composition should also have produced $TiOSO_4 \cdot 2H_2O$ when withdrawn at 72 hours.

As can be seen from Table 4.8, reliability was a key issue in this batch of capillary sets. Of the six solutions, only capillary set 11 showed the expected progression from

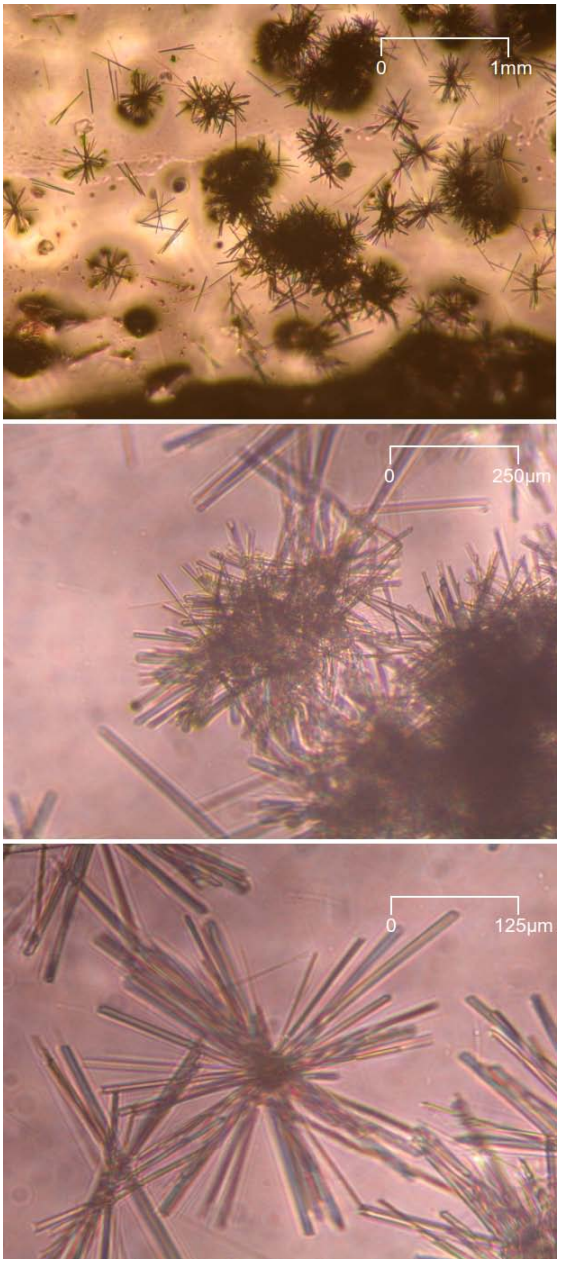

FIGURE 4.15: (top); 100x optical microscope image of product formed in capillary set 2; (middle) 400x optical microscope image of product formed in capillary set 2; (bottom) 800x optical microscope image of product formed in capillary set 2.

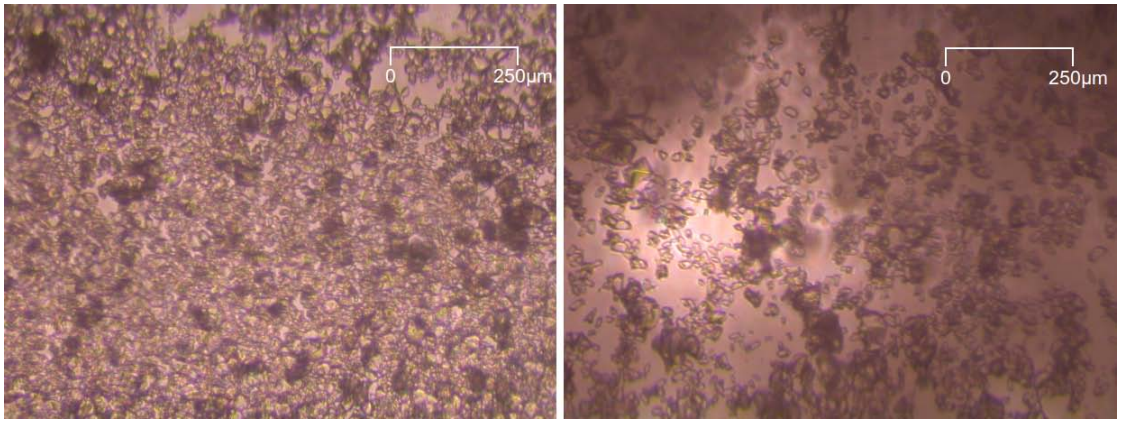

FIGURE 4.16: (left) 400x optical microscope image of product formed in capillary set 3; (right) 400x optical microscope image of product formed in capillary set 4.

FIGURE 4.17: (left) 100x optical microscope image of product formed in capillary set 6; (right) 400x optical microscope image of product formed in capillary set 6.

	Time (hours)			
Capillary Set No.	**1**	**4**	**24**	**72**
7	No product	'Dots'	Long needles	Prismatic crystals
8	No product	No product	No product	Mixed phase
9	No product	No product	'Dots'	No product
10	No product	Short needles	No product	Mixed phase
11	No product	No product	Short needles	Long needles
12	No product	Short needles	No product	No product

TABLE 4.8: Summary of the morphology of products formed during the tertiary capillary experiments

no product, to partially formed needles, and finally fully formed needles. The rest of the solutions either showed different crystal morphologies at different times, or an unexpected behaviour whereby a product might be formed at an early stage but not at a later time.

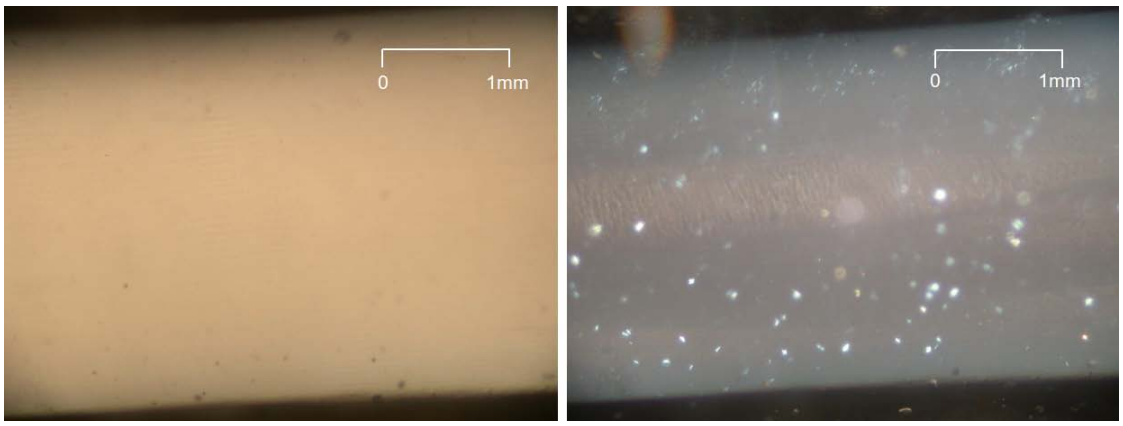

FIGURE 4.18: (left) Standard 100x optical microscope image showing the seeming absence of particles in capillary set 7 solution after 4 hours; (right) Dark field 100x optical microscope image showing the presence of disperse particles in capillary set 7 solution after 4 hours.

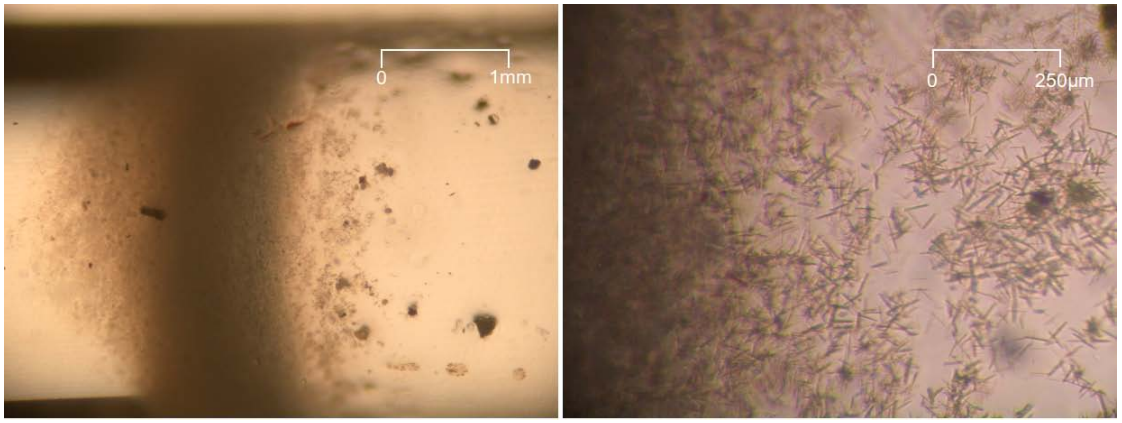

FIGURE 4.19: (left) Standard 100x optical microscope image showing the formation of short needles at the meniscus of capillary set 10 solution after 4 hours; (right) Standard 400x optical microscope image of the same.

As no product was formed in any of the capillaries after one hour, no images will be provided for this time. Figure 4.18 shows how 'dark field' imagery (a technique that increases the contrast of the image by excluding the unscattered light from being collected) can be used to show the presence of particles where they might not have been spotted with a standard or 'bright field' image. It is difficult to say what these particles are; undissolved $TiOSO_4$, or possibly the nucleation sites of $TiOSO_4{\cdot}H_2O$ or $TiOSO_4{\cdot}2H_2O$.

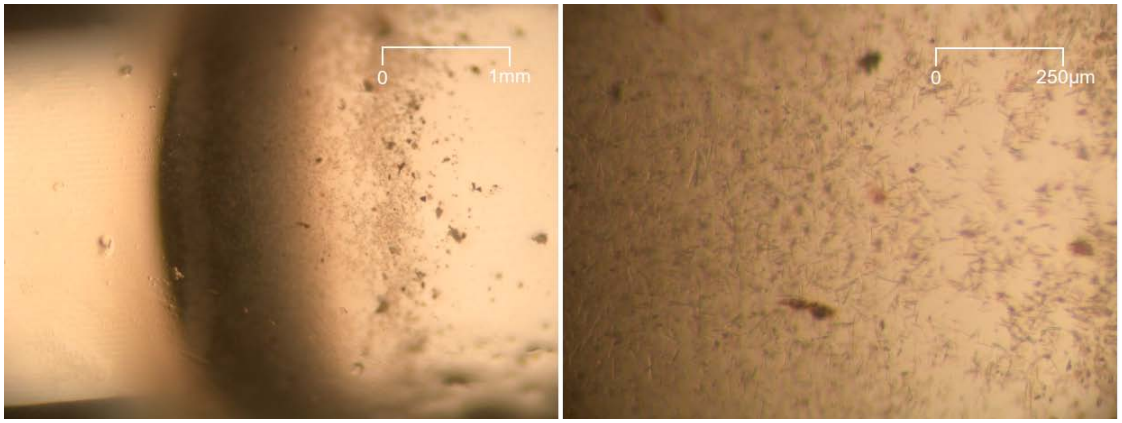

FIGURE 4.20: (left) Standard 100x optical microscope image showing the formation of short needles at the meniscus of capillary set 12 solution after 4 hours; (right) Standard 400x optical microscope image of the same.

Figures 4.19 and 4.20 show the formation of very short crystals with a needle-like character in capillaries 10 and 12 respectively. While the needle-like character might suggest the formation of $TiOSO_4 \cdot 2H_2O$, the length and number of crystals are at odds with crystals from previous experiments, such as those shown in Figure 4.15. However, as both occurrences of the short needles were imaged after only 4 hours compared to the longer crystals in previous experiments being imaged after 24 hours, it is conceivable that they have not had enough time to fully form in solution.

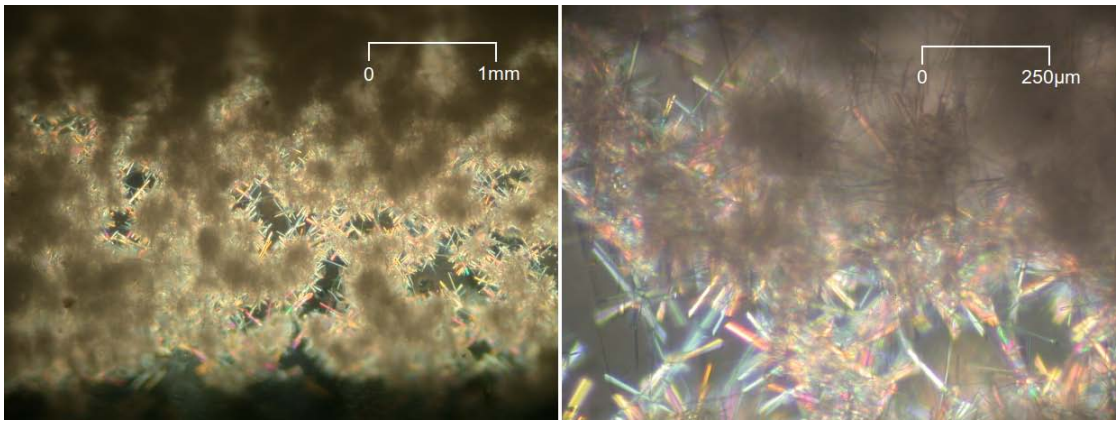

FIGURE 4.21: (left) Dark field 100x optical microscope image showing the formation of thick clusters of needles in capillary set 7 solution after 24 hours; (right) Dark field 400x optical microscope image of the same.

Figure 4.21 shows capillary set 7 after 24 hours containing a large amount of precipitate with the needle-like characteristics seen in previous experiments. It should be noted that the colour present at the edges of the 400x image is an artefact of the dark field method combined with the curvature of the capillary and not any colouration of the sample. Figure 4.22 presents what appears to be the first example of multiphase precipitation,

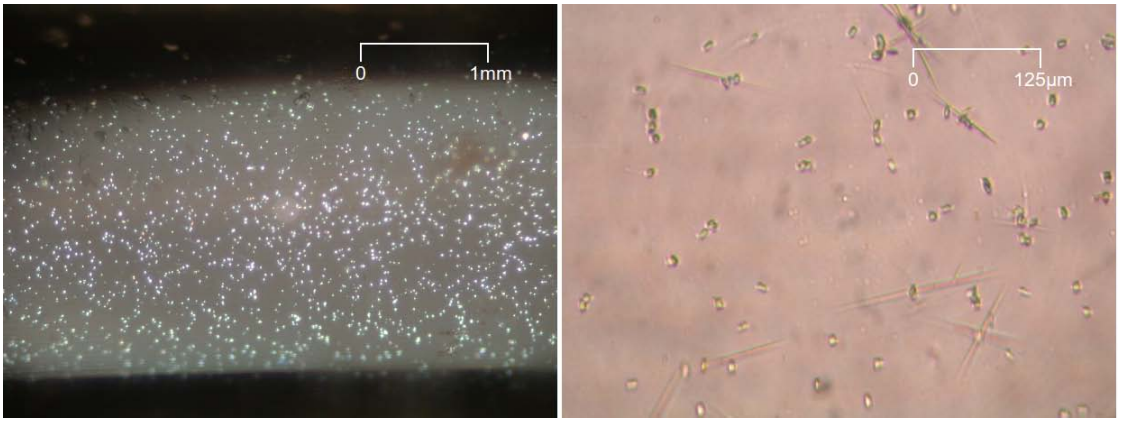

FIGURE 4.22: (left) Dark field 100x optical microscope image showing the presence of particles in capillary set 9 after 24 hours; (right) 800x standard optical microscope image of the particles and what appears to be some needle-like crystals.

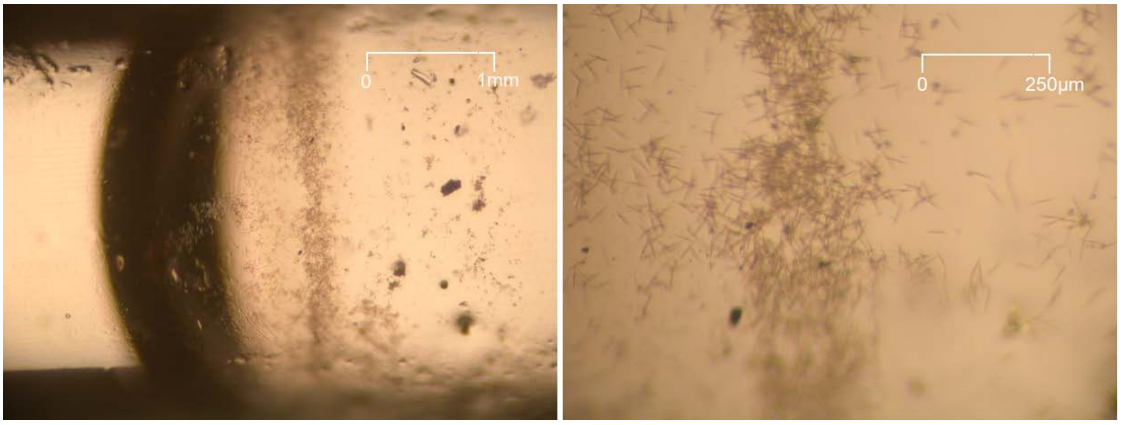

FIGURE 4.23: (left) Standard 100x optical microscope image showing the formation of small needles at the meniscus of capillary set 11 after 24 hours; (right) Standard 400x optical microscope image showing the formation of small needles in greater detail.

with capillary set 9 resulting in prismatic crystals intersected by very thin needles. Finally, Figure 4.23 shows capillary set 11 forming the same kind of short needles after 24 hours as seen in capillary set 10 and 12 after 4 hours.

The capillaries that were left to react for 72 hours showed more diverse morphologies. Figure 4.24 shows capillary set 7 having formed prismatic crystals assumed to be those of $TiOSO_4 \cdot 2H_2O$, a result which is at odds with the capillary from the same set removed at 24 hours, which showed the formation of needles. Figure 4.25 shows the production of multiple phases that appear to be of a similar nature, though longer, to those shown in Figure 4.22. Figure 4.26 again shows the precipitation of primsatic crystals where previous results (see Figure 4.19) might have suggested otherwise. However, Figure 4.27 provides some degree of continuity in that the small needles that had formed in the

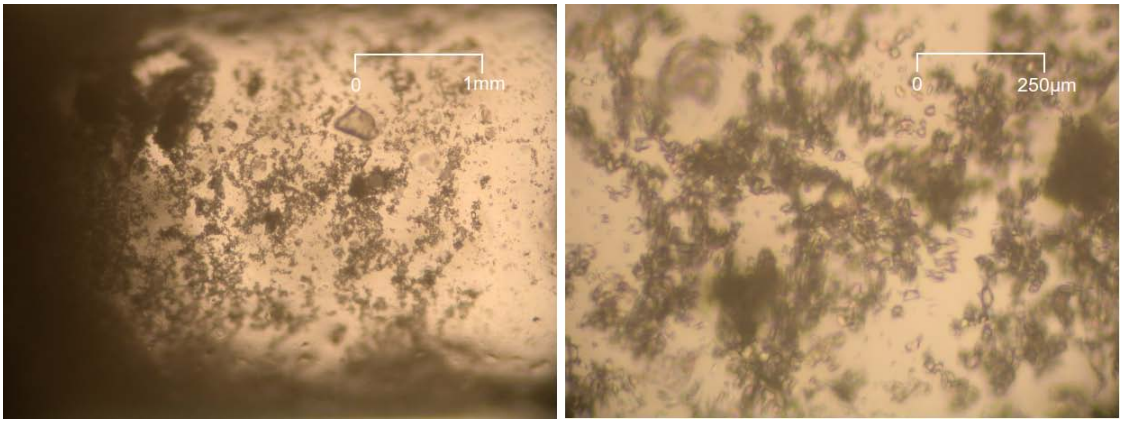

FIGURE 4.24: (left) Standard 100x optical microscope image showing the formation of small prismatic crystals in capillary set 7 solution after 72 hours; (right) Standard 400x optical microscope image showing greater detail of small prismatic crystals in capillary set 7 solution after 72 hours.

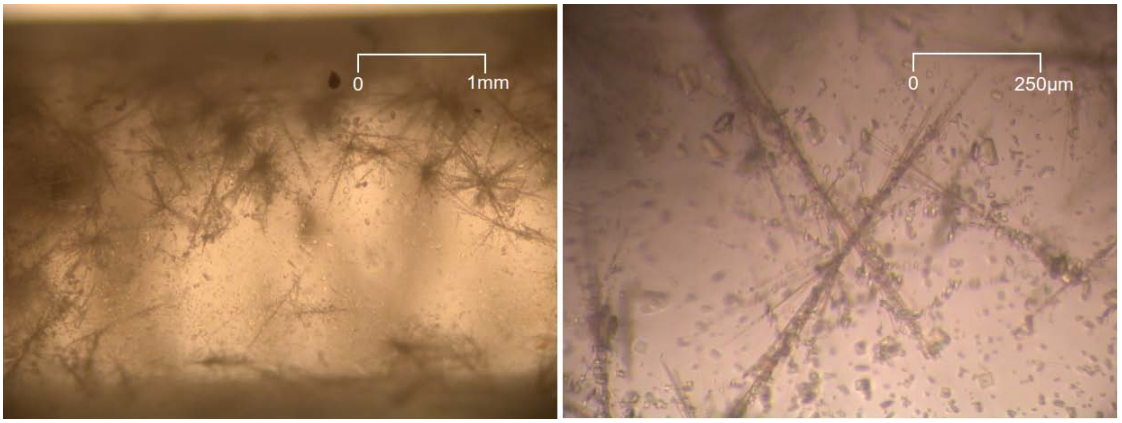

FIGURE 4.25: (left) Standard 100x optical microscope image showing the formation of multiple phases in capillary set 8 solution after 72 hours; (right) Standard 400x optical microscope image showing greater detail of multiple phases in capillary set 8 solution after 72 hours.

capillary from set 11, removed after 24 hours, have recurred and are seen to be longer in the capillary that was removed after 72 hours.

The results from this experiment can be seen to be an example of the difficulty achieving reproduction of results in a system that can result in multiple phases. Capillary set 7 showed the most ambiguous results, producing both the most dense concentration of needle-like and prismatic crystals in its 24- and 72-hour capillaries, respectively. Only the 72-hour capillary in set 8 showed any reaction, and this was a mixed-phase product. Capillary set 9 similarly produced only one example of precipitation. However, it was within the 24-hour capillary, and therefore one would assume that the 72-hour capillary might also show some precipitate; this was not the case. Capillary set 10 was most confusing, in that its 4-hour capillary showed precipitation of small needles, its 24-hour

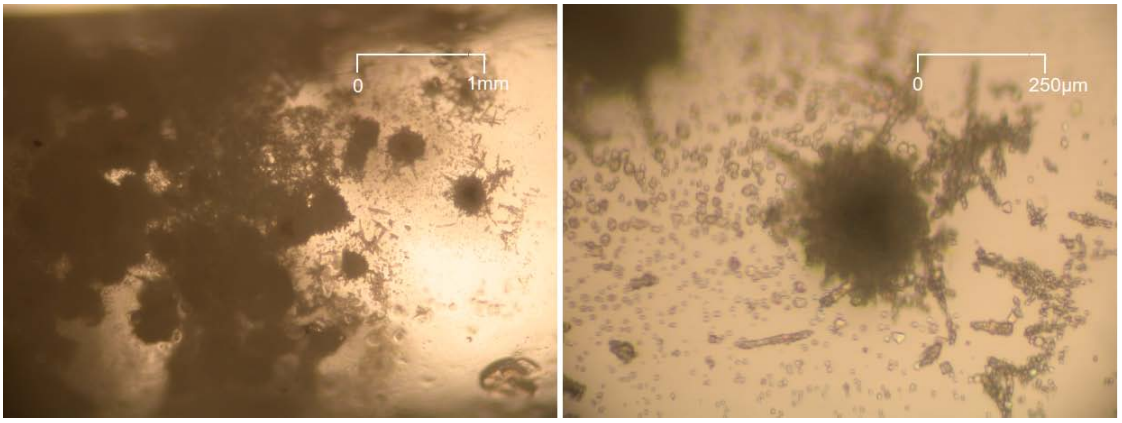

FIGURE 4.26: (left) Standard 100x optical microscope image showing the formation of small prismatic crystals in capillary set 10 solution after 72 hours; (right) Standard 400x optical microscope image showing greater detail of small prismatic crystals in capillary set 10 solution after 72 hours.

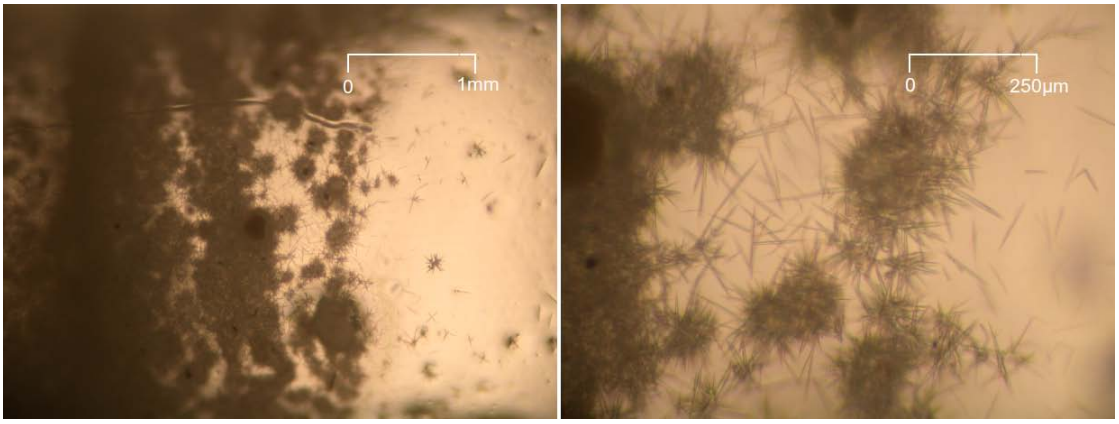

FIGURE 4.27: (left) Standard 100x optical microscope image showing the formation of clusters of needles in capillary set 11 solution after 72 hours; (right) Standard 400x optical microscope image showing greater detail of clusters of needles in capillary set 11 solution after 72 hours.

capillary nothing at all, and its 72-hour capillary produced prismatic crystals. Capillary set 11 was alone in showing a progression from no precipitate, to small needles, and finally to large needles. Finally, capillary set 12 produced small needles in its 4-hrs capillary, but no other precipitate in capillaries reacting for longer periods of time.

There was an obvious point of uncertainty in the experimental method, in that the method used to suspend the capillaries in the test tubes meant that once they had been removed, they could not be reattached to the glass rods without the chance of breakage in the remaining capillaries. This meant that once a capillary was removed, say those removed at 1 hour, all potential it may have had for a product at a later time was lost. Had this data been able to be recorded, perhaps the uncertainty in the scheme of precipication events would be somewhat reduced.

It was ultimately decided that in order to guarantee the production of $TiOSO_4{\cdot}2H_2O$ in the capillary, we would need to heavily bias the reaction by using a lower concentration of acidity. While this approach carried with it some complications of its own, by way of a possibly lengthened induction time, ensuring a single phase was considered a greater priority.

4.5 Synchrotron diffraction experiments

As stated in section 4.3, while laboratory X-ray diffraction provided us with positive identification of the phases of $TiOSO_4{\cdot}2H_2O$ and $TiOSO_4{\cdot}H_2O$ produced by reacting amorphous $TiOSO_4$ with different concentrations of H_2SO_4, the quality of the data was not deemed sufficient to begin structure determination or Rietveld refinement. In order to obtain the resolution of diffraction peaks necessary to begin such exploration of the possible structure of $TiOSO_4{\cdot}2H_2O$, it was decided that high energy synchrotron X-ray radiation would be required. In addition to providing insight into the unknown structure of $TiOSO_4{\cdot}2H_2O$ using standard *ex-situ* experiments, *in-situ* crystal growth experiments were carried out to investigate the possibility of multiple phases forming during the crystal growth process, and to further characterise the growth of the sample.

The following sections will detail the methods and results of the *ex-situ* and *in-situ* synchrotron X-ray diffraction experiments undertaken.

4.5.1 Australian Synchrotron

The location and availability of beam-time on the Australian synchrotron meant that it was the logical first candidate for synchrotron powder X-ray diffraction experiments. The Australian synchrotron is located in the suburb of Clayton, in the outskirts of Melbourne. Two applications for beam time were successful: one in August of 2008 and another a year later in August of 2009. The sample preparation, data collection methodology, and combined results from the two trips will be presented in the following sections.

4.5.1.1 Sample preparation and data collection methodology

***Ex-situ* sample preparation**

Loading of *ex-situ* capillaries was initially found to be quite difficult given the 'wet' nature of the sample. Extensive washing of the sample with ethanol and placing it in a

dessicator for periods of up to two weeks was found to give the best results for drying the sample. Subsequent X-ray diffraction experiments confirmed that there had been no appreciable change in the structure by this technique. Once the sample had been dried, it was loaded into the capillaries. The drying of the product notwithstanding, this still proved to be difficult, with the trouble owing to the continuing tendency of the particles to clump together and stick to the sides within the narrow tube of the capillary. This behaviour was circumvented by rubbing a finely threaded screw across the length of the capillary. This action served to vibrate the capillary and dislodge the small clumps from the sides to the bottom of the capillary. From there, they could be compacted with the blunt end of glass Pasteur pipette which had been drawn out using a bunsen burner flame in order to fit within the confines of the capillary.

After enough product had been packed into the capillary (approximately 5 centimeters is sufficient according to the Australian Synchrotron guidelines) the open end of the capillary was sealed with a bunsen burner flame to prevent loss of sample. The *ex-situ* samples had the advantage that they could be prepared well in advance of travelling to the Australian Synchrotron facility.

Collection of *ex-situ* diffraction data

Collection of the *ex-situ* data was performed on the X-ray powder diffraction beamline at the Australian Synchrotron. The geometry of the Australian Synchrotron powder diffraction beamline is that of Debye-Scherrer, requiring that the sample be placed in a capillary of 1.0-3.0 mm diameter and inserted in a goniometer for alignment to the beam. While the capillaries for the *ex-situ* experiments could be easily constructed using product made within the reaction block test tubes, ensuring that the *in-situ* experiments could be completed reliably required extensive testing of production of both $TiOSO_4{\cdot}2H_2O$ and $TiOSO_4{\cdot}H_2O$ within a capillary, as detailed in section 4.4.2.

The sample capillary is first mounted into a goniometer, a simple stage that allows the capillary to be rotated and to have its angle of rotation adjusted. This is used to align the capillary in the beam, so that when the spinner is engaged the capillary won't ever fall outside of the beam footprint, or result in a non-uniform sampling of the capillary. Adjustments are made to the orientation of the goniometer manually using a small Allen (or hex) key and observing the rotation using a remote control and a zoomed camera. The capillary itself is held in place in the goniometer by melted wax, in a small brass holder that is then screwed into the goniometer itself. For the *in-situ* work, it was necessary to use a material with a lower melting point, so commercially available 'Blu-tac' was used instead of wax.

Once the capillary has been aligned in the beam, the experiment is controlled and monitored by a series of software programs on computers linked to the beamline. The software operates much like a regular laboratory X-ray diffractometer in that the 2θ range and overall time to count for is specified by the user. Due to the geometry of the synchrotron's four data collection plates, an additional 2θ shift parameter is required. This tells the instrument to take two patterns, one shifted by the input angle, that are then combined together using a command-line data merging program to create one full pattern. This compensates for the physical gap present between the data collection plates.

Processing of these samples was straightforward, requiring nothing more than simple mounting and measurement. Usually a short time of 30 seconds was measured over as a check before a longer exposure of 10 minutes was taken. As a sidenote, when a run is referred to as taking 300 seconds, in reality it takes 600 seconds for the measurement to finish once the compensatory shifted exposure has been performed. The only complication with these samples was the occasional dropping and injection of the beam, which usually resulted in an approximately 20 minute period within which no samples could be analysed. This was not so much of a problem in the solid samples, as it was just a matter of waiting and rerunning any measurement that had been interrupted. The beam was monochromated to an energy of approximately 15 keV, corresponding to a nominal wavelength of 0.82656 Å.

Each experiment was first given a test run for 60 seconds to confirm alignment of the beam and to ensure that adequate counting statistics were being collected from the sample. If the test run proved satisfactory, then a further set of two 300 second runs was executed, followed by a final set of two 600 second runs. Unless an exceptional event caused the data to be rendered useless, measurement of the capillary was considered to be completed, and it could then be swapped for the next sample.

A list of the *ex-situ* samples examined and the labels by which they will be referred to can be found in Table 4.9.

Experiment label	Description of sample
DIH01	$TiOSO_4 \cdot 2H_2O$ produced from BHP Billiton $TiOSO_4$ precursor
DIH02	$TiOSO_4 \cdot 2H_2O$ as provided by BHP Billiton
MON01	$TiOSO_4 \cdot H_2O$ as produced from BHP Billiton $TiOSO_4$ precursor
ANH01	BHP Billiton $TiOSO_4$ precursor

TABLE 4.9: A list of the *ex-situ* X-ray diffraction experiments performed at the Australian Synchrotron.

In-situ sample preparation

The samples for the *in-situ* experiments were prepared within the Australian Synchrotron laboratories. As transport of our equipment, including the Labortechnik reaction block, to the facility was not feasible, a new setup had to be devised by which samples could be heated and sampled into capillaries easily and safely. To this end, a simple experimental setup was created consisting of a standard 100mL beaker as a reaction vessel placed upon a heating plate, with a 120°C thermometer for maintaining constant heating. Once the solution was transferred into the capillary *via* a Pasteur pipette, they were heat sealed using a butane burner.

In order to heat the capillary in the beam, a Cryostream system needed to be installed and moved into place over the capillary. A heating scheme can be specified using the same program as used to specify measurement ranges. For the duration of the experiments a temperature of 110°C was maintained. Whenever a sample needed to be changed, a period of waiting was required for the Cryostream system to cool to less than 50°C in order to limit exposure to the heat source. Five solutions were prepared during the course of the *in-situ* experiments. The experiment label and description of the solutions are show in Table 4.10.

Experiment label	Description of sample
SOL01	$75gL^{-1}$ Ti in $1170gL^{-1}$ H_2SO_4
SOL02	$37.5gL^{-1}$ Ti in $585gL^{-1}$ H_2SO_4
SOL03	$42gL^{-1}$ Ti in $650gL^{-1}$ H_2SO_4
SOL04	$45gL^{-1}$ Ti in $600gL^{-1}$ H_2SO_4 (filtered, BHP)
SOL05	$45gL^{-1}$ Ti in $600gL^{-1}$ H_2SO_4 (filtered, RDH)

TABLE 4.10: A list of the *in-situ* X-ray diffraction experiments performed at the Australian Synchrotron

SOL01 was not heated by the Cryostream, and was used to try and gain an idea of what sort of background we would be encountering during the rest of the experiments. The solution left in the beaker was heated in order to see if it would precipitate in a timely fashion. However, this solution did not appear to be precipitating within a reasonable timeframe, so we decided to alter the concentration for the subsequent solutions to try and promote crystal growth.

SOL02 was produced by diluting SOL01 with deionised water in a 1:1 ratio. After the capillary had been loaded and heated for approximately 2 hours, the beamline hutch video camera showed that the meniscus of the solution was moving. This resulted in an immediate halt of the experiment, as it was clear that the capillary had not been sufficiently sealed, resulting in evaporation in the beam. While this solution was in the beam, a third solution, SOL03 had been prepared by diluting the first solution in a

slightly different ratio of 5:4, using 1mL of SOL01 and 0.8mL of deionised water. The *in-situ* growth of $TiOSO_4 \cdot 2H_2O$ was completed using SOL03.

SOL04 and SOL05 were prepared on a separate occasion to SOL01-SOL03 by first dissolving the $TiOSO_4$ in $400gL^{-1}$ H_2SO_4. Once the solid had dissolved, the solution was piped through a vacuum filter fitted with Teflon membranes featuring a 0.22 μm cut-off. Once the solution had been filtered, the concentration of the acid was brought up to $600gL^{-1}$ by the addition of concentrated H_2SO_4. This was done in order to promote the crystallisation of $TiOSO_4 \cdot 2H_2O$, based on the induction time studies performed by Marco Peng [11].

Collection of *in-situ* diffraction data

Diffraction patterns were collected over a period of approximately 14 hours for 1,200 seconds each, split into two 600 second collections to compensate for the nature of the detector. The patterns did show the slow formation of what appeared to be the characteristic $TiOSO_4 \cdot 2H_2O$ needle crystals. These were visible by eye 5 hours and 45 minutes into the experiments through the hutch video camera, which showed a zoomed view of the capillary. Prior to this, there did exist small dots of crystal on the monitor, which were thought to be residual undissolved particles of $TiOSO_4$ from the creation of the solution.

In-situ collection of data differs from that of *ex-situ*, in that the decay of the beam comes into effect. The Australian Synchrotron runs in an operation mode known as 'top-up mode'. From the Australian Synchrotron website [151]:

> "Top-up is a mode of operation that aims to maintain a steady current in the storage ring by periodically injecting small amounts of current. It produces a more stable beam by keeping the heat loads and signal strengths constant over long time periods in both the storage ring and on the beamlines."

What this results in for the end user is a variable beam strength over time, as the beam strength decays between the injections. Unless the decay of the beam is accounted for through the use of post-processing software, the results of an *in-situ* experiment will be skewed, i.e. the peak intensities just before an injection will be reduced compared to the peak intensities just after an injection. During our visit, the software to account for the beam's variability and normalise the data accordingly was still being developed. Therefore, in addition to the 2θ versus intensity data that is usually produced in X-ray diffraction experiments, a parameters file was also provided. Contained within this file, along with various other parameters of the machine, was the integrated ion chamber

count; essentially a numerical measure of the beam strength that could be used to normalise the data with respect to time and the decay of the beam.

A typical beam injection may take up to 20 minutes which, while not disastrous, still results in a portion of data lost from the experiment. In order to minimise the number of injections that would occur during our experiment, we aligned the sample and started collecting data just before a scheduled injection. This was done so that only one data collection during the first half a dozen collections, which we expected to reflect the amorphous nature of SOL01, would suffer from the interruption.

SOL04 and SOL05 differed from SOL03 in that, due to time restraints, total data collection times were dictated by direct observation of the diffraction patterns. Once the pattern's evolution had been deemed close to completion by comparison with previous diffraction patterns, the experiment was stopped and the samples switched. This resulted in a total data collection time for the SOL04 sample of approximately half that of the SOL05 sample.

4.5.1.2 *Ex-situ* and *in-situ* data analysis

General attributes of ex-situ $TiOSO_4{\cdot}2H_2O$ *diffraction patterns*

Before a detailed comparison of the various diffraction patterns is undertaken, it is useful to provide a general analysis of their quality and features. An example of a $TiOSO_4{\cdot}2H_2O$ diffraction pattern can be seen in Figure 4.28.

Synchrotron X-ray diffraction, with its higher energies and better full width at half maximum (FWHM) resolution, has been reported throughout the literature as giving much better peak separation. However, if we look at the diffraction pattern shown in Figure 4.28, significant peak overlap is already starting to occur at as low as 11-12° 2θ, corresponding to d-spacings of approximately 4 Å. Sheldrick's rule for direct methods states that:

> "Direct methods assume randomly distributed resolved atoms. Direct methods are crucially dependent on having atomic resolution data, say better than 1.2 Angstrom. A good rule of thumb is that [at] least one half of the theoretically possible number of reflections between 1.1 and 1.2 Angstrom should have been measured with $I > 2\sigma$ for direct methods to be successful, though this rule can be relaxed somewhat for centrosymmetric structures and structures containing heavier atoms." [152]

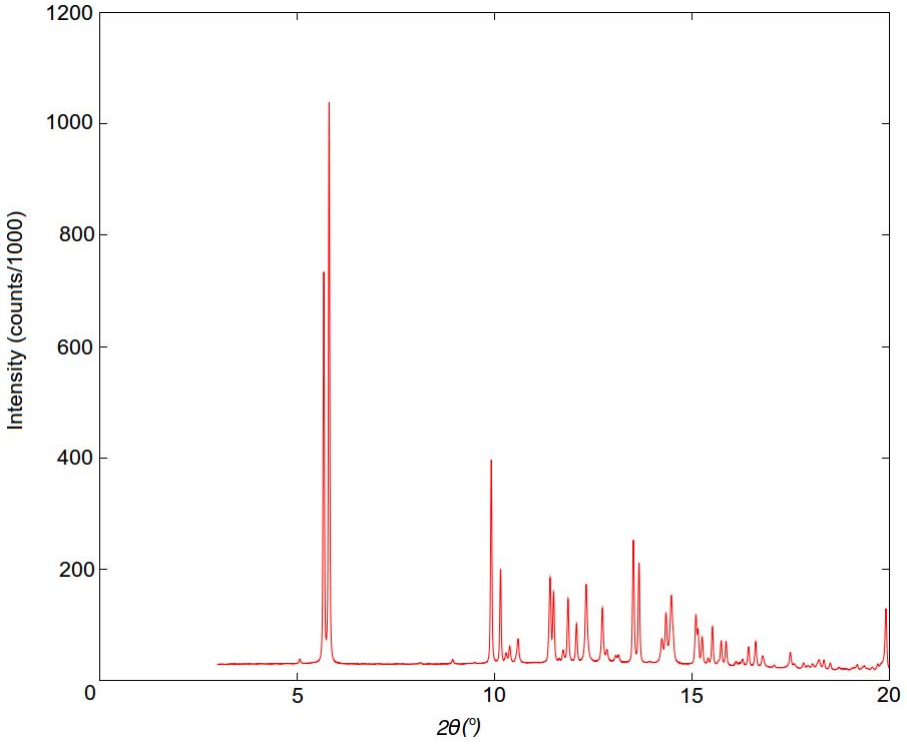

FIGURE 4.28: A section of the DIH02 synchrotron powder XRD pattern of $TiOSO_4 \cdot 2H_2O$.

If this is the case, then our typical diffraction pattern does not look to have the information available to be able to perform structure determination by direct methods. Already the choice of method for structure determination from powder diffraction (SDPD) has been reduced to direct-space methods that require prior knowledge of chemical connectivity information.

The loss of information from peak overlap, due to the collapse down to a one-dimensional diffraction pattern, is often compounded by the presence of line broadening. Line broadening occurs due to the instrument being used, and the sample being analysed. The former is usually as a result of the distribution of wavelengths in the beam, as well as such properties as the beam divergence and instrument misalignment; the latter is due to the microstructure of the material being studied. Sample broadening is generally broken up into two distinct types: 'size' broadening, which arises from the finite domains of coherent scattering present in the sample, and 'strain' broadening, which manifests itself as a result of lattice distortions from dislocations or other internal stresses. It could also be the fact that the crystallites themselves are not particularly well-crystallised.

A FWHM analysis of the peaks can be used to determine if there is extensive broadening as a result of instrumental or size/strain effects. An individual peak fit FWHM analysis was performed on all peaks with intensity sufficient to do so using the WINFIT

software package developed by Stefan Krumm (contained within the CRYSFIRE suite of programs [153]). The results are shown below in Table 4.11 and Figure 4.29.

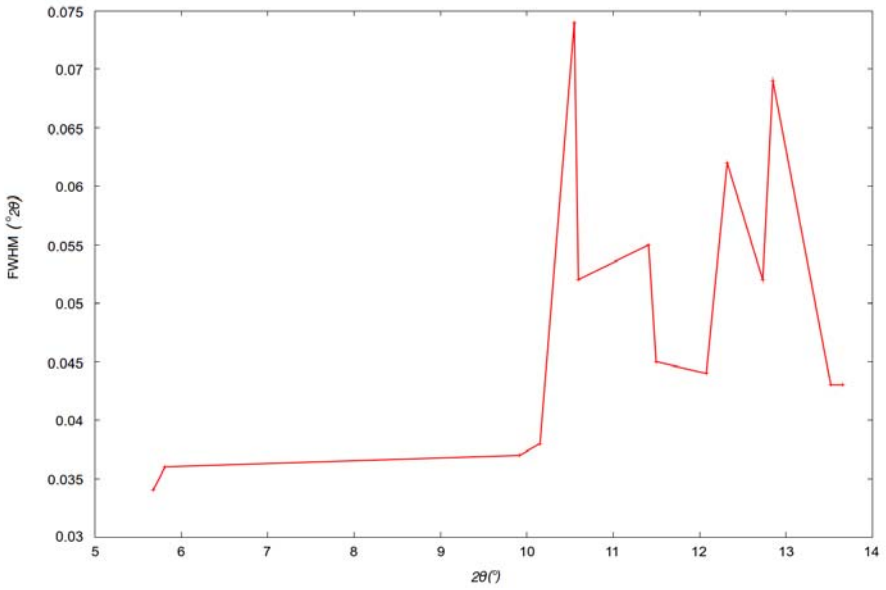

FIGURE 4.29: FWHM analysis of the $TiOSO_4 \cdot 2H_2O$ synchrotron X-ray diffraction pattern shown in Figure 4.28.

2θ (°)	Intensity (counts)	Integral area	FWHM (°2θ)
5.675	713144	30167	0.034
5.811	1028018	43833	0.036
9.917	372499	16495	0.037
10.152	42039	1837	0.038
10.549	6579	594	0.074
10.596	38679	2433	0.052
11.409	153204	10157	0.055
11.496	125525	6807	0.045
12.077	69593	3992	0.044
12.319	34447	2700	0.062
12.730	91504	5522	0.052
12.848	20237	1995	0.069
13.515	219933	11387	0.043
13.659	178564	9255	0.043

TABLE 4.11: Tabulated list of peaks used in FWHM analysis of $TiOSO_4 \cdot 2H_2O$.

The data shown in Figure 4.29 seems to be quite random. However, it should be noted that almost all of the peaks were within one FWHM of another peak, and therefore required a numerical deconvolution in which some error may have been introduced. In any case, the range of FWHM values can be seen to be quite tight, with a minimum at 0.034° 2θ and a maximum at 0.074° 2θ.

From looking at the general properties of the $TiOSO_4{\cdot}2H_2O$ diffraction patterns it can be said that there may be some difficulty in extracting enough information from the pattern to perform a structural determination, especially if the unit cell parameters are similar to those of the other hydrates in the series, with a relatively large number of unique atoms present in the cell.

General attributes of ex-situ *$TiOSO_4{\cdot}H_2O$ diffraction patterns*

Along with samples of $TiOSO_4{\cdot}2H_2O$, *ex-situ* diffraction experiments were conducted on $TiOSO_4{\cdot}H_2O$. The primary goal of the collection of this data was to provide a pattern to compare to the $TiOSO_4{\cdot}2H_2O$ sample and make certain that there was not multiphase growth occurring in the solution that would complicate structure determination at a latter stage in the project.

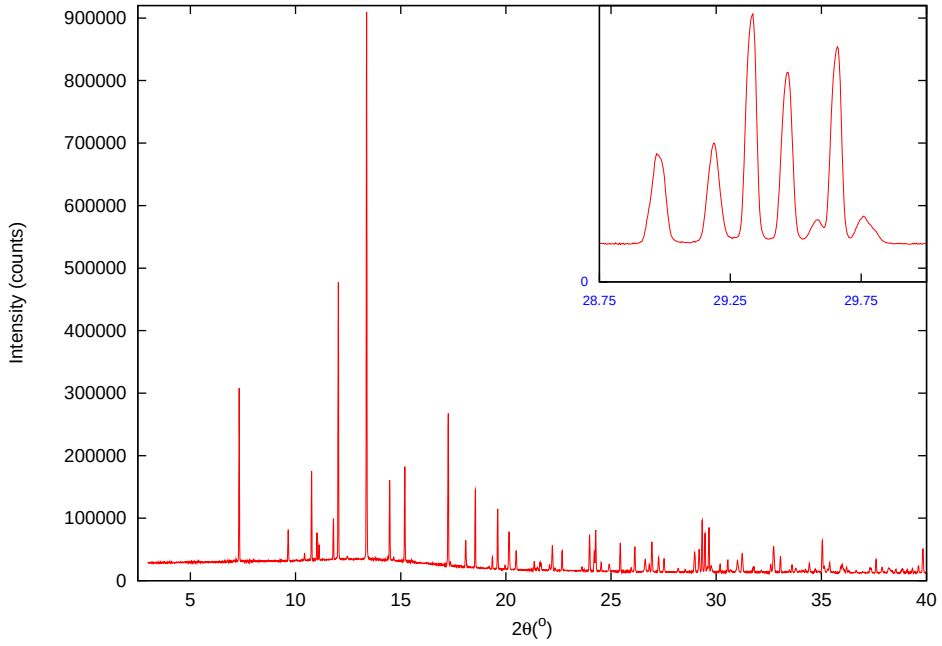

FIGURE 4.30: Synchrotron powder XRD pattern of sample MON01. Insert: A close-up of the congested area of peaks in the 28-30° 2θ region.

Figure 4.30 shows the synchrotron X-ray diffraction pattern of sample MON01; a sample of $TiOSO_4{\cdot}H_2O$ as produced from BHP Billiton $TiOSO_4$ precursor. It is immediately obvious that this is a very different diffraction pattern from that of the $TiOSO_4{\cdot}2H_2O$ sample, despite their similarity in origin. A comparison of the DIH01 and MON01 diffraction patterns is shown in Figure 4.31. The DIH01 pattern has been scaled to match the intensity of its maximum intensity peak with that of the MON01 pattern. As can be seen from this comparitive graph, there are very few peaks in the MON01 pattern that overlap entirely with the DIH01 pattern. This leads us to believe that under

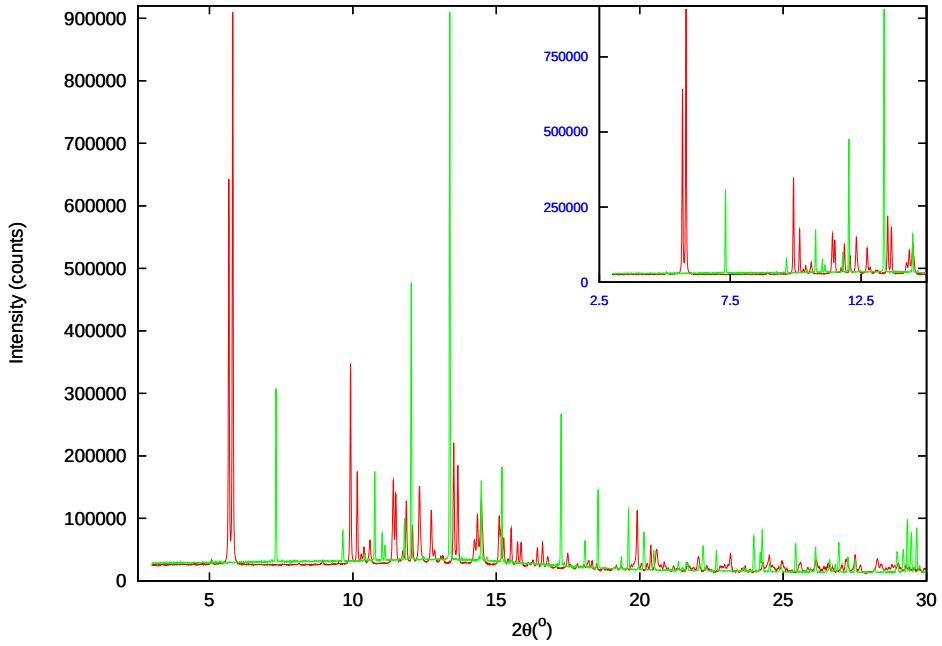

FIGURE 4.31: A comparison of synchrotron powder XRD patterns of samples MON01 and DIH02. Insert: A close-up of the region of 0-15° 2θ.

the conditions that these two samples were produced there is little to no multiphase crystallisation of $TiOSO_4{\cdot}H_2O$ and $TiOSO_4{\cdot}2H_2O$ occurring.

The $TiOSO_4{\cdot}H_2O$ diffraction pattern appears to be of a much higher quality than that of $TiOSO_4{\cdot}2H_2O$. Its peaks are well-resolved, with very little peak overlap visible before approximately 1.3-1.4 Å d-spacing. We presume that this is due to the crystal morphology being one of well-formed, large prismatic crystals, rather than the somewhat less reliably well-formed, fibrous needles of $TiOSO_4{\cdot}2H_2O$.

Comparison of DIH01 and DIH02 ex-situ *$TiOSO_4{\cdot}2H_2O$ diffraction patterns*

While the two $TiOSO_4{\cdot}2H_2O$ samples shared a common origin in being either produced from, or composed of, the $TiOSO_4{\cdot}2H_2O$ solid provided by BHP Billiton, their diffraction patterns exhibited some notable discrepencies from one another. The synchrotron X-ray diffraction patterns of DIH01 and DIH02 can be found in Figures 4.32 and 4.33 respectively.

When comparing the two patterns, there is an immediately obvious loss of quality present in the DIH01 sample when compared to the DIH02 sample. This is not surprising: the method of preparation (outlined previously in this chapter) means that the solid is almost certainly going to be less crystalline than that produced *via* BHP Billiton's process. The peaks are wider and less well-resolved, and there is a significant presence of background that can be attributed to unreacted amorphous $TiOSO_4$ precursor retained

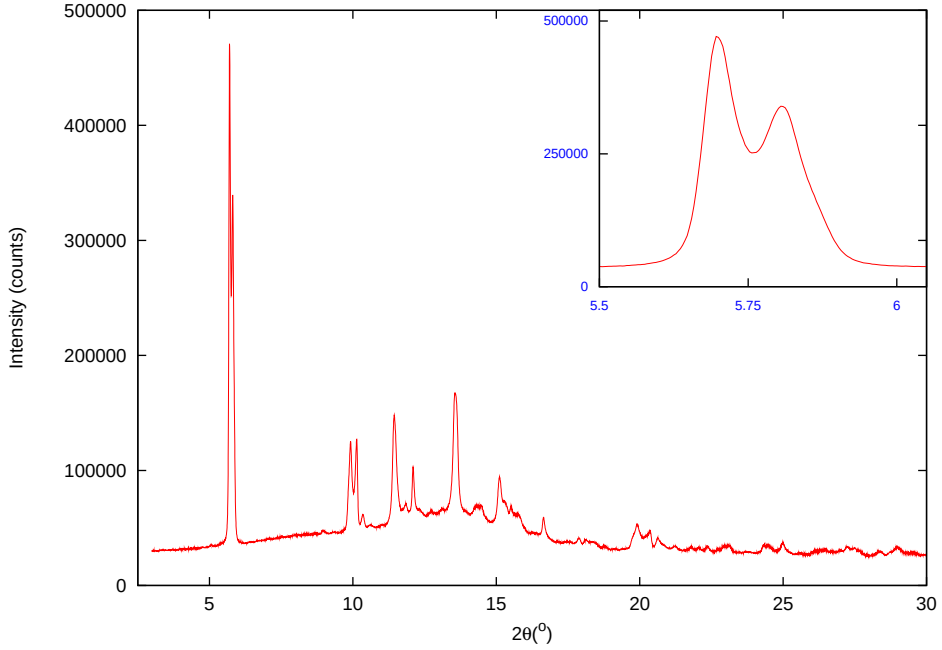

FIGURE 4.32: Synchrotron powder XRD pattern of sample DIH01. Insert: A close-up of the double peak feature.

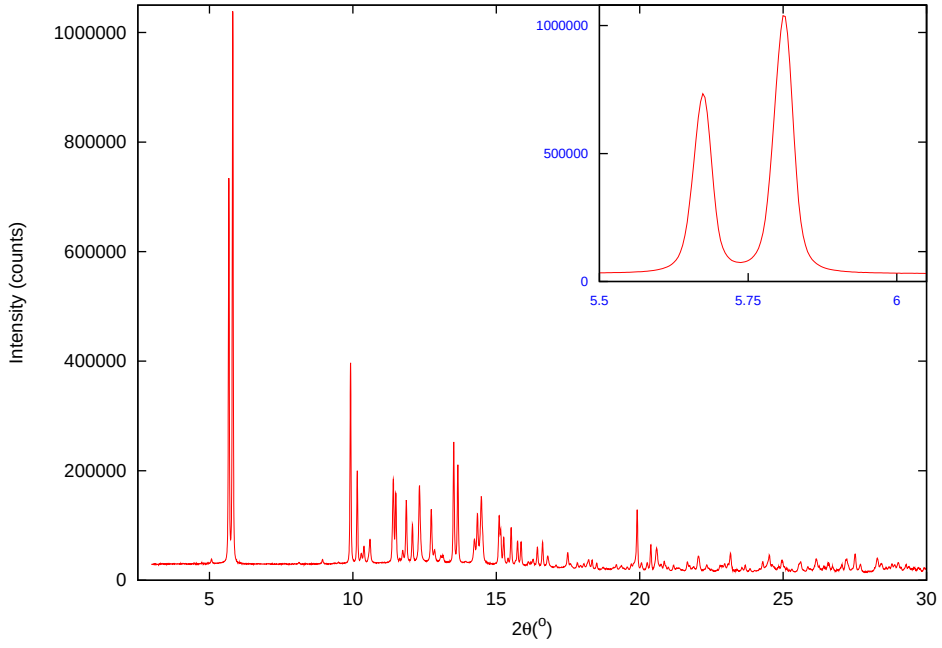

FIGURE 4.33: Synchrotron powder XRD pattern of sample DIH02. Insert: A close-up of the double peak feature.

in the product. Figure 4.34 shows more clearly the difference in quality between the two samples with a normalised plot of both diffraction patterns.

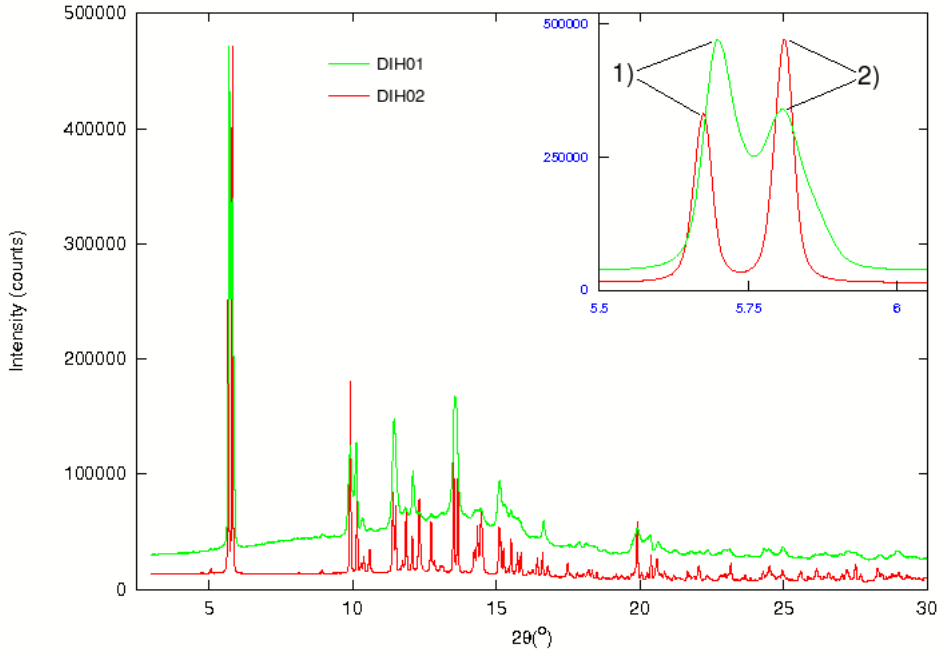

FIGURE 4.34: A comparison of synchrotron powder XRD patterns of samples DIH01 and DIH02. Insert: A close-up of the double peak feature showing the numbering and variation in the two largest peaks.

One of the main concerns with regards to the sample was the acicular crystal habit of $TiOSO_4 \cdot 2H_2O$. Acicular, or needle-like, crystal morphology results in skewed intensities in the diffraction pattern as a result of the way the crystal particles orient themselves during sample preparation (see section 2.3.3 for a more detailed discussion). It was therefore necessary to monitor the presence of any variations in intensity throughout the patterns that might be attributable to preferred orientation effects. With this in mind, the comparison of the two patterns proved quite interesting.

The most notable feature in each of the diffraction patterns is the presence of a very large pair of peaks at approximately 5.67 and 5.81° 2θ, shown in greater detail in the insert and labelled 'peak 1' and 'peak 2', respectively, for simplicity. Immediately obvious when the two patterns are overlaid is that the ratio of intensities of peak 1 and peak 2 have been reversed. In the DIH01 sample the peak 1/peak 2 ratio is 1.39, while for the DIH02 sample the peak 2/peak 1 ratio is 1.41. The peak ratios have reversed, and there has been a shift of peak 1 by approximately 0.02° 2θ. While the degradation of the DIH01 pattern with respect to the DIH02 pattern means that any concrete interpretation of this feature is difficult, the case could be made for different levels of preferred orientation between the samples causing the variation in intensity. Alternatively, the different methods of

producing $TiOSO_4{\cdot}2H_2O$ could be causing different crystal morphologies to be present in the beam.

From this comparison of peak ratios, it is seeming less likely that a reliable structure determination can be performed while the general poor quality of the patterns and uncertainty regarding the effect of preferred orientation or crystal morphology on peak intensities remains. The extraction of integrated intensities is a fundamental step in SDPD; if the intensities of particular reflections are known to be unreliable it would be misleading to include them. The removal of such peaks represents a loss of information further to that of peak overlap.

Peak ratios of in-situ $TiOSO_4{\cdot}2H_2O$ *diffraction patterns*

Figure 4.35 shows the background-subtracted, normalised final diffraction pattern plots from the *in-situ* diffraction experiments of SOL03, SOL04, and SOL05 over the range of 5.55-6.0° 2θ. The background subtraction was achieved with the Powder4 software package [154], using the Sonneveld and Visser algorithm [155]. What is immediately obvious upon viewing this figure are the significant differences between these *in-situ* diffraction patterns and the *ex-situ* diffraction patterns shown in Figure 4.34. In the *in-situ* work, there appears to be two extra peaks associated with each of the two major peaks, which were not present in the *ex-situ* diffraction patterns. Given the development of peaks in new positions being present in all the *in-situ* diffraction patterns, it must be the case that the *in-situ* environment results in some fundamental change to the structure. Shifts in peak ratios can be attributed to a change in the internal atomic coordinates of the sample structure, while new peaks are a result of structures with different space group symmetries.

While variability of these two major peaks in the $TiOSO_4{\cdot}2H_2O$ pattern has been shown previously in the *ex-situ* work (samples directly from BHP and samples that had been recrystallised using BHP stock showed different peak ratios) the introduction of new peaks into the diffraction pattern during the *in-situ* growth of the crystals is novel. SOL03 shows the weakest example of these new peaks, while SOL04 and SOL05 present much stronger reflections. It is thought that the much higher background levels in SOL03 might contribute to some extent in lowering the apparent intensity of its additional peaks. However, this relative shift does not account entirely for the lower intensity seen when compared to the SOL04 and SOL05 diffraction patterns.

In addition to the new peaks forming, there can be seen to be variations in the peak ratioss between the new peaks, adding yet another layer of complexity. SOL03 and SOL04 seem to have approximately the same peak ratio character, disregarding the

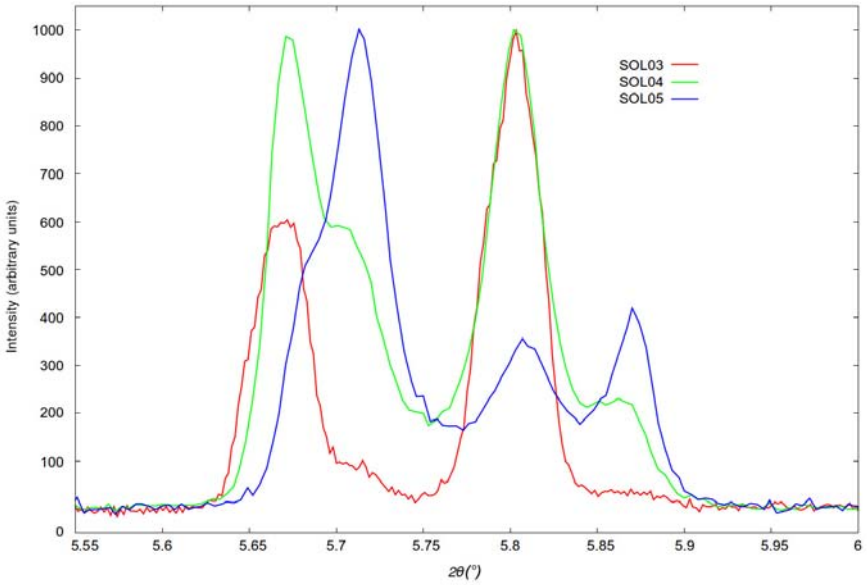

FIGURE 4.35: Background-subtracted, normalised final diffraction pattern plots from the *in-situ* diffraction experiments of SOL03, SOL04, and SOL05 over the range of 5.55-6.0° 2θ.

variations in collection time between them, while SOL05 shows a markedly different set of peak ratios.

The qualitative similarity in character between SOL03 and SOL04 diffraction patterns could be explained by the fact that they were produced using Riedel-de Haen-sourced $TiOSO_4$, while SOL05 was produced using BHP-Billiton-sourced $TiOSO_4$. The question remains as to whether the extra peaks are due to some metastable product only present in the solution phase, or if there is some intermediate present in the production of $TiOSO_4{\cdot}2H_2O$, though the former is thought to be the more favourable hypothesis. The quality of the *in-situ* samples is, unsurprisingly, worse than of the *ex-situ* DIH01 sample. Peak overlap is abundant and background noise from amorphous $TiOSO_4$ and sulphuric acid contributes considerably to the lack of peak resolution. This is obviously due to the time limitations when performing *in-situ* experiments and the closed nature of the system.

Growth rates of in-situ $TiOSO_4{\cdot}2H_2O$ *diffraction patterns*

Kinetic analysis can offer a more comprehensive visualisation of the growth of the peaks, as well as some insight into the possibility of the formation of these new peaks corresponding to multiple phases. For this, the extent of the formation reaction is calculated as a function of the ratio of a particular peak's intensity at time t, over that of the same peak at its final intensity:

$$\alpha_{hkl}(t) = \frac{I_{hkl}(t)}{I_{hkl}(t_{final})} \tag{4.1}$$

Using equation (4.1), we can produce α vs. reaction time graphs, shown in Figure 4.36 for each sample. Looking at these figures, we can make some comments about the behaviours of the different samples.

The reaction of SOL03 can be seen to have run to completion, with a characteristic induction time, reaction time, and flattening out signifying equilibrium. The noise present in peaks 2 and 4 is to be expected given the greater uncertainty in determining the height of smaller peaks with less reliable statistics.

The reaction of SOL04 gives a much smoother curve that seems to come very close to an end equilibrium point. The smoothness of the curve when compared to that of SOL03 is likely due to the fact that SOL03 had a number of interruptions in the data series (due to beam injections, software failures, etc.) and as a result, some portions of the time that the sample spent reacting in the beam were not recorded. SOL04 had very few interruptions, which shows in the greater number of points included in the data series. Again, a characteristic induction time and reaction curve are seen in the α plot, and, while not as pronounced as SOL03, the noise present in the calculation of α contributes to a more variable curve for the smaller peaks.

It is clear that SOL05 did not achieve an equilibrium state. Due to the time restraints mentioned previously, it was necessary to remove the capillaries when it was thought that the reaction had proceeded to completion. Obviously the time allowed for this was not sufficient. Importantly, there does not seem to be any gradient change in the shape of any curve to suggest the formation of an intermediate. Additionally, since all the peaks for each sample follow approximately the same curve, it is reasonable to assume that they are being formed by the same product, i.e. there is a single phase being produced in the capillary.

It would appear that after around 60 diffraction pattern collection times (each corresponding to 600 seconds, therefore 10 hours total) the reaction has typically reached equilibrium. Induction times vary, but on average crystallisation has begun at around the 20^{th} diffraction pattern (approximately 3-4 hours) corresponding well to the induction times seen in section 4.4.2.

The growth of the peaks can also be seen with more clarity using a typical 'stacked' diffraction pattern, colour coded to the intensity of the plot. To give an idea of the level of background present in the diffraction patterns, Figure 4.37 shows the difference between

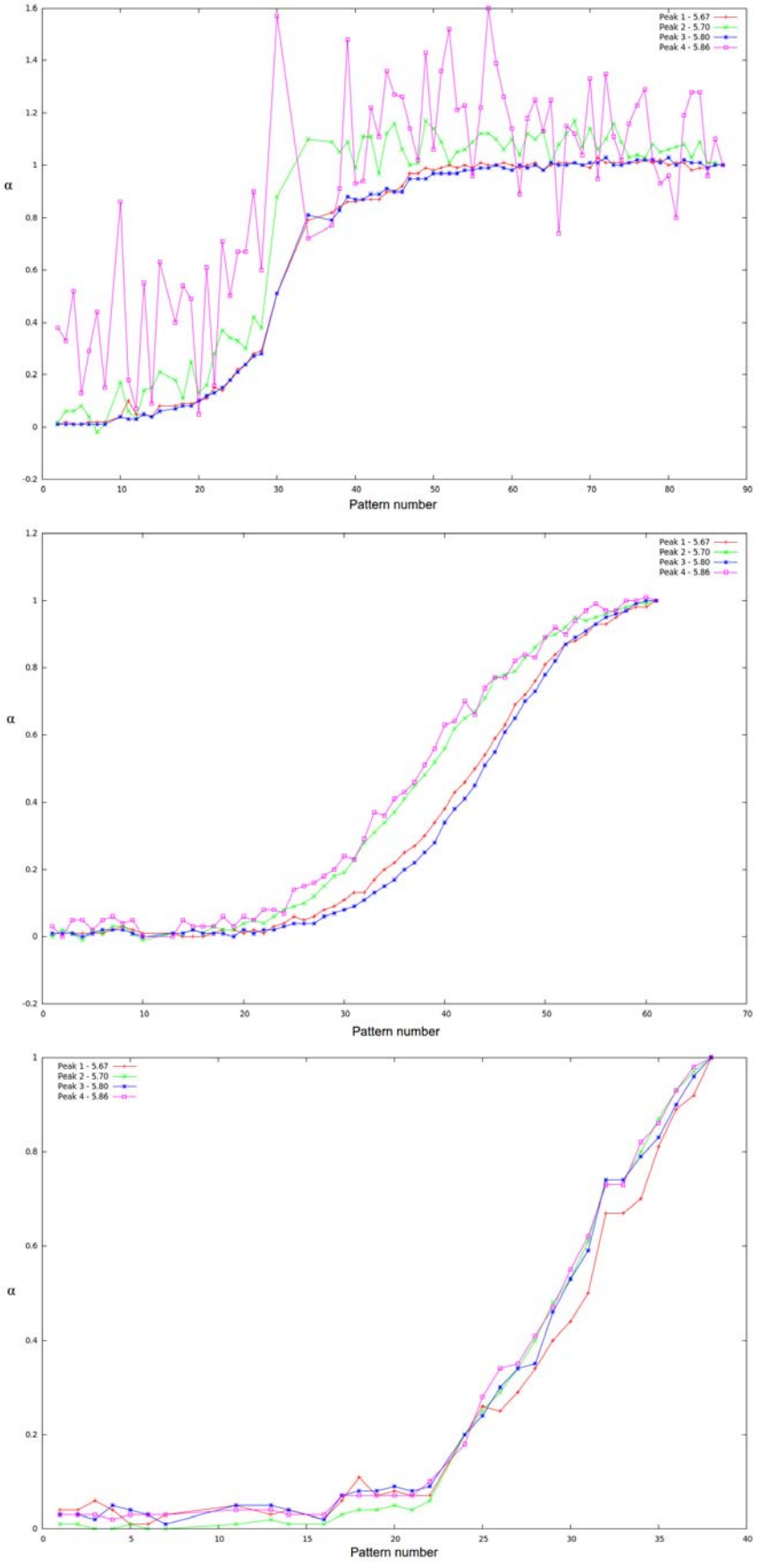

FIGURE 4.36: α versus diffraction pattern number plots for samples SOL03 (top), SOL04 (middle), and SOL05 (bottom).

a diffraction pattern with and without background subtraction. Again, the background subtraction was achieved with the Powder4 software package using the Sonneveld and Visser algorithm.

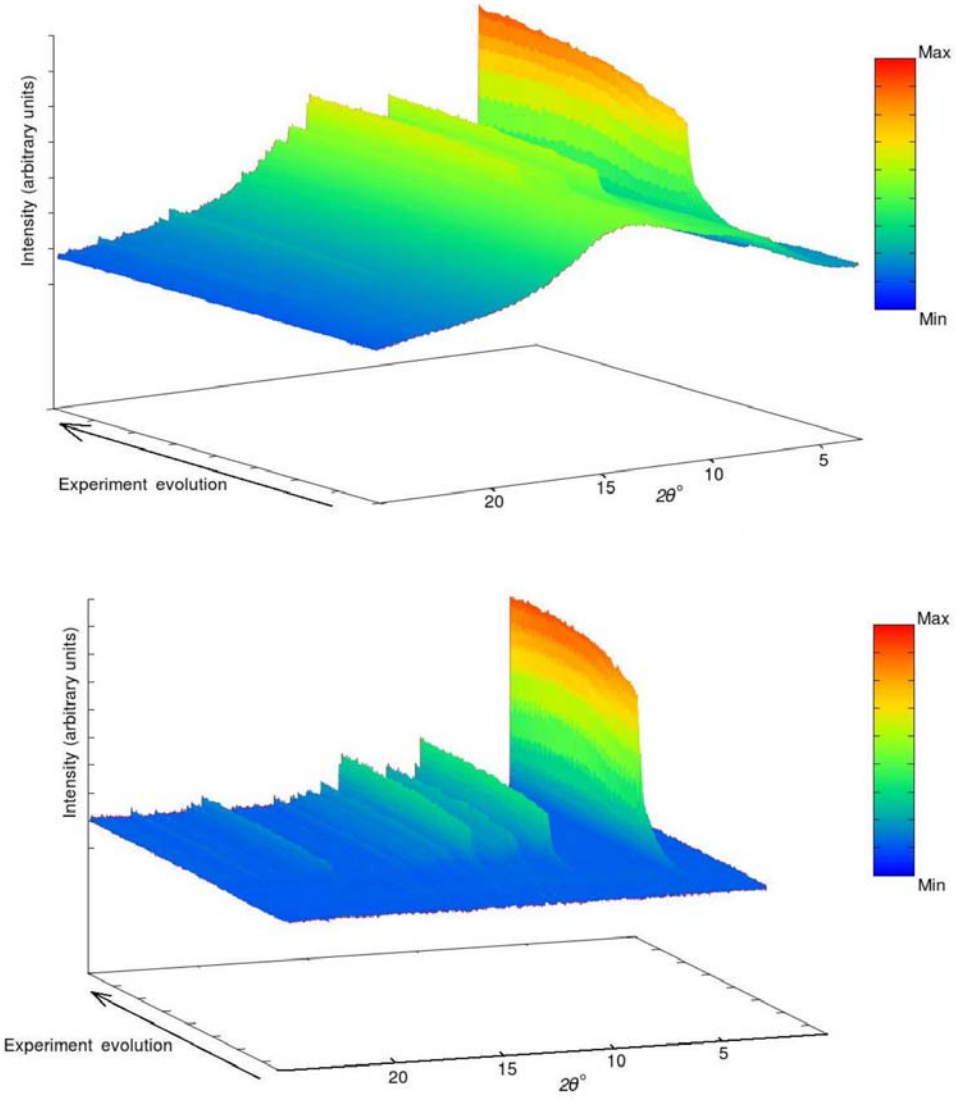

FIGURE 4.37: (left) Aggregated diffraction patterns showing *In-situ* growth of $TiOSO_4 \cdot 2H_2O$ and the high level of background resulting from the presence of H_2SO_4. (right) The same aggregated data after being treated to remove the background.

Comparison of ex-situ and in-situ diffraction patterns

In order to try and explain the presence of the two extra peaks at positions 5.70 and 5.86° 2θ observed during *in-situ* diffraction experiments, a comparison of the *in-situ* and *ex-situ* diffraction patterns is required. Figure 4.38 shows a comparison of the SOL03, SOL04, SOL05, DIH01, and DIH02 diffraction patterns in this area.

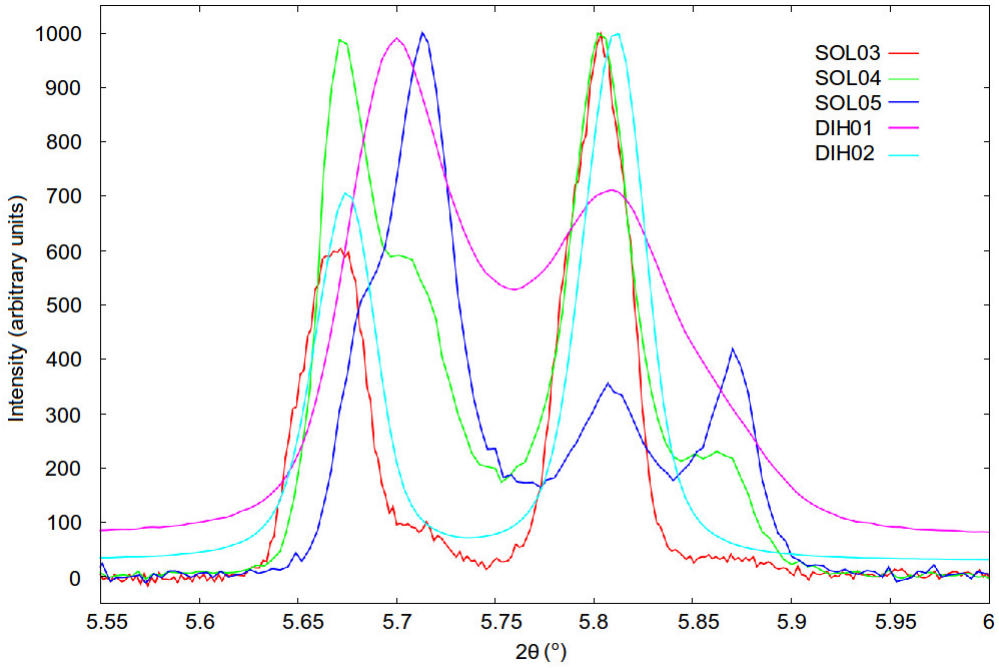

FIGURE 4.38: A comparison of normalised *ex-situ* and *in-situ* X-ray diffraction patterns.

There are a number of observations that can be made from Figure 4.38. Starting with the DIH01 diffraction pattern, it can be seen that the two peaks are much broader than any of the other patterns, encompassing almost the entire range of peaks present in the other patterns. It shows the most similarity to the SOL05 *in-situ* diffraction pattern, with peak 2 (5.70° 2θ) being the most intense, while the breadth of this peak is too large to determine if there is the presence of the peak 1 (5.67° 2θ) shoulder that was seen in SOL05. Peak 3 (5.80° 2θ) is present with a greater intensity than in SOL05. The presence or absence of peak 4 (5.87° 2θ) is interesting, as there exists a slight change in peak asymmetry at approximately 5.85° 2θ that could be taken as a shoulder indicating the presence, limited as it might be, of peak 4.

The DIH02 diffraction pattern has, as mentioned before, a vastly different character to that of DIH01. The peak ratios are reversed, and the resolution of the two peaks appears to be much greater. The closest *in-situ* diffraction pattern is that of SOL03, maintaining almost exactly the same peak ratios of peaks 1 and 3. Unlike DIH01, there does not appear to be any asymmetry in either of the peaks that might indicate the presence of peaks 2 and 4.

Along with the previously mentioned preferred orientation effects, the high amount of variability in this region of the diffraction patterns could be an indication of a degree of flexibility within the structure. This flexibility would most likely be due to the significant amount of water present in the structure. Given the greatest deviations occur in the

in-situ diffraction patterns, it is not difficult to imagine that a variety of meta-stable phases may exist in equilibrium, differing from each other in slight ways to give the differences in peak location and intensity.

4.5.2 Advanced Photon Source

The Argonne National Facility Advanced Photon Source is a synchrotron facility located near Chicago, Illinois. It was suggested that the particular area detector in use at the facility might provide a solution to the question of preferred orientation affecting the diffraction. This is as a result of area detectors recording Debye-Scherrer rings, making it possible to see the presence of preferred orientation manifest as discontinuous rings [156].

4.5.2.1 Sample preparation, data collection, and analysis of data

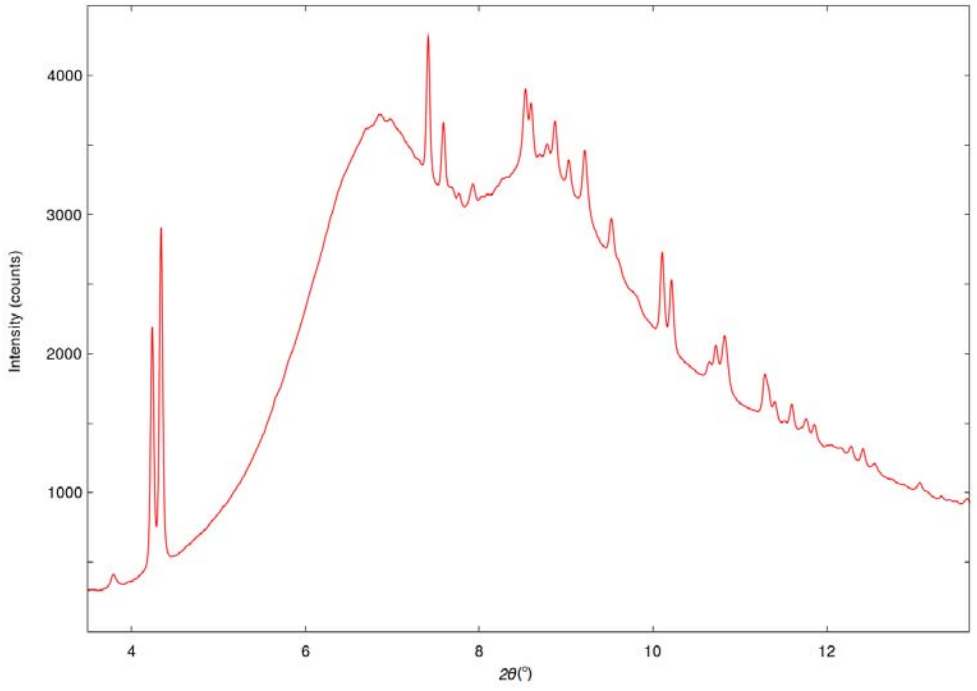

FIGURE 4.39: Synchrotron powder XRD pattern of a preliminary sample sent to the Argonne National Facility Advanced Photon Source, showing the high background produced by insufficient $TiOSO_4{\cdot}2H_2O$ material in the epoxy mixture.

A sample was prepared by grinding BHP-provided $TiOSO_4{\cdot}2H_2O$ with epoxy glue. Each pattern was collected at a wavelength of 0.61518 Å and a sample-to-detector distance of approximately 600 mm. Initially, the amount of $TiOSO_4{\cdot}2H_2O$ in the epoxy was not

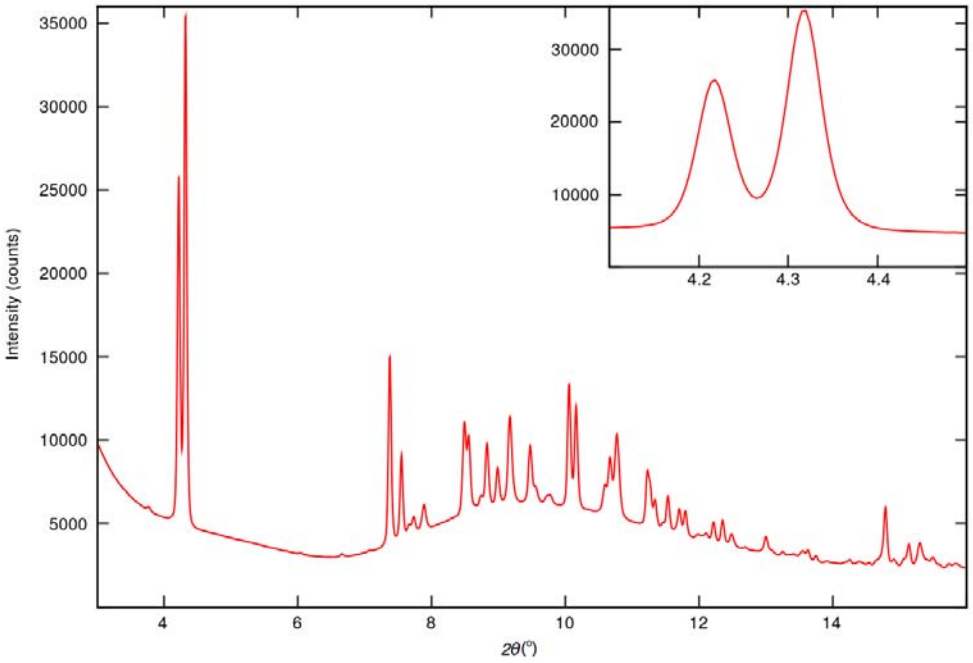

FIGURE 4.40: Synchrotron powder XRD pattern of the sample sent to the Argonne National Facility Advanced Photon Source. Insert: A close-up of the typical double peaks at 4.2 and 4.3° 2θ.

sufficient to provide adequate counting statistics, and this manifests itself as a large background in the initial diffraction pattern shown in Figure 4.39.

The second mixture was prepared with an aim of achieving approximately 50% by volume $TiOSO_4 \cdot 2H_2O$ to epoxy. On this occasion the background was significantly reduced and no preferred orientation effects were observed in the Debye-Scherrer rings integrated over to produce the diffraction pattern. The new pattern is shown in Figure 4.40 and shows a large reduction in background as compared to 4.39, however it is still quite significant. Interestingly, the Debye-Scherrer rings showed 'no significant preferred orientation' according to the resident beam line scientist [156]. Unfortunately, the poor resolution of the pattern when compared to the Australian Synchrotron patterns effectively rules it out for use in most SDPD studies. However, as will be shown in chapter 6, the data set can be used to confirm the indexing of a unit cell at a different wavelength.

4.6 Neutron diffraction

While X-ray diffraction occurs *via* interaction with an atom's electron cloud, neutron diffraction is a result of direct interaction with the atom's nucleus. As has been

mentioned previously, this means that X-ray diffraction patterns are dominated by any heavy atoms due to their greater relative electron density. This is not the case with neutron diffraction, as the direct interaction with the nucleus means the scattering of incoming neutrons varies randomly between isotopes. There is no clear relationship between atomic number and contribution to a neutron diffraction pattern like there is in X-ray diffraction.

The above can make X-ray diffraction a much more attractive option for the initial placement of heavy elements in a structure determination. However, when it comes to structure solution (defined here as the complete placement and refinement of all atoms in the unit cell) neutron diffraction offers unique advantages, especially when it comes to placing atoms of lighter elements, such as hydrogen and oxygen. Neutron diffraction allows these elements to be just as distinguishable as heavier atoms, and therefore to be placed with some confidence as to their position. This has resulted in the practise of using X-ray powder diffraction as the method of choice for structure determination, while neutron powder diffraction is more advantageous when used for the latter stages of structure refinement.

With all this in mind, neutron diffraction experiments were conducted at the Open Pool Australian Lightwater (OPAL) reactor housed at the Australian Nuclear Science and Technology Organisation (ANSTO) facility in Lucas Heights, New South Wales. The presence of hydrogen atoms in the sample meant that it required deuteration prior to the diffraction experiment. This is due to the very high incoherent cross-section of hydrogen, $\sigma_{inc} = 80.27$ barn [157], around 40 times larger than any other element, which results in a high degree of hydrogen scattering noise that washes out all other reflections. Deuteration alleviates this problem by replacing hydrogen with deuterium, which has very little incoherent scattering, $\sigma_{inc} = 2.05$ barn.

The deuteration of $TiOSO_4{\cdot}H_2O$ was achieved by following a similar reaction as that used to produce the regular product. A photograph of the experimental setup is shown in Figure 4.41. Deuterated sulphuric acid was added to amorphous $TiOSO_4$ and reacted under nitrogen to prevent atmospheric hydrogen from exchanging with the deuterium. An oil bath was used to maintain a temperature of 110°. The product eventually used in the successful neutron diffraction was not washed after reaction, as even when supposedly dry methanol was used to do so, it was found to cause some hydrogen exchange with the product.

The resultant background subtracted neutron diffraction pattern of $TiOSO_4{\cdot}2D_2O$ is shown in Figure 4.42. The pattern was collected over 9 hours at a wavelength of 2.439 Åusing the 'Echidna' high-resolution powder diffractometer. This is the first successful neutron diffraction pattern thus far produced of deuterated $TiOSO_4{\cdot}2H_2O$. While the

FIGURE 4.41: Photograph of the laboratory setup used to produce $TiOSO_4 \cdot 2D_2O$.

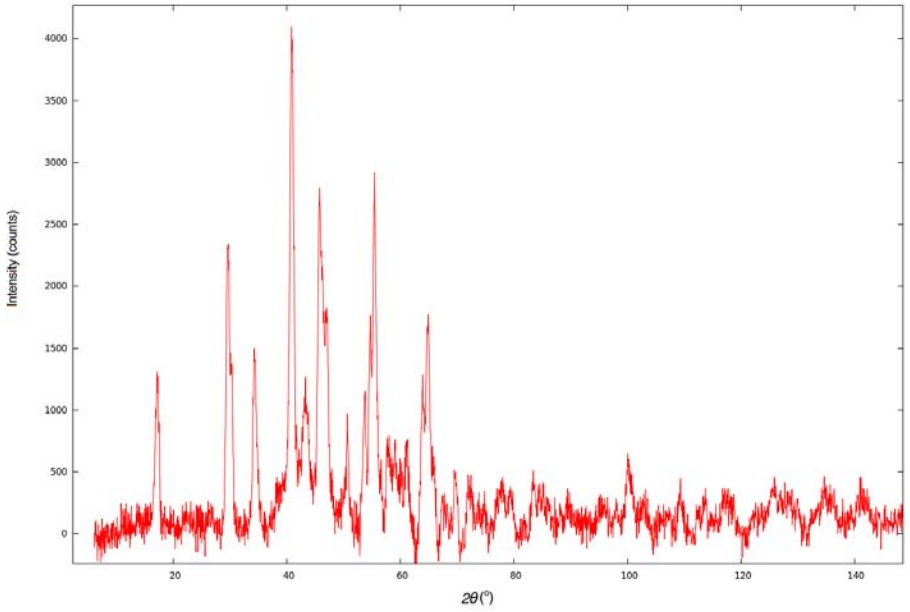

FIGURE 4.42: Background subtracted neutron diffraction pattern of $TiOSO_4 \cdot 2D_2O$.

quality of the pattern is not the best (mainly due to some residual hydrogen which, when subtracted, causes the Bragg peaks to be less well-defined) the positions of reflections are still quite obvious.

4.7 Conclusions

In this chapter we have shown the production methods of single-phase $TiOSO_4 \cdot H_2O$ and $TiOSO_4 \cdot 2H_2O$ using amorphous $TiOSO_4$ as a precursor and confirmed their phase purity using a conventional laboratory X-ray diffractometer. In preparation for synchrotron X-ray diffraction, we showed that the production of both phases in a capillary vessel is, while somewhat unpredictable, possible. Synchrotron X-ray diffraction patterns were recorded at two facilities, the Australian Synchrotron and the Advanced Photon Source. In addition to standard *ex-situ* diffraction patterns, an *in-situ* reaction experiment was carried out at the Australian Synchtrotron, whereby a sample of $TiOSO_4 \cdot 2H_2O$ was grown in a capillary in the diffraction beam. Across the X-ray diffraction experiments, a variation in certain peak ratios was noticed, although some speculation still remains as to whether the cause is structural or arises from the different origins of the $TiOSO_4 \cdot 2H_2O$ samples. A partially deuterated sample of $TiOSO_4 \cdot 2D_2O$ was analysed using neutron diffraction at the OPAL facility. While there was a small amount of residual hydrogen that resulted in a significant background, the neutron diffraction pattern was, like the synchrotron X-ray diffraction patterns, the first of its kind to be recorded.

It was shown that obtaining X-ray diffraction data for $TiOSO_4 \cdot 2H_2O$ resolved to the extent of Sheldrick's rule for direct methods is a difficult proposition, even with the higher energies and correspondingly higher resolution that multiple synchrotron facilities offered. Our *ex-situ* diffraction patterns showed a poor overall quality that was attributed to a combination of the poor crystallinity of the crystals themselves and preferred orientation arising from the acicular nature of the crystals. However, this latter point was later called into question by the results from the Advanced Photon Source, where the use of an area detector showed no preferred orientation effects in the Debye-Scherrer rings. Ultimately, while the quality of the diffraction patterns collected did not achieve the high quality expected, it remains the highest quality thus far obtained for $TiOSO_4 \cdot 2H_2O$, and therefore offers the best chance of illuminating some of its structural properties.

Chapter 5

Computer modelling and development of hypothetical structures of $TiOSO_4 \cdot 2H_2O$

In chapter 3, the theoretical framework behind computer simulation was presented, and this framework forms the basis for exploring the energy landscape of structures. It was thought that both first principles and forcefield methods would offer unique advantages in the exploration of candidate hypothetical structures of $TiOSO_4 \cdot 2H_2O$. However, the simulation of an unknown structure is not a trivial task, and every caution must be taken to ensure that the many variables that might affect the simulation quality are accounted for before attempting to assign results any measure of validity.

This validation manifests itself in the form of the development of the input parameters that guide the simulations: pseudopotentials, basis sets for first principles density functional theory calculations, and forcefields for molecular dynamics simulations. These input parameters must then be rigorously tested on multiple, well-defined systems in order to confirm transferability between structures. In this case, TiO_2 polymorphs were used initially due to the efficiency of calculations using them and the extensive literature regarding their simulation, while the two known structures of the titanyl sulphate series, $TiOSO_4$ and $TiOSO_4 \cdot H_2O$, were used as a final test.

This chapter will outline the approaches used to construct the pseudopotentials and basis sets for *ab initio* calculations, and their results. Their refinement against the TiO_2 polymorphs will be discussed, as will their transferability to $TiOSO_4$ and $TiOSO_4 \cdot H_2O$. The parameterisation of forcefields capable of exploring hypothetical structures will be shown. Finally, the development of a hypothetical structure of $TiOSO_4 \cdot 2H_2O$ based on its observed properties and the structures of $TiOSO_4$ and $TiOSO_4 \cdot H_2O$ will be presented.

5.1 First principles calculations

5.1.1 Methodology

5.1.1.1 The SIESTA method

The implementation of DFT into software code that can be executed by computers has created a wide variety of methodologies. Some of these methodologies are based around precision, while others try and find a compromise between computational precision and computational expense. The primary software used in this project was that based on the SIESTA methodology, contained within the software suite of the same name [158, 159]. SIESTA is an order-N method, meaning that the computational cost can be made to scale linearly with the number of basis functions in the calculation [160].

SIESTA uses norm-conserving pseudopotentials and a flexible, numerical LCAO basis set to describe Kohn-Sham wavefunctions. These basis functions are projected onto a real-space grid on which the electron density is calculated, in order to determined the Hartree and exchange-correlation potentials; exchange-correlation is approximated by the LDA or GGA. The fineness of the grid can be tuned to ensure a greater precision of calculation. This fineness is expressed as the maximum kinetic energy of a plane wave that can be represented on the grid.

When running optimisation calculations, convergence is governed by the forces and stresses experienced by the atoms and the unit cell, respectively. The threshold after which the simulation is considered converged can be altered by the user. Optimisation is driven by a conjugate gradient or Newton-Raphson minimisation, based on a modified Broyden algorithm [161].

Within the context of this project, the SIESTA method and software has been used to optimise the geometry of structures and determine their energies. This will allow us to draw conclusions related to the structural stability and feasibility of hypothetical $TiOSO_4{\cdot}2H_2O$ structures.

5.1.1.2 Pseudopotential generation

Pseudopotentials are functions that replace the explicit interactions of core electrons and the nucleus with the valence electrons by an effective potential. This is an approximation to the all-electron potential, which takes into account all electronic and nuclear interactions. As previously mentioned in chapter 3, pseudopotentials are constructed such that they converge to the all-electron potential beyond a certain cut-off

radius, while within the radius the pseudopotential is constructed such that it does not have the complicated nodal behaviour of an all-electron potential (an all-electron potential would have n - l - 1 nodes within the radius cut-off). The SIESTA method uses a particular type of pseudopotential known as a 'norm-conserving' pseudopotential.

Pseudopotentials are generally required to be generated and tested for each atom they will be used for. The generation of pseudopotentials to be used with the SIESTA software package is handled by the ATOM software package. As in the SIESTA software package, an input file with various variables defined within is provided for the program by the user, which is then used to generate the pseudopotential.

The variables that need to be defined in order for a pseudopotential to be generated are:

- exchange-correlation functional type;
- whether the calculation includes relativistic effects, only spin-polarisation effects, or neither;
- the number of core and valence orbitals;
- the principal and angular momentum quantum numbers of each valence orbital, and the number of electrons occupying each valence orbital;
- the values of the radius cut-off for the s, p, d, and f angular momentum channels;
- and any core correction that needs to be applied.

Before use, the pseudopotential must be tested against all-electron calculations to show that, despite the pseudopotential having been generated with just one specific atomic configuration, it can reproduce the all-electron transition energies for many different environments. Transferability tests involve performing both all-electron and pseudopotential calculations on a series of atomic configurations, and comparing the excitation and ionisation energies that result from each. If these energies are found to fall within an acceptable range, then the pseudopotentials can be used to perform calculations on a real system and these results compared to the literature and experiment.

5.1.1.3 Basis set optimisation parameters

To prepare for simulating structures that have yet to be explored with computational methods, it is often necessary to develop basis sets that are appropriate for these

structures and test them on well-known model structures for which there is ample previous literature and experimental data to compare to.

Within the framework of the linear combination of atomic orbitals method used in the SIESTA method, a choice must be made as to how precise the calculation should be without driving the computational cost up unreasonably. The precision of the calculation can be increased by variationally optimising the parameters that define the basis set on a model structure, where the model structure chosen is one that is representative of the interactions that are expected in the unknown structure. The model structure chosen to optimise the basis set parameters in this case was the rutile polymorph of TiO_2. The default values for the basis set parameters within SIESTA are generally thought to be quite reasonable and can, in general, be used without the need for explicit optimisation. In the case of transition metals and their semicore states, SIESTA requires that these states be explicitly included. However, default values for the parameters in the basis set can still be used. While some of these basis set parameters were discussed in section 3.2.5.1, it is appropriate to revisit them in the context of the present calculations.

Multiple zeta orbitals

The number of radial orbitals ('zetas') is equivalent to how many functions are being added together per valence orbital to describe that orbital. Thus a single zeta orbital has just one function describing its wavefunction, while a double zeta has two, triple has three, and so on. Adding zetas has the effect of allowing the orbital to vary between the spatial extents of the extra basis functions, enabling it to accommodate changes in molecular environment while requiring greater computational expense. Therefore it is necessary to be judicious in the determination of how many zetas an orbital really needs, and how much of the norm of the orbital to assign to each zeta. For example, a core orbital (e.g. a 3s orbital in a titanium basis set) does not vary much as a function of environment and so can often be assigned one zeta. Conversely, a valence orbital (e.g. a 3d orbital in a titanium basis set) should be assigned multiple zetas in order to grant it the flexibility it requires when interacting with other orbitals, i.e. during bonding. Assigning more functions to a valence orbital than a core orbital in this way is known as creating a 'split-valence' basis set.

Figure 5.1 shows the double-zeta 2p orbital of a titanium basis set. Here we can see that by adding an additional zeta, we are able to get quite a large flexibility of sizes the orbital can occupy. This flexibility comes as a result of orbital coefficients, which can be varied to give the orbital more or less character from the first and subsequent zetas.

Polarisation orbitals

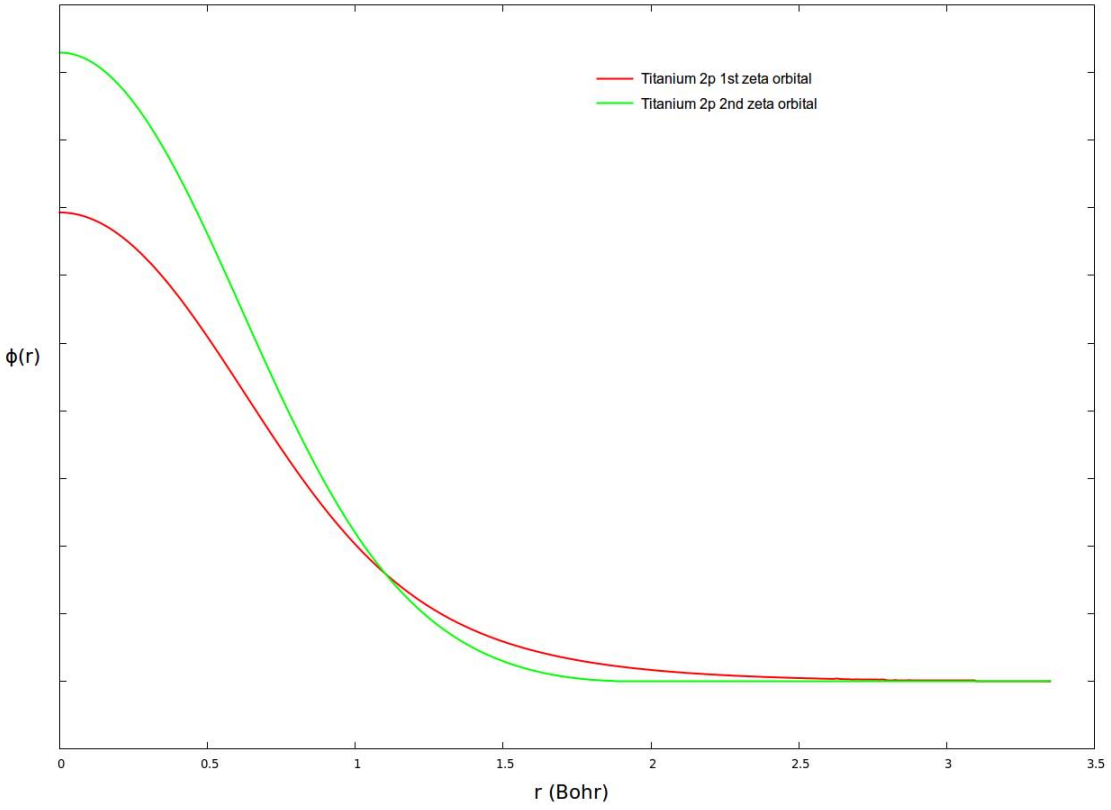

FIGURE 5.1: Figure showing multiple-zeta basis functions for a titanium 2p orbital.

When atoms are brought together, their charge distribution can shift from the ideal model of existing as separate s, p, d, f, etc. orbitals towards each orbital containing some measure of characteristics from other orbitals. To account for this, we add a basis function that is formally unoccupied in the atom (known as a polarisation orbital) of one angular momentum quantum number above the highest occupied orbital in the original basis set. For example, if we were adding a polarisation orbital to a titanium basis set (electronic structure [Ar] $3d^2$ $4s^2$) we would add an unoccupied 4f orbital for the 3d orbital to hybridise with, and a 4p for the 4s to do the same.

Radius cut-off

In order to create localised orbitals, a cut-off radius is employed beyond which the orbital is zero. This radial cut-off can be specified for each value of zeta in a multiple-zeta orbital. Alternatively a global energy shift value can be used to set the cut-off radius of each orbital in terms of the energy increase from their confinement. Increasing the radial cut-off will increase the precision of the calculation, and therefore cannot be minimised variationally. Instead a value must be chosen which offers a compromise between precision and computational expense.

Split-norm

The split-norm value is a way of defining the radial variation of multiple zeta orbitals. It is a real fraction that defines how much of the 'norm' is carried by successive zeta orbitals. For example if SplitNorm were set to 0.15, then the second zeta orbital would be calculated as one carrying 0.85% of the total 'norm', and then re-normalized. Figure 5.2 shows this process more clearly.

Soft confinement

Different methods of enforcing the cut-off radius have been developed, the default being an infinite square well confinement potential which works relatively well. However, this method has the disadvantage of producing a discontinuous derivative in the basis function which can lead to problems when calculating forces, stresses, and, to a lesser extent, energies.

SIESTA can solve this problem by introducing a new soft confinement potential that smooths the discontinuity and contracts the orbital:

$$V(r) = \frac{v_0 e^{\frac{(-r_c - r_i)}{(r - r_i)}}}{(r_c - r)} \tag{5.1}$$

This function starts at some internal radius, r_i, diverges at r_c, and ensures strict localisation and continuous derivatives. If soft confinement is invoked within a SIESTA basis set, V_0 and r_i must be defined and can be variationally optimised.

Figure 5.3 shows as an example the effect of altering the value of the internal radius, r_i, on the 3s orbital of a titanium basis set. From this graph it can be seen that the smoothing has quite a noticeable effect when initiated closer to zero. It should be noted that this alteration away from the initial shape of the orbital may in fact result in a less accurate description of valence orbitals.

5.1.1.4 Simplex basis set optimisation parameters

A program by which the basis set can be automatically optimised has been recently developed for use with the SIESTA package. This program is known as the 'SIGPOS' (SImple General-Purpose Optimization System) program [162]. The SIGPOS program contains an implementation of the downhill simplex method (also called the Nelder-Mead, or amoeba, method) [163] and particle-swarm-optimisation [164], but for our optimisations only the downhill simplex method was invoked.

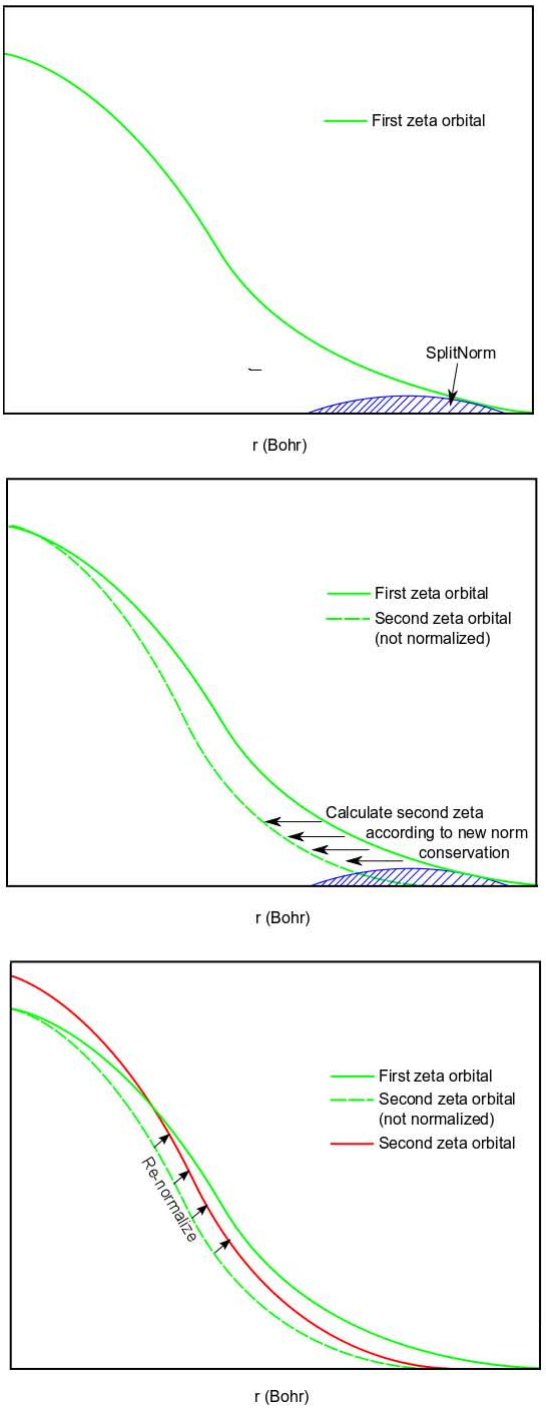

FIGURE 5.2: Figure showing the process of calculating successive zeta orbitals using the SplitNorm variable.

In order to run the simplex algorithm on any one basis set, the variables the user wishes to optimise are flagged. A series of single point calculations are then run, and these adjust the basis set parameters based on the variational principle, i.e. accepting values that provide the lowest energy for the system, subject to user input bounds on parameters. Eventually, after a number of calculations proportional to the number of variables being

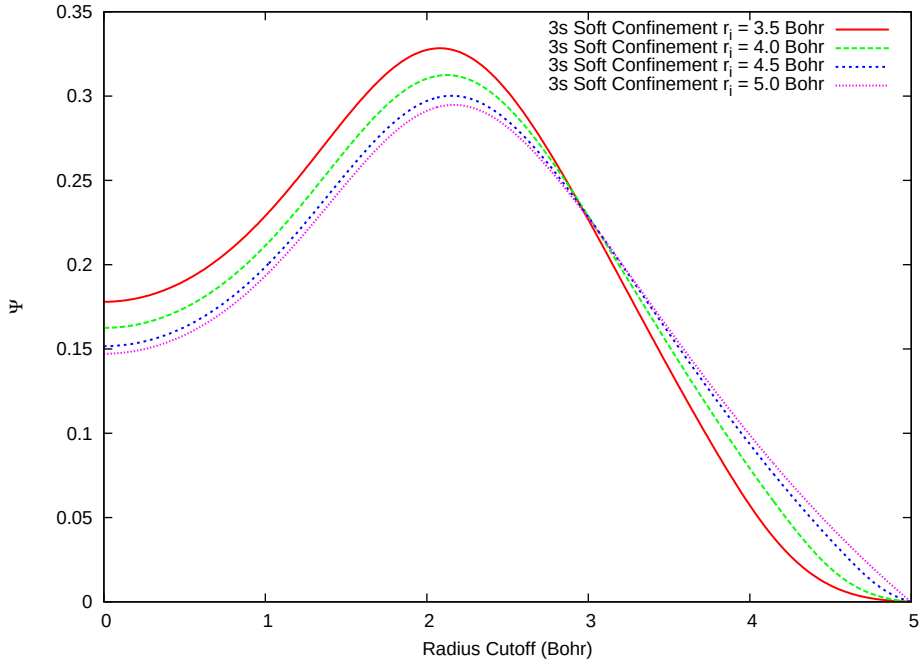

FIGURE 5.3: Figure showing the smoothing effect of different values of r_i within a soft confinement potential on a titanium 3s orbital.

optimised, the algorithm will reach a set of values for the variables that give the lowest energy, within some tolerance. These variables are then used in subsequent calculations. Unfortunately, at the time of writing, the SIGPOS program was only available in serial mode. This means that such an automated basis set calculation might take weeks to find an optimal solution, depending on how many variables are set to optimise.

5.1.1.5 Optimisation parameters

Other than the basis sets, there are a number of parameters related to the optimisation calculations that must be defined before running a system. The values for these were mostly taken from either the SIESTA manual, by employing conventional wisdom relating to the degree of accuracy required, or through variational optimisation. Their values are listed in Table 5.1. While fairly self-explanatory, further explanations of these variables can be found in the SIESTA manual [165] and Moreno and Soler's paper on optimal meshes for integrals [166].

Parameter	Value
Maximum force tolerance	0.01 eV/Å
Maximum stress tolerance	200 bar
Maximum atomic displacement/step	0.025 Å
Mesh cut-off	400 Rydberg
K-grid cut-off	12 Å

TABLE 5.1: Values of general calculation parameters required to run the simulations in the SIESTA software.

5.1.2 Parameterisation results

5.1.2.1 Pseudopotential generation

The values for the variables used to produce the pseudopotentials for titanium are shown below in Table 5.2. Four different pseudopotentials were produced; a large core (so-called because it includes the 3s atomic orbital as a core orbital) pseudopotential using the Perdew-Burke-Ernzerhof (PBE) exchange-correlation functional [113], a small core (so-called because it includes the 3s atomic orbital as a valence orbital) pseudopotential using the PBE exchange-correlation functional, and small and large core pseudopotentials using the Armiento and Mattsson 2005 (AM05) exchange-correlation functional [105]. The small core and large core pseudopotentials will be labelled 'SC' and 'LC', respectively. These pseudopotentials were tested for transferability and found to lead to acceptable energy differences. Spin-polarisation and relativistic effects were included for all the pseudopotentials.

Label	X-C functional	Core size	*s*	*p*	*d*	*f*
PBE-SC	PBE	Small	1.19	1.58	1.00	1.58
PBE-LC	PBE	Large	2.99	1.58	1.00	1.58
AM05-SC	AM05	Small	1.19	1.58	1.00	1.58
AM05-LC	AM05	Large	2.99	1.58	1.00	1.58

TABLE 5.2: Values used for the generation of the PBE pseudopotential for titanium. Core radii are in units of Bohr for s, p, d, and f channels.

Figure 5.4 shows an example of the pseudopotential and all-electron wavefunctions that are generated using the titanium PBE-SC variables. These graphs are used to inspect the pseudopotentials before using them in calculations. As previously mentioned, by construction, a good pseudopotential will be smooth inside the r_c and follow the all-electron wavefunction exactly after the radius r_c. But how these properties are fulfilled may vary, and it can be difficult to choose one set of radii over another.

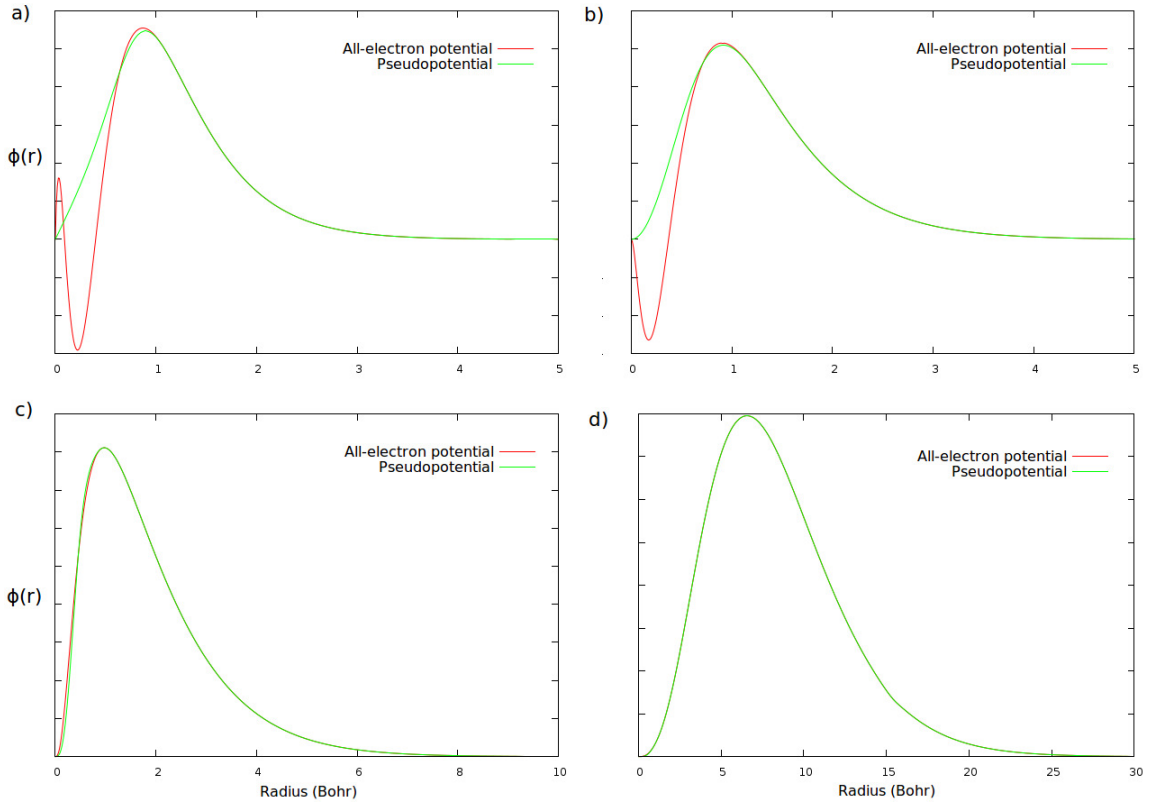

FIGURE 5.4: The pseudo and all-electron wavefunctions of the a) s, b) p, c) d, and d) f atomic orbitals for the titanium pseudopotential.

Transferability test calculations were then run for each of these pseudopotentials, and while it would be impractical to reproduce the results of each here, an example will be made in the form of the titanium PBE-SC pseudopotential. The states that were used to test the pseudopotential are shown in Table 5.3 below.

Atomic Configuration	**State**
$3p^6\ 4s^2\ 3d^2\ 4f^0$	Ground state
$3p^6\ 4s^2\ 3d^1\ 4f^0$	Ti^+ (3d orbital ionised)
$3p^6\ 4s^2\ 3d^0\ 4f^0$	Ti^{2+} (3d orbital doubly ionised)
$3p^6\ 4s^1\ 3d^2\ 4f^0$	Ti^+ (4s orbital ionised)
$3p^6\ 4s^0\ 3d^2\ 4f^0$	Ti^{2+} (4s orbital doubly ionised)
$3p^6\ 4s^1\ 3d^2\ 4f^1$	1 e^- transfer from 4s to 4f
$3p^6\ 4s^2\ 3d^1\ 4f^1$	1 e^- transfer from 3d to 4f

TABLE 5.3: Atomic configurations used in the transferability tests of the titanium pseudopotential.

Through the transferability tests, we obtain an energy difference between the all-electron and pseudopotential calculations. Table 5.4 below shows this difference for different transitions.

Transition	ΔE_{AE} (Ryd)	ΔE_{PP} (Ryd)	$\Delta\Delta E_{AE\text{-}PP}$ (Ryd)
Ground state $\rightarrow$ $3p^6\ 4s^2\ 3d^1\ 4f^0$	0.7177	0.7195	0.0018
Ground state $\rightarrow$ $3p^6\ 4s^2\ 3d^0\ 4f^0$	2.4150	2.4160	0.0010
Ground state $\rightarrow$ $3p^6\ 4s^1\ 3d^2\ 4f^0$	0.5395	0.5396	0.0001
Ground state $\rightarrow$ $3p^6\ 4s^0\ 3d^2\ 4f^0$	1.5362	1.5361	-0.0001
Ground state $\rightarrow$ $3p^6\ 4s^1\ 3d^2\ 4f^1$	0.0800	0.0830	0.0030
Ground state $\rightarrow$ $3p^6\ 4s^2\ 3d^1\ 4f^1$	0.6501	0.6518	0.0017

TABLE 5.4: Results from the transferability tests of the titanium pseudopotential. Energies are expressed as the energy required to excite from the ground state to the atomic configuration specified. AE and PP indicated all-electron and pseudopotential, respectively.

The recommended difference in energy between an all-electron and pseudopotential transition is <1 mRyd, though larger energy differences can occur for larger perturbations to the system (e.g. multiple electrons moving). While some of the energies were outside this recommendation, this may be due to the 4f orbital being unbound in the atom. In any case, they were considered sufficiently precise to continue using the pseudopotential. While the titanium PBE pseudopotentials were developed and tested ourselves due to the issue of semi-core states, the PBE pseudopotentials of the other elements of sulphur, oxygen, and hydrogen were considered to have been sufficiently studied and refined by others for their values to be taken from the SIESTA pseudopotential repository in the case of sulphur, or supplied by Prof. Julian Gale and used with his permission. The AM05 pseudopotentials were all developed by Prof. Julian Gale and used with his permission. The cut-off values of all pseudopotentials used are listed below in Table 5.5.

Element	X-C functional	*s*	*p*	*d*	*f*
Sulphur	PBE	1.63	1.76	1.94	1.94
	AM05	1.29	1.29	1.14	1.14
Oxygen	PBE	1.14	1.14	1.14	1.14
	AM05	1.14	1.14	1.14	1.14
Hydrogen	PBE	1.25	1.25	1.25	1.25
	AM05	1.25	1.25	1.25	1.25

TABLE 5.5: Values used for the generation of the PBE pseudopotential for sulphur, oxygen, and hydrogen. Core radii are in units of Bohr for s, p, d, and f channels.

5.1.2.2 Basis set optimisation

Multiple basis sets were produced during the exploration of the optimisation process using TiO_2 polymorphs. The four that showed the greatest promise for approaching the accuracy limit for DFT are discussed here.

Manually optimised basis set

The manual basis set was obtained by manual optimisation of the parameters dictating the properties of the basis set. This process of manual optimisation involved setting all of the parameters, bar one, to some default value. This one parameter was then varied across a range of possible values, using the variational optimisation of the energy of the system as an indicator of the quality of the basis set. Once that one parameter was found to be reasonably optimised, the next parameter could be varied and so on. On occasion, the step-by-step optimisation of a parameter needed to be repeated as it may have possessed some correlation with another of the parameters within the basis set. The basic properties of the manually optimised basis set are shown in Table 5.6, while a full input of the basis set, including the soft confinement parameters, for the SIESTA software is shown in Appendix A.2.

Variable	**Value**
Single zeta orbitals	3s, 3p
Double zeta orbitals	4s, 3d, 4f
Soft confinement?	Yes, explicit
Radial cut-offs (Bohr)	3s = 6.0 3p = 7.0 4s = 6.0 3d = 8.0 4f = 6.0
Split-norm	0.2

TABLE 5.6: Properties of the manual basis set

Simplex optimised basis set.

As described in methods section, simplex basis set optimisation requires the specification of variables to be optimised and the physically realistic constraints within which these variables should be explored. Table 5.7 shows the variables that were optimised during the first simplex optimisation, the constraints over which they were explored, and the final values obtained. v_0 and r_i refer to the parameters defining the soft confinement potential, as shown in equation (5.1).

On completion of the first basis set optimisation it was thought that some improvements could be made to the basis set, particularly in the areas of charge and radial cut-off, not included in this first optimisation. Therefore, in the subsequent optimisation using rutile TiO_2, the charge of both the titanium and the oxygen were included in the optimisation. In addition, the radial cut-offs for the titanium 4s, 3d, and 4p orbitals were increased to 7.0, 7.0, and 8.0 Bohr, respectively. Finally, the 4p was altered from being a soft-confined single orbital to a double-zeta split orbital. The optimisation was then repeated on the

Variable	Range minimum	Range maximum	Initial value	Final value
Ti 4s split-norm	0.05	0.50	0.25	0.498014
Ti 3d split-norm	0.05	0.50	0.25	0.50
Ti 4p v_0 (Rydberg)	1.00	100.00	50.00	59.040080
Ti 4p r_i (Bohr)	1.00	5.70	2.50	1.000000
Ti 4f v_0 (Rydberg)	1.00	100.00	50.00	57.145947
Ti 4f r_i (Bohr)	1.00	5.70	2.50	1.650685
O 2s split-norm	0.05	0.50	0.25	0.315223
O 2p split-norm	0.05	0.50	0.25	0.310181
O 3d v_0 (Rydberg)	1.00	100.00	50.00	20.034397
O 3d r_i (Bohr)	1.00	6.30	3.00	4.139549

TABLE 5.7: Limits, and initial and final values for the parameters optimised during the first simplex basis set optimisation on rutile TiO_2.

rutile TiO_2 polymorph. The resultant final values are listed, along with their limits and initial values, in Table 5.8.

Variable	Range minimum	Range maximum	Initial value	Final value
Ti Charge	0.50	2.50	1.5	2.352973
Ti 4s split-norm	0.05	0.50	0.25	0.498014
Ti 3d split-norm	0.05	0.50	0.25	0.204710
Ti 4p split-norm	0.05	0.50	0.25	0.50
Ti 4f v_0 (Rydberg)	1.00	100.00	50.00	30.9789290
Ti 4f r_i (Bohr)	1.00	5.70	2.50	1.491593
O 2s split-norm	0.05	0.50	0.25	0.261947
O 2p split-norm	0.05	0.50	0.25	0.335970
O 3d v_0 (Rydberg)	1.00	100.00	50.00	44.768815
O 3d r_i (Bohr)	1.00	6.30	3.00	1.504868

TABLE 5.8: Limits, and initial and final values for the variables optimised during the second simplex basis set optimisation on rutile TiO_2.

After this second optimisation run, there are still parameters that have hit the limit of their constraints, e.g. the titanium 4p split-norm. While initially it may seem straight-forward to relax the limits and optimise the basis set again, some consideration must be given to the fact that these constraints are physically motivated. If we were to continue to relax the limits and rely on variational optimisation, we run the risk of the parameters becoming unphysical. Hence, it was decided that further optimisation would not provide an improvement to the basis set that was both physically reasonable, and the basis set was considered optimised. The full input is shown in Appendix A.3.

Literature basis set

A literature basis set was retrieved from the SIESTA basis set repository [167]. It was created by Javier Junquera in his study of $BaTiO_3$ ferroelectricity, with the following notes regarding its optimisation [168]:

> "Basis set optimized with Simplex for the bulk cubic cell of $BaTiO_3$. The semicore states 3s and 3p are included in the valence. The quality of the basis is DZP for the valence (two radial functions for the 4s, and two radial functions for the 3d state, and one radial fuction for the 4p states), and SZ for the semicore states (one radial function for the 3s and the 3p). This amounts to 19 basis functions per Ti atom."

The basic properties of the Junquera basis set are shown in Table 5.9, while the full input is again shown in Appendix A.4

Variable	**Value**
Single zeta orbitals	3s, 3p, 4p
Double zeta orbitals	4s, 3d
Soft confinement?	Yes, explicit
Radial cut-offs (Bohr)	3s = 5.6995 3p = 5.6995 4s = 6.1000, 5.0994 3d = 5.9433, 4.7001 4p = 3.0537

TABLE 5.9: Properties of the Junquera basis set.

Default basis set

The default basis set was created without optimisation against a model, instead relying–as the name suggests–on the default values provided. The properties of the default basis set are shown in Table 5.10 while the full input is shown in Appendix A.5 and Appendix A.6.

Variable	**Value**
Single zeta orbitals	3s, 3p
Double zeta orbitals	4s, 4p, 3d
Radial cut-offs	Determined by energy shift of 0.005 Rydberg

TABLE 5.10: Properties of the default basis set.

5.1.3 Validation of quantum mechanical methodology on known structures

5.1.3.1 Rutile and anatase TiO_2

SIESTA calculations:

As we were mostly interested in the ability of our basis sets to reproduce structural properties – with the ultimate aim of the exploration of physically realistic structures of $TiOSO_4{\cdot}2H_2O$ – the criteria for the testing of basis sets was that of geometry. The SIESTA methodology, as implemented in the SIESTA software package, was used to optimise the internal coordinates from experimental values. These optimised atomic coordinates were then parsed back through SIESTA while the unit cell was allowed to vary in order to give a fully optimised structure. Optimisations were performed with the same calculation tolerances as the basis set optimisations, as previously shown in Table 5.1.

During the course of the project, we thought that there may be benefit in using another exchange-correlation functional, in addition to that of the Perdew-Burke-Ernzerhof (PBE) functional, namely the Armiento and Mattsson 2005 (AM05) functional [105]. This functional has been shown to calculate unit cell values much closer to experimental values than the PBE functional [169] as well as offering better calculations for water molecules [170], which was an attractive property given our planned simulation of the titanyl sulphate hydrate series. The calculations with the various basis sets were therefore repeated with this new functional.

With rutile having been the model for the optimisation of the 'manual' and 'simplex' basis sets, it was important to test the accuracy and the transferability of the basis set by running structural optimisations of both rutile and another model structure. This additional model structure was chosen to be the anatase polymorph of TiO_2. Figure 5.5 shows the structures of rutile and anatase TiO_2.

In both polymorphs, each titanium atom is octahedrally coordinated by oxygen atoms. Bond lengths vary according to position, with equatorial Ti-O bonds being slightly shorter in both polymorphs: rutile has a range of 1.95 Å to 1.98 Å, and anatase 1.93 Å to 1.98 Å. Optimisations were performed starting from the experimental unit cell determined by Burdett *et al.* [171].

Table 5.11 presents the optimised structural parameters calculated using different pseudopotentials and basis sets for both the rutile and anatase polymorphs of TiO_2. During the production of this table, some insights were gained into the basis set

Basis/Pseudopotential	**a** (Å)	**c** (Å)	$\frac{\mathbf{c}}{\mathbf{a}}$	**Volume** (Å^3)
Rutile				
Manual/PBE-SC	4.5502 (-0.80)	2.9428 (-0.38)	0.647 (0.427)	60.93 (-1.97)
Manual/PBE-LC	4.6982 (2.42)	3.0880 (4.54)	0.657 (2.062)	68.16 (9.67)
Simplex/PBE-SC	4.6285 (0.91)	2.9635 (0.32)	0.640 (-0.578)	63.49 (2.14)
Simplex/PBE-LC	4.6180 (0.68)	2.9885 (1.17)	0.647 (0.489)	63.73 (2.54)
Literature/PBE-SC	4.6402 (1.16)	2.9715 (0.59)	0.640 (-0.561)	63.98 (2.94)
Default(polar P)/PBE-SC	4.6270 (0.87)	2.9605 (0.22)	0.640 (-0.646)	63.38 (1.97)
Default(polar E)/PBE-SC	4.6377 (1.11)	2.9593 (0.18)	0.638 (-0.916)	63.65 (2.41)
Manual/AM05-SC	4.5539 (-0.72)	2.9269 (-0.92)	0.643 (-0.197)	60.70 (-2.34)
Manual/AM05-LC	4.7177 (2.85)	3.0717 (3.98)	0.651 (1.104)	68.37 (10.00)
Simplex/AM05-SC	4.6018 (0.32)	2.9759 (0.74)	0.647 (0.417)	63.02 (1.39)
Simplex/AM05-LC	4.5946 (0.17)	2.9425 -0.39)	0.640 (-0.554)	62.30 (0.24)
Literature/AM05-SC	4.6019 (0.33)	2.9565 (0.08)	0.642 (-0.239)	62.61 (0.74)
Default(polar P)/AM05-SC	4.5856 (-0.03)	2.9283 (-0.87)	0.639 (-0.840)	61.58 (-0.93)
Default(polar E)/AM05-SC	4.5911 (0.09)	2.9324 (-0.73)	0.639 (-0.820)	61.81 (-0.55)
Experimental (Neutron @ 15K) [171]	4.587	2.954	0.644	62.15
Anatase				
Manual/PBE-SC	3.7758 (-0.16)	9.2975 (-2.15)	2.462 (-1.992)	132.55 (-2.47)
Manual/PBE-LC	3.9147 (3.51)	9.8122 (3.26)	2.507 (-0.236)	150.37 (10.64)
Simplex/PBE-SC	3.7927 (0.28)	9.6666 (1.73)	2.549 (1.445)	139.05 (2.31)
Simplex/PBE-LC	3.8088 (0.71)	9.6661 (1.73)	2.538 (1.011)	140.22 (3.17)
Literature/PBE-SC	3.7775 (-0.12)	9.8562 (3.73)	2.609 (3.851)	140.64 (3.48)
Default(polar P)/PBE-SC	3.8030 (0.56)	9.5490 (0.49)	2.511 (-0.060)	138.11 (1.62)
Default(polar E)/PBE-SC	3.8238 (1.11)	9.4623 (-0.42)	2.475 (-1.506)	138.35 (1.80)
Manual/AM05-SC	3.7607 (-0.56)	9.3888 (-1.19)	2.497 (-0.632)	132.79 -2.30)
Manual/AM05-LC	3.8764 (2.50)	10.0002 (5.24)	2.580 (2.680)	150.27 (10.56)
Simplex/AM05-SC	3.7956 (0.36)	9.6639 (1.70)	2.546 (1.339)	139.22 (2.44)
Simplex/AM05-LC	3.7714 (-0.28)	9.5816 (0.84)	2.541 (1.121)	136.28 (0.27)
Literature/AM05-SC	3.7548 (-0.72)	9.8194 (3.34)	2.615 (4.089)	138.44 (1.86)
Default(polar P)/AM05-SC	3.7716 (-0.28)	9.4977 (-0.05)	2.518 (0.230)	135.10 (-0.59)
Default(polar E)/AM05-SC	3.7778 (-0.11)	9.4639 (-0.40)	2.505 (-0.290)	135.06 (-0.62)
Experimental (Neutron @ 15K) [171]	3.782	9.502	2.512	135.91

TABLE 5.11: The optimised structural parameters of rutile and anatase computed using the SIESTA methodology. Numbers in parentheses indicate the percent deviation from experiment.

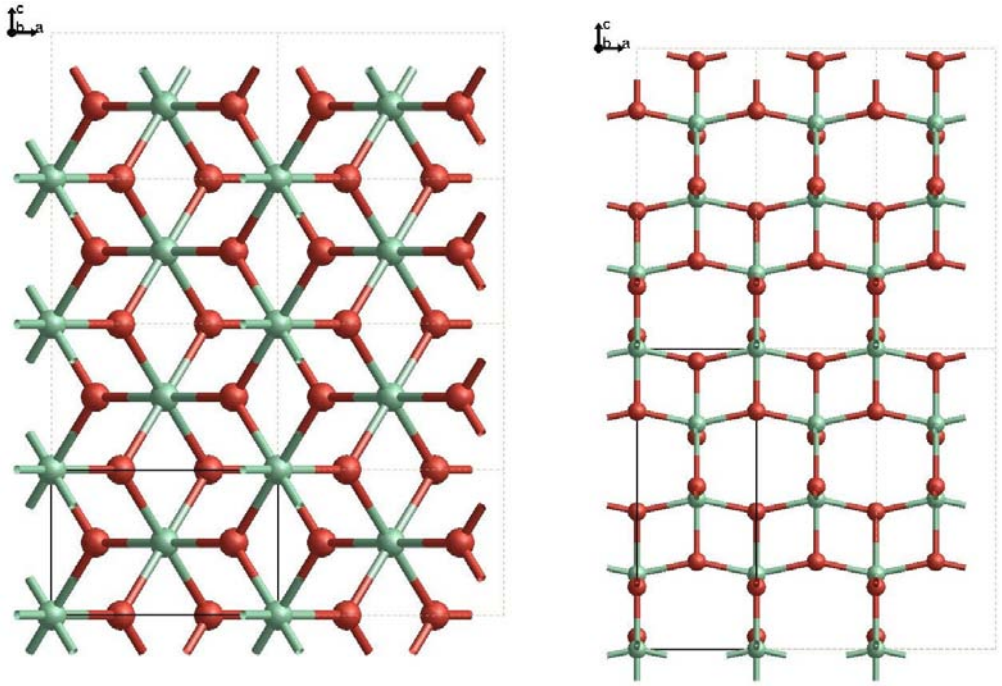

FIGURE 5.5: The rutile (left) and anatase (right) polymorphs of TiO_2. Titanium atoms are green and oxygen atoms are red.

construction process. The explicit inclusion of the 3s semi-core orbital in the pseudopotential valence was demonstrated to be important, as can be seen by the results given by the PBE-LC and AM05-LC pseudopotentials. These large core pseudopotentials did not feature the 3s orbital in the pseudopotential or the basis set, and as a direct result of this the optimised unit cell parameters can not be considered accurate. Only the simplex and manual basis sets were run with the large core variant; after seeing the results from these runs, it was obvious that further calculation using large core pseudopotentials would be of no value due to the level of imprecision.

Another important inclusion was that of polarisation functions, which can be achieved in one of two ways in SIESTA. The first is *via* the perturbative method, in which SIESTA automatically takes the highest occupied orbital and computes the orbital that is one angular momentum state higher. This new orbital is then given the same radial cut-off as the highest occupied orbital. The other way is explicit, with control over the size and shape given by adjustment of its radial cut-off, number of zetas, and the soft confinement parameters, r_i, and v_0. During our calculations, it became apparent that there was a significant difference between results when using the two methods of defining a polarisation function. To show this difference, the structure optimisations using the default basis set were run using a titanium basis set that included the 4f atomic orbital using the perturbative method, and another using an explicit definition. These are

labelled 'polar P' and 'polar E' respectively. The calculations made using the literature basis set are the only ones not to include a 4f polarisation orbital for titanium.

While energies of structures optimised using different exchange-correlation functionals cannot be compared, there exists a general relationship between the PBE and AM05 results. As discussed earlier, the AM05 functional has been found to yield unit cells that agree more closely with experiment values, while the PBE functional has been found to give the unit cell parameters that are approximately 1% larger than experiment. It should be stressed that these are empirical relationships only, and a wide range of behaviours have been found using these functionals, as shown in Table 5.12 which reports values from previous literature. However, following this expected behaviour it can be seen that the 'simplex' and 'general (polar E)' small-core basis sets gave the most promising results, showing the expected 1% overestimation in the a unit cell parameter and echoing previous literature (such as that of Labat's PBE calculations in VASP [172]) by showing an approximately 0.5% overestimation in the c unit cell parameter for rutile. The results for anatase can also be seen to follow trends shown by previous literature.

After seeing the variability in the lattice parameters using the single zeta polarised and double zeta polarised basis sets, it was thought useful to try increasing the basis set complexity to triple zeta double polarised (TZDP) and quadruple zeta triple polarised (QZTP) to observe the effect on the calculation of lattice parameters and energy. Despite the simplex optimised basis set having given the best energy, the default basis set was chosen to be used for these experiments. This was due to the fact that for the simplex basis set, variationally optimising the parameters of a triple and quadruple zeta basis set would be computationally expensive as a result of the simplex routine's inability to use multiple processors. In contrast the default basis set could have the extra zetas added then optimised by varying one parameter, the split-norm.

All calculations were performed with the PBE XC functional and a small-core pseudopotential; the polarised orbitals were defined explicitly.

As can be seen from the results in Table 5.13, the addition of extra zetas to the basis sets did not result in any significant improvement in the estimation of unit cell parameters. While the a unit cell parameter is consistently 1% larger than experiment as expected, the c unit cell parameter varies and does not seem to approach the typical 1% overestimation with increased basis set complexity.

A secondary criterion for the appraisal of basis sets is the estimation of phase stability, i.e. the correct prediction of which phase is more stable. Previous DFT calculations in the literature have shown a relationship contrary to experimental results, predicting anatase as being more thermodynamically stable than rutile [173], when it is has been

Reference	**a** (Å)	**c** (Å)	$\frac{\mathbf{c}}{\mathbf{a}}$	**Volume** (Å^3)
Rutile				
Labat Crystal LDA 'Ti*-O*' [172]	4.5550 (-0.83)	2.9290 (-0.98)	0.643 (-0.15)	60.77 (-2.61)
Labat Crystal PBE 'Ti*-O*' [172]	4.6530 (1.31)	2.9750 (0.57)	0.639 (-0.72)	64.41 (3.22)
Labat VASP (PAW) LDA [172]	4.5570 (-0.78)	2.9280 (-1.01)	0.643 (-0.23)	60.80 (-2.56)
Labat VASP (PAW) PBE [172]	4.6470 (1.18)	2.9740 (0.54)	0.640 (-0.62)	64.22 (2.92)
Muscat LCAO LDA TVAE** [173]	4.5480 (-0.98)	2.9440 (-0.47)	0.647 (0.52)	60.89 (-2.41)
Muscat LCAO GGA TVAE** [173]	4.6230 (0.65)	2.9870 (0.98)	0.646 (0.33)	63.84 (2.30)
Muscat SC PW LDA 380 [173]	4.5620 (-0.67)	2.9200 (-1.28)	0.640 (-0.61)	60.77 (-2.61)
Muscat SC PW GGA 380 [173]	4.6410 (1.05)	2.9580 (0.00)	0.637 (-1.03)	63.71 (2.10)
Anatase				
Labat Crystal LDA 'Ti*-O*' [172]	3.7350 (-1.43)	9.5800 (0.61)	2.565 (2.09)	133.64 (-2.24)
Labat Crystal PBE 'Ti*-O*' [172]	3.7860 (-0.08)	9.8670 (3.62)	2.606 (3.73)	141.43 (3.46)
Labat VASP (PAW) LDA [172]	3.7480 (-1.08)	9.4950 (-0.28)	2.533 (0.83)	133.38 (-2.43)
Labat VASP (PAW) PBE [172]	3.8020 (0.34)	9.7740 (2.65)	2.571 (2.32)	141.29 (3.35)
Muscat LCAO LDA TVAE** [173]	3.7290 (-1.58)	9.6950 (1.82)	2.600 (3.48)	134.81 (-1.38)
Muscat LCAO GGA TVAE** [173]	3.8010 (0.32)	9.7179 (2.06)	2.557 (1.76)	140.40 (2.70)
Muscat SC PW LDA 380 [173]	3.7460 (-1.13)	9.4800 (-0.44)	2.531 (0.73)	133.03 (-2.69)
Muscat SC PW GGA 380 [173]	3.7770 (-0.32)	9.8180 (3.11)	2.599 (3.46)	140.06 (2.46)

TABLE 5.12: Optimised structural parameters of rutile and anatase gathered from various literature sources. Numbers in parentheses indicate the percent deviation from experiment. '380' refers to the plane wave cut-off (in eV) used in the calculations.

Functional/basis	**Split-norm**	**a** (Å)	**c** (Å)	$\frac{\mathbf{c}}{\mathbf{a}}$	**Volume** (Å^3)
Rutile					
PBE/DZP	0.15	4.6377 (1.11)	2.9593 (0.18)	0.638 (-0.92)	63.65 (2.41)
PBE/TZDP	0.05	4.6346 (1.04)	2.9628 (0.30)	0.639 (-0.73)	63.64 (2.39)
PBE/TZDP	0.10	4.6301 (0.94)	2.9671 (0.44)	0.641 (-0.50)	63.61 (2.34)
PBE/TZDP	0.15	4.6308 (0.95)	2.9608 (0.23)	0.639 (-0.72)	63.49 (2.15)
PBE/TZDP	0.20	4.6308 (0.95)	2.9597 (0.19)	0.639 (-0.76)	63.47 (2.12)
PBE/QZTP	0.15	4.6375 (1.10)	2.9626 (0.29)	0.639 (-0.80)	63.71 (2.51)
AM05/TZDP	0.15	4.5900 (0.07)	2.9336 (-0.69)	0.639 (-0.76)	61.81 (-0.56)
AM05/QZTP	0.15	4.5912 (0.09)	2.9360 (-0.61)	0.639 (-0.70)	61.89 (-0.43)
Anatase					
PBE/DZP	0.15	3.8238 (1.11)	9.4623 (-0.42)	2.475 (-1.51)	138.35 (1.80)
PBE/TZDP	0.05	3.8120 (0.79)	9.5578 (0.59)	2.507 (-0.20)	138.89 (2.19)
PBE/TZDP	0.10	3.8042 (0.59)	9.5535 (0.54)	2.511 (-0.05)	138.26 (1.73)
PBE/TZDP	0.15	3.8080 (0.69)	9.5324 (0.32)	2.503 (-0.37)	138.23 (1.71)
PBE/TZDP	0.20	3.8070 (0.66)	9.5365 (0.36)	2.505 (-0.30)	138.22 (1.70)
PBE/QZTP	0.15	3.8031 (0.56)	9.5593 (0.60)	2.514 (0.05)	138.26 (1.73)
AM05/TZDP	0.15	3.7723 (-0.26)	9.4975 (-0.05)	2.518 (0.21)	135.15 (-0.56)
AM05/QZTP	0.15	3.7780 (-0.11)	9.4948 (-0.08)	2.513 (0.03)	135.52 (-0.29)

TABLE 5.13: The optimised structural parameters of rutile and anatase computed using larger basis sets. Numbers in parentheses indicate the percentage deviation from experiment.

experimentally shown that rutile is more stable than anatase by approximately 2.61 kJ/mol [174]. Moreover, the choice of XC functional has been shown to be very influential on phase stabilities [175]. These dependencies are evident in Table 5.14, which shows a range of ΔU from 1.51 kJ/mol using the AM05 functional and the default basis set, to 5.18 kJ/mol using the AM05 functional and the simplex basis set. All calculations showed the anatase phase to be more stable than the rutile phase, contrary to experiment [176]. This is relatively common in the literature, with Muscat *et al.* having made the comment that the relative phase stability of rutile and anatase is '...very sensitive to the numerical approximations and to the treatment of exchange and correlation adopted.' [173]

Calculation method	ΔU (kJ/mol)
PBE/Literature	1.55
PBE/Simplex	4.07
PBE/Default (polar P)	4.62
PBE/Default (polar E)	2.21
PBE/Default TZDP/Split-norm 0.15	4.50
PBE/Default QZTP/Split-norm 0.15	4.90
AM05/Literature	2.72
AM05/Simplex	5.18
AM05/Default (polar P)	2.49
AM05/Default (polar E)	1.51
AM05/Default TZDP/Split-norm 0.15	4.82
AM05/Default QZTP/Split-norm 0.15	5.12

TABLE 5.14: Calculated energy differences ($\Delta U = U_{rutile} - U_{anatase}$) between rutile and anatase as a function of basis set and exchange-correlation functional.

The main conclusions from the SIESTA calculations on rutile and anatase are summarised in the points below:

- The best calculations, as determined by the lowest final energy per formula unit for a given exchange-correlation functional, were those using the simplex optimised basis set. The computed structural parameters using this basis set and the small core pseudopotential were within 0.91% of experimental data for rutile, and 1.73% for anatase. These results compare favourably to similar calculations previously reported in the literature.
- For the rutile calculations our results followed a trend of overestimation of the unit cell parameters; the overestimation was present to a lesser degree for the c parameter than the a parameter.

- For the anatase calculations our results did not seem to follow a trend, with some basis sets overestimating c more than a, some overestimating a more than c, and still others underestimating both to various degrees.

- The expected trend between PBE and AM05 functionals was present, with all structural parameters being calculated to be larger with the PBE functional than with the AM05 functional; the only exceptions were the a parameter for the manual basis set in rutile, and the c parameter for the manual and general (polar E) basis sets in anatase.

- The calculations for the anatase polymorph proved to be much less accurate than that of rutile, with variations of up to 3.73% in the structural parameters calculated using small core pseudopotentials, compared to a maximum of 1.16% in the rutile polymorph.

- It is interesting to note that the web basis set offers some of the better quality results despite the 4f polarisation orbital being absent. This might suggest that the 4p orbital plays a greater role in describing the interactions between atoms than the 4f orbital, or there may merely be a fortunate cancellation of errors.

- The TZDP and QZTP calculations did not show any particularly large improvement over the DZP calculations in terms of unit cell parameter estimation, however there were improvements in energies.

- The large variation in the results indicate a strong basis dependence for the structures of both rutile and anatase, and features such as polarisation orbitals on oxygen, and the inclusion of semi-core orbitals for titanium must be considered for there to be any meaning to the results.

As a result of this last point – a strong variability of results depending on the basis set used – it was decided that the modelling of both rutile and anatase polymorphs through the use of a plane-wave methodology would be useful as a method of validation. The implementation of the plane-wave method used by the PWscf code within the QUANTUM-Espresso software package [177] was chosen as appropriate for the present work. Its use in simulating the rutile polymorph has already been documented [178]. The practical method of calculation is similar to the SIESTA software suite, with the exception that the basis sets do not need to be explicitly defined. Instead, a plane-wave cut-off is employed and systematically increased to ensure that the basis set is converged. As will be shown, our convergence tests showed that a plane-wave cut-off of approximately 56 Rydberg was adequate. Both Perdew-Burke-Ernzerhof (PBE)[113] and Perdew-Wang 91 (PW91) [106] exchange-correlation functionals were used with

their corresponding ultrasoft pseudopotentials, obtained from the standard library of pseudopotentials included in the software. The titanium pseudopotential included 3s and 3p semi-core atomic orbitals in the valence. The results from these calculations are shown in Table 5.15.

Functional/cut-off	**a** (Å)	**c** (Å)	**Volume** (Å^3)	**Energy/f.u.** (eV)
Rutile				
PBE/46 Ryd	4.5985 (0.25)	2.9612 (0.24)	62.62 (0.75)	-1643.5492
PBE/56 Ryd	4.6012 (0.31)	2.9629 (0.30)	62.73 (0.92)	-1643.6050
PBE/66 Ryd	4.6028 (0.34)	2.9637 (0.33)	62.79 (0.25)	-1643.6095
PW91/56 Ryd	4.6008 (0.30)	2.9628 (0.30)	62.71 (0.90)	-1648.6065
Anatase				
PBE/46 Ryd	3.7858 (0.10)	9.5189 (0.18)	136.43 (0.38)	-1643.6136
PBE/56 Ryd	3.7865 (0.12)	9.5206 (0.20)	136.50 (0.43)	-1643.6730
PBE/66 Ryd	3.7871 (0.14)	9.5222 (0.21)	136.57 (0.48)	-1643.6776
PW91/56 Ryd	3.7864 (0.12)	9.5208 (0.20)	136.50 (0.43)	-1648.6672

TABLE 5.15: The optimised structural parameters of rutile and anatase computed using the PWscf code. Numbers in parentheses indicate the percentage deviation from experiment.

Again, these results fail to show the 1% overestimation of unit cell parameters that is expected with GGA/PBE calculations. The results are very consistent over the two functionals, which is in contrast to the plane wave calculations from the literature previously shown in Table 5.12, where the estimation of unit cells ranges widely over different calculations.

Calculation method	ΔU (kJ/mol)
PBE/PW cut-off 46 Ryd	6.21
PBE/PW cut-off 56 Ryd	6.56
PBE/PW cut-off 66 Ryd	6.56
PW91/PW cut-off 56 Ryd	5.86

TABLE 5.16: Calculated energy difference ($\Delta U = U_{rutile} - U_{anatase}$) between rutile and anatase.

While the results obtained by SIESTA and PWscf were slightly different from each other, this inconsistency is somewhat expected given the strong dependence on basis set optimisation and exchange correlation functional. The literature seems to support this idea, with results from different DFT codes, pseudopotentials, and exchange correlation functionals leading to vastly different results (as shown previously in Figure 5.12). Similarly, the relative energies of the two phases are consistent with literature results, with the anatase phase given as the more stable in all calculations. This general agreement with literature results meant that we could move forward into further tests to investigate the transferability of the basis sets using the $TiOSO_4$ and $TiOSO_4{\cdot}H_2O$

structures. It was anticipated that these calculations would not be as straightforward as the TiO_2 calculations, given their increased complexity and that their calculation using DFT would be a first.

5.1.3.2 $TiOSO_4$ and $TiOSO_4 \cdot H_2O$

Following on from the validation of pseudopotentials and basis sets using the structures of rutile and anatase TiO_2, the next step was to use a more complex system to test their transferability. The most obvious choice for this were the two other members of the titanyl sulphate series, $TiOSO_4$ and $TiOSO_4 \cdot H_2O$. The simplex and default basis sets performed best in the TiO_2 studies, and so these were chosen to be used in the SIESTA calculations on $TiOSO_4$. The parameters for the PWscf calculations were kept consistent with those used for TiO_2. Again, optimisations were performed starting from the experimental unit cell given by Ahmed *et al.* [15] for the case of $TiOSO_4$, and Gatehouse *et al.* [13] for the case of $TiOSO_4 \cdot H_2O$. Table 5.17 shows the results with percentage deviation from experiment in brackets.

From these results, we can see that there is a general trend of overestimation in the SIESTA results. This overestimation is quite a lot higher than would be expected for both of the XC functionals, although the previously mentioned empirical relationship between the PBE and AM05 functionals can be seen throughout the results. Increasing the basis set size from DZP to QZTP results in better energy values, and it can be seen that there is a large change in unit cell parameters when using the QZTP basis set. This change was interpreted as meaning that a lack of geometry convergence was occurring with insufficient basis set size. In light of this, new calculations starting from the optimised QZTP atomic coordinates and unit cell were computed for each of the basis sets, to ensure that they had converged sufficiently. The results from this new set of calculations are shown in Table 5.18. These calculations resulted in a much better energy convergence for all basis set sizes, confirming the QZTP structure as having been a more stable one.

In contrast, the PWscf results are considered closer to experiment than would be expected. All unit cell lengths are within 0.07% of the experimental values, where an overestimation of approximately 1% due to the PBE functional is expected. Increasing the plane wave cut-off from 46 to 76 Rydberg did not see any appreciable change in results. Despite the difference between the calculated and expected values of the calculations, it was thought that the results were not unreasonable as their variance is comparable to that of the TiO_2 literature results. Consideration must also be given to the fact that some temperature effects are present in the experimental results that

Calculation	a (Å)	b (Å)	c (Å)	**Volume** (Å^3)	**Energy** (eV)
$TiOSO_4$					
Simplex/PBE	11.2326 (2.55)	5.2889 (2.66)	6.6533 (3.54)	395.26 (9.00)	-16192.9669
Default/PBE DZP	11.1883 (2.15)	5.2753 (2.39)	6.5974 (2.67)	389.39 (7.38)	-16188.0539
Default/PBE TZDP	11.1747 (2.02)	5.2849 (2.58)	6.6078 (2.83)	390.23 (7.62)	-16193.2095
Default/PBE QZDP	11.1755 (2.03)	5.2861 (2.60)	6.6134 (2.92)	390.69 (7.74)	-16194.9910
Simplex/AM05	11.1768 (2.04)	5.2760 (2.41)	6.6288 (3.16)	390.89 (7.80)	-16153.7601
Default/AM05 DZP	11.1317 (1.63)	5.2330 (1.93)	6.5755 (2.33)	383.04 (5.63)	-16156.2398
Default/AM05 TZDP	11.1140 (1.47)	5.2457 (1.82)	6.5866 (2.50)	384.01 (5.90)	-16160.7075
Default/AM05 QZTP	11.0140 (0.56)	5.1612 (0.18)	6.4962 (1.09)	369.28 (1.84)	-16162.5516
PWscf/PBE/46 Ryd	10.9602 (0.07)	5.1546 (0.05)	6.4300 (0.06)	363.26 (0.18)	-16209.3837
PWscf/PBE/56 Ryd	10.9570 (0.04)	5.1542 (0.04)	6.4285 (0.04)	363.05 (0.12)	-16204.3102
PWscf/PBE/66 Ryd	10.9587 (0.05)	5.1546 (0.05)	6.4291 (0.05)	363.17 (0.15)	-16210.2803
PWscf/PBE/76 Ryd	10.9581 (0.05)	5.1544 (0.05)	6.4288 (0.04)	363.11 (0.14)	-16210.3797
PWscf/PW91/56 Ryd	10.9583 (0.05)	5.1544 (0.05)	6.4289 (0.04)	363.13 (0.14)	-16250.0498
Experimental[15]	10.953	5.152	6.426	362.62	N/A

TABLE 5.17: The optimised structural parameters of $TiOSO_4$ computed using the SIESTA and PWscf codes. Numbers in parentheses indicate the percentage deviation from experiment.

Calculation	a (Å)	b (Å)	c (Å)	**Volume** (Å^3)	**Energy** (eV)
$TiOSO_4$					
Simplex/PBE	11.2083 (2.33)	5.2723 (2.33)	6.6325 (3.21)	391.94 (8.08)	-16192.9678
Default/PBE DZP	11.0125 (0.54)	5.1494 (-0.05)	6.4796 (0.83)	367.44 (1.33)	-16188.4597
Default/PBE TZDP	11.0442 (0.83)	5.1641 (0.23)	6.5121 (1.34)	371.41 (2.42)	-16193.5460
Default/PBE QZTP	11.0481 (0.87)	5.1680 (0.31)	6.5214 (1.48)	372.35 (2.68)	-16195.3243
Simplex/AM05	11.1255 (1.58)	5.2240 (1.40)	6.5720 (2.27)	381.96 (5.34)	-16159.7734
Default/AM05 DZP	11.0041 (0.47)	5.1309 (-0.98)	6.4673 (0.64)	365.15 (0.70)	-16156.5704
Default/AM05 TZDP	11.0066 (0.49)	5.1549 (0.06)	6.4897 (0.99)	368.21 (1.54)	-16160.9804
Experimental[15]	10.953	5.152	6.426	362.62	N/A

TABLE 5.18: The optimised structural parameters of $TiOSO_4$ computed using the SIESTA code, starting from the optimised QZTP atomic coordinates and unit cell. Numbers in parentheses indicate the percentage deviation from experiment.

are not in the theoretical calculations. Unfortunately, among the literature detailing the experimental determination of the structures of $TiOSO_4$ and $TiOSO_4{\cdot}H_2O$, no temperature dependent studies were performed. Thus there are no thermal expansion coefficients available to determine the effect of temperature on unit cell parameters.

Following on from the $TiOSO_4$ results, the $TiOSO_4{\cdot}H_2O$ calculations proved less reliable. Table 5.19 shows the calculated unit cell parameters and energies using both SIESTA and PWscf codes. There is a very obvious overbinding present in the series of default basis set calculations which is not readily explainable. The simplex basis set fares better, providing unit cell parameters of similar deviation to that of the $TiOSO_4$ results when used with the PBE XC functional, although the AM05 XC functional is seen to underbind a lot more than is expected.

Ultimately these results show the care that must be taken in preparing basis sets and pseudopotentials that will be transferable across multiple structures and systems. While there was no clear best combination of pseudopotential and basis set that was useful across all three TiO_2, $TiOSO_4$, and $TiOSO_4{\cdot}H_2O$ structures, the default basis set provides the easiest way to improve the precision of the calculation by the addition of extra zetas, and provides lower energies with these enlarged basis sizes.

5.2 Development of a hypothetical structure of $TiOSO_4{\cdot}2H_2O$

In parallel to experimental investigations using powder X-ray diffraction, attempts were made at developing a hypothetical structure of $TiOSO_4{\cdot}2H_2O$ through alternate means. These alternate means took the form of extrapolation from analogous structures, and the use of molecular dynamics as an investigative tool. The results from these attempts will be described in the following sections.

5.2.1 Forcefield simulations

5.2.1.1 The General Utility Lattice Program

In this project, the General Utility Lattice Program (GULP) [179–181] was used to fit potential models to empirical data and perform structure optimisations by energy minimisation. It uses the Newton-Raphson method to find local minima in the potential energy surface, and a choice of genetic algorithms or simulated annealing in order to ensure that a global energy minimum is reached [182].

Calculation	a (Å)	b (Å)	c (Å)	**Volume** (Å^3)	**Energy** (eV)
$TiOSO_4{\cdot}H_2O$					
Simplex/PBE	10.0961 (2.83)	5.1539 (0.41)	8.7703 (1.81)	456.3538 (5.12)	-18067.7581
Default/PBE DZP	9.0794 (-7.52)	4.8303 (-5.90)	8.3104 (-3.52)	364.4669 (-16.04)	-18043.1674
Default/PBE TZDP	9.2917 (-5.36)	4.9216 (-4.12)	8.3821 (-2.69)	383.3175 (-11.70)	-18058.3544
Default/PBE QZTP	9.3332 (-4.94)	4.9194 (-4.16)	8.3702 (-2.83)	384.3062 (-11.47)	-18059.3533
Simplex/AM05	10.0941 (2.81)	5.2256 (1.80)	8.9595 (4.01)	472.5893 (8.86)	-16051.7567
Default/AM05 DZP	9.2485 (-5.80)	5.1412 (0.16)	8.6231 (0.11)	410.0124 (-5.55)	-16022.4509
Default/AM05 TZDP	9.2992 (-5.28)	5.1221 (-0.21)	8.7255 (1.29)	415.6091 (-4.26)	-16029.5103
Default/AM05 QZTP	–	–	–	–	–
PWscf/PBE/25 Ryd	9.8152 (-0.03)	5.1314 (-0.03)	8.6118 (-0.03)	434.1094 (0.00)	-1329.0224
PWscf/PW91/25 Ryd	9.8152 (-0.03)	5.1314 (-0.03)	8.6118 (-0.03)	433.7328 (-0.09)	-1332.2258
Experimental[13]	9.8180	5.133	8.6140	434.11	-

TABLE 5.19: The optimised structural parameters of $TiOSO_4{\cdot}H_2O$ computed using the SIESTA and PWscf codes. Numbers in parentheses indicate the percentage deviation from experiment. The 'General/AM05 QZTP' simulation could not be made to converge.

5.2.1.2 Methodology

As mentioned previously, all optimisations and molecular dynamics calculations were performed using the General Utility Lattice Program (GULP) [180]. Before these could be run, the forcefields governing the interactions of atoms needed to be parameterized for input into GULP. This parameterisation was performed by Prof. Julian Gale, and involved fitting the parameters to model structures which, in this case, were $TiOSO_4$ and $TiOSO_4{\cdot}H_2O$. The full input file is available in Appendix A.7. The motivation behind using forcefield calculations was that any hypothetical $TiOSO_4{\cdot}2H_2O$ structure proposed would likely have a number of conformational polymorphs, and having a forcefield method available to quickly explore these conformations would allow us to identify which of them were the most energetically favourable and focus our attention on those.

Trial calculations were run on $TiOSO_4$ and $TiOSO_4{\cdot}H_2O$. The final unit cell of $TiOSO_4$ was a = 11.09 (1.33) Å, b = 5.34 (3.67) Å, and c = 6.61 (2.88) Å, with an energy of -28.76 eV per formula unit, where the numbers in brackets are the percentage deviations from the experimental structure [15]. The final unit cell of $TiOSO_4{\cdot}H_2O$ was calculated to be a = 10.67 (8.72) Å, b = 5.33 (3.85) Å, and c = 8.58 (-0.35) Å, with an energy of -29.01 eV per formula unit. Again, the numbers in brackets are percentage deviations from the experimental structure [13]. These results were considered of sufficient quality to proceed with the exploration of candidate structures of $TiOSO_4{\cdot}2H_2O$ given that the cell can ultimately be refined through the use of diffraction data.

5.2.1.3 Extrapolation from titanyl sulphate series

When approaching the task of proposing hypothetical structures, the initial step was to inspect the structural transition between $TiOSO_4$ and $TiOSO_4{\cdot}H_2O$ and apply these changes to the addition of the extra water molecule. This transition can be simply described as replacing one cross-linking sulphate oxygen of the titanium octahedra with a water molecule. Performing this manipulation once more to the $TiOSO_4{\cdot}H_2O$ structure led to the structure shown in Figure 5.6. It can be described as separated chains of titanium octahedra whose links are composed of bridging oxygens and sulphate molecules, with the remaining two coordination sites occupied by the water molecules which provide hydrogen bonding between chains.

There is some credibility given to this structure by the nature of $TiOSO_4{\cdot}2H_2O$ itself, in that the needle-like fibres could be explained by the long chains, and the tendency to break down into bundles of such fibres could be indicative of the weakness of the

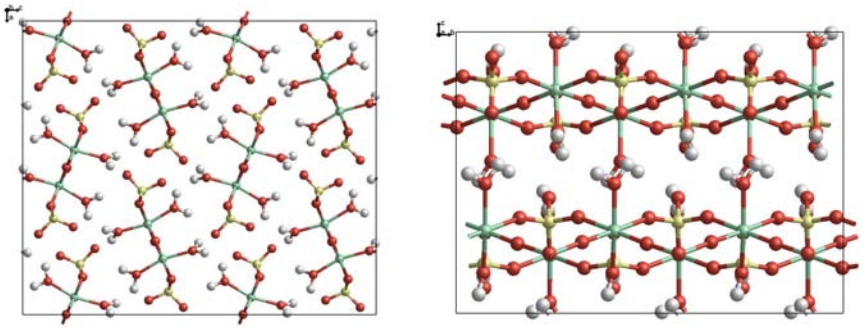

FIGURE 5.6: Hypothetical titanyl sulphate dihydrate structure viewed (left) down the chains of titanium octahedra, and (right) across the chains of titanium octahedra. Titanium atoms are shown in green, sulphur in yellow, oxygen in red, and hydrogen in white.

hydrogen bonds holding the chains together. It could also be imagined that upon heating, the removal of the water molecules might cause random cross-linkages between chains, resulting in the amorphous anhydrate structure mentioned previously. While this hypothetical dihydrate was developed without knowledge of the unit cell that would become evident from the indexing of the synchrotron data (which will be shown in section 6.1), once this unit cell became known it was possible to transfer the structure into it. However, the size of the unit cell and the different ways the chains could be placed inside it led to some configurational ambiguity. The separate nature of the chains meant that variations in orientation between them could be made and different structures produced. These are shown in Figure 5.7.

Only 8 formula units of $TiOSO_4{\cdot}2H_2O$ could be made to fit into the experimental unit cell, meaning that the density was quite low in each of the structures. Once these various configurational polymorphs had been constructed, they were run through forcefield optimisation. The results from this are shown in Table 5.20 below.

Configuration	*a* (Å)	*b* (Å)	*c* (Å)	*Energy per F.U.* (eV)
a)	5.33 (-3.87)	16.21 (-2.80)	16.24 (-12.98)	-29.30
b)	3.31 (-4.18)	14.52 (-12.93)	19.09 (2.25)	-29.33
c)	5.32 (-3.96)	14.35 (-13.98)	18.84 (0.93)	-29.36
d)	5.33 (-3.77)	14.12 (-15.44)	18.69 (0.14)	-29.21
Indexed unit cell	5.54	16.68	18.67	–

TABLE 5.20: Forcefield optimised unit cell parameters and energies per formula unit for various hypothetical polymorphs of $TiOSO_4{\cdot}2H_2O$. Numbers in parentheses indicate the percentage deviation from the indexed unit cell.

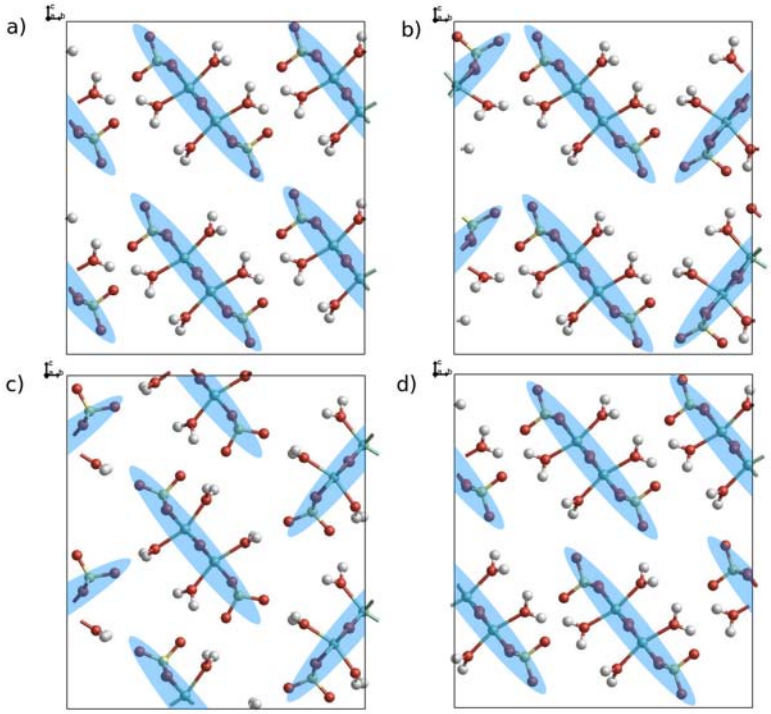

FIGURE 5.7: Variations of the hypothetical $TiOSO_4{\cdot}2H_2O$ structure produced by changing the orientation of the chains. Overlaid blue ellipses are provided to make the variations more apparent. Titanium atoms are shown in green, sulphur in yellow, oxygen in red, and hydrogen in white.

Most of the deviations away from the indexed unit cell appear to come from the aforementioned fact that the hypothetical dihydrate structure, when transferred to the indexed unit cell, had a large amount of vacant space. This meant that the chains had a tendency to compress to occupy this space more efficiently, leading to a significant reduction in the unit cell parameters. With respect to the stabilities of the structures, configuration c) gave the lowest energy.

While there was no conceivable orientation with which additional chains could be made to fit within the indexed unit cell, it was thought that the addition of a water molecules as waters of crystallisation (defined here again as waters contained within the crystal structure but not directly bonded to a metal centre) in the spaces between the chains would prevent the constriction of the unit cell. 1 H_2O molecule was added per formula unit of $TiOSO_4{\cdot}2H_2O$, giving it the new formula of $TiOSO_4{\cdot}3H_2O$. The optimised structure of configuration c) with and without the extra water molecule is shown in Figure 5.8. It can be seen that the extra water molecule per formula unit does stabilise the structure somewhat against contraction (optimised unit cell: a=5.357 Å, b=18.017 Å, c=18.055 Å, β=90.63°).

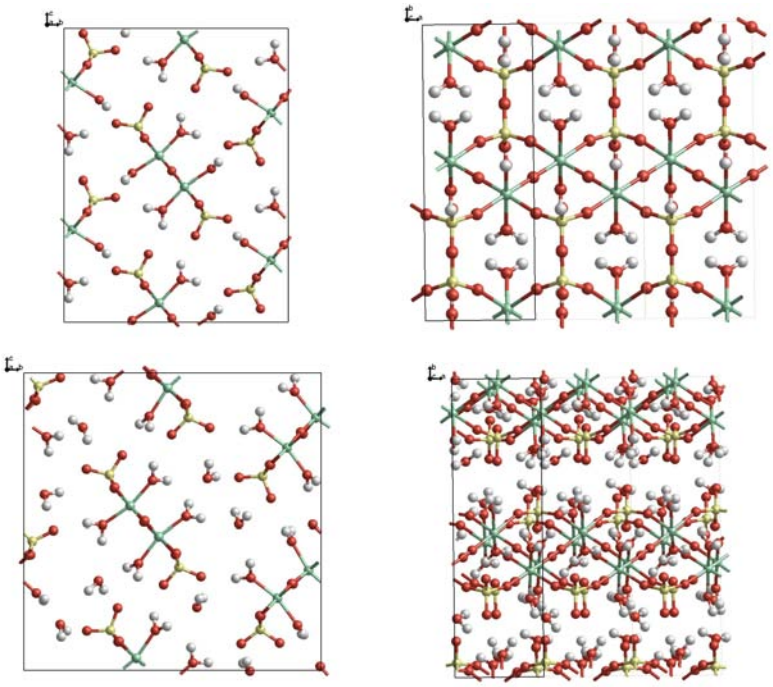

FIGURE 5.8: Optimised structure of configuration c) viewed down the (top left) *a* axis and (top right) *c* axis; optimised structure of configuration c) with extra H_2O molecules viewed down the (bottom left) *a* axis and (bottom right) *c* axis. Titanium atoms are shown in green, sulphur in yellow, oxygen in red, and hydrogen in white.

5.2.1.4 Manipulation of $TiOSO_4{\cdot}H_2O$

After seeing that the hypothetical structure of $TiOSO_4{\cdot}3H_2O$ was able to give a reasonable structure, we returned to the structure of $TiOSO_4{\cdot}H_2O$ in an attempt to explore the addition of water molecules at different sites. As in the creation of the $TiOSO_4{\cdot}3H_2O$ structure, we added one H_2O molecule per formula unit to the monohydrate structure, resulting in an overall formula of a dihydrate, $TiOSO_4{\cdot}2H_2O$. It was found that there were really only two ways that the extra water molecule could be inserted without introducing unphysical bond lengths. These two configurations are shown before and after optimisation in Figure 5.9.

As can be seen in this figure, the two initial configurations resulted in two different ways of incorporating the water molecule into the titanium octahedra. Starting with configuration 2, we can see that the addition of the water molecules has resulted in the replacement of both of the sulphate tetrahedra that bridge between chains, while retaining the bridging tetrahedra down the chains. This results in a very similar structure to that of the initially proposed hypothetical dihydrate shown above in section 5.2.1.3. This is in contrast to configuration 1, in which the sulphate tetrahedra that link the chains of titanium octahedra together have been retained, while the sulphate bridges

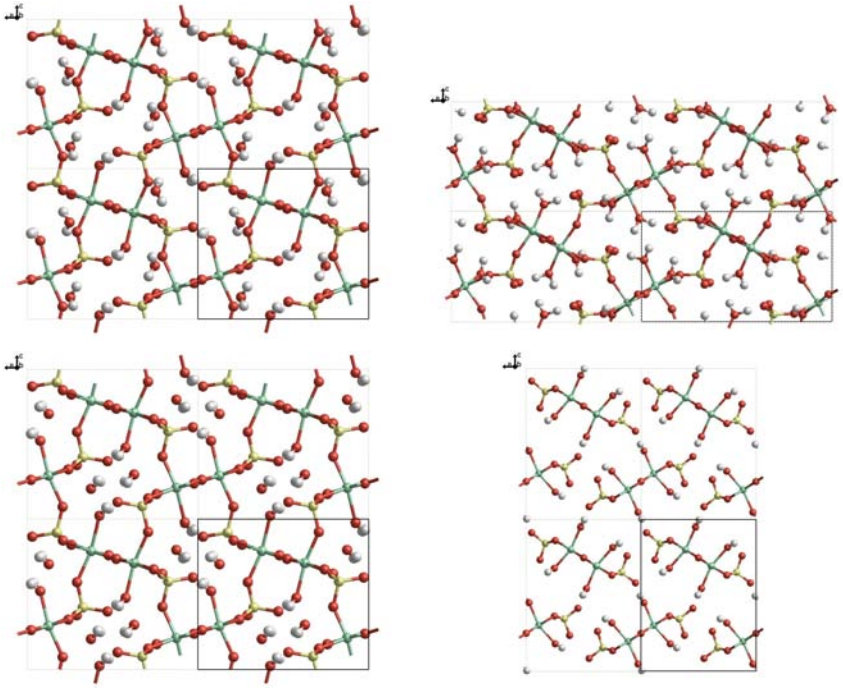

FIGURE 5.9: (top left) Configuration 1 showing the addition of one formula unit of free water molecules to the structure of $TiOSO_4{\cdot}H_2O$ before (top left) and after (top right) forcefield optimisation. Configuration 2 showing the addition of one formula unit of free water molecules to the structure of $TiOSO_4{\cdot}H_2O$ before (bottom left) and after (bottom right) forcefield optimisation. Titanium atoms are shown in green, sulphur in yellow, oxygen in red, and hydrogen in white.

down the chains have been broken, leading to a much more interconnected structure than that of configuration 2. This may explain why this structure is the slightly more energetically stable of the two, as seen in the energies of the structures in Table 5.21.

Configuration	*a* (Å)	*b* (Å)	*c* (Å)	*Energy* (eV)
Configuration 1	13.40 (36.49)	5.76 (12.29)	7.75 (-10.07)	-29.28
Configuration 2	9.46 (-3.62)	5.39 (4.98)	12.47 (44.80)	-29.26
Experimental [13]	9.818	5.130	8.614	–

TABLE 5.21: Forcefield optimised unit cell parameters and energies for the two configurations shown in Figure 5.9. Numbers in parentheses indicate the percentage deviation from the experimentally determined unit cell.

From the simple manipulation of the titanyl sulphate series we have developed two robust, hypothetical structures of $TiOSO_4{\cdot}2H_2O$. The following section will investigate the use of the analogous basic zirconium sulphates in producing more of these candidate structures.

5.2.1.5 Manipulation of basic zirconium sulphates

As mentioned in the introduction, it is often instructive to consider analogous structures when attempting to determine the unknown structure of a material. In our case, the basic zirconyl sulphates were identified as being the closest analogues to the titanyl sulphate hydrates. This is most likely due to their similar chemistry, zirconium sitting as it does directly below titanium in the periodic table. As such, the structures of basic zirconyl sulphates were explored, with the aim being to determine if there were any trends or similarities between the two series that could be used to aid in the determination of the unknown structure of $TiOSO_4{\cdot}2H_2O$. This section will explore the different approaches taken in attempting to determine candidate structures for $TiOSO_4{\cdot}2H_2O$ using basic zirconium sulphate analogues.

The first method used in exploring the relationship between the two series of structures was the manipulation of the basic zirconium sulphate hydrates, such that the zirconium atom was replaced with a titanium one. As zirconium has a higher coordination number than titanium in many of the structures, it was necessary to perform some alterations to the structures to reduce the coordination from 7 or 8, to titanium's 6. In order to do that, the general bonding structure of the basic zirconium sulphates was analysed to identify where bonds could be lost. It was found that in all of the basic zirconium sulphate structures a double hydroxyl bridge exists between zirconium polyhedra, as can be seen in Figures 1.9-1.12.

Our approach to altering the structures was to take this double hydroxyl bridge and remove one water molecule from it, thereby reducing the double hydroxyl bridge to a single bridging oxygen; a feature that is seen in the two known titanyl sulphates. It should be noted that the naming convention for these structures will be to refer to them in the style of the titanyl sulphates, i.e. the structure resulting from the removal of a water molecule and replacement of Zr atoms with Ti atoms in $Zr(OH)_2SO_4{\cdot}3H_2O$, will be referred to as $TiOSO_4{\cdot}3H_2O$.

In addition to simply modifying the basic zirconium sulphates, two more structures were produced by inserting an extra water molecule into the structure resulting from the manipulation of $Zr(OH)_2SO_4{\cdot}H_2O$ and removing one of the water molecules in the structure resulting from the manipulation of $Zr(OH)_2SO_4{\cdot}3H_2O$. Both of these manipulations gave a nominal formula of $TiOSO_4{\cdot}2H_2O$, but for the sake of clarity they will be referred to as $TiOSO_4{\cdot}(1{+}1)H_2O$ and $TiOSO_4{\cdot}(3\text{-}1)H_2O$, respectively, to show their derivations.

Even before we discuss the simulations, there is something interesting to be said about the $TiOSO_4{\cdot}(3\text{-}1)H_2O$ structure. Looking at the view down the chains, there is a marked

similarity between the manipulated structure and the hypothetical dihydrate structure that was first proposed from consideration of the titanyl sulphate series in section 5.2.1.3 and found again in section 5.2.1.4 when adding a water molecule to the $TiOSO_4{\cdot}H_2O$ structure. Given that these structures were constructed completely independently, the similarities are significant. Typical chains of titanium octahedra run down the short axis direction, with each chain being 'capped' by bridging sulphate tetrahedra and only interacting with other chains *via* hydrogen bonding between water molecules and end sulphate oxygens.

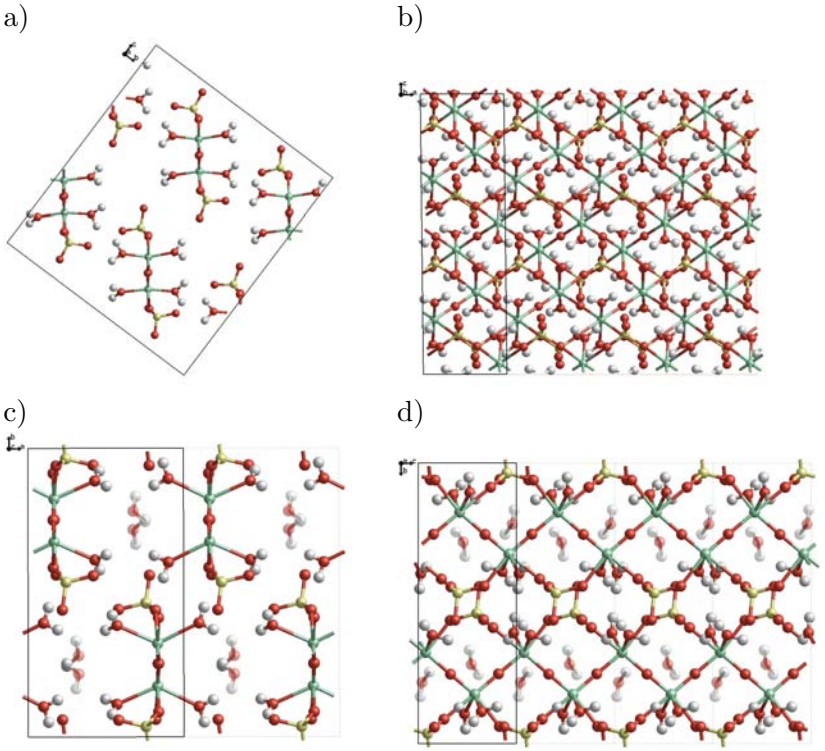

FIGURE 5.10: The structure of the hypothetical $TiOSO_4{\cdot}2H_2O$ a) down the bridged titanium chains and b) across the bridged titanium chains; and the structure of $TiOSO_4{\cdot}$(3-1)H_2O viewed c) down the bridged titanium chains and d) across the bridged titanium chains, with the free water molecules made semi-transparent for ease of comparison.

Figure 5.10 more clearly shows the comparison between the two structures. From this comparison we can see that the hypothetical $TiOSO_4{\cdot}2H_2O$ structure shown is essentially a less dense version of the $TiOSO_4{\cdot}$(3-1)H_2O structure, with some slight changes in the positions of the water molecules coordinated to the titanium octahedra as a result of it not having the extra water molecules (sometimes called 'waters of crystallisation') that the $TiOSO_4{\cdot}$(3-1)H_2O structure has between the bridged titanium chains. Having identified this similarity in potential structures for $TiOSO_4{\cdot}2H_2O$, a number of additional calculations were performed on these structures. These will be presented, alongside

other calculations involving the titanium-substituted basic zirconium sulphates, in the following sections.

Forcefield calculations were performed using the GULP software and the same methodology described in previous sections. Constant pressure optimisations were performed on each of the titanium-subtituted versions of the experimental zirconyl sulfate structures, as well as the structures of $TiOSO_4{\cdot}(1{+}1)H_2O$ and $TiOSO_4{\cdot}(3\text{-}1)H_2O$. Table 5.22 shows the optimised structure parameters, while Table 5.23 shows the corresponding optimised figures for qualitative analysis.

Structure	*a* (Å)	*b* (Å)	*c* (Å)	*Energy* (eV)
$TiOSO_4$	11.10 (0.08)	5.34 (-3.64)	6.61 (-0.67)	-28.76
$TiOSO_4{\cdot}H_2O$	6.33 (-2.63)	15.17 (21.74)	6.47 (-5.24)	-28.82
$TiOSO_4{\cdot}(1{+}1)H_2O$	6.37 (-1.88)	13.35 (7.15)	7.40 (8.37)	-29.11
$TiOSO_4{\cdot}3H_2O$	9.26 (10.67)	17.77 (17.13)	5.40 (-0.83)	-29.40
$TiOSO_4{\cdot}(3\text{-}1)H_2O$	11.24 (34.41)	13.29 (-12.36)	5.31 (-2.35)	-29.30
$Ti_2O(SO_4)_3{\cdot}4H_2O$	12.92 (-1.03)	7.87 (20.94)	15.76 (4.45)	-27.40

TABLE 5.22: Forcefield optimised structural parameters for titanium-substituted basic zirconium sulphate structures. Percentage deviations from the experimental values of the original basic zirconium sulphates are shown in brackets.

From Table 5.22 we can see that there have been some large deviations from the original basic zirconium sulphate unit cell parameters. This was to be expected; the replacement of the zirconium atoms with titanium, and the dihydroxyl bridge with a simple bridging oxygen are both quite significant structural adjustments. However, despite the large changes in unit cell parameters, the general structural motifs seen in the original zirconium sulphates are retained. The unit cell changes are often large and positive due to the loss of hydroxyl groups leading to a lack of hydrogen bonding, causing the chains to expand.

TABLE 5.23: Forcefield-optimised titanium-substituted basic zirconium sulphate structures.

Structure	**Down chain**	**Across chain**
$TiOSO_4$	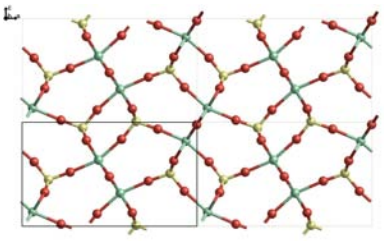	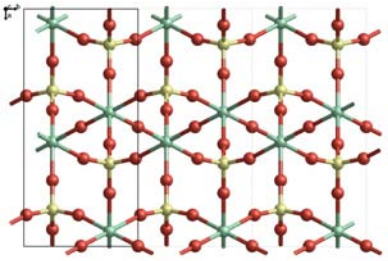

Continued on next page...

Table 5.23 – Continued

Structure	Down chain	Across chain
$TiOSO_4 \cdot H_2O$	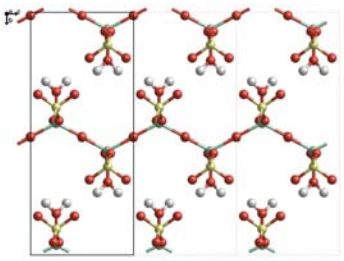	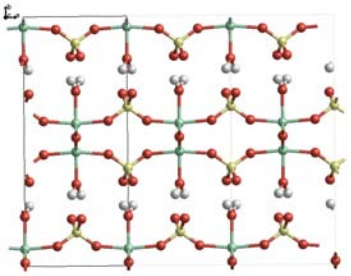
$TiOSO_4 \cdot (1+1)H_2O$	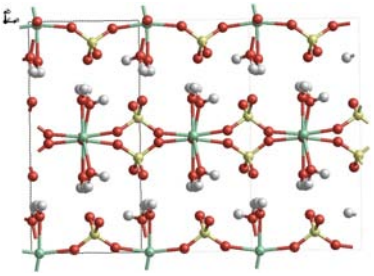	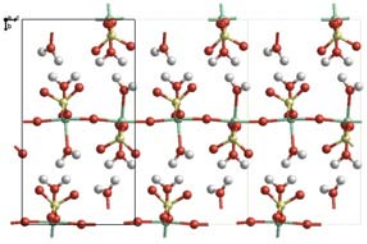
$TiOSO_4 \cdot 3H_2O$	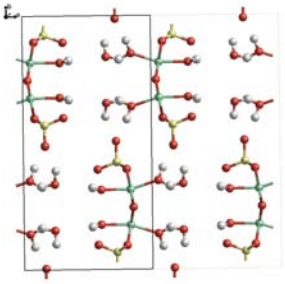	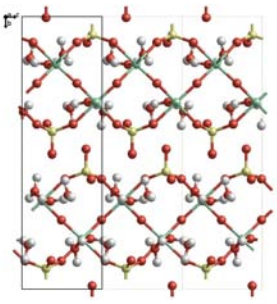
$TiOSO_4 \cdot (3\text{-}1)H_2O$	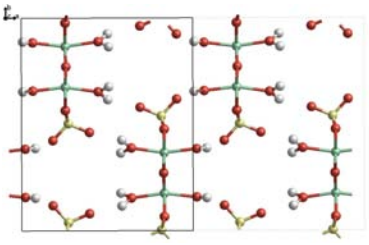	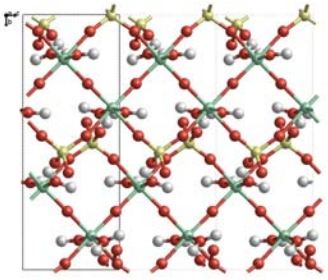
$Ti_2O(SO_4)_3 \cdot 4H_2O$	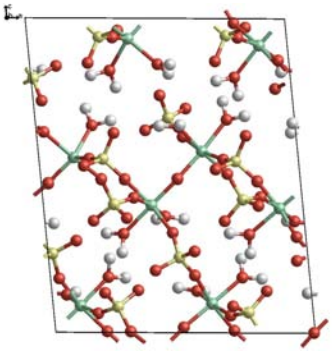	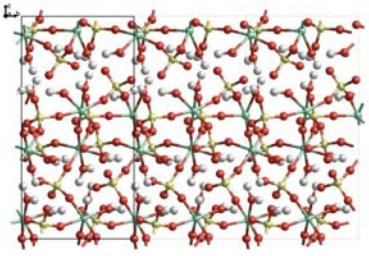

Of the two constructed dihydrates, $Ti(OH)_2SO_4{\cdot}(1+1)H_2O$ and $Ti(OH)_2SO_4{\cdot}(3\text{-}1)H_2O$, the latter seems to hold more promise, echoing as it does the same structural character as the those dihydrates shown in sections 5.2.1.3 and 5.2.1.4, and converging with the lower energy.

Having explored these systems thoroughly and constructed candidate structures for $TiOSO_4{\cdot}2H_2O$ with multiple conformational options using forcefield methods, our next aim was to simulate them with the more accurate quantum mechanical methods developed and tested in sections 5.1.1-5.1.3. The following section will show the results of optimising the hypothetical dihydrate structures using DFT.

5.2.2 DFT calculations

DFT calculations were carried out on each of the hypothetical dihydrate structures shown in the previous sections. Due to the complexity of the systems, all calculations were performed using the default basis set with a double-zeta polarised basis set and PBE exchange-correlation functional. The atomic coordinates and unit cell parameters of the different dihydrate structure configurations determined from the forcefield-optimisations were used as input for the DFT optimisations in order to reduce calculation time.

5.2.2.1 Extrapolation from titanyl sulphate series

DFT optimised structures of the $TiOSO_4{\cdot}2H_2O$ configurations shown previously in Figure 5.7 are listed in Table 5.25. The general structure of each of the configurations seem to have remained stable, with no dissociation of the water molecules or bonding behaviour between chains, and no physically unreasonable interactions are evident. Interesting to note is the packing behaviour of structures a) and d), which show the kind of channels, or cleavage planes, between these chains that were observed quite frequently in the SDPD work which will be shown in chapter 6.

From the unit cell parameters and energies shown in Table 5.24, we can see that the major difference between these and the GULP calculations is an even greater contraction of the structure; the titanyl chains have moved significantly closer during the DFT calculations, leading to some large negative percentage deviation from the indexed unit cell, especially in the b unit cell parameter. In fact, the b unit cell parameter of configuration c) contracts to almost half the original indexed value. That the structure may be so empty as to be able to allow the volume to halve suggests that perhaps the

Configuration	*a* (Å)	*b* (Å)	*c* (Å)	*Energy per F.U.* (eV)
a)	4.81 (-13.26)	14.05 (-15.79)	14.04 (-24.82)	-4978.25
b)	4.58 (-17.43)	11.60 (-30.46)	16.83 (-9.84)	-4978.00
c)	5.12 (-7.66)	9.83 (-41.08)	17.35 (-7.04)	-4978.22
d)	4.93 (-11.08)	11.19 (-32.91)	16.63 (-10.91)	-4978.26
Indexed unit cell	5.54	16.68	18.67	–

TABLE 5.24: Optimised unit cell parameters and energies per formula unit for various hypothetical polymorphs of $TiOSO_4{\cdot}2H_2O$. Numbers in parentheses indicate the percentage deviation from the indexed unit cell.

number of formula units per unit cell may be larger than first supposed. Energetically speaking, the most stable structure is that of configuration d), which appears to be slightly more ordered than the others, featuring a visibly layered structure.

TABLE 5.25: DFT optimised structures of a) – d), previously shown in Figure 5.7. Titanium atoms are shown in green, sulphur in yellow, oxygen in red, and hydrogen in white.

Configuration	**Viewed down a-axis**	**Viewed down b-axis**
a)	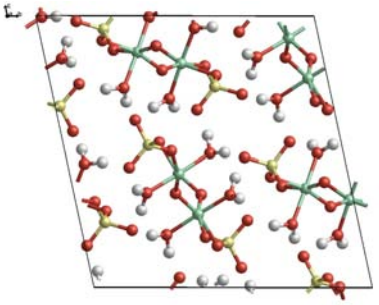	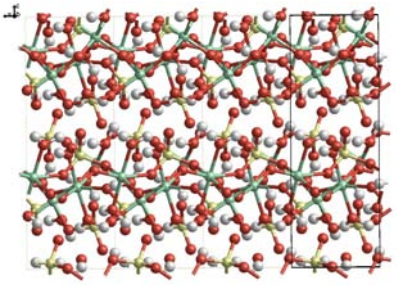
b)	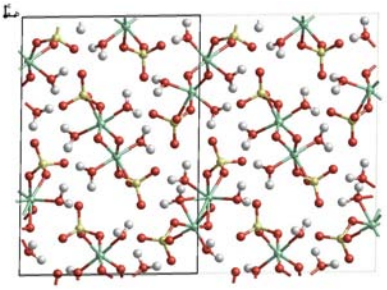	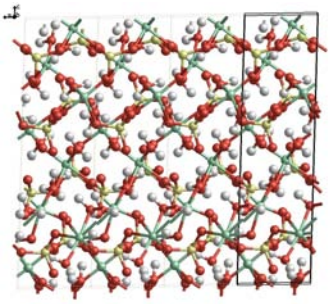
c)	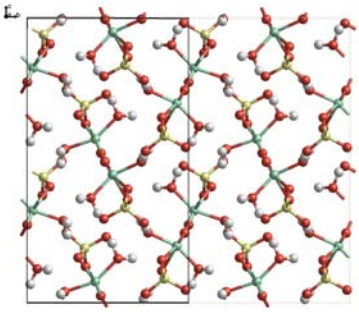	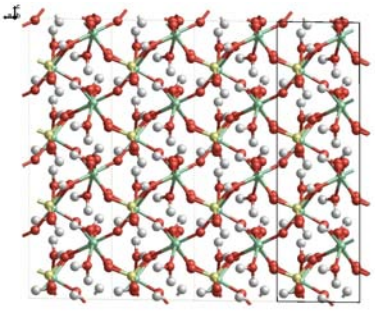

Continued on next page...

Table 5.25 – Continued

Structure	Down chain	Across chain
d)	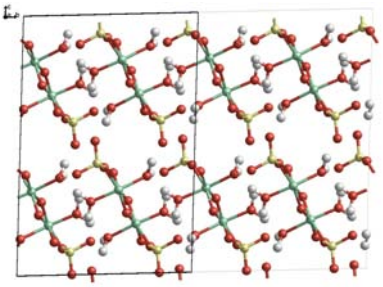	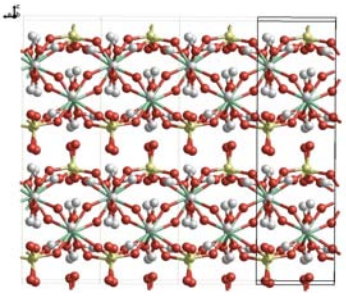

5.2.2.2 Manipulated $TiOSO_4{\cdot}H_2O$

DFT optimised structures of the $TiOSO_4{\cdot}2H_2O$ configurations created by adding an extra formula unit of water to the structure of $TiOSO_4{\cdot}H_2O$, shown previously in Figure 5.9, are shown below in Figure 5.11. Configuration 1 has retained its interconnectivity, with each sulphate tetrahedra linking between chains rather than down them, and this may be the reason why it is slightly more energetically stable than Configuration 2. Again, the main difference between the forcefield optimised results and the DFT optimised results is the overall tighter bonding of the atoms, resulting in largely reduced unit cell dimensions. Interesting to note is the fact that the energies of the two configurations have reversed with respect to the optimisations performed with forcefields.

Configuration	*a* (Å)	*b* (Å)	*c* (Å)	*Energy per F.U.* (eV)
Configuration 1	12.2323 (24.59)	5.1529 (0.39)	6.7104 (-22.10)	-4978.50
Configuration 2	9.0451 (-7.87)	5.2426 (2.14)	8.9163 (3.51)	-4978.38
Experimental [13]	9.818	5.130	8.614	–

TABLE 5.26: DFT optimised unit cell parameters and energies per formula unit for the two configurations shown in Figure 5.9. Numbers in parentheses indicate the percentage deviation from the experimentally determined unit cell.

5.2.2.3 Titanium-substituted basic zirconium sulphates

The DFT calculations of the titanium-substituted basic zirconium sulphates were started from the structures optimised by the forcefield method. As noted in the table caption,

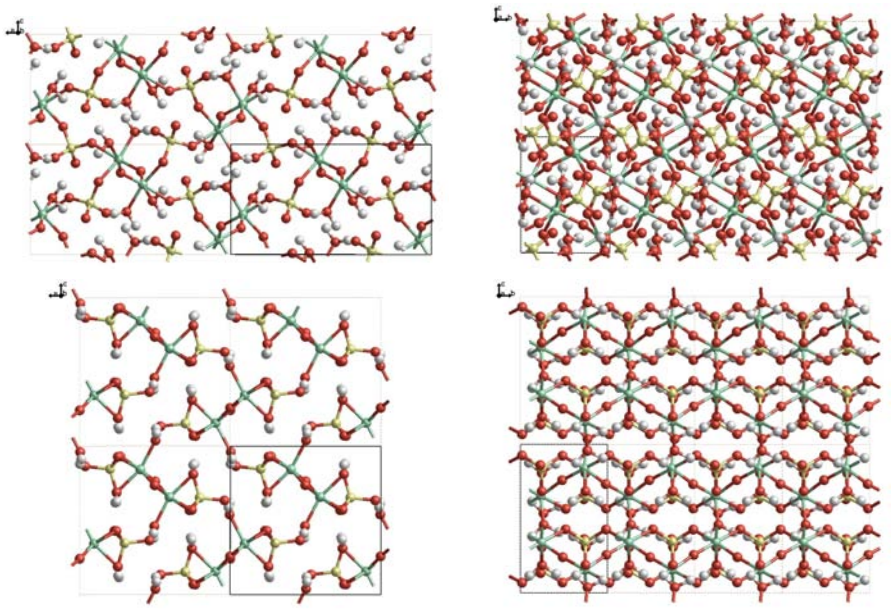

FIGURE 5.11: DFT optimised structures of Configuration 1 and Configuration 2, previously shown in Figure 5.9: (top-left) Configuration 1 viewed down the *b*-axis; (top-right) Configuration 1 viewed down the *a*-axis; (bottom-left) Configuration 1 viewed down the *b*-axis; (bottom-right) Configuration 2 viewed down the *a*-axis. Titanium atoms are shown in green, sulphur in yellow, oxygen in red, and hydrogen in white.

the structures of $TiOSO_4{\cdot}3H_2O$ and $Ti_2O(SO_4)_3{\cdot}4H_2O$ are omitted as their structures could not be made to converge. These failures to converge, and the much higher energies of the structures in general, is likely related to the fairly extreme bonding conditions that were inherited from the zirconyl sulphate hydrates from which these structures were created.

Structure	*a* (Å)	*b* (Å)	*c* (Å)	*Energy* (eV)
$TiOSO_4$	16.1038 (45.09)	5.6084 (5.00)	4.6344 (-29.90)	-13580.36
$TiOSO_4{\cdot}H_2O$	7.6450 (20.86)	18.2363 (20.23)	4.8567 (-24.92)	-15451.81
$TiOSO_4{\cdot}(1{+}1)H_2O$	10.6021 (66.31)	9.1465 (-31.49)	7.5048 (1.45)	-17323.95
$TiOSO_4{\cdot}(3{-}1)H_2O$	7.7038 (-31.48)	14.4454 (8.66)	6.7776 (27.53)	-19192.14

TABLE 5.27: Quantum mechanically optimised structural parameters for titanium-substituted basic zirconium sulphate structures. Percentage deviations from the experimental values of the original basic zirconium sulphates are shown in brackets. $TiOSO_4{\cdot}3H_2O$ and $Ti_2O(SO_4)_3{\cdot}4H_2O$ are omitted as their structures could not be made to converge.

5.2.3 Thermodynamics of model dihydrate structures

Through the use of the energies calculated with DFT, we can gain further insight into whether the hypothetical dihydrate structures we have proposed are energetically reasonable. The reaction we followed was that of adding two molecules of water to $TiOSO_4$ to form $TiOSO_4{\cdot}2H_2O$, as per the synthetic procedure:

$$TiOSO_{4(s)} + 2H_2O_{(l)} \rightleftharpoons TiOSO_4 \cdot 2H_2O_{(s)} \tag{5.2}$$

We already have the energies of $TiOSO_4{\cdot}2H_2O$ and $TiOSO_4$, but it is difficult to compute the energy of $H_2O_{(l)}$ from density functional theory calculations. Therefore, we calculated the energy of $H_2O_{(g)}$ using a single molecule of H_2O in a 15 $Å^3$ box with the DZP basis set. This energy was then converted to $H_2O_{(l)}$ by the addition of the experimental value for the latent heat of vapourisation of water (44 $kJmol^{-1}$ [183]). The enthalpy of forming the dihydrate from the addition of water molecules to the anhydrate is then:

$$\Delta H(TiOSO_4 \cdot 2H_2O_{(s)}) - [\Delta H(TiOSO_{4(s)}) + 2\Delta H(H_2O_{(l)})] \tag{5.3}$$

In these calculations we are neglecting the zero-point energy and the heat capacity of the systems, but it should be noted that this is a general indication of validation rather than any specific prediction of the enthalpy of reaction. The mean reaction enthalpy for the hydration of materials has been reported in Glasser and Jones [184] to have a range of -77.4 – -52.4 kJ mol^{-1} for the insertion of two water molecules.

Structure	**Enthalpy of reaction** (kJ mol^{-1})	**Relative energy** (kJ mol^{-1})
a)	-54.8	23.5
b)	-30.5	47.9
c)	-51.4	27.0
d)	-55.3	23.0
Configuration 1)	-78.5	0.0
Configuration 2)	-67.5	10.9

TABLE 5.28: Enthalpies of reaction calculated using equation (5.3) and relative energies for various hypothetical dihydrate structures. Relative energies are expressed as a difference relative to the lowest energy structure.

Table 5.28 shows the enthalpies of reaction and relative energies of the hypothetical dihydrates determined from the titanyl sulphate series, and the manipulated $TiOSO_4{\cdot}H_2O$ configurations. The titanium-substituted zirconyl sulphate hydrates are not included due to their energies being up to three orders of magnitude beyond those

listed. As can be seen from the table, almost all the enthalpies of reaction fall within the range reported by Glasser and Jones, leading us to believe that the structures listed are thermodynamically reasonable. With regards to the relative energies of the structures, Configuration 1 formed by the addition of water to the monohydrate proved to be the most stable, although the difference in energy between it and the rest of the structures is relatively small.

5.2.4 Conclusions

In this chapter, we have shown the process required to prepare and validate both quantum mechanical and forcefield methods in order to simulate unknown structures. An exhaustive optimisation of the parameters used in the SIESTA software was demonstrated. TiO_2 polymorphs and the known titanyl sulphates, $TiOSO_4$ and $TiOSO_4{\cdot}H_2O$, were used to confirm the validity of the parameterisation. Various hypothetical titanyl sulphate dihydrate structures were proposed and simulated, and their thermodynamic validity confirmed. While comparison of calculated XRD patterns of these hypothetical $TiOSO_4{\cdot}2H_2O$ structures with those obtained experimentally did not yield any matches, the wide configurational space of the layered structure expected, and the sensitivity of XRD patterns to small changes in atomic positions and unit cell parameters may go some way to explain this lack of correlation and verification. The general tendency towards particular structural motifs shown throughout the calculations provides valuable information for use in the structure determination step, as will be shown in chapter 6.

Chapter 6

Structure determination by powder diffraction

In section 2.4, the methodology for structure determination from powder diffraction (SDPD) was outlined. In recent times, the number of software suites that are able to execute all aspects of this methodology has grown. The free and open availability of such software, combined with the increasing power of computer processors, has meant that SDPD has become quite a commonplace practise, even using conventional laboratory-based X-ray diffractometers. This chapter will present the results of the SDPD process as applied to the unknown structure of $TiOSO_4 \cdot 2H_2O$, using the data collected and presented in chapter 4.

6.1 Pattern indexing

The first step in SDPD is to attempt an indexing of the pattern. Indexing a pattern involves the calculation of the unit cell of the crystal structure and therefore the Miller indices of the reflections, using the positions of the reflections as input. Presently it is common practise to use an automatic indexer contained in a computer program to give a ranked list of possible indexing results.

While the automatic indexing of a pattern can usually be relied on to give a valid result, it is still recommended that multiple programs be used. This is done in order to eliminate the possibility of a particular program's algorithm returning a spurious result due to some unique set of circumstances not accounted for within the code. In addition to using multiple indexing programs, multiple diffraction patterns recorded at different wavelengths are useful in ensuring that no one data set carries the entire responsibilty for

indexing. To that end, the indexing results of multiple patterns using various software will be presented in the interest of providing a more definitive result.

The most important features of a pattern in the determination of a unit cell is high resolution at lower angles, and precision in the list of peak positions to be used. Synchrotron radiation offers the best results in this regard, given its much higher resolution and counting statistics when compared to conventional laboratory XRD data. As such, only the diffraction patterns collected at the Australian Synchrotron and APS will be considered here.

6.1.1 Australian Synchrotron

Peak list and initial results

In order to perform a thorough investigation of the indexing method, a critical eye was turned to the pattern itself. While a multiphase system of $TiOSO_4 \cdot 2H_2O$ and $TiOSO_4 \cdot H_2O$ was ruled out based on their lack of overlap, as seen in section 4.3, it was not impossible that some other multiphase system may be present. Given the propensity of the diffraction patterns to change depending on their precursor source, or the nature of the experiment being performed, it was thought necessary to be slightly more thorough in the treatment of the indexing step beyond taking for granted the accuracy of the automatic peak search and indexing procedure that is present in modern software. To this end, a series of indexing runs were performed, taking into account the particulars of the diffraction patterns.

Figure 6.1 shows the numbered peaks of the diffraction pattern DIH02. The DIH02 pattern was used for all indexing attempts due to its much greater quality compared to DIH01, as shown previously in section 4.5.1.2. This numbering scheme will serve as a reference for the remainder of the discussion of the indexing. Table 6.1 shows the peak positions more explicitly in terms of d-spacings.

Indexing was performed using the CRYSFIRE [185], TOPAS [186], DASH [187], and FOX [81] programs. The CRYSFIRE program offers a suite of methodologies, and the KOHL [188] and ITO [61] routines were run using it. DASH indexing was performed under the supervision of beamline scientist Peter Lee during a visit to the Argonne National Laboratory Advanced Photon Source. Additionally, the FOX indexing methodology used was verified by beamline scientist Max Avdeev of the ANSTO nuclear facility. Table 6.2 shows the top auto-indexing results using at least the first 20 and at most the first 25 peaks of the DIH02 diffraction pattern for each program.

In-depth analysis of FOX indexing procedure

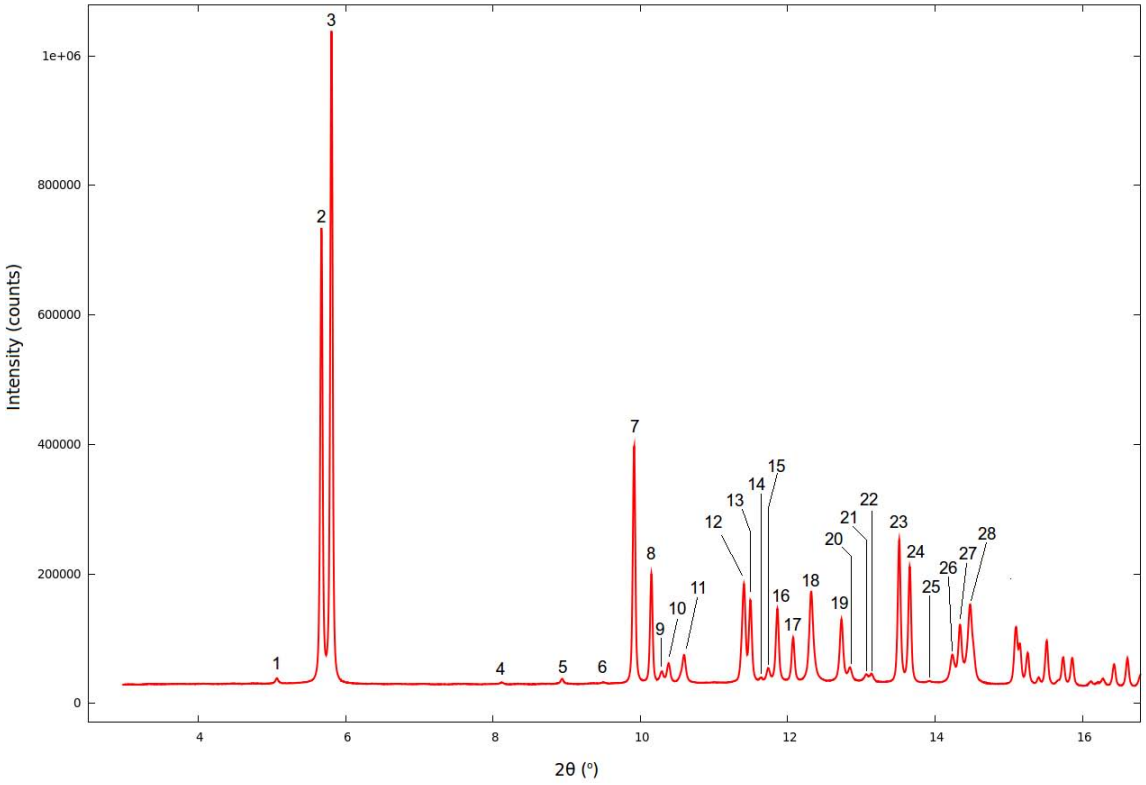

FIGURE 6.1: Peak labels in the diffraction pattern obtained at the Australian Synchrotron $TiOSO_4 \cdot 2H_2O$.

As mentioned previously, the propensity for the diffraction pattern to change in dramatic ways – e.g. the swapping of the two large peaks' ratios – meant that a great deal of caution was required when considering the results given using auto-indexing programs. In particular, the presence and inclusion of very weak reflections at low angles was questioned. As such, a series of indexing runs was performed using the FOX software which allows peaks to be added and removed specifically in order to test their effect on the indexing of the pattern. Within the indexing routine, possible indexing solutions are presented in order of their 'score' or figure of merit, M(n). A good score is considered to be above 20, providing the peak positions have been accurately defined [189].

The first indexing run used all of the first 20 peaks and its results are shown in Table 6.3.

From this table it can be seen that all indexing solutions maintained some similarities in the a, b, and c unit cell parameters, while the major difference was seen in the value of β. However, despite the changes in the value of β, the total volume of the unit cell was not seen to change to any considerable extent. Thus it seems that these indexing results are quite closely related, perhaps relying on the positions of a small subset of the peaks to differentiate between them.

Peak number	**2θ (°)**	**d-spacing (Å)**
1	5.070	9.336
2	5.673	8.343
3	5.809	8.151
4	8.119	5.834
5	8.944	5.299
6	9.503	4.989
7	9.919	4.779
8	10.151	4.668
9	10.294	4.602
10	10.384	4.562
11	10.594	4.471
12	11.408	4.156
13	11.494	4.125
14	11.636	4.073
15	11.734	4.040
16	11.861	3.996
17	12.075	3.927
18	12.319	3.848
19	12.731	3.725
20	12.848	3.692
21	13.065	3.630
22	13.140	3.609
23	13.515	3.509
24	13.658	3.473
25	13.927	3.406
26	14.235	3.333
27	14.340	3.308
28	14.477	3.278

TABLE 6.1: Peak numbers and positions for the DIH02 Australian Synchrotron diffraction pattern.

Software	a (Å)	b (Å)	c (Å)	β (°)	V (Å^3)
TOPAS	5.547	16.693	19.426	105.63	1727.6
DASH	5.544	16.674	18.666	90.64	1725.5
FOX	5.544	16.685	18.671	90.65	1726.8
KOHLv7.01b	5.546	16.685	18.666	90.64	1726.9
ITO12	5.543	16.676	18.657	90.64	1724.5

TABLE 6.2: Unit cell parameters obtained from the top indexing results for various software programs.

Following on from the indexing performed on all of the peaks, consideration was given to the presence of the weaker peaks in the pattern: peaks 1, 4-6, 14, 21, 22, and 25 as shown in Figure 6.1. As indexing results are dominated by the low-angle (high d-spacing) reflections, the question of whether to include the weak reflections in the determination

Score	a (Å)	b (Å)	c (Å)	β (°)	V (Å^3)
63.6	5.544	16.685	18.671	90.65	1726.8
46.2	5.544	16.688	19.418	105.94	1727.4
46.2	5.544	16.688	19.538	107.13	1727.4
22.3	5.540	16.721	18.686	90.63	1730.9
20.6	5.550	16.696	18.700	90.56	1732.9
16.7	5.534	16.698	18.626	90.55	1721.1

TABLE 6.3: Indexing results returned from FOX indexing of first 20 peaks in the DIH02 pattern.

of a unit cell was a pressing one. To this end, a series of indexing runs in FOX were performed with fewer of the weak reflections in each. The results are shown in Tables 6.4-6.8. In the interest of brevity, in cases where more than 10 results were returned by FOX only the top 10 are listed.

Score	a (Å)	b (Å)	c (Å)	β (°)	V (Å^3)
53.9	5.544	16.685	18.671	90.65	1727.0
44.6	5.544	16.689	19.539	107.13	1727.6
44.6	5.544	16.689	19.419	105.94	1727.6

TABLE 6.4: Indexing results returned from FOX indexing of DIH02 excluding peak number 1.

Score	a (Å)	b (Å)	c (Å)	β (°)	V (Å^3)
57.5	5.544	16.689	18.673	90.64	1727.5
48.1	5.544	16.689	19.536	107.12	1727.3
48.1	5.544	16.689	19.418	105.95	1727.3

TABLE 6.5: Indexing results returned from FOX indexing of DIH02 excluding peak numbers 1, and 4-6.

Score	a (Å)	b (Å)	c (Å)	β (°)	V (Å^3)
56.4	5.544	16.688	18.678	90.65	1728.0
43.4	5.545	16.682	19.412	105.96	1726.4
20.6	5.535	16.732	18.699	90.60	1731.7
20.3	5.543	16.701	18.651	90.58	1726.5

TABLE 6.6: Indexing results returned from FOX indexing of DIH02 excluding peak numbers 1, 4-6, and 14.

As can be seen from the progression of taking more and more of the smaller peaks out through Tables 6.4-6.8, the top result for FOX seen in Table 6.2 (a=5.544 Å, b=16.685 Å, c=18.671 Å, β=90.65°) is quite resilient to the removal of the small peaks at low angle. It is only when almost all of the smaller peaks are removed that this result is

Score	a (Å)	b (Å)	c (Å)	β (°)	V (Å^3)
26.3	11.571	4.456	29.085	103.24	1459.7
26.3	11.571	4.456	28.734	99.84	1459.7
22.7	9.643	8.057	15.366	91.99	1193.1
19.3	9.650	8.058	17.874	120.73	1194.7
18.9	4.679	18.909	16.576	94.85	1461.3
18.0	17.285	4.471	20.312	95.86	1561.5
17.5	17.277	4.467	25.273	126.97	1558.3
17.4	15.769	4.886	18.124	114.12	1274.4
16.5	15.767	5.581	18.112	114.14	1454.5
16.1	4.833	16.733	14.829	104.81	1159.3

TABLE 6.7: Indexing results returned from FOX indexing of DIH02 excluding peak numbers 1, 4-6, 14, and 25.

Score	a (Å)	b (Å)	c (Å)	β (°)	V (Å^3)
16.9	8.514	18.573	10.490	119.37	1445.7
16.5	11.067	4.590	18.886	105.40	925.0
16.5	9.553	4.593	33.224	93.33	1455.1
16.3	8.529	18.588	10.528	119.47	1453.2
16.2	14.905	5.055	16.538	101.48	1221.1
16.0	4.677	18.902	16.832	101.22	1459.7
15.7	11.706	8.370	13.894	98.88	1345.0
15.7	5.983	8.062	27.288	93.29	1314.2
15.6	9.119	9.231	15.503	93.00	1302.5
15.2	4.802	18.514	16.388	107.94	1386.0

TABLE 6.8: Indexing results returned from FOX indexing of DIH02 excluding peak numbers 1, 4-6, 14, 21, 22, and 25.

lost. It should be noted that when these peaks are removed, FOX does not attempt its indexing with less than 20 peaks, e.g. indexing without peaks 1, 4-6, and 14 is not done with only 15 peaks. Instead, it incorporates peaks from later in the pattern to keep the number of peaks used at 20. This helps to explain the fact that the main result is lost when greater than five small peaks are removed, as the peaks incorporated into the indexing from later in the pattern are more likely to have errors associated with them, due to instrumental and sample line broadening. [57].

The result that can be taken away from this analysis is that the influence of the smaller peaks is minimal on the indexing of the pattern. Therefore, despite the slight uncertainty in including these smaller peaks in the indexing, their inclusion does not influence the result to any appreciable degree.

Dominant zone investigation

Despite the general robustness of the de Wolff figure-of-merit, M_{20}, [64] that FOX employs, it can be shown that it may fail and lead to erroneous figures when a condition known as a dominant zone is present in the diffraction pattern. This occurs when one of the unit cell parameters is significantly smaller than the others, and can lead to multiple solutions with high M_{20} values [190]. From our top results, it might be intuited that a dominant zone may be present, as the a unit cell parameter is less than a third of the next-smallest b unit cell parameter, and there is another solution present with a comparatively high M_{20} value.

The main result of a dominant zone is that two of the reciprocal lattice vectors become very well defined, while the remaining one becomes poorly defined and may not be sampled at all in the first 20 peaks [191]. This means that, quite often, the first 20 peaks are attributable to a hk0 lattice plane, producing an issue in most indexing programs that take the first 20 peaks by default. A common solution to this problem is to perform an indexing run on an increasingly greater number of peaks in the diffraction pattern in order to try and overcome the dominant zone. This is obviously quite a difficult task in powder diffraction work due to the increased signal degradation at higher angles. However, an attempt was made using this process with the crystal system limited to monoclinic, and the results shown in Table 6.9.

No. of peaks	**Score**	a (Å)	b (Å)	c (Å)	β (°)	V (Å^3)
25	46.873	5.543	16.685	18.669	90.65	1726.30
30	45.509	5.544	16.681	18.669	90.64	1726.28
35	44.753	5.544	16.681	19.417	105.95	1726.55
	44.751	5.544	16.681	18.670	90.64	1726.55
40	38.129	5.545	16.683	18.670	90.64	1726.91
	38.128	5.545	16.683	19.416	105.95	1726.91
	38.128	5.545	16.683	18.670	90.64	1726.91
45	32.318	5.544	16.683	18.670	90.64	1726.75
	32.047	5.546	16.682	19.416	105.96	1727.08
50	28.567	5.544	16.681	19.414	105.95	1726.27
	16.852	5.539	16.677	18.666	90.65	1724.15
	12.805	5.552	16.677	18.677	90.69	1729.22
55	26.191	5.544	16.680	19.413	105.95	1726.04
	25.155	5.543	16.680	18.668	90.65	1726.02
	23.634	5.543	16.682	18.667	90.65	1726.14
60	22.947	5.544	16.682	19.412	105.95	1726.14
	21.566	5.543	16.679	18.666	90.65	1725.54
65	22.086	5.544	16.680	19.412	105.95	1725.84
	18.988	5.545	16.678	18.664	90.65	1725.87
120	7.042	5.543	16.6777	19.407	105.92	1725.18

TABLE 6.9: Indexing results returned from the dominant zone investigation involving the increase of the number of peaks used in the indexing attempt.

From these results, it can be seen that there is very little variation in the results with the increased number of peaks used, suggesting that we do not have a dominant zone problem.

6.1.2 Chicago Advanced Photon Source

The suggested practise of using multiple data sets to boost confidence in indexing work resulted in the use of Chicago APS data in addition to that obtained from the Australian Synchrotron. As mentioned previously, the background is still quite significant despite attempts to provide better mixed samples. While the resolution of the APS diffraction pattern was not quite as high as that of the Australian Synchrotron data, the set of peaks, shown in Figure 6.2, used in the indexing procedure were very nearly the same. Only peak number 14 from the Australian Synchrotron diffraction pattern was unable to be discerned in the APS synchrotron diffraction pattern.

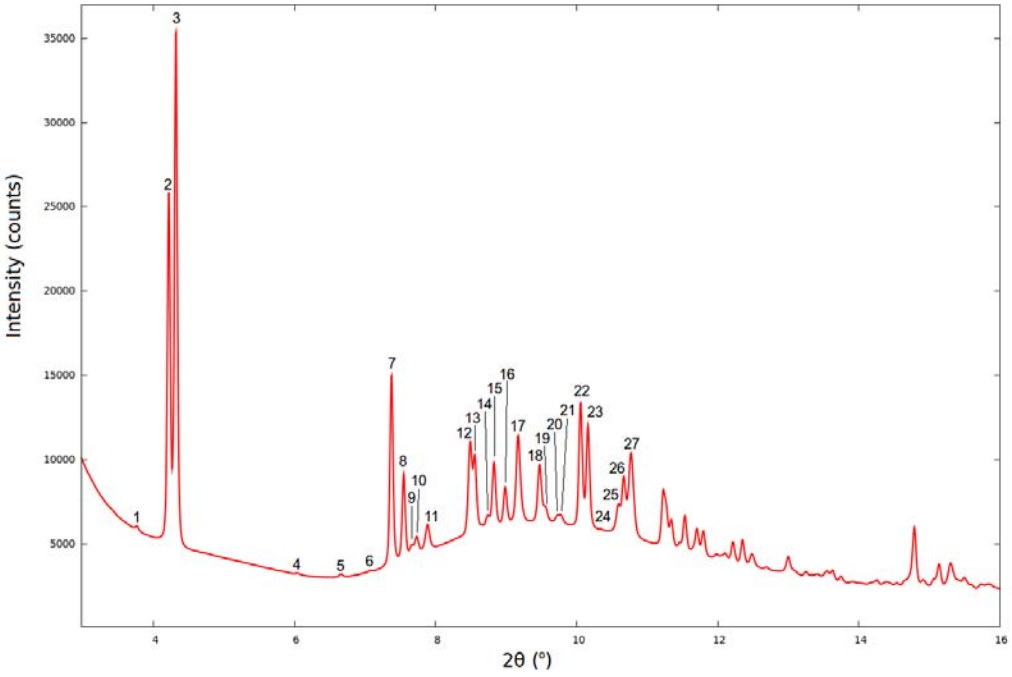

FIGURE 6.2: Peak labels of the Chicago APS synchrotron X-ray diffraction pattern.

Again, the top six results are very similar, with only the c unit cell parameter and β varying between results, but giving approximately the same volume. This is essentially the same result as is seen in Table 6.3 using the Australian Synchrotron data. However, results with $\beta \approx 106^\circ$ are much closer in M_{20} to the $\beta \approx 90.6^\circ$ results that have been suggested as being the most likely unit cell. This suggests that the two results are closer in probability than previously thought. However, it is thought that despite

Score	a (Å)	b (Å)	c (Å)	β (°)	V (Å^3)
47.6	5.540	16.703	18.693	90.61	1729.8
47.2	5.536	16.722	19.456	105.97	1731.5
47.2	5.536	16.722	19.560	107.00	1731.5
39.1	5.540	16.705	19.550	107.02	1730.1
36.2	5.538	16.704	19.439	106.02	1728.3
35.6	5.534	16.739	18.687	90.57	1730.9
35.5	9.715	16.702	11.075	105.99	1727.6
35.5	9.715	16.702	12.561	122.04	1727.6
31.6	11.078	16.704	12.566	131.98	1728.8
26.1	5.544	16.704	18.701	89.46	1732.0

TABLE 6.10: Indexing results returned from FOX indexing of Chicago APS data using the set of peaks shown in Figure 6.2.

this ambiguity, the unit cell of a=5.544 Å, b=16.685 Å, c=18.671 Å, and β=90.65° is essentially the correct one, allowing for small fluctuations due to peak position precision.

The indexing of the $TiOSO_4 \cdot 2H_2O$ unit cell is a first, having never been reported in the literature previously, excepting the erroneous attribution reported in chapter 1 by Johnsson *et al* [19]. Given the fact that unit cell determination is a crucial first step in the solution of a structure from powder diffraction, it comes as no surprise that no structure for $TiOSO_4 \cdot 2H_2O$ has been proposed in the literature.

6.2 Integrated intensity extraction and space group determination

The second stage in SDPD is the extraction of integrated intensities from the diffraction pattern and the subsequent use of these intensities to determine the space group of the crystal structure. Compared to the variability of technique that can be present in the indexing procedure, the extraction of intensities is a relatively straightforward step. However, it is followed by what is probably the most ambiguous step in the SDPD process; the determination of the space group.

While straightforward in practise, the previously mentioned collapse of three-dimensional reciprocal space onto the one-dimensional powder diffraction pattern, and the information that is lost to peak overlap as a result, can often lead to conflicting results. For example, while exactly equivalent d-spacings will perfectly overlap and not cause problems, two peaks from d-spacings which are very nearly the same may be lost to the insufficient resolution of the X-ray source. This is especially the case for crystal systems with less than orthorhombic symmetry, as there are a much greater number

of independent reflections and therefore greater probability of some of those reflections being overlapped.

While our use of synchrotron X-ray sources overcame some of the problems associated with resolution–for example, the two large peaks that dominate the diffraction pattern of $TiOSO_4 \cdot 2H_2O$ were not fully resolved in laboratory X-ray diffraction patterns–they do not completely do so, and peaks that occur at higher 2θ that may have contributed to a more specific space group determination are often lost to accidental overlap. Therefore it is in our best interests to be as comprehensive as possible when extracting the integrated intensities of a pattern's peaks, whether experiencing peak overlap or not, in order to use these peak positions to determine the systematic absences of the diffraction pattern in question.

Again, where previously the space group determination has been done by hand, pinpointing systematic absences from the extracted peak profiles is now implemented into many software programs, including FOX. The results from the FOX program will be now presented and discussed.

6.2.1 Space group determination

FOX uses the iterative Le Bail algorithm [69] to obtain profile fits to diffraction data, and then employs the R-factor obtained from these fits in its estimation of space groups. The term 'determination' is therefore somewhat of a misnomer; the end result of a space group determination routine in FOX is a list of possible space groups, each associated with a goodness of fit (GoF) much like the indexing results. One such list is shown in Table 6.11, generated following an indexing of the diffraction pattern as described in the previous section. It should be noted that a lower GoF value corresponds to a more probable result.

From this table it can be seen that the space groups of P 1 2_1/c 1, a monoclinic P space group, is the most likely one given the peaks present in the pattern. However, it is relevant to quote from the FOX manual at this point [189]:

> "Important note: the true space group will not necessarily be the one with the lowest Rwp/GoF! Usually there will be group of space group settings which have systematic extinctions compatible with the observed pattern, and will all have an Rwp or GoF close to the best."

The latter statement is obviously the case in our list. The goodness of fit (GoF) of the top three space groups are within 1.2% of each other, while the top 6 are within 8.8%.

Space group	R_{wp}	Goodness of fit	Crystal system	Space group number
P 1 2_1/c 1	5.22%	98.506	Monoclinic P	14
P 1 c 1	5.25%	99.673	Monoclinic P	7
P 1 2/c 1	5.25%	99.673	Monoclinic P	13
P 1 2_1/a 1	5.44%	106.930	Monoclinic P	14
P 1 a 1	5.47%	108.046	Monoclinic P	7
P 1 2/a 1	5.47%	108.046	Monoclinic P	13
P 1 2_1 1	5.51%	110.294	Monoclinic P	4
P 1 2_1/m 1	5.51%	110.294	Monoclinic P	11
P 1 2 1	5.53%	111.297	Monoclinic P	3
P 1 m 1	5.53%	111.297	Monoclinic P	6
P 1 2/m 1	5.53%	111.297	Monoclinic P	10
P 1	5.37%	118.462	Triclinic P	1
P 1 2_1/n 1	5.74%	118.954	Monoclinic P	14
P 1 n 1	5.77%	120.145	Monoclinic P	7
P 1 2/n 1	5.77%	120.145	Monoclinic P	13
P $\bar{1}$	5.54%	125.921	Triclinic P	2

TABLE 6.11: Ranked space group probabilities as determined by the FOX space group explorer function.

Not only that, but all of the space groups listed are within the same monoclinic crystal system (with the exception of the triclinic P1 and P $\bar{1}$ space groups). It should be noted that there is a recurrence of certain space group numbers with different unique axes, e.g. P 1 2_1/a 1 and P 1 2_1/n 1 are both non-standard settings of the P 1 2_1/c 1 space group.

Due to these small variations between suggested space groups, it might seem useful to move to a lower symmetry and engage in space group determination in that way before trying to apply a higher symmetry operation. However, given the straight-forward manner with which SDPD experiments could be executed and the relative similarity of each suggested space group, it was decided that a series of calculations could be run at higher symmetries. If these efforts failed then a lower symmetry could be used.

6.3 Structure determination

6.3.1 Methodology

Once the diffraction pattern had been indexed and a list of possible space groups determined, the next step involved deciding on which trial structure motifs could be used in the structure determination step. Along with single atoms, we can use molecular fragments in order to speed up calculations. For example, various types of polyhedra

can be used if it is suspected they are present in the final structure, e.g. tetrahedral units of SiO_4 in zeolites. The structures of $TiOSO_4$, $TiOSO_4{\cdot}H_2O$, and the hypothetical structure of $TiOSO_4{\cdot}2H_2O$ that we have shown in chapter 5 were the basis for the fragments used. A list of the different fragments is shown in Table 6.12. The SO_4 tetrahedra are created with bond lengths 1.5 Å and 109.5° bond angles, while the TiO_6 octahedra with bond lengths equal to 1.95 Å and bond angles equal to 90°, although these are allowed to vary within constraints.

Fragment type	**Fragment image**
Ti, S, and O atoms	
SO_4 tetrahedra	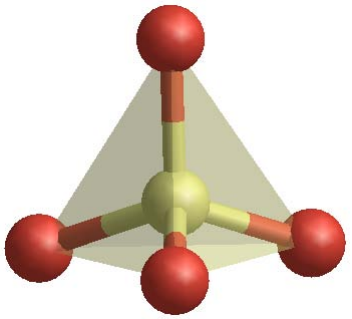
TiO_6 octahedra	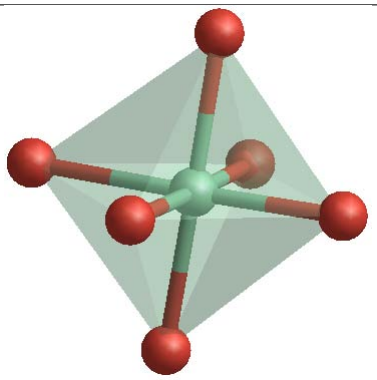

TABLE 6.12: Fragment names and images. Titanium atoms are shown in green, sulphur atoms are yellow, and oxygen atoms are red.

Before structure determination schemes combining these fragments can be devised, the number of formula units present in the indexed unit cell needs to be calculated. We can use the volume of $TiOSO_4{\cdot}H_2O$ (approximately 434 $Å^3$ with four formula units) and the volume of the unit cell indexed (1727 $Å^3$) to intuit that 16 formula units of $TiOSO_4{\cdot}2H_2O$ are required. Bearing in mind the multiplicities of the space groups, various combinations of fragments could be used to give the right number of formula units within the cell, while exploring the possibility of different motifs within the structure.

It should be noted that these direct-space calculations were run with dynamical occupancy enabled. Dynamical occupancy allows for atoms of the same element to 'merge' with each other in order to explore different topologies of connectivity. So, for example, if a system consisted of TiO_6 octahedra and a SO_4 tetrahedra, dynamical occupancy would allow for corner sharing of an oxygen by changing the occupancy of the shared oxygen to 0.5 for each of the polyhedra, essentially reducing the two oxygen atoms to one. The computational cost of including this feature is considerable, but not prohibitive given the processing power available to address the problem. The ability of dynamical occupancy to adjust the presence of atoms is important when considering how best to combine fragments. The ability of dynamical occupancy to adjust the presence of atoms is important when considering how best to combine fragments and, more specifically to our system, how many free oxygens must be added to ensure a consistent stoichiometry.

While the different fragment combinations could be tested by adding all of the fragments at the start of a run, it can also be useful to stagger the addition of atoms or fragments. For example, when adding free atoms, it might be useful to add the heavier Ti atoms first in order for them to take up the positions of greatest electronic density before adding the lighter S and O atoms. The wide variation in the schemes that can be followed to determine the possible atomic coordinates means that the configurational space to be explored is correspondingly vast.

The optimisation algorithm used is that of parallel tempering, which encourages a greater exploration of configurational space by simulating multiple systems at different temperatures and allowing them to swap between each other at specified intervals. The temperature and displacement amplitudes are both determined by a 'smart' schedule, which aims to achieve between 10% and 30% acceptance of trial structures.

The optimisation procedure can be run in either single or multiple run modes. In the single run mode, a number of trials are specified and the optimisation is run starting with whatever the current configuration is and stops when the number of trials specified has been completed. However, this has the problem that after a certain number of trials, the structure is unlikely to move from whatever best configuration it has found so far in that single run. It is for this reason that the multiple run mode should be used. Multiple run mode performs a number of runs, each with a set number of trials. Unlike the single run, it randomises the atomic configuration at the start of each run and stores the best configuration from each run before restarting. The idea behind this is that if a particular structure is repeatedly obtained, it is more likely to be a good candidate for the structural determination of the system. The choice of the number of trials in each run is dependent on the system being studied. Conventional wisdom

suggests that simple structures, such as $PbSO_4$, require around 50,000 trials per run to approach a solution, while more complex structures, such as that of cimetidine, might require 1,000,000 trials per run [189]. Our system was thought to be somewhat more complex than $PbSO_4$, so 1,000,000 trials were chosen for each run, with a total of 200 runs for each structure fragment configuration explored.

Once the 200 runs had finished for each of the configurations, the top 10 best configurations, as determined by their GoF match with the powder diffraction data, were analysed. The GoF match is referred to as the 'cost' value, which for the optimisation procedure is the χ^2 value, as described in [192]. For the sake of brevity, only the top result will be shown in the results section. However, the tables in Appendix B show the entirety of each top ten with their associated cost scores, and these will be referred to during the discussion.

6.3.2 Results

P 1 $2_1/c$ 1; Ti and S atoms

These runs consisted of the appropriate number of free Ti and S atoms to give 16 or 12 formula units (FU). The 12 formula unit runs were included to accommodate a lower density stucture than that extrapolated from the monohydrate structure. Also, the difficulty in fitting large amounts of formula units in the indexed unit cell, as shown in 5.2, might suggest a lower density.

The top 10 results of the 16 FU runs gave almost exactly the same atomic configuration, with very minor changes in atomic positions between them, of the order of less than a percent. This configuration is shown in Figure 6.3.

Even with so few atoms to populate the unit cell, we can already see some features evident in the configuration. There does appear to be some kind of chain forming in the short **c** unit cell direction, in addition to hexagonal voids forming down the **a** unit cell direction. This might suggest the placement of 'waters of crystallisation'; water molecules that are in the crystal structure but are not directly bound to the metal ion, instead they are kept in place by hydrogen bonds.

A similar formation can be seen in Figure 6.4, the recurring result found with 12 FU of Ti and S atoms. Again, the hexagonal motif is present looking down the **a** unit cell direction, while a less clear, but still distinct, chain can be seen down the **c** direction.

One issue that became apparent while looking through the structures was the tendency for the atoms to be placed in similar positions, but with Ti and S swapped between

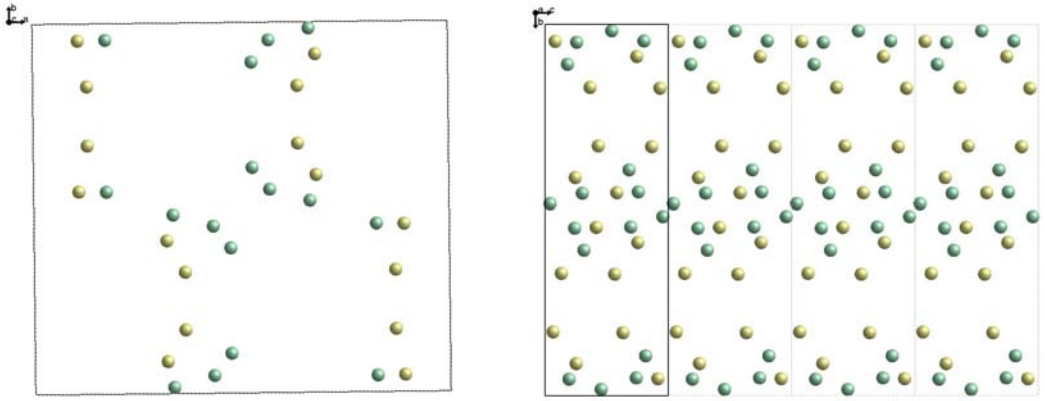

FIGURE 6.3: The best atomic configuration as determined by cost value using 16 FU of free Ti and S atoms, viewed down the **c** (left) and **a** (right) lattice directions. Green atoms are Ti and yellow are S. The unit cell is outlined in solid lines, while images of the unit cell are shown in dashed lines.

them. This points to a difficulty in determining heavy atom positions, which might be expected given the close relative heaviness of titanium (Z=22) and sulphur (Z=16), where the 'heaviness' of an atom is related to its atomic number, i.e. the number of electrons in the atom. This is further complicatied by the location of sulphur in SO_4 units, where the electron density of the oxygen atoms further obscures the sulphur.

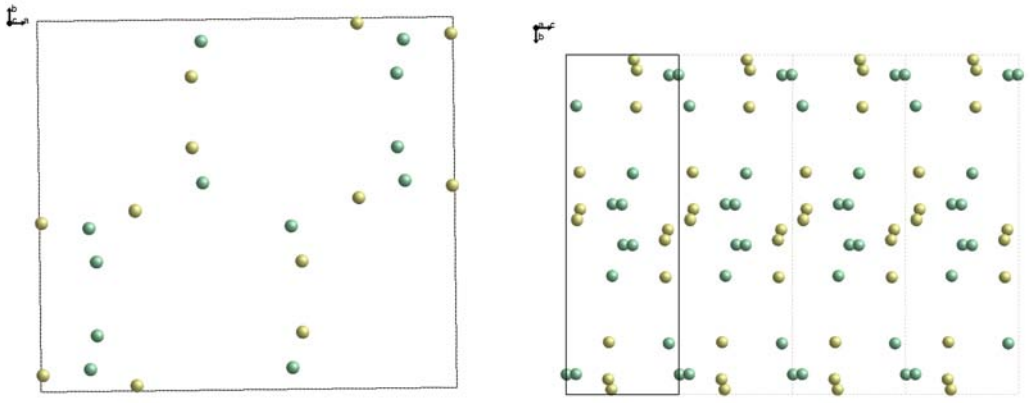

FIGURE 6.4: The best atomic configuration as determined by cost value using 12 FU of free Ti and S atoms, viewed down the **c** (left) and **a** (right) lattice directions. Green atoms are Ti and yellow are S. The unit cell is outlined in solid lines, while images of the unit cell are shown in dashed lines.

P 1 $2_1/c$ 1; Ti, S, and O atoms

The next combination to be tested maintained the same number of Ti and S atoms, and introduced different numbers of free O atoms. The first run consisted of 16 FU of Ti and S atoms, and 16 oxygen atoms (after accounting for space group multiplicity). The best atomic configuration, as determined by cost value, is shown in Figure 6.5. The

hexagonal motif is retained, though slightly deformed, and the chains in the **c** direction are also less distinct, but still appear to be present.

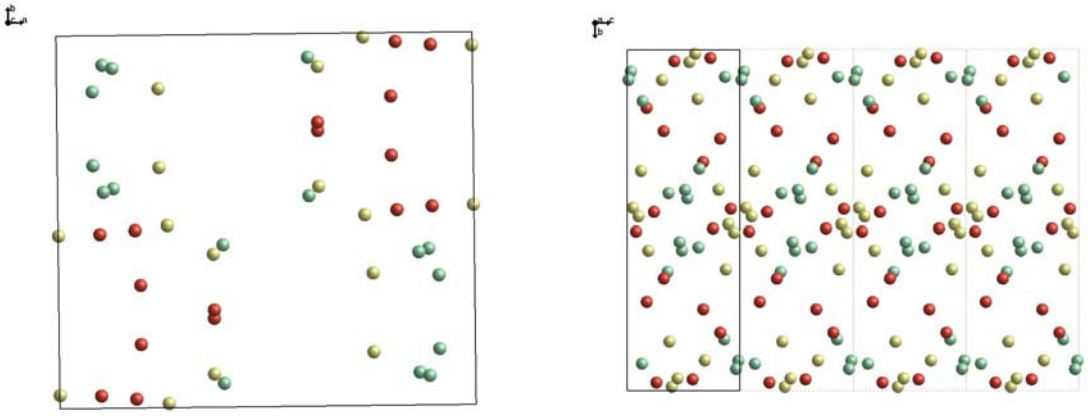

FIGURE 6.5: The best atomic configuration as determined by cost value using 16 FU of Ti and S atoms, and 16 oxygen atoms, viewed down the **c** (left) and **a** (right) lattice directions. Green atoms are Ti, yellow atoms are S, and red atoms are O. The unit cell is outlined in solid lines, while images of the unit cell are shown in dashed lines.

Adding extra oxygens to give 16 FU of Ti and S atoms, and 32 oxygen atoms resulted in the best configuration shown in Figure 6.6, which perhaps provides some insight into the placement of atoms from random starting points. Looking at this figure, and also the other top ten configurations listed in Table B.3 in Appendix B, it is apparent that many of the configurations feature the same approximate positions of atoms as that of the Ti and S runs. However, there appears that there is swapping between single heavy atoms and multiple light atoms, i.e. a Ti atom position is replaced by two or three tightly-bunched O atoms. This is related to the previously stated lack of heavy atoms that might be definitively placed and not moved during the optimisation.

Another feature of these runs that may not be immediately obvious from the figures is that the placement of atoms was quite often physically unfeasible. Atoms might be placed within 1 Å of each other, or at distances that were too close for a particular type of bond (i.e. closer than 1.5 Å for S-O bonds). Ultimately, what these runs show us is that if free atoms are to be added in a system in which there are no outstandingly heavy atoms, it may be best to do so in a stepwise fashion, i.e. adding titanium atoms, fixing their positions before adding sulphur atoms, then fixing those and adding oxygen atoms. This approach was explored, and will be discussed in a later section.

P 1 $2_1/c$ 1; Ti atoms and SO_4 tetrahedra

The runs that included polyhedra proved to be quite troublesome as a result of the tendency of the arrangement of the polyhedra to be entirely dependent on the center

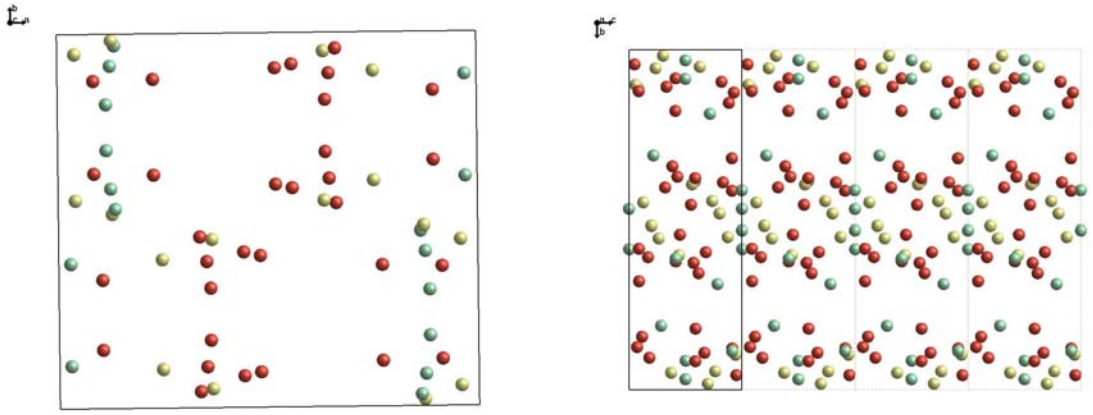

FIGURE 6.6: The best atomic configuration as determined by cost value using 16 FU of Ti and S atoms, and 32 oxygen atoms, viewed down the **c** (left) and **a** (right) lattice directions. Green atoms are Ti, yellow atoms are S, and red atoms are O. The unit cell is outlined in solid lines, while images of the unit cell are shown in dashed lines.

atom. As there is no way of enforcing minimum distances between individual polyhedra and free atoms, the somewhat arbitrary positioning of the oxygen atoms around, for example, sulphur in a sulphate tetrahedron resulted in impossibly close atomic distances. This can be seen in the best atomic configuration for Ti atoms and SO_4 tetrahedra shown in Figure 6.7, as well as the other top ten configurations shown in Table B.4, Appendix B.

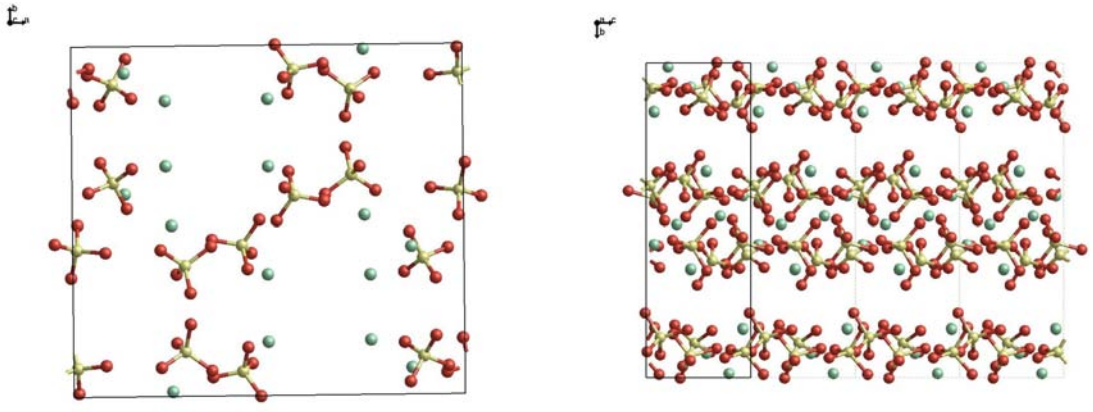

FIGURE 6.7: The best atomic configuration as determined by cost value using 16 FUs of Ti atoms and SO_4 tetrahedra, viewed down the **c** (left) and **a** (right) lattice directions. Green atoms are Ti, yellow atoms are S, and red atoms are O. The unit cell is outlined in solid lines, while images of the unit cell are shown in dashed lines.

Nevertheless, the chains down the **c** axis can still be seen. While this configuration should also be repeated with the addition of free oxygen atoms (an additional three per

formula unit), the already unfeasible results did not offer an incentive for any further calculations.

P 1 $2_1/c$ 1; TiO_6 octahedra and S atoms

Similar to the previous runs of Ti atoms and SO_4 tetrahedra, the runs consisting of TiO_6 octahedra and S atoms suffered from the placement of oxygen atoms becoming unreasonable due to the inability to enforce minimum distance constraints between fragments.

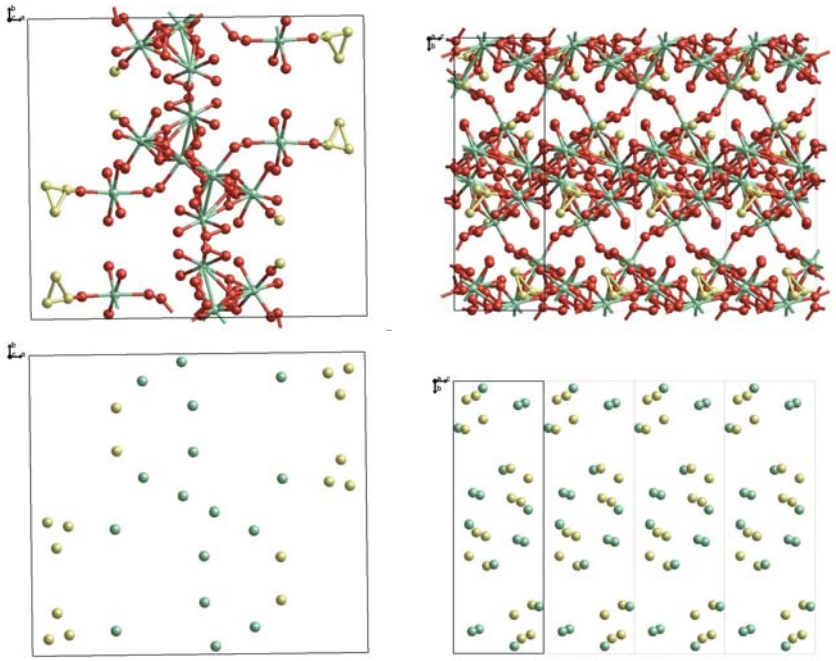

FIGURE 6.8: The best atomic configuration as determined by cost value using 16 FU of TiO_6 octahedra and S atoms, viewed down the **c** (top-left) and **a** (top-right) lattice directions; and with oxygens removed (bottom-left and bottom-right). Green atoms are Ti, yellow atoms are S, and red atoms are O. The unit cell is outlined in solid lines, while images of the unit cell are shown in dashed lines.

Again, the chains can be seen as present down the *c* axis, although there appears to be more occurences of cross-chain linkages by oxygen atoms in the ten best structures according to cost function shown in Appendix B.5.

P 1 $2_1/c$ 1; TiO_6 octahedra and SO_4 tetrahedra

This search could be considered one of the more ambitious, as it relies on the fact that some of the oxygens will undergo merging through dynamical occupancy, eliminating the extra three oxygens per formula unit. However, as can be seen from Figure 6.9 it is clear that the anticipated intervention by the dynamic occupancy algorithm has not occurred, as evidenced by the large number of unshared oxygen atoms.

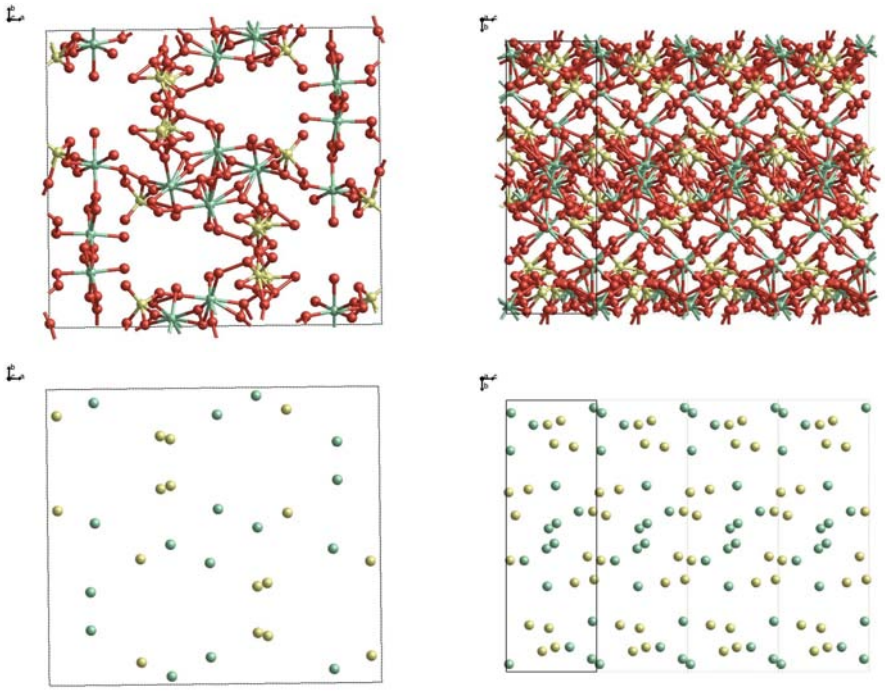

FIGURE 6.9: The best atomic configuration as determined by cost value using 16 FU of TiO_6 octahedra and SO_4 tetrahedra, viewed down the **c** (top-left) and **a** (top-right) lattice directions; and with oxygens removed (bottom-left and bottom-right). Green atoms are Ti, yellow atoms are S, and red atoms are O. The unit cell is outlined in solid lines, while images of the unit cell are shown in dashed lines.

The 'noise' introduced by more oxygens seems to have resulted in an obscured set of chains down the **c** axis, though the densities of the atoms can be seen to follow the expected chain/void positions. The images that have had the oxygen atoms removed show that the hexagonal motif in the **a**-**b** plane is retained, though again, slightly smaller and deformed.

P 1 2_1/c 1; Stepwise addition of Ti, S, and O atoms

As mentioned previously, the addition of all free atoms at the same time tended to produce atomic distances that were physically unreasonable. The addition of atoms in a stepwise fashion is one way of dealing with this difficulty in placing atoms of similar atomic weight.

16 FU of titanium atoms were added first and allowed to move within the unit cell. Due to the smaller amount of atoms being moved, the number of runs and steps within each run were reduced to 100 and 200,000, respectively. Figure 6.10 shows the two main configurations that resulted from the runs; all the configurations falling within the areas were identical but for very slight atomic displacements.

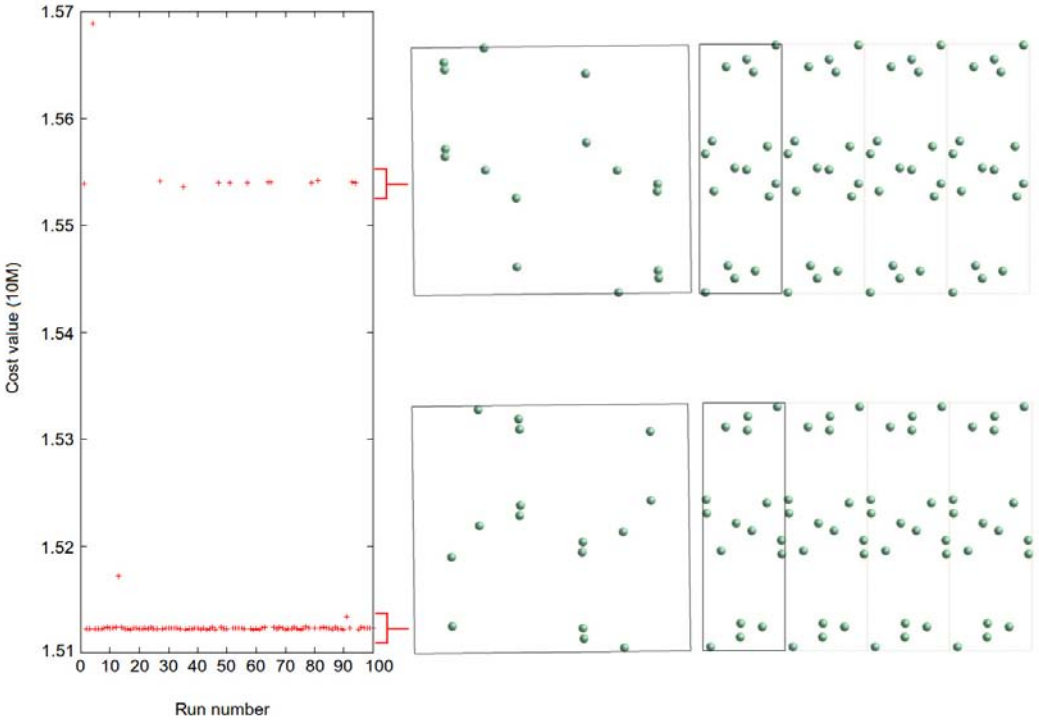

FIGURE 6.10: Graph showing the two distinct configurations resulting from the placement of 16 FU of titanium atoms in the unit cell.

The most interesting feature of Figure 6.10 is the discrete levels of structural configurations that are expressed. As a comparison, Figure 6.11 shows the typical cost/run graph from adding Ti, S, and O free atoms at the same time. The distribution of cost value in this graph shows no evidence of discrete levels of probable configurations. For there to be no clear preferred configuration after so many runs indicates that there is likely not to be enough information in the pattern for a clear cut differentiation between the atoms and their weights. This further rationalises the stepwise procedure as appropriate for this data set.

Continuing the stepwise procedure, the titanium atoms were fixed using the best atomic configuration, and 4 sulphur atoms were introduced and allowed to vary using the same run numbers and steps. Figure 6.12 shows the cost value graph and configurations that resulted from this set of runs. As can be seen from this figure, the three configurations were still quite similar despite the discrete levels of cost associated with them. While some atoms were beginning to be placed at unreasonable distances, it was thought that the addition of oxygen would provide a better indication of which atoms should be removed (i.e. which atoms had the most unreasonable Ti-O or S-O bond distances).

Following on from the above, the sulphur atoms were fixed in their positions and the first of a set of runs designed to introduce the oxygen atoms gradually was initiated. 7

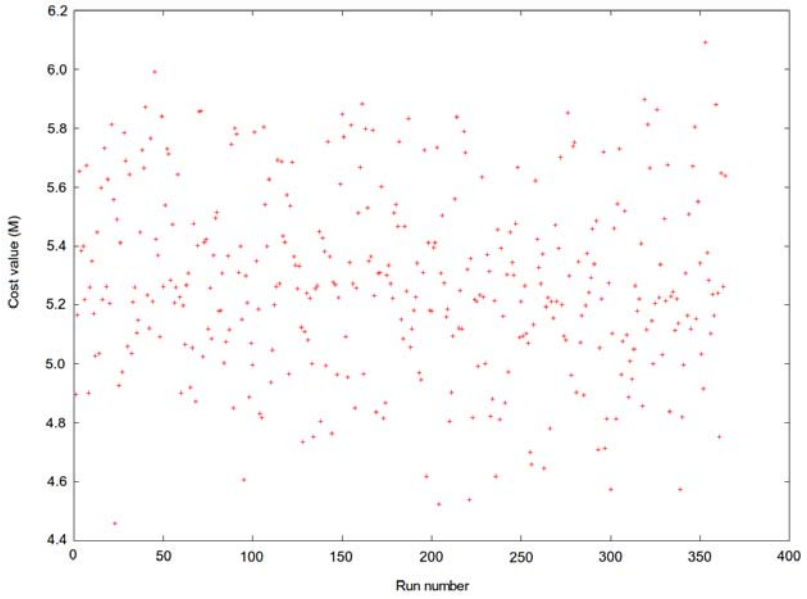

FIGURE 6.11: Graph of cost values for the runs of P 1 $2_1/c$ 1; 16 FU of Ti and S atoms, and 8 O atoms.

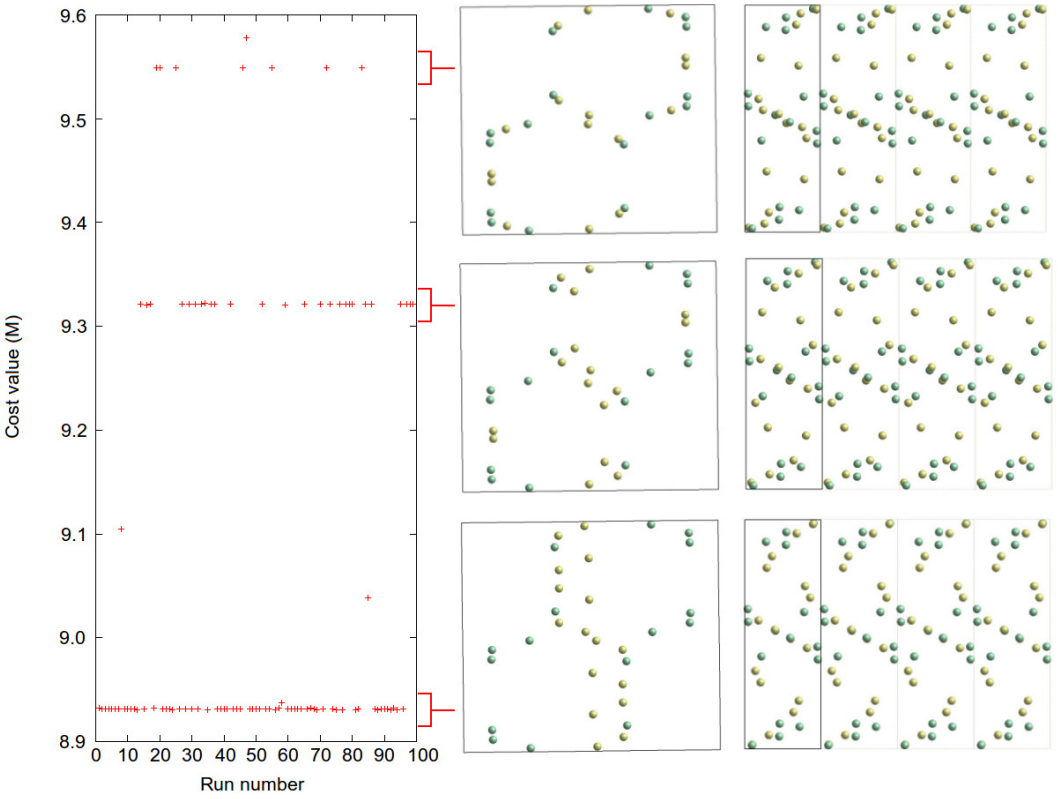

FIGURE 6.12: Graph showing the three similar configurations resulting from the placement of 16 FU of Ti and S atoms in the unit cell and their corresponding cost function plots.

oxygen atoms (the number of oxygens in the formula unit) were added and allowed to optimise, before being fixed and the next 7 being added, and so on until 28 atoms had been added and optimised. Because of the higher number of atoms being introduced at each step, it was thought that a larger number of runs and steps per run should be used in order to ensure sufficient statistics for the evaluation of resulting configurations. To accommodate this, 200 runs of 500,000 steps were used. Figure 6.13 shows the graph of cost value versus run number for the first of this set of runs, with labelled groups of points that correspond to configurations that were repeatedly found with very little difference between successive configurations. Representative configurations of these groups are then shown in Table 6.13.

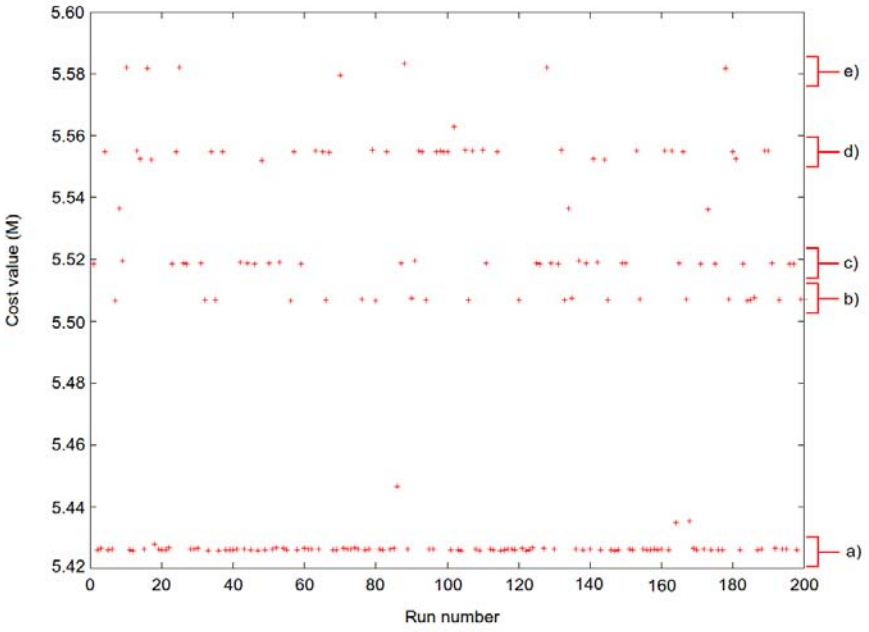

FIGURE 6.13: Graph showing the cost regions of five distinct configurations resulting from the placement of four titanium atoms, four sulphur atoms, and seven oxygen atoms in the unit cell.

As can be seen from the figures contained in Table 6.13, all the configurations are very similar. The previously mentioned hexagon/void motif and chain-type structure is present in all the configurations, reinforcing the earlier results. Unfortunately there did not seem to be any strong indications of octahedra or tetrahedra formed around the sulphur and titanium atoms that might lead to the elimination of some of the physically unreasonable atom placements.

TABLE 6.13: Representative configurations of each of the labelled groups shown in Figure 6.13. Titanium atoms are green, sulphur atoms are yellow, oxygen atoms are red, and hydrogen atoms are white.

Label	Viewed along **c-axis**	Viewed along **a-axis**
a)	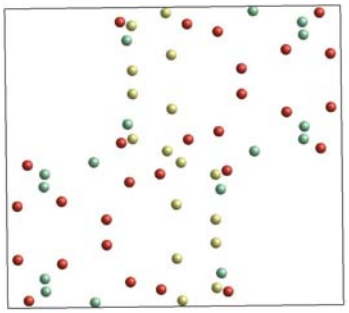	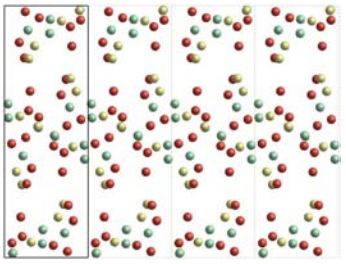
b)	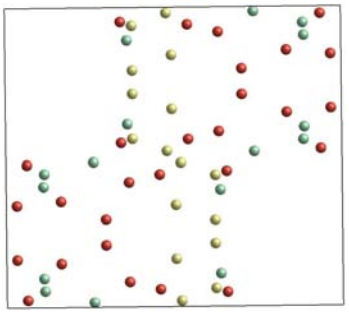	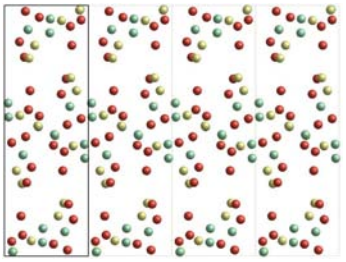
c)	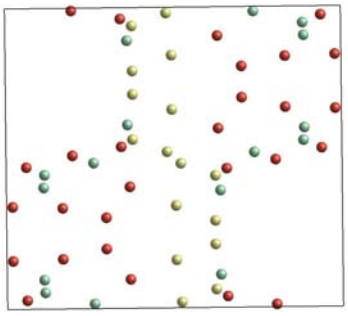	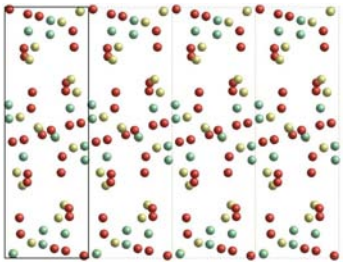
d)	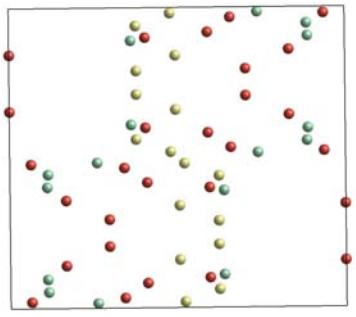	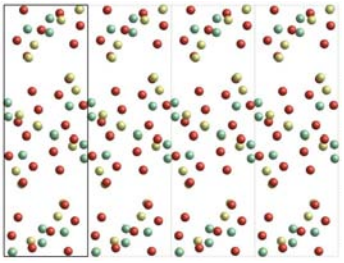

Continued on next page...

Table 6.13 – Continued

Label	**c-axis**	**a-axis**
e)	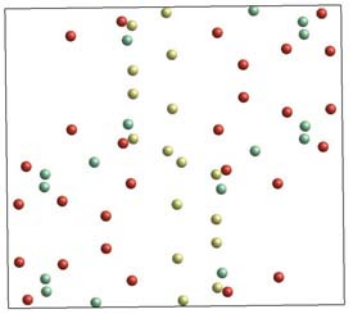	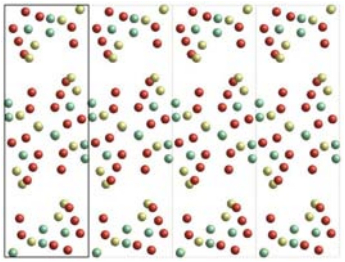

It was found that within each step addition of oxygen atoms that, despite the difference in cost values of repeated configurations, their structures were very similar. Thus for the sake of brevity only the best configurations (determined by cost value) will be presented, and these are shown in Figure 6.14. With the progression from 7 through to 28 oxygens added, it can be seen that the suggestion of chains becomes more and more indistinct, eventually resulting in a very congested unit cell. This makes it very difficult to separate any significant structure from the large numbers of atoms that appear too close together, or in positions that do not suggest expected, regular geometries, such as tetrahedra or octahedra.

TABLE 6.14: Best configurations of the sequence of stepwise addition of oxygen atoms, as determined by cost value function. Titanium atoms are green, sulphur atoms are yellow, oxygen atoms are red, and hydrogen atoms are white.

Label	Viewed along **c-axis**	Viewed along **a-axis**
4 Ti, 4 S, and 14 O atoms	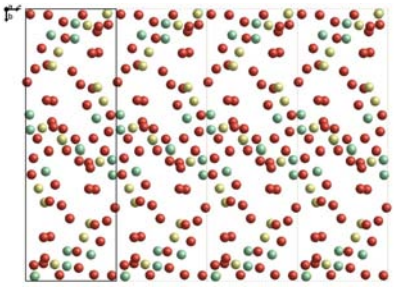	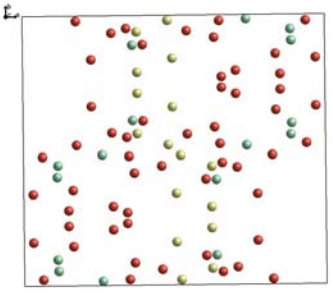

Continued on next page...

Table 6.14 – Continued

Label	c-axis	a-axis
4 Ti, 4 S, and 21 O atoms	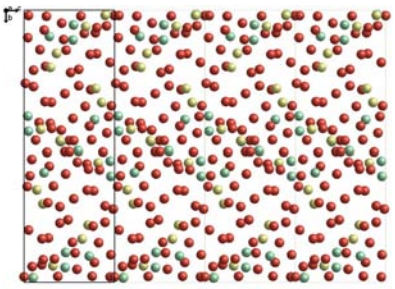	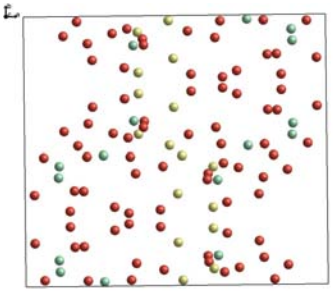
4 Ti, 4 S, and 28 O atoms	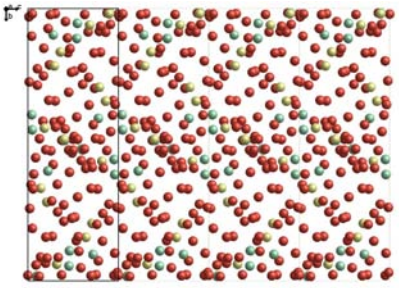	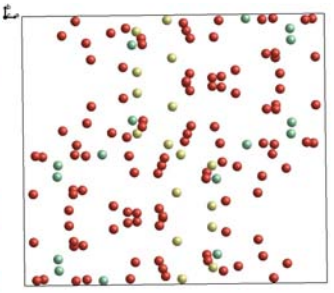

6.3.3 Further testing

While the initial FOX structure determination did not yield any definitive result, there existed the opportunity to revisit some of the previous parameters and extend the experiments to see if any better solution might be found. The main parameters under re-examination were the unit cell and the space group.

Reconsideration of the unit cell led to the examination of the second most likely unit cell seen in Table 6.3: a=5.544 Å, b=16.688 Å, c=19.418 Å, and β=105.94°. A space group determination was then performed, resulting in the list of likely space groups seen in Table 6.15.

Again, the ambiguity that is inherent in the space group determination procedure is present, although a more noticeable jump in R_{wp} values does occur after the top three results. As a result of this, all three space groups were subsequently trialled. Citing the failure of complicated fragment-based methods in the previous experiments, it was reasoned that the stepwise addition of Ti, S, and O atoms would provide more reliable results. Two different schemes for the stepwise addition of atoms were used: the first

TABLE 6.15: List of space groups for $TiOSO_4 \cdot 2H_2O$ in order of GoF, determined by the FOX space group explorer algorithm.

Space Group	$\mathbf{R}_{wp}$	**GoF**
P 1 2_1/c 1	5.53%	127.632
P 1 c 1	5.57%	129.735
P 1 2/c 1	5.57%	129.735
P 1 2_1/a 1	5.75%	138.004
P 1 a 1	5.78%	139.843
P 1 2/a 1	5.78%	139.843
P 1 2_1 1	5.85%	143.724
P 1 2_1/m 1	5.85%	143.724
P 1 2 1	5.89%	145.572
P 1 m 1	5.89%	145.572
P 1 2/m 1	5.89%	145.572
P 1	5.87%	151.256
P $\bar{1}$	5.87%	151.257
P 1 2_1/n 1	6.11%	155.668
P 1 n 1	6.14%	157.531
P 1 2/n 1	6.14%	157.531

TABLE 6.16: Numbers of runs and trials within each run for the two different atom addition schemes.

Run scheme	**Scheme step**	**Runs**	**Iterations**
(Ti + S) + O	Ti + S	200	500000
	O	200	500000
Ti + S + O	Ti	100	200000
	S	100	200000
	O	200	500000

being simultaneous placement of Ti and S followed by placement of O, and the second being separate placement of all different elements.

In total, 4 Ti, 4 S, and 28 O atoms were added, corresponding to 16 formula units of $TiOSO_4 \cdot 2H_2O$. The numbers of runs, and the iterations in each run are shown in Table 6.16.

Finally, it was decided that running the previous unit cell with the new space groups and run schemes would provide a more complete data set. Thus, the total list of runs is shown in Table 6.17. It should be noted that the 'Atom addition' method of labelling means that, for example, '(Ti + S) + O' corresponds to the simultaneous optimisation of Ti and S atoms, followed by the fixing of these atoms and the addition and optimisation of oxygen atoms. Similarly, 'Ti + S + O' corresponds to the optimisation of Ti atom positions, followed by that of S atom positions, and finally O atom positions.

TABLE 6.17: Numbers of runs and trials within each run for the two different atom addition schemes.

Unit cell	Space group	Atom configuration	Atom addition
a=5.544 Å, b=16.685 Å, c=18.671 Å, β=90.65°	P 1 2_1/c 1	Ti + S	Simultaneous
		Ti + S + 4O	Simultaneous
		Ti + S + 8O	Simultaneous
		Ti + SO4	Simultaneous
		TiO6 + S	Simultaneous
		TiO6 + SO4	Simultaneous
		Ti + S + O	Stepwise
	P 1 2/c 1	Ti + S + O	Stepwise
	P 1 c 1	Ti + S + O	Stepwise
a=5.536 Å, b=16.722 Å, c=19.456 Å, β=105.97°	P 1 2_1/c 1	(Ti +S) + O	Stepwise
		Ti + S + O	Stepwise
	P 1 2/c 1	(Ti + S) + O	Stepwise
		Ti + S + O	Stepwise
	P 1 c 1	(Ti + S) + O	Stepwise
		Ti + S + O	Stepwise

For the sake of brevity, the detailed analysis of results that was shown in Figure 6.10-6.13 for the stepwise addition of T, S, and O will not be repeated for each of the new runs shown in Table 6.17. Instead, the top result from the final run of each will be presented. System labels will follow this convention:

- '105' or '90' to indicate the different unit cells;
- The space group of the system;
- The order and method by which the atom positions were optimised, following the convention set out in Table 6.16.

So for example: a run with unit cell a=5.536 Å, b=16.722 Å, c=19.456 Å, β=105.97° of space group P 1 2_1/c 1, which optimised the positions of Ti and S atoms simultaneously then O atoms separately, would be designated '105 – P 1 2_1/c 1 – (Ti + S) + O'. As a further example, a run with unit cell a=5.544 Å, b=16.685 Å, c=18.671 Å, β=90.65° of space group P 1 c 1, which optimised all atoms separately, would be designated '90 – P 1 c 1 – Ti + S + O'. Tables 6.18 and 6.19 show the top results from each atom and space group configuration for the two different unit cells.

TABLE 6.18: The best results from the '105' unit cell runs in FOX as determined by cost value function

Label	Viewed along **b-axis**	Viewed along **a-axis**
105 – P 1 2_1/c 1 – Ti + S + O	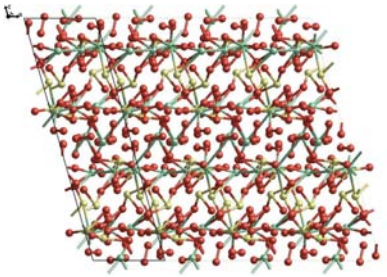	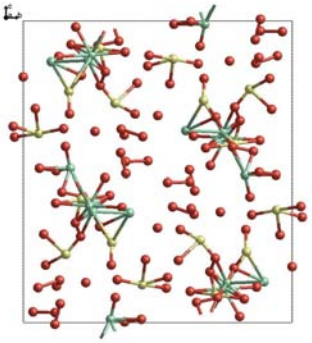
105 – P 1 2_1/c 1 – (Ti + S) + O	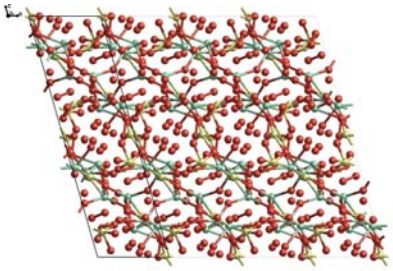	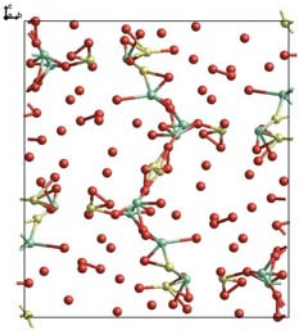
105 – P 1 2/c 1 – Ti + S + O	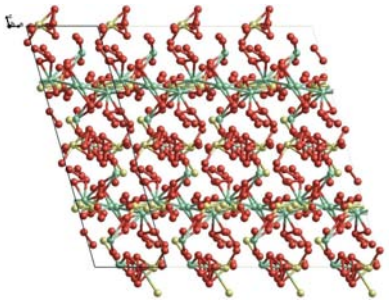	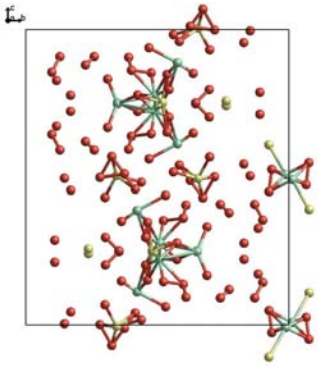
105 – P 1 2/c 1 – (Ti + S) + O	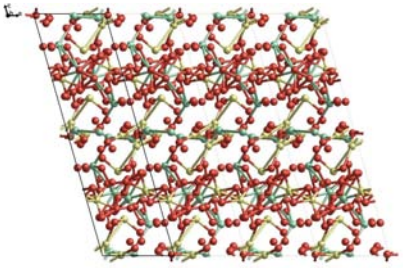	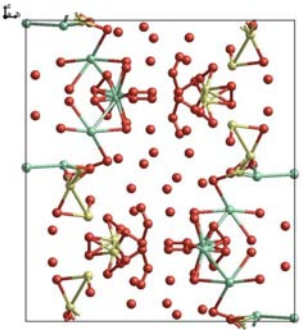

Continued on next page...

Table 6.18 – Continued

Label	Viewed along **b-axis**	Viewed along **a-axis**
105 – P 1 c 1 – Ti + S + O	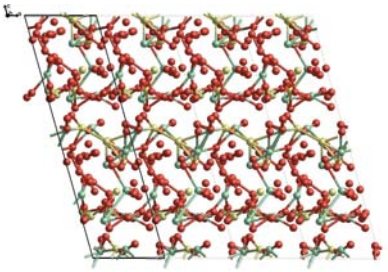	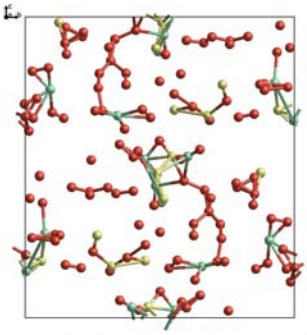
105 – P 1 c 1 – (Ti + S) + O	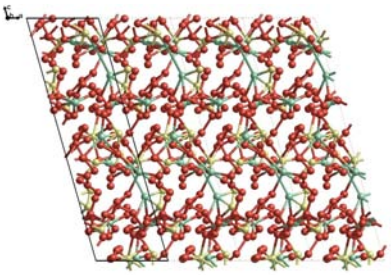	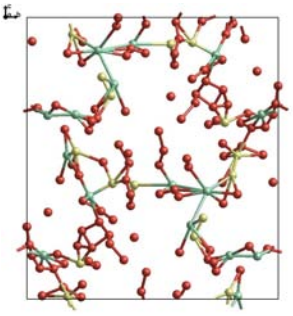

TABLE 6.19: The best results from the '90' unit cell runs in FOX as determined by cost value function.

Label	**a-axis**	**c-axis**
90 – P 1 2_1/c 1 – Ti + S + O	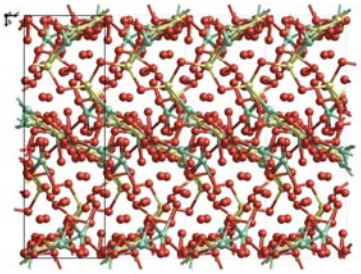	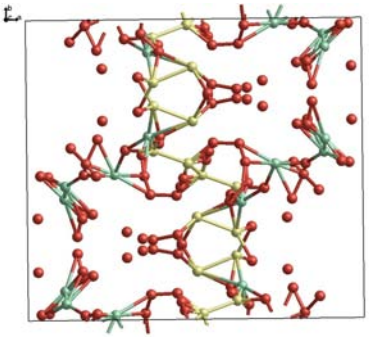
90 – P 1 2_1/c 1 – (Ti + S) + O		

Continued on next page...

Table 6.19 – Continued

Label	a-axis	c-axis
90 – P 1 2/c 1 – Ti + S + O	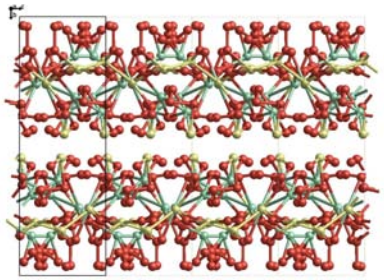	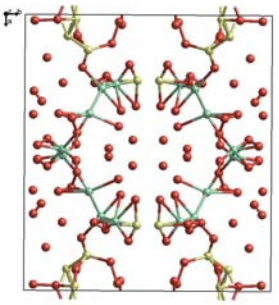
90 – P 1 2/c 1 – (Ti + S) + O	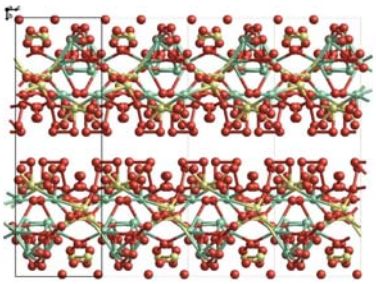	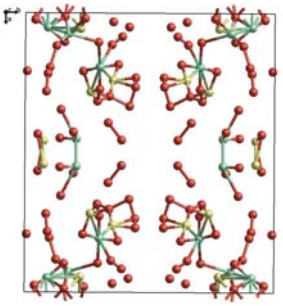
90 – P 1 c 1 – Ti + S + O	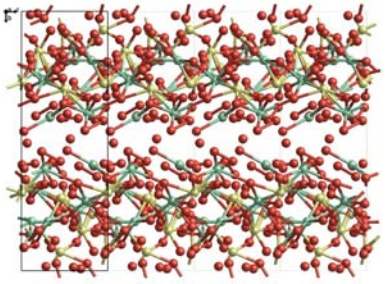	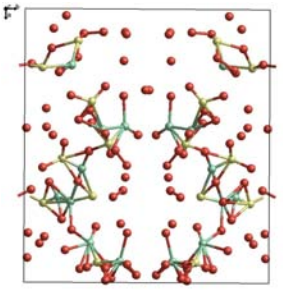
90 – P 1 c 1 – (Ti + S) + O	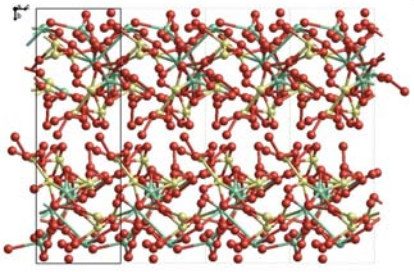	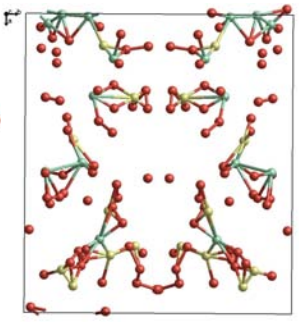

6.3.4 Discussion

From examining the atomic configurations shown in Figures 6.3-6.12 and Tables 6.13, 6.18, and 6.19, we can see that no definitive atomic positions have been determined.

However, we can certainly observe some repeated characteristics throughout the series of calculations:

- Magnitude of the unit cell in the short direction suggests chains of titanium atoms linked by oxygens, as seen in many of the other analogous structures;
- A tendency towards cleavage planes between these chains;
- Formation of quasi-hexagonal arrangements of titanium and sulphur atoms in the axial plane that does not include the short axis;
- Formation of voids down the centres of these hexagonal arrangements, which may incorporate non-framework H_2O.

The repeated formation of what appear to be chains of atoms in the short axis direction with cleavage planes between them is very similar to many of the titanyl sulfate and basic zirconium sulfate structures; in particular, the structure of the basic zirconium sulfate $Zr(OH)_2SO_4{\cdot}3H_2O$, as seen in Figure 1.11. This resemblance is made a lot more obvious if we hide the hydrogen and oxygen atoms. Figure 6.14 shows a comparison between a structure determined by FOX, as previously shown in Figure 6.3, and the structure of $Zr(OH)_2SO_4{\cdot}3H_2O$ after having had its oxygen and hydrogen atoms hidden.

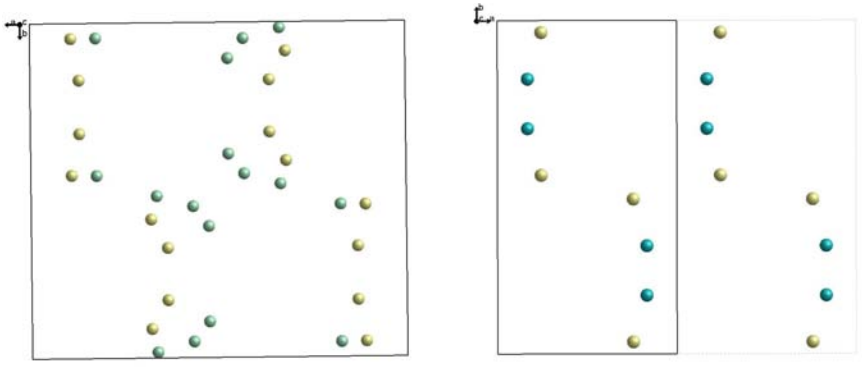

FIGURE 6.14: (left) The best atomic configuration as determined by cost value using 16FUs of free Ti and S atoms; (right) The structure of $Zr(OH)_2SO_4{\cdot}3H_2O$ (with unit cell doubled in the **a** direction, indicated by the dashed outline) with oxygen and hydrogen atoms hidden. Green atoms are Ti, yellow atoms are S, and blue atoms are Zr.

From Figure 6.14, there can be seen to be some similarity in the way the atoms are distributed within the different unit cells. However, it can also be seen that FOX has difficulty in placing the atoms definitively, with sulphur and titanium atoms placed interchangeably and a generally less well-defined sense of atom placement evident from the unphysical distances between atoms. It is difficult to ascribe the fundamental cause of this inability to place the atoms with reasonable certainty. As suggested previously,

there may be a barrier in the form of the diffraction patterns not containing enough data to overcome the loss incurred when collapsing from a three-dimensional data set (as in single crystal diffraction) to the one-dimensional data set of a powder diffraction pattern. In addition, preferred orientation, while thought to be minimised through good sample preparation and appropriate XRD geometry, may still be causing interference. Ultimately, while we can say with reasonable certainty that particular geometrical motifs such as TiO_6 octahedra, SO_4 tetrahedra, repeating chains and layers are likely to appear in the final structure of $TiOSO_4{\cdot}2H_2O$, direct-space methods were not able to provide a definitive structural determination.

6.4 $TiOSO_4{\cdot}H_2O$ case study

With the ambiguity of the results obtained from the method described in the previous sections, it was thought that there was a need for a case study of a known material to validate their use. In this case, the material used was $TiOSO_4{\cdot}H_2O$, as samples had been examined with synchrotron powder XRD at the Australian Synchrotron under the same conditions as $TiOSO_4{\cdot}2H_2O$. The thinking was that if a successful structure determination from powder diffraction could be completed assuming no knowledge of the previously determined structure, then some of the difficulty in achieving a structural determination of $TiOSO_4{\cdot}2H_2O$ could be ascribed to its unique challenges, rather than a failure in the methodology adopted.

6.4.1 Methodology

Indexing of the unit cell was achieved using the first 20 strong peaks in the pattern, yielding only one recommended result with orthorhombic unit cell parameters a=5.1266 Å, b=8.6031 Å, and c=9.8187 Å. Following the unit cell determination, space group assignment was attempted. Some ambiguity exists within the literature as to the exact space group assignment of $TiOSO_4{\cdot}H_2O$. Ahmed *et al.* [15] suggest that the most correct structure is found by using *Pnma* and allowing for anisotropic temperature factors to describe disorder in some oxygen positions. However, Gatehouse *et al.* [13] ascribe a space group of $P2_12_12_1$. In this case, the inclination is to follow the determination presented by Gatehouse *et al.*, as the use of single crystal diffraction is known to be much more accurate in structural determinations.

In our case, the top 20 space groups for $TiOSO_4{\cdot}H_2O$ as determined by FOX's space group explorer function are listed in Table 6.20. It is important to recall the ambiguity of space group determination which prevents the acceptance the first space group result

TABLE 6.20: List of space groups for $TiOSO_4 \cdot H_2O$ in order of GoF, determined by the FOX space group explorer algorithm.

Space Group	$\mathbf{R}_{wp}$	**GoF**
P 1	4.54%	68.845
P $\bar{1}$	4.76%	75.642
P 1 2_1 1	4.79%	75.740
P 1 2_1/m 1	4.79%	75.740
P 1 2 1	4.81%	76.377
P 1 m 1	4.81%	76.377
P 1 2/m 1	4.81%	76.377
P 2_1 2_1 2_1	4.83%	76.658
P 2 2_1 2_1	4.83%	76.672
P 1 $_1$/c 1	4.83%	76.939
P 1 1 2_1	4.83%	77.126
P 1 1 2_1/m	4.83%	77.126
P 1 1 2_1/n	4.84%	77.327
P 2_1 2 2_1	4.85%	77.335
P 2 2 2_1	4.85%	77.349
P 1 c 1	4.85%	77.526
P 1 2/c 1	4.85%	77.526
P 2_1 1 1	4.88%	78.841
P 2_1/m 1 1	4.88%	78.841
P 2_1 c n	4.90%	79.002

as being the real one. This is especially important in this case, given the very close values of R_{wp} throughout the table. If we discard the *P1* and *P1̄* space groups, we are left with the rest of the top 20 space groups all being within 0.11% R_{wp} of each other with no large gaps between solutions. This makes the question of which space group to choose even more ambiguous than the case of $TiOSO_4 \cdot 2H_2O$, whose range was slightly larger at 0.55% R_{wp}. While a thorough investigation of each space group would be the preferred course of action, for the sake of brevity we will assume that we have investigated the first five space group solutions and found incomplete results.

Once the $P2_12_12_1$ space group was adopted, the structure determination was surprisingly quick, converging in less than 500,000 steps with 1 Ti, 1 S, and 6 O atoms free to move within the cell. The structure produced from this determination is shown in Figure 6.15, next to the structure proposed by Gatehouse *et al.*

While the determination of hydrogen atom positions was not possible, it would not be unreasonable to assume that they could be placed using either a short DFT simulation with the Ti, S, and O atoms frozen, or by logic and experience alone. At this point, the structural determination would be considered complete, and structure refinement would be commenced using a separate program such as GSAS [193] or FullProf [86].

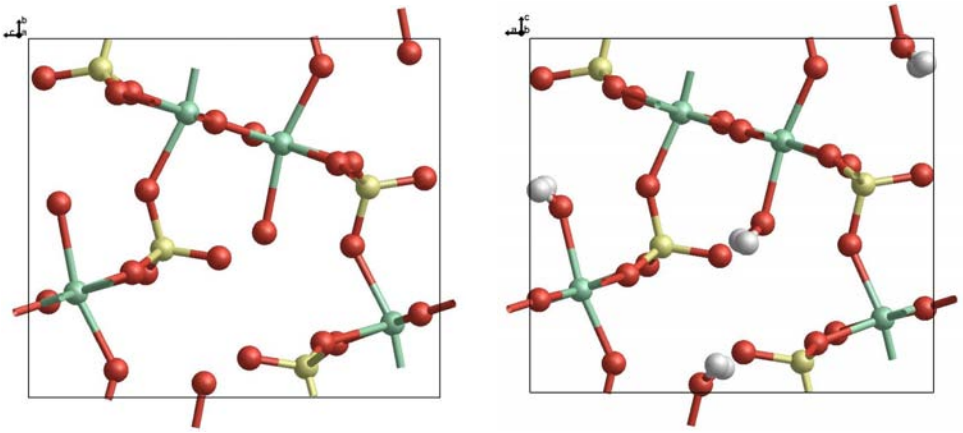

FIGURE 6.15: Atomic configurations of $TiOSO_4 \cdot H_2O$ determined by the FOX software (left), and by Gatehouse *et al.* (right) [13].

6.5 External partnerships

The incomplete nature of the structural determination of $TiOSO_4 \cdot 2H_2O$ encouraged us to seek collaboration with parties outside of Curtin University. A message was posted to the SDPD Yahoo newsgroup maintained by Armel Le Bail [194], in which help was sought from the community. A summary of the process of external involvement is shown in the following sections.

6.5.1 Dr. Holger Putz

The first collaboration was with Dr. Holger Putz, one of two producers of the commercial structure determination software 'Endeavour'. Correspondence with Dr. Putz culminated with a structure which he was not confident to promote as a solution. In light of viewing the structure, shown in Figure 6.16, the reasons behind his reticence are obvious. Bond distances are physically unreasonable, and the placement of the atoms does not seem to suggest any kind of chemically ordered structural motifs, such as chains or regular bond patterns.

It was therefore unfortunate, but necessary, to discard this solution and extend an invitation to one of the other respondents to the initial request for external help. The next respondent was chosen as a result of his obvious expertise in the area: Professor Armel Le Bail.

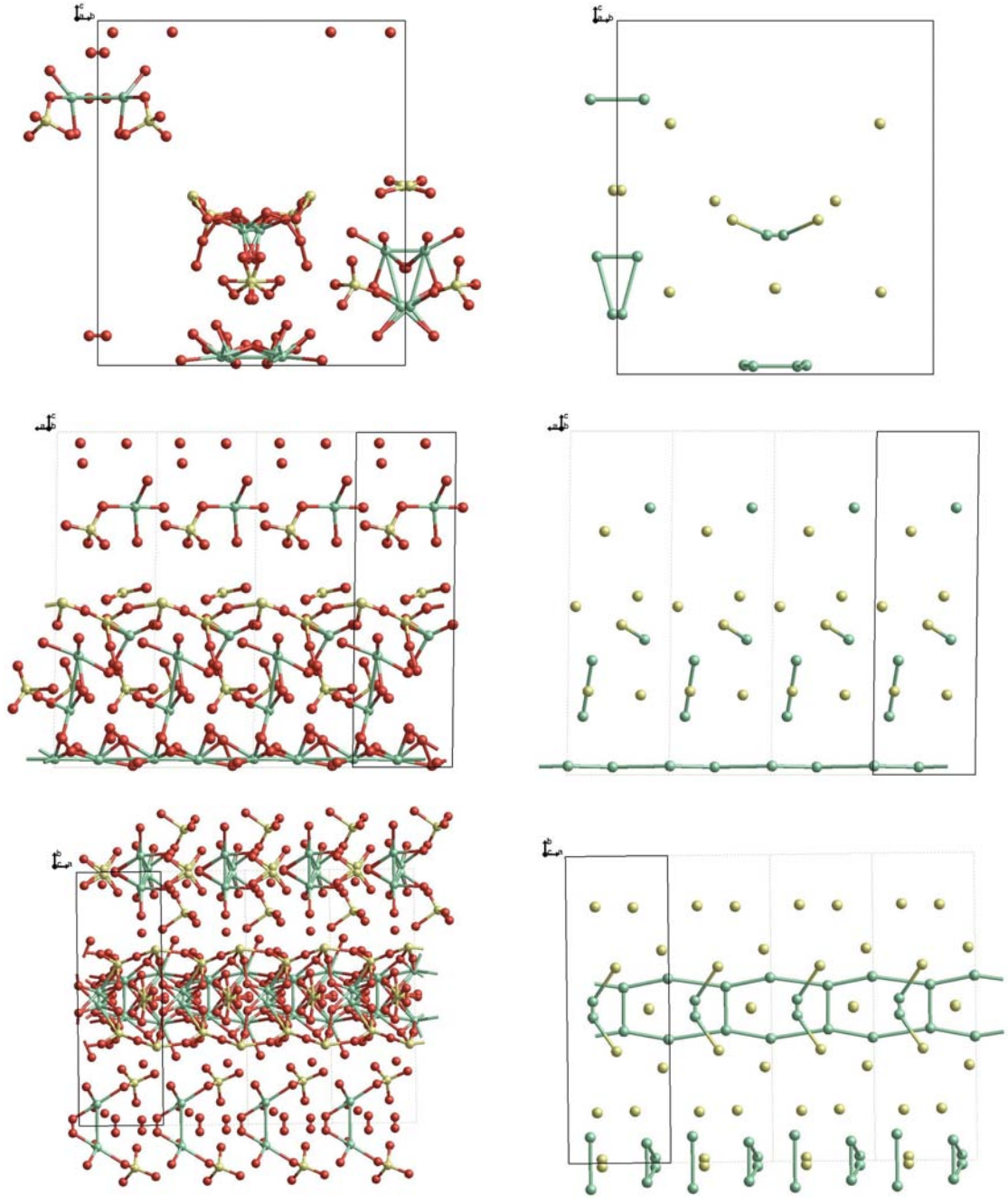

FIGURE 6.16: Final structure proposed by Dr. Holger Putz using his Endeavour software as viewed along the three crystallographic directions. Figures on the right are the same as those on the left, but with oxygen atoms removed for clarity. Some atoms may have appeared to move due to the image conventions for bonds extending across unit cells.

6.5.2 Prof. Armel Le Bail

6.5.2.1 Indexing and space group estimation

Prof. Le Bail performed indexing using the McMaille [195] software with both the first 20 and 60 peaks. Indexing with 20 peaks gave the following unit cell: a=18.6664 Å, b=16.6794 Å, c=5.5432 Å, α=90.000 °, β=90.643 °, γ=90.000 °. Indexing with 60 peaks gave almost exactly the same unit cell: a=18.6665 Å, b=16.6828 Å, c=5.5436 Å, α=90.000 °, β=90.642 °, γ=90.000 °.

From this unit cell, space group determination was attempted using the Fullprof software suite. It was concluded that the most likely space group of the unit cell given above would be P 1 2_1/n 1, "However, the gain on R_P if compared to results [using] P 1 2_1/c 1 and P 1 2_1/a 1 is small (0.5%)" pointing to the fact that peaks that might provide a more definite answer to the space group are weak.

6.5.2.2 Structure determination

Attempts at structure determination were performed with the ESPOIR software [80]. Prof. Le Bail worked off the assumption that the number of formula units was 16 based on the cell volume and comparison to $TiOSO_4 \cdot H_2O$ and $TiOSO_4$ cell volumes and densities. ESPOIR can be used similarly to FOX, in that polyhedra can be used as building blocks, or a mode can be invoked which allows atoms to move around the cell independently. The former gave no convincing results when used with SO_4 tetrahedra and TiO_6/TiO_5 polyhedra, while the latter gave a similar lack of a coherent structure, even when atoms were added or subtracted based on Fourier difference maps.

The SHELX software [196] was also used with both direct methods and Patterson maps, using both full and selective data sets (full being all reflections, selected being those that did not show overlap). Unfortunately, a similar lack of reasonable structures resulted. At the end of the first report, Prof. Le Bail stated that all that was left to do was to keep trying, "But the fact is that the case is difficult."

After further discussion, the structure determination was continued in the second report, where a return to the use of the free atom mode in the ESPOIR software converged to build a set of heavy atom (e.g. Ti and S) positions. Figure 6.17 shows these positions.

While fixing these heavy atom positions and allowing 28 oxygen atoms to optimise did not provide any reasonable oxygen positions, Prof. Le Bail did find some success in inserting atoms manually. It was apparent that the interatomic distances of the Ti-Ti, Ti-S, and S-S pairs were such that the insertion of oxygen atoms resulted in a clear,

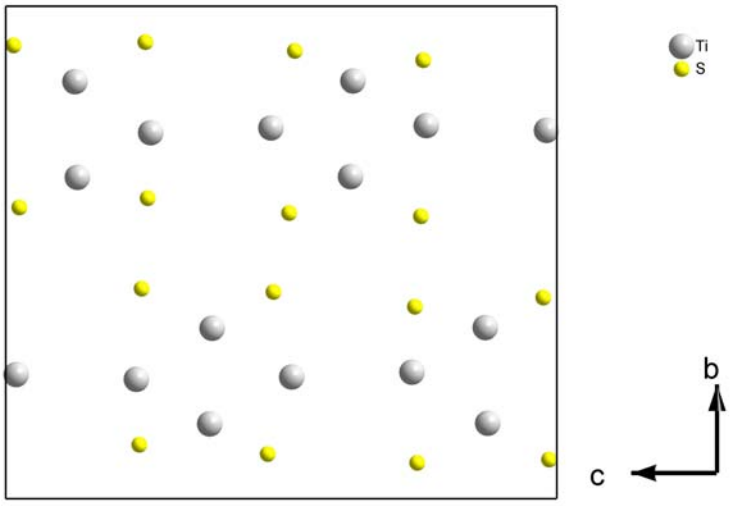

FIGURE 6.17: Figure showing the converged placement of heavy atoms Ti (grey) and S (yellow), reproduced from Prof. Le Bail's report. [197]

albeit partial, structural model. This partial model, formula $Ti_4S_4O_{15}$, is shown in Figure 6.18.

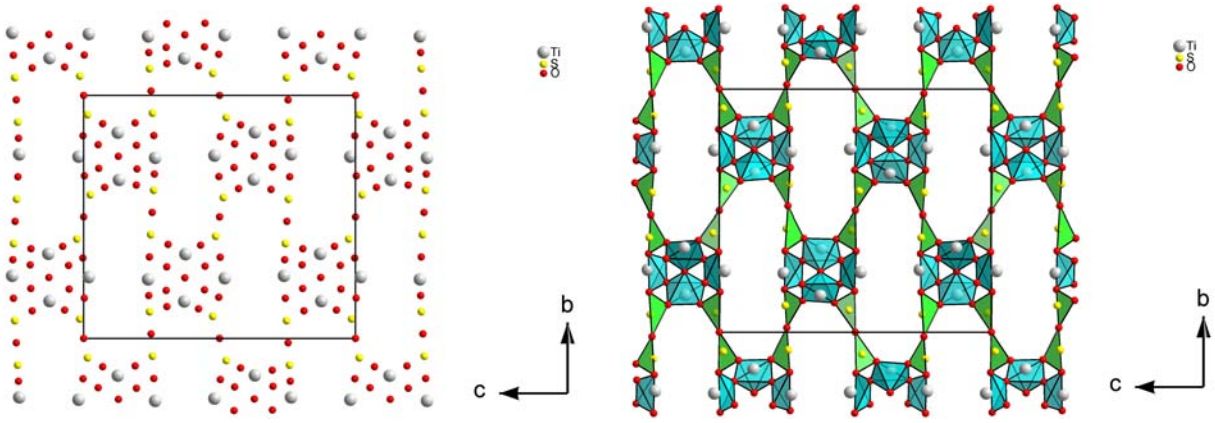

FIGURE 6.18: (left) Structure shown in Figure 6.17 with oxygen atoms (red) placed manually based on chemical reasoning by Prof. Le Bail; (right) Same structure showing the incomplete polyhedra present, reproduced from Prof. Le Bail's report. [197]

This model was used for the Rietveld refinement with FULLPROF [86, 198]. Within the refinement, the two large, typical peaks were discarded due to their weights dominating the refinement process. The final structure, based on the addition of oxygens during the refinement process through analysis of the Fourier map, is shown in Figure 6.19.

However, it can be seen that there are still some incomplete polyhedra. The final comment in Prof. Le Bail's report made these statements:

"Relaxing everything by removing the constraints led to crazy distances. It was not possible to improve the model. It is believed that the synchrotron

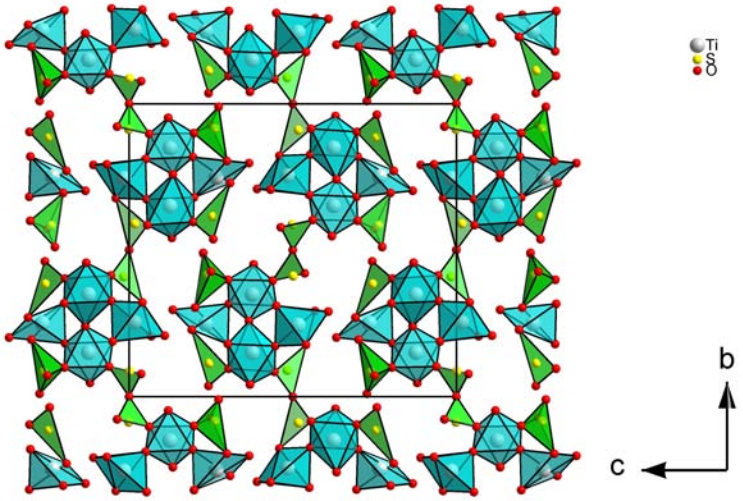

FIGURE 6.19: Figure showing the addition of O atoms (red) to complete the polyhedra around heavy atoms Ti (grey) and S (yellow), reproduced from Prof. Le Bail's report. [197]

> pattern is corrupted by a huge preferred orientation due to the acicular crystal shape. However, attempts to refine with various orientation choices could not improve the fit better than 3% on R_P and R_{WP}."

While it is reasonable to assume that Prof. Le Bail's solution has a basis in reality – his solution is, in all likelihood, the best candidate structure presented in this thesis – ultimately it was concluded that the data does not contain enough information to provide a complete structural determination with no ambiguity in atomic positions.

6.6 Conclusions

In this chapter we have presented the results from our attempts at the structure determination of $TiOSO_4 \cdot 2H_2O$ from the powder diffraction patterns discussed in chapter 4. In accordance with standard SDPD procedure, we have demonstrated an exhaustive indexing procedure using the synchrotron powder diffraction patterns obtained from the Australian Synchrotron, and backed up by those obtained from the Advanced Photon Facility. We have shown the space group determination step and the inherent ambiguity that led to the inclusion of multiple space group settings in the subsequent exploration of structures using direct-space methodology. A broad range of results were shown, calculated using a variety of molecular fragments and atomic arrangements, which, while inconclusive, showed a tendency towards repeated structural motifs. In the face of these inconclusive results, a determination of $TiOSO_4 \cdot H_2O$ using

a synchrotron diffraction pattern was completed assuming no prior knowledge of the structure, suggesting that the methodology was sound and the data was the source of the ambiguity.

Correspondence with two external crystallographers, Dr. Holger Putz and Prof. Armel Le Bail, has been summarised. While Dr. Putz was unable to reach a definitive conclusion, Prof. Armel Le Bail's efforts resulted in a structure that, despite being unable to be refined, made chemical sense. The overall comments from both of the external partnerships were that the data was not of sufficiently high quality to be useful in the structure determination.

Chapter 7

Conclusions

The aim of the work described in this thesis was to determine the structure of $TiOSO_4 \cdot 2H_2O$. While this aim was not completed in its entirety, a great deal of information has been gleaned from the studies performed.

Chapter 4 illustrated the experimental approach to the structure solution. The preparation of $TiOSO_4 \cdot 2H_2O$ samples from amorphous $TiOSO_4$ was presented, showing the difficulty in assuring the growth of a particular crystal product in a capillary environment. *Ex-situ* diffraction patterns recorded using conventional laboratory X-ray diffractometers were used to confirm the successful single-phase production of $TiOSO_4 \cdot 2H_2O$. Diffraction patterns recorded at the Australian Synchrotron and the Advanced Photon Source were also presented. Despite preparation designed to eliminate preferred orientation effects (grinding, spinning the sample, etc.) these showed a tendency towards poor quality not in accordance with the high resolution ordinarily achieved by synchrotron radiation. The Debye-Scherrer rings recorded using the area detector at the Advanced Photon Source were reported not to contain the variable intensity that would be indicative of preferrered orientation, thus the reason behind the relatively poor diffraction data was proposed to be poor crystallinity of the sample. Regardless, the synchrotron diffraction patterns obtained during this project are the highest quality known to have been collected for $TiOSO_4 \cdot 2H_2O$. Finally, a neutron diffraction pattern was produced by preparing a sample of $TiOSO_4 \cdot 2D_2O$ using deuterated sulfuric acid. While this diffraction pattern was not of the best quality due to a significant hydrogen background, the peaks were clearly able to be identified in the pattern.

An *in-situ* study of the growth of $TiOSO_4 \cdot 2H_2O$ crystals was completed successfully, and an analysis of its kinetics showed a single step process with typical induction, reaction, and equilibrium states. The *in-situ* patterns showed the formation of additional peaks

not seen in the *ex-situ* diffraction patterns, which were thought to be indicative of some kind of flexibility in the structure or meta-stable phases present in solution, though any formal conclusions based on these observations were hard to justify.

Chapter 5 explored the use of computational chemistry methods used to develop and explore candidate structures for $TiOSO_4{\cdot}2H_2O$. The process of parameter optimisation for density functional theory calculations was shown in detail through the development of pseudopotentials and basis sets for the systems being studied. These parameters were then tested and validated on the model structures of two TiO_2 polymorphs, rutile and anatase, with the optimised structures comparing favourably to previous literature results. Following on from these validations, the more complex systems of the two known titanyl sulfates, $TiOSO_4$ and $TiOSO_4{\cdot}H_2O$, were used to test the transferability of the basis sets and pseudopotentials. These are the first reported computational studies of these two systems, and show a well-converged set of energies, unit cell parameters, and atomic positions.

From the foundations provided by the development of the pseudopotential and basis set parameters, a series of exploratory calculations were performed which aimed to develop a hypothetical dihydrate structure. This was done *via* three different methods: extrapolation the structural changes between $TiOSO_4$ and $TiOSO_4{\cdot}H_2O$ to apply them to a new $TiOSO_4{\cdot}2H_2O$ structure; the addition of a formula unit of water to the $TiOSO_4{\cdot}H_2O$ structure; and the conversion of zirconyl sulphate hydrates into titanyl sulphate hydrates *via* the removal of double hydroxyl bridges between zirconium atoms and conversion of said zirconium atoms into titanium atoms. These studies provided us with a wide variety of configurational polymorphs of $TiOSO_4{\cdot}2H_2O$ that could be optimised by both forcefield methods (GULP) and first principles methods (SIESTA). These structures showed a considerable overlap in common features, such as titanium-oxygen chains down the short axis, as well as hydrogen bonding between chains; characteristics that would certainly contribute towards the needle-like crystal morphology seen in experiments. The energies of the dihydrate structures, when used to determine the enthalpy of reaction for the addition of two water molecules to the anhydrate structure, showed that they were within a reasonable energetic range. These hypothetical dihydrates were then used as a template for the input of chemical fragments in the subsequent structure determination from powder diffraction step.

Chapter 6 showed various attempts at structure determination from powder diffraction (SDPD) using the powder diffraction patterns discussed in Chapter 4 and the hypothetical structures determined in Chapter 5. The indexing of the pattern was subjected to various tests using multiple diffraction pattern sets, and showed a consistency that would suggest that the correct unit cell has been calculated. The

determination of the space group showed a typical ambiguity, leading to a larger configurational space to sample in the subsequent structure exploration. Structure determination was performed over a series of runs, exploring multiple densities and various combinations of molecular fragments, giving a broad range of results. Unfortunately these results were inconclusive beyond some general statements that could be made about structural motifs that may be present in the final structure. Following these inconclusive results, a determination of $TiOSO_4 \cdot H_2O$ using a synchrotron diffraction pattern was completed assuming no prior knowledge of the structure, suggesting that the methodology of SDPD was sound and the data was the source of the ambiguity.

To further investigate this hypothesis, correspondence with two external crystallographers, Dr. Holger Putz and Prof. Armel Le Bail, was initiated. While Dr. Putz was unable to reach a definitive conclusion, Prof. Armel Le Bail's efforts resulted in a structure that, despite being unable to be refined, made chemical sense. The overall comments from both of the external partnerships were that the data was not of sufficiently high quality to be useful in the structure determination. While it is somewhat disappointing that a full structural determination has not been able to be completed, this work has shown that there are benefits to a combined computational and experimental approach.

Future work on this system would almost certainly benefit from an investigation into how to obtain the best quality diffraction data possible. While previous literature was clear in its inability to produce a single crystal of $TiOSO_4 \cdot 2H_2O$, a more thorough investigation of reaction conditions could lead to a quality sample of sufficient size being produced, upon which the advantages of structure solution from single crystal diffraction could be brought to bear. If a single crystal product were still unable to be produced, an effort to produce higher quality powder samples could lead to a diffraction pattern containing enough information to determine the positions of the heavier atoms in the structure.

While the focus of this project has always been on using X-ray and neutron diffraction techniques to obtain structural information, other techniques such as transmission electron microscopy and scanning electron microscopy could also provide valuable information, although sample degradation in the electron beam is a high possibility given the nature of the fibres. If a more reliable method of producing deuterated $TiOSO_4 \cdot D_2O$ could be perfected, then a useful experiment would be the use of titanium isotopes in neutron diffraction [199]. This would allow the titanium atom positions to be identified through the simultaneous use of multiple data sets, from which a cycle of atom placement could be performed using the X-ray diffraction data. This experiment would allow us

to circumvent the lack of a heavy atom in the system, but the cost of obtaining the titanium isotopes for such an experiment would be somewhat prohibitive.

X-ray absorption spectroscopy techniques, such as Extended X-ray Absorption Fine Structure (EXAFS) and X-ray Absorption Near Edge Structure (XANES) could also be considered to probe the local environment of the titanium [200]. However, the uncertainty in the bond distances and coordination numbers produced by such techniques, coupled with the knowledge that we have of the titanium atoms typically being in octahedral arrangements in the titanyl sulphate hydrate series, may render them less instructive in this instance. However, coupling these with Wide-Angle X-ray Scatting (WAXS) would allow the pair distribution function (PDF) to be calculated and analysed to give longer range correlations, revealing further information about the environment of the titanium octahedra that may prove useful [201].

While a higher quality diffraction pattern may provide the SDPD methods used in this project with enough information to provide a final structure, there are other avenues that could be explored if this were not the case. For example, global optimisation techniques which, due to time constraints, were not able to be thoroughly explored in this project. Programs such as USPEX (Universal Structure Predictor: Evolutionary Xtallography) [202], which use a combination of evolutionary algorithms with *ab initio* calculations to explore the global *ab initio* energy landscape, could be used to return structure solutions. While successes have been reported in the literature ([203–205]), none of these were for systems as complex as the present one. Ultimately, while structure determination from powder diffraction is well on its way to becoming a routine process thanks to more intuitive software and faster processor speeds, there are still cases, such as the one explored in this project, which will prove difficult to fully solve.

Appendix A

Computational input data

A.1 SIESTA basis sets

A.1.1 Basis set notation:

We will now use the titanium basis (Table A.1) from the simplex optimised basis set to provide a short explanation of the basis set notation [165]:

Ti	5	2.3529732	
n=3	1	1	
6.0			
1.0			
n=4	0	2	S 0.5
7.0	0.0		
1.0	1.0		
n=3	2	2	S 0.2047099
7.0	0.0		
1.0	1.0		
n=4	1	2	S 0.5
8.0	0.0		
1.0	1.0		
n=4	3	1	E 30.9789290 1.4915934
6.0			
1.0			

TABLE A.1: Titanium basis from the simplex optimised basis set.

- **1**st line: atom label (usually taken to be the element); number of shells of orbitals with different angular momentum for the atom; Net charge of the atom.

- **2**nd line: principle quantum number of the shell; angular momentum of basis orbitals of this shell; number of zetas for this shell; soft confinement/polarisation/splitnorm flag (see below).
- **3**rd **and 4**th lines: Cut-off radii for each of the n zetas in the shell.

Lines 5-6, 8-10, 11-13, and 14-16 are repeats of lines 3-4, but for different shells. The softconfinement/polarisation/split-norm flag mentioned above can be set to E, S, or P, respectively:

- If set equal to E, soft confinement is invoked and the next two numbers are the prefactor of the soft confinement potential (v_0) and the inner radius (r_i), repectively.
- If set equal to S, the following number sets the split-norm parameter for that shell.
- If set equal to P, a shell of polarisation functions will be constructed from the first zeta orbital of angular momentum l, and the following number is the number of zetas for this polarisation shell.

The four basis sets referenced in the text follow overleaf.

```
Ti      5
n=3     0       1     E 70 1.0
6.0
1.0
n=3     1       1     E 95 3.0
7.0
1.0
n=4     0       2     E 20 3.0
6.0     0.0
1.0     1.0
n=3     2       2     E 70 3.0
8.0     0.0
1.0     1.0
n=4     3       2     E 30 1.0
6.0     0.0
1.0     1.0
O       2
n=2     0       2
0.0     0.0
1.0     1.0
n=2     1       2     P 1
0.0     0.0
1.0     1.0
```

TABLE A.2: Manually optimised basis set.

```
Ti      5       2.3529732
n=3     1       1
6.0
1.0
n=4     0       2               S 0.5
7.0     0.0
1.0     1.0
n=3     2       2               S 0.2047099
7.0     0.0
1.0     1.0
n=4     1       2               S 0.5
8.0     0.0
1.0     1.0
n=4     3       1               E 30.9789290 1.4915934
6.0
1.0
O       3       0
n=2     0       2               S 0.2619466
7.0     0.0
1.0     1.0
n=2     1       2               S 0.3359704
7.0     0.0
1.0     1.0
n=3     2       1               E 44.7688154 1.5048681
7.0
1.0
```

TABLE A.3: Simplex optimised basis set

Ti	5	1.91	
n=3	0	1	E 93.95 5.20
5.69946662616249			
1.0			
n=3	1	1	E 95.47 5.20
5.69941339465994			
1.0			
n=4	0	2	E 96.47 5.60
6.09996398975307	5.09944363262274		
1.00000000000000	1.00000000000000		
n=3	2	2	E 46.05 4.95
5.94327035784617	4.70009988294302		
1.00000000000000	1.00000000000000		
n=4	1	1	E 0.50 1.77
3.05365979938936			
1.0			
O	3	0.09	
n=2	0	2	E 24.13 2.59
4.601 2.082			
1.000 1.000			
n=2	1	2	E 47.15 2.61
5.813	2.127		
1.000	1.000		
n=3	2	1	E 41.49 4.31
7.798			
1.0			

Table A.4: Literature basis set

```
Ti          5
n=3         0     1
0.0
1.0
n=3         1     1
0.0
1.0
n=4         0     2
0.000000    0.0
1.000000    1.0
n=4         1     2
0.000000    0.0
1.000000    1.0
n=3         2     2    P 1
0.0         0.0
1.0         1.0
O           2
n=2         0     2
0.0         0.0
1.0         1.0
n=2         1     2    P 1
0.0         0.0
1.0         1.0
```

TABLE A.5: Default basis set, 'polar P' variant

```
Ti          5
n=3         0     1
0.0
1.0
n=3         1     1
0.0
1.0
n=4         0     2
0.000000    0.0
1.000000    1.0
n=4         1     2
0.000000    0.0
1.000000    1.0
n=3         2     2
0.0         0.0
1.0         1.0
n=4         3     1    E 100.0 0.0
0.0
1.0
O           2
n=2         0     2
0.0         0.0
1.0         1.0
n=2         1     2
0.0         0.0
1.0         1.0
n=3         2     1    E 100.0 0.0
6.0
1.0
```

TABLE A.6: Default basis set, 'polar E' variant

A.2 GULP forcefield parameters

Table A.7: GULP forcefield input

species					
Ti	core	2.000000			
S	core	1.400000			
O1	core	-1.000000			
O2	core	-0.600000			
O3	core	-0.820000			
H	core	0.410000			
end					
elements					
covalent	Ti	0.00000			
end					
nobond	O2	O3			
nobond	O3	O2			
lennard	combine	12	6	inter	
Ti	core	Ti	core	0.000	16.000
lennard	combine	12	6	inter	
O1	core	Ti	core	0.000	16.000
lennard	combine	12	6	inter	
O1	core	O1	core	0.000	16.000
lennard	combine	12	6	inter	
O2	core	Ti	core	0.000	16.000
lennard	combine	12	6	inter	
O1	core	O2	core	0.000	16.000
lennard	combine	12	6	inter	
O2	core	O2	core	0.000	16.000
lennard	combine	12	6	inter	
O3	core	Ti	core	0.000	16.000
lennard	combine	12	6	inter	
O1	core	O3	core	0.000	16.000
lennard	combine	12	6	inter	

Continued on next page...

```
O2      core    O3      core    0.000   16.000
lennard combine 12      6       inter
O3      core    O3      core    0.000   16.000
lennard combine 12      6       inter
H       core    Ti      core    0.000   16.000
lennard combine 12      6       inter
H       core    O1      core    0.000   16.000
lennard combine 12      6       inter
H       core    O3      core    0.000   16.000
lennard combine 12      6       inter
H       core    H       core    0.000   16.000
lennard combine 12      6       inter
H       core    O2      core    200.0   0.0     0.000   16.000


harmonic intra  bond
H       core    O3      core    46.8885 0.960000 0.00000 0       0
harmonic intra  bond
O2      core    S       core 10.0000 1.45000 0.00000 0       0


atomab
Ti      core    32.2318 0.0000  0       0
atomab
O1      core    24389.7699 0.0000 0     0
atomab
O2      core    10000.0 0.0000  0       0
atomab
O3      core    27291.7522 27.1245 0    0
atomab
H core  216.8222 0.0000 0       0


three   bond    intra   regular
O3      core    H       core    H       core    4.05    104.50  0  0
three   bond    intra   regular
S       core    O2      core    O2      core    10.000  109.50  0  0
```

Appendix B

FOX Structures

TABLE B.1: Images of the top ten results returned by FOX for a P 1 2_1 C 1 space group with 16 formula units of Ti and S atoms.

Cost value	c-axis	a-axis
7160739	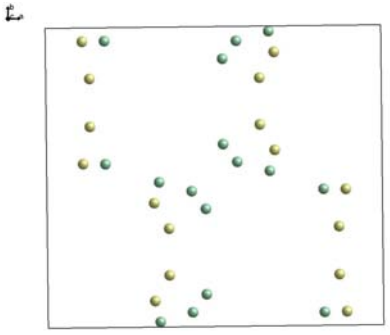	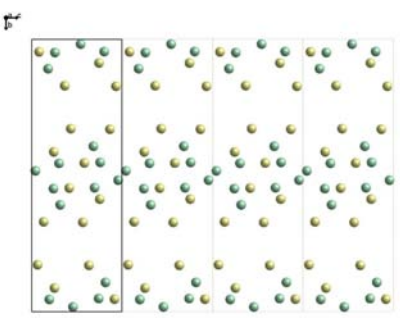
7161855	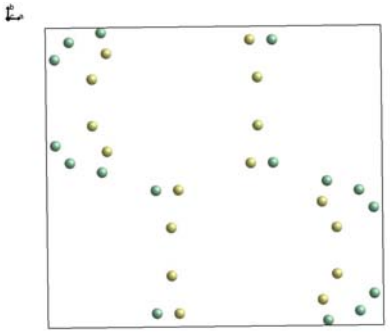	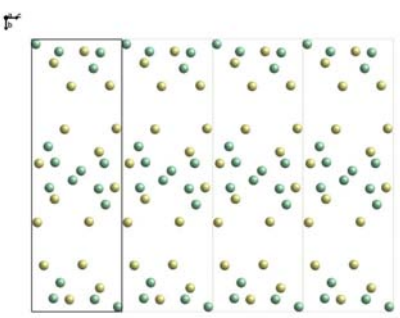

Continued on next page...

Table B.1 – Continued

Cost value	c-axis	a-axis
7162095	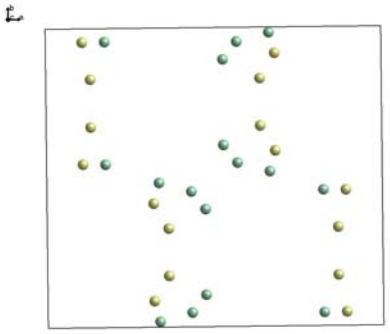	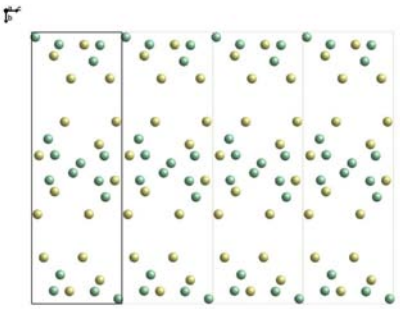
7162275	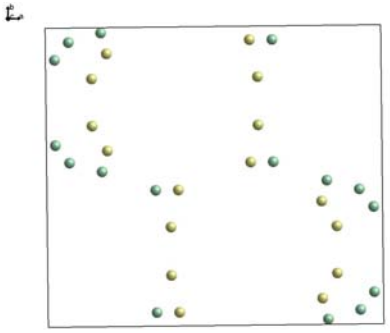	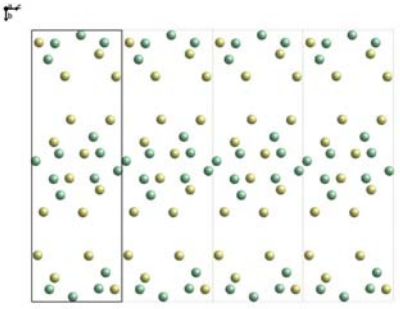
7162322	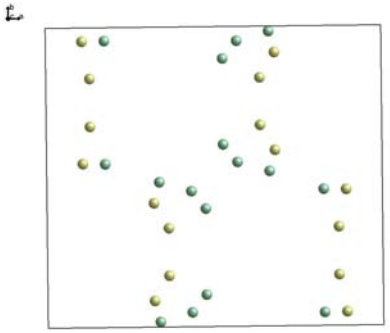	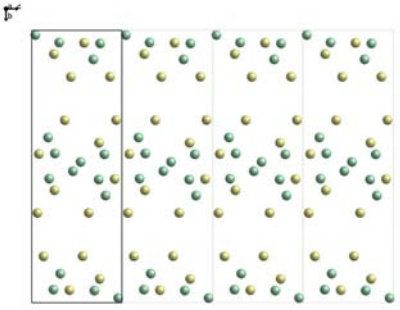
7162453	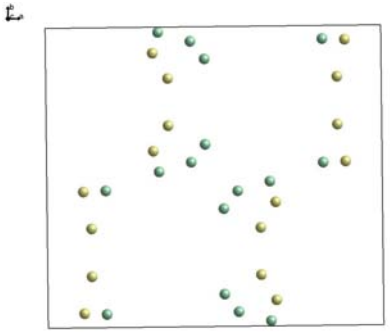	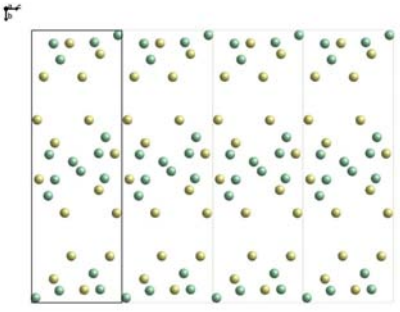

Continued on next page...

Table B.1 – Continued

Cost value	**c-axis**	**a-axis**
7162499	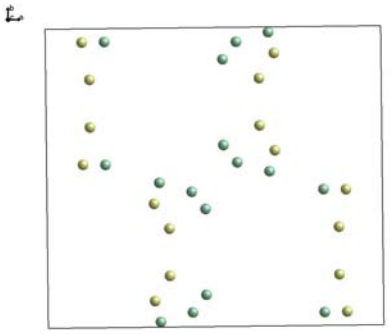	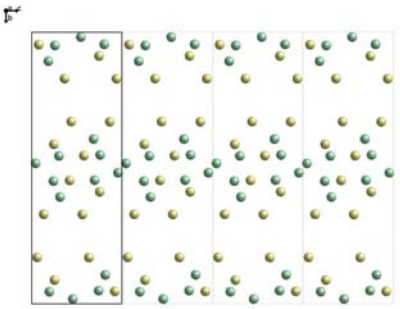
7162511	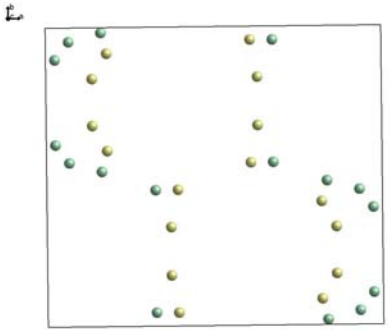	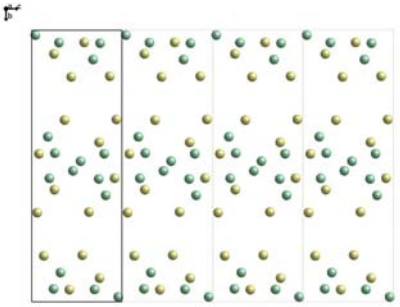
7162530	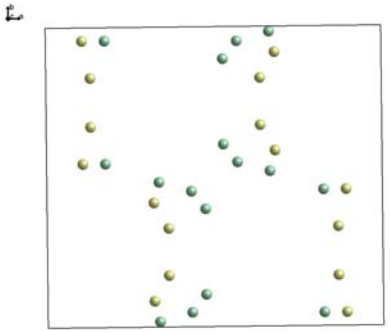	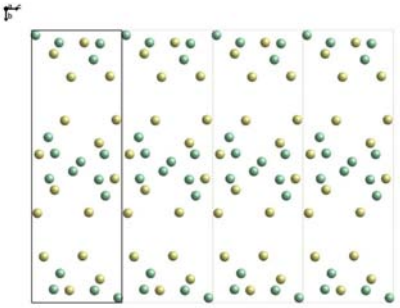
7162628	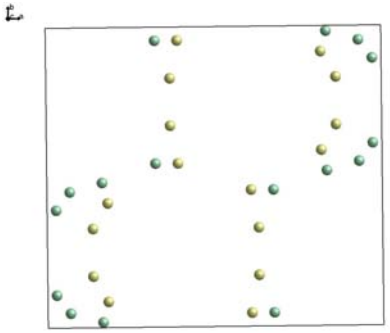	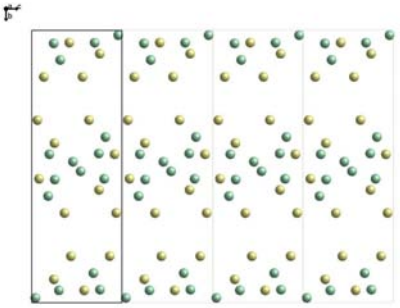

TABLE B.2: Images of the top ten results returned by FOX for a P 1 2_1/c 1 space group with 16 formula units of Ti and S atoms, and 16 O atoms.

Cost value	**c-axis**	**a-axis**
5640231	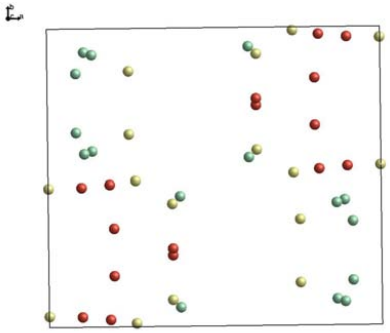	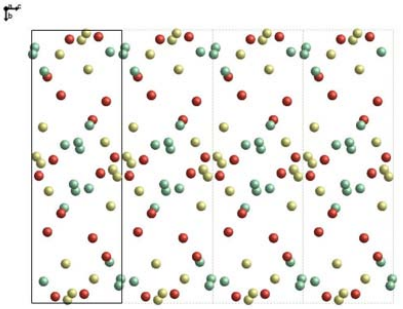
5645064	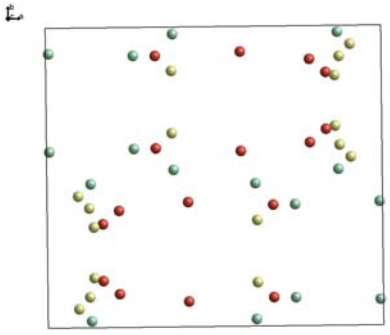	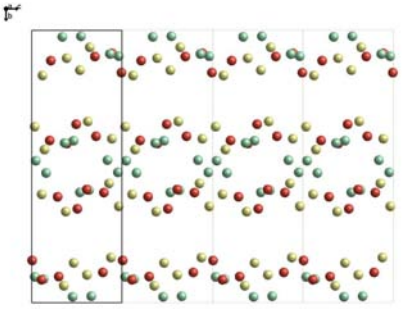
5659340	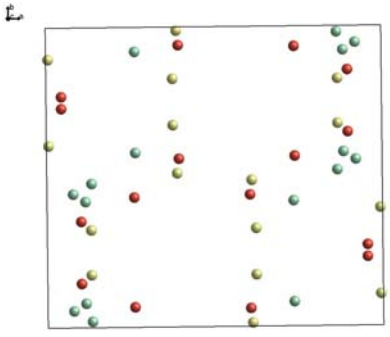	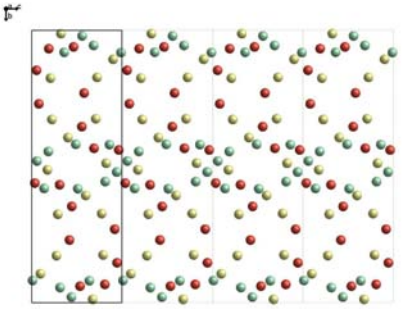
5745594	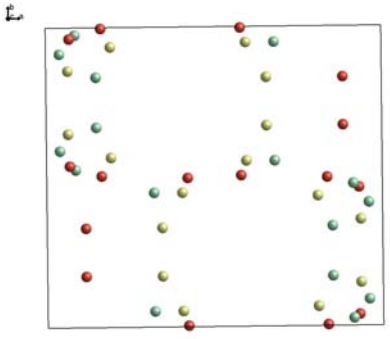	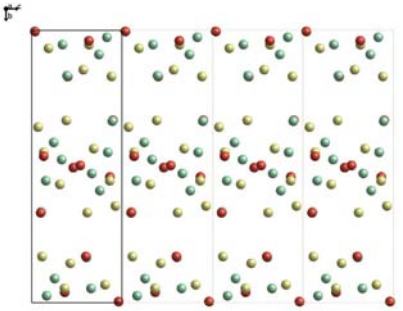

Continued on next page...

Table B.2 – Continued

Cost value	c-axis	a-axis
5754670	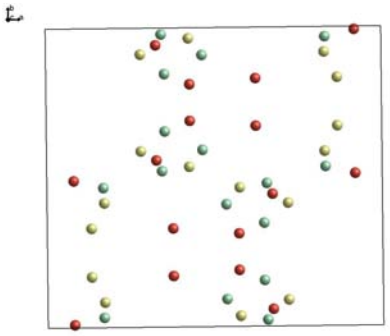	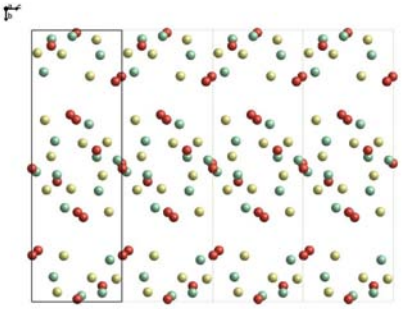
5754992	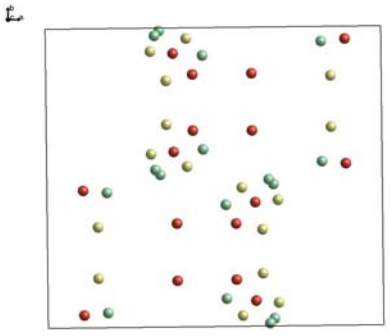	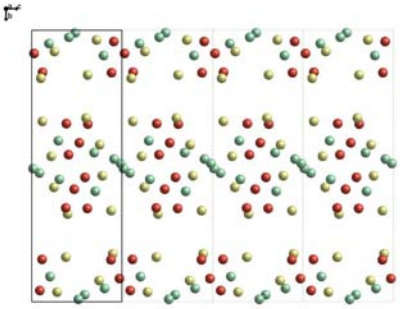
5770541	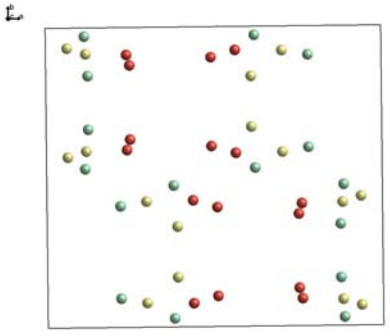	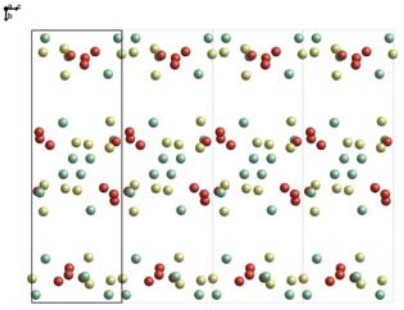
5800738	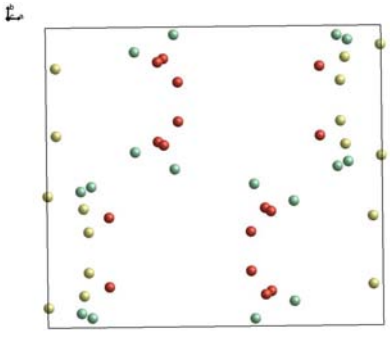	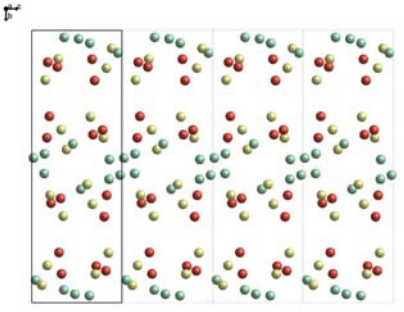

Continued on next page...

Table B.2 – Continued

Cost value	**c-axis**	**a-axis**
5854661	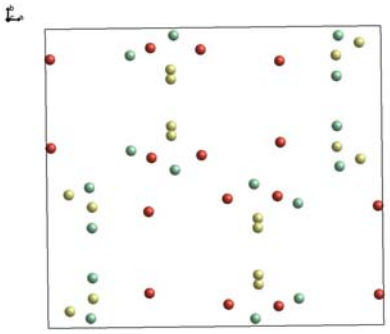	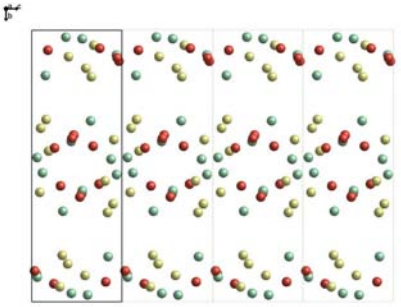
5869012	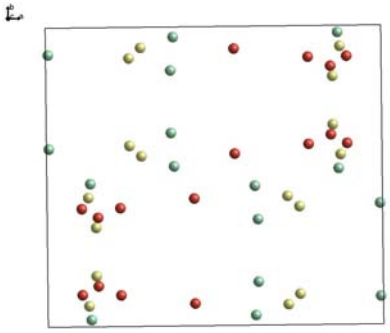	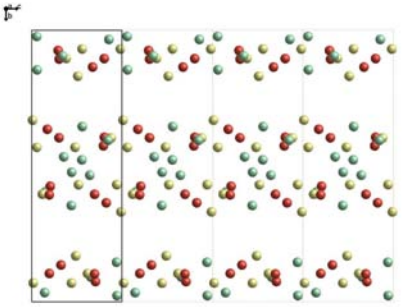

TABLE B.3: Images of the top ten results returned by FOX for a P 1 2_1/c 1 space group with 16 formula units of Ti and S atoms, and 32 O atoms.

Cost value	**c-axis**	**a-axis**
4457976	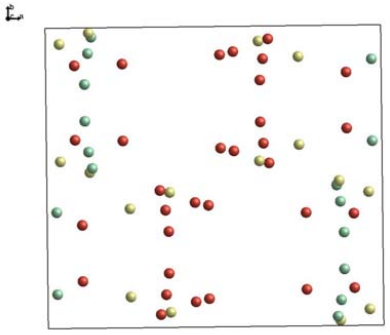	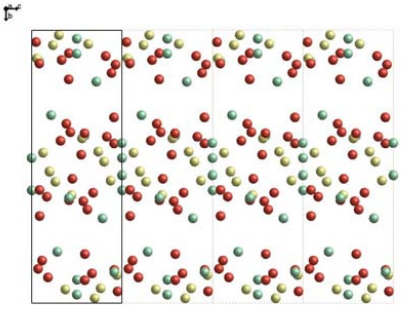
4523834	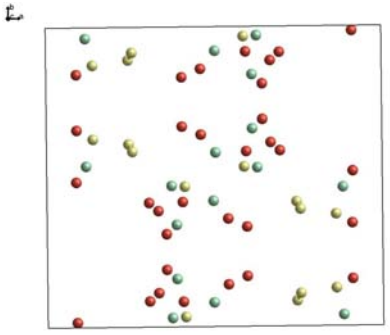	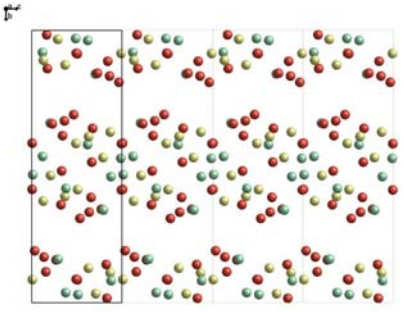
4539169	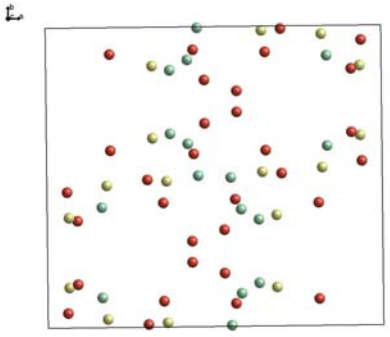	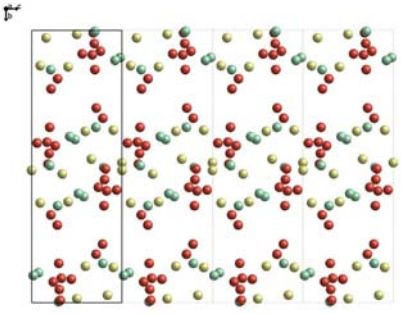
4572080	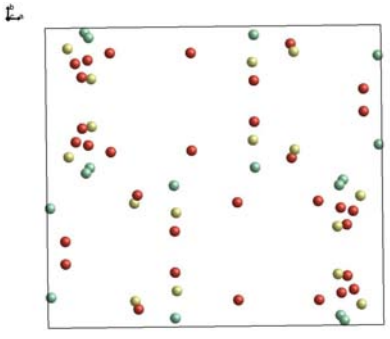	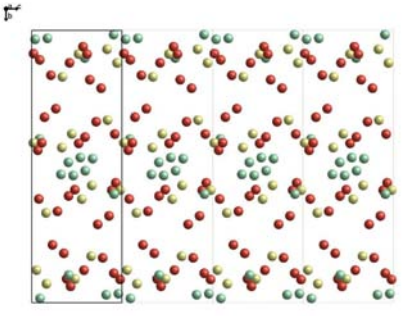

Continued on next page...

Table B.3 – Continued

Cost value	c-axis	a-axis
4573310	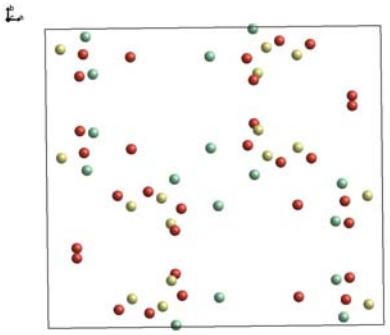	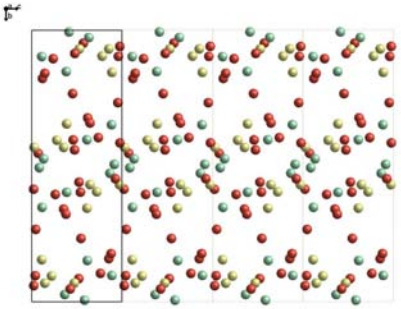
4606043	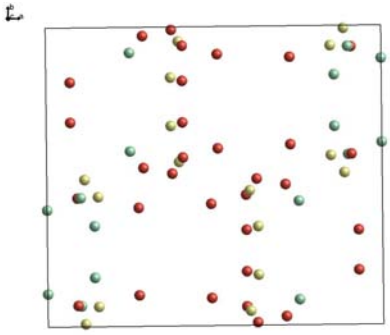	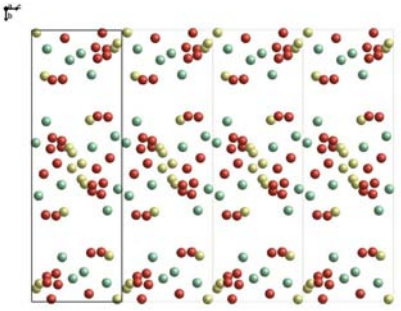
4617486	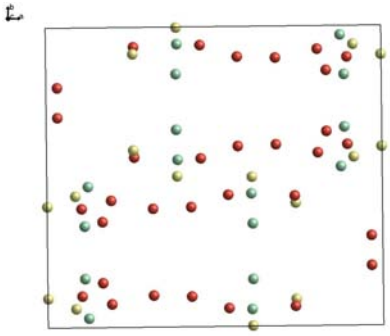	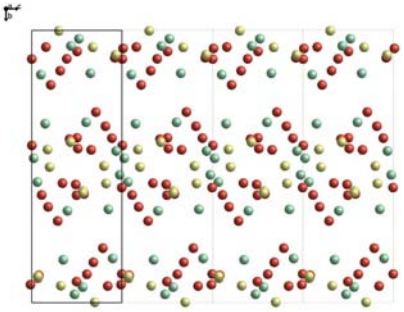
4619284	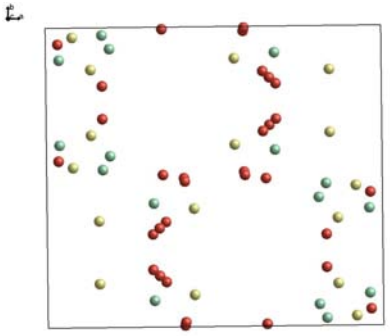	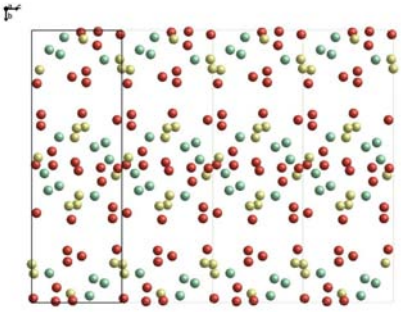

Continued on next page...

Table B.3 – Continued

Cost value	**c-axis**	**a-axis**
4644447	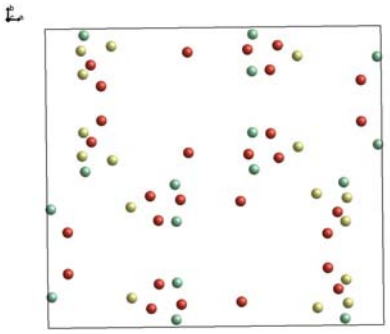	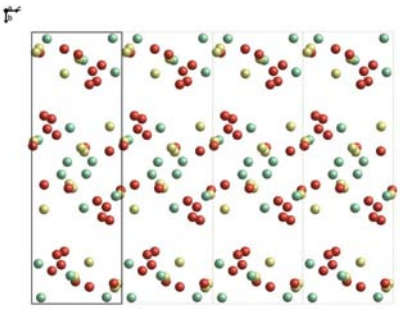
4659242	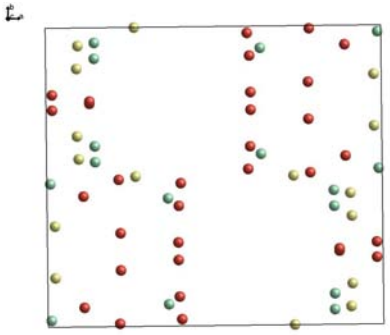	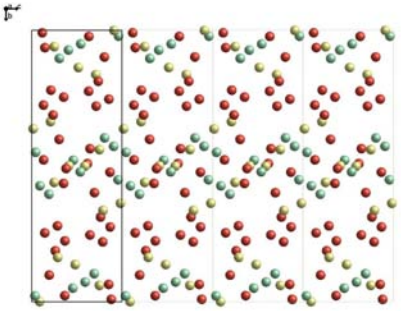

TABLE B.4: Images of the top ten results returned by FOX for a P 1 2_1/c 1 space group with 16 formula units of Ti atoms and SO_4 tetrahedra.

Cost value	c-axis	a-axis
4996209	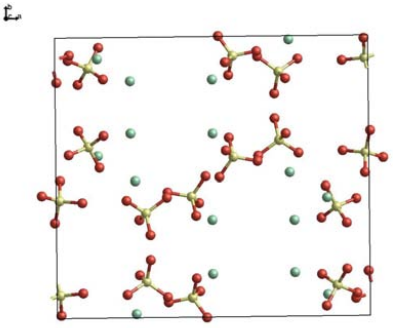	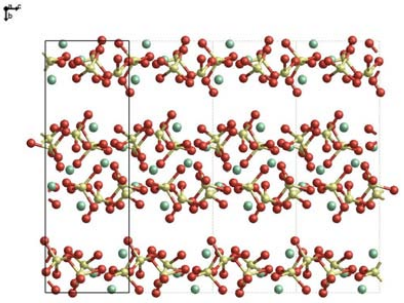
5122485	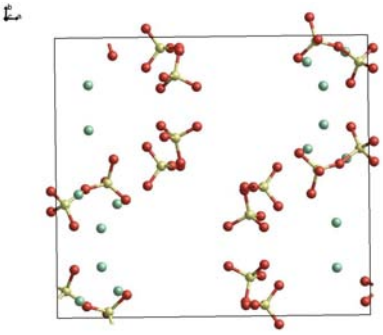	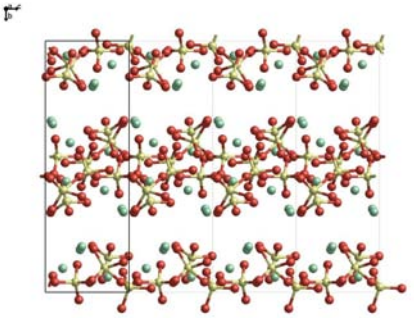
5206739	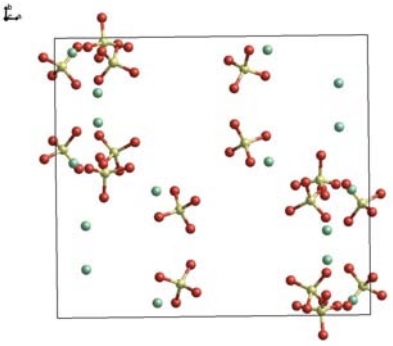	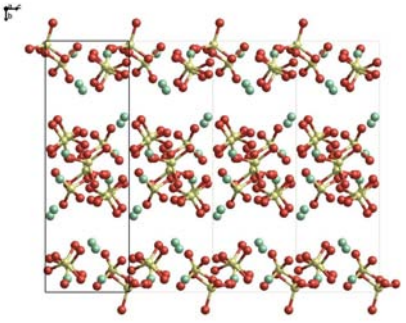
5316557	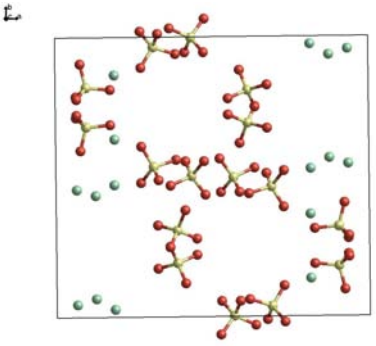	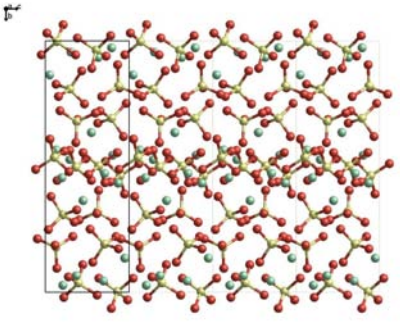

Continued on next page...

Table B.4 – Continued

Cost value	c-axis	a-axis
5323093	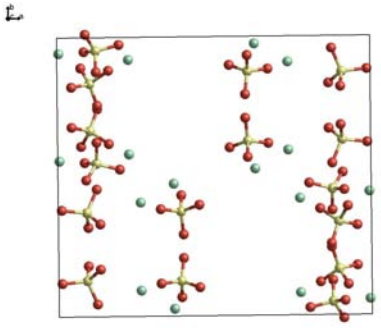	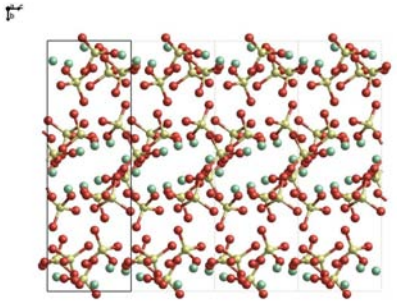
5379015	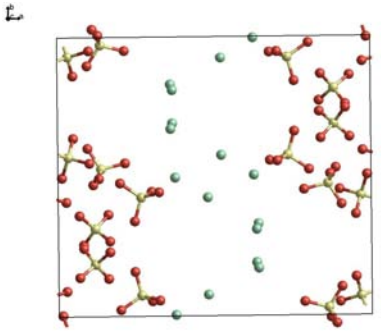	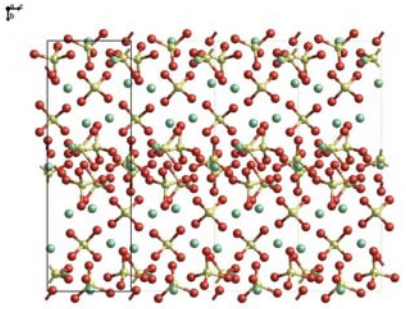
5468309	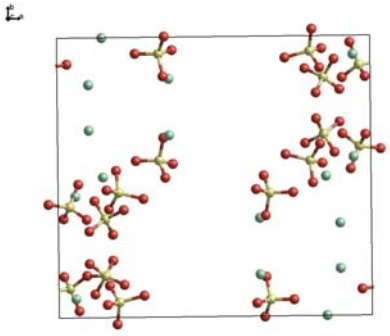	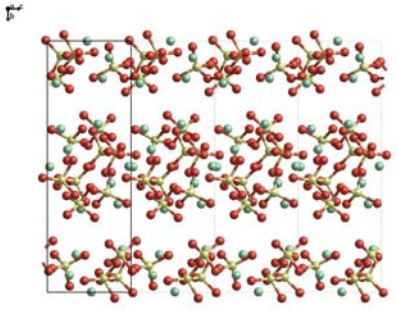
5504685	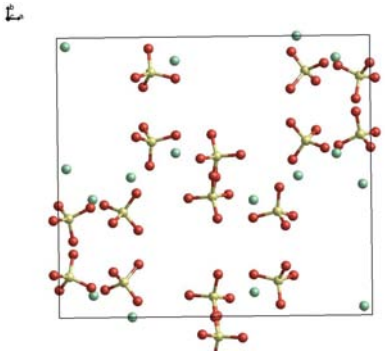	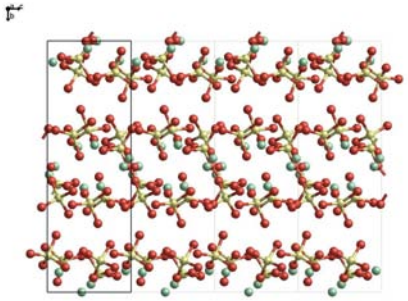

Continued on next page...

Table B.4 – Continued

Cost value	**c-axis**	**a-axis**
5528047	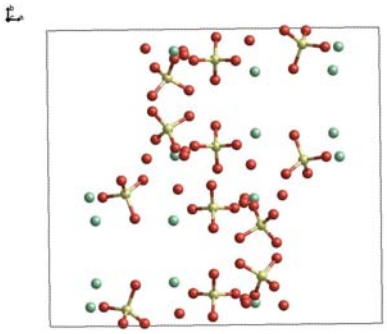	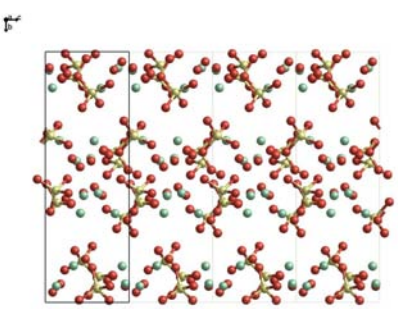
5553280	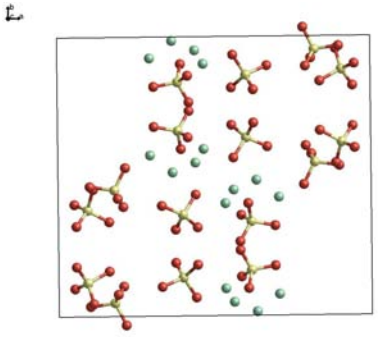	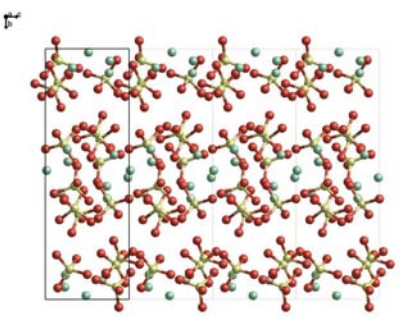

TABLE B.5: Images of the top ten results returned by FOX for a P 1 2_1/c 1 space group with 16 formula units of S atoms and TiO_6 octahedra.

Cost value	c-axis	a-axis
6100982	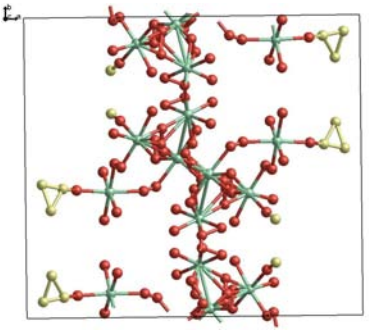	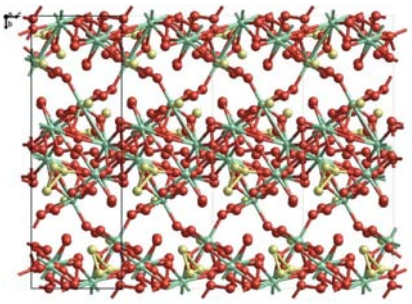
6253870	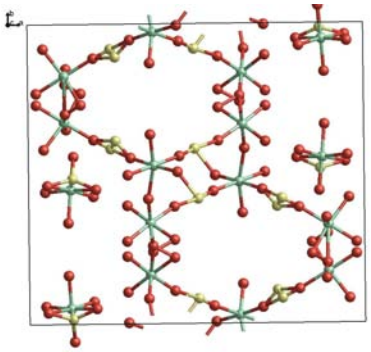	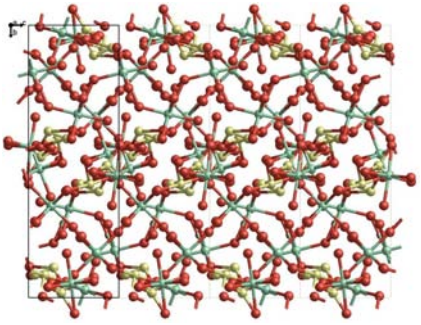
6281772	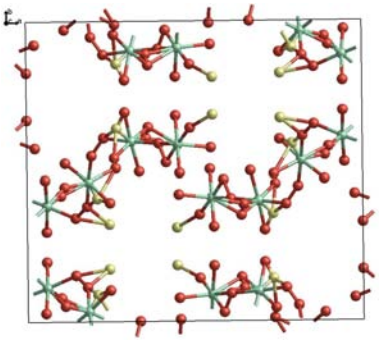	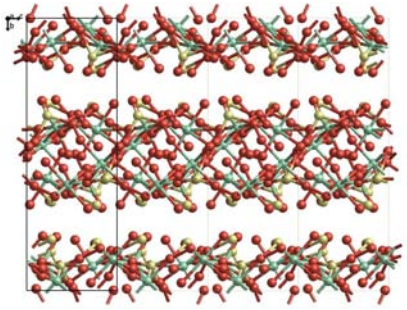
6344462	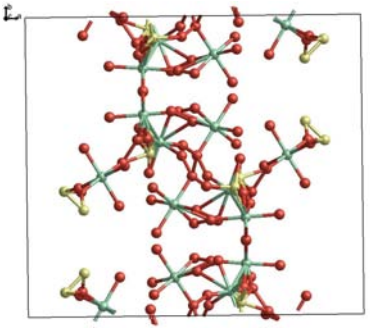	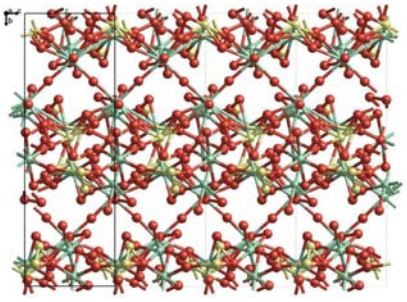

Continued on next page...

Table B.5 – Continued

Score	c-axis	a-axis
6384638	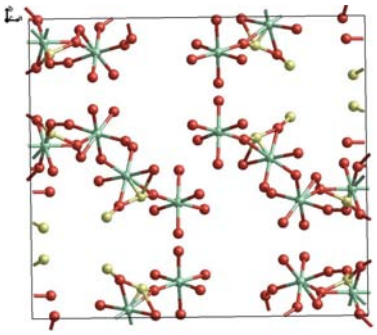	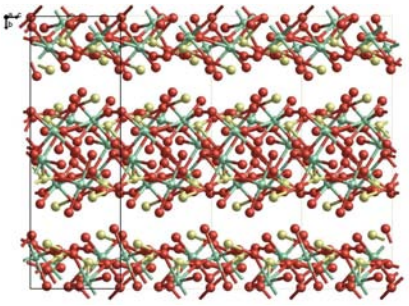
6407520	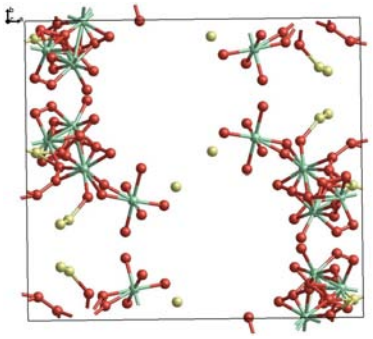	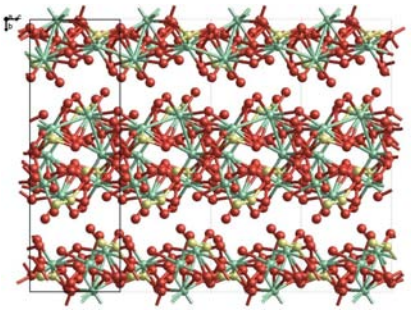
6422831	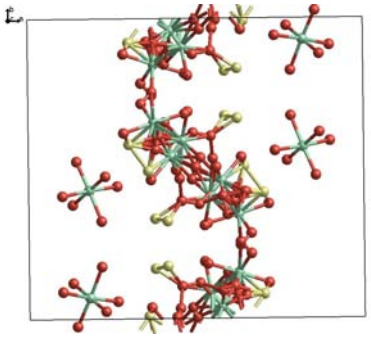	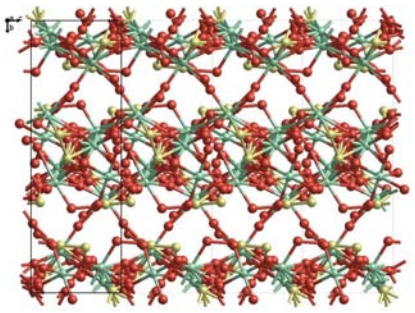
6424082	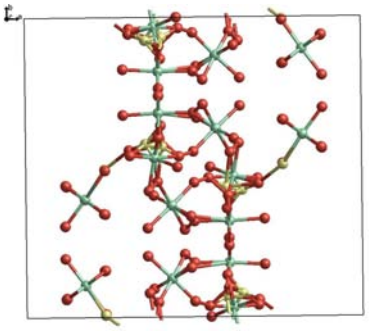	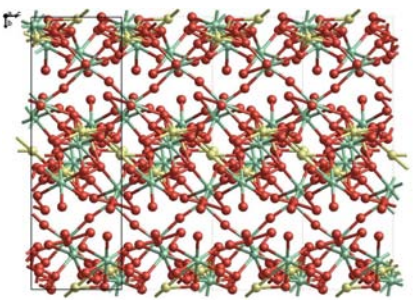

Continued on next page...

Table B.5 – Continued

Score	**c-axis**	**a-axis**
6432397	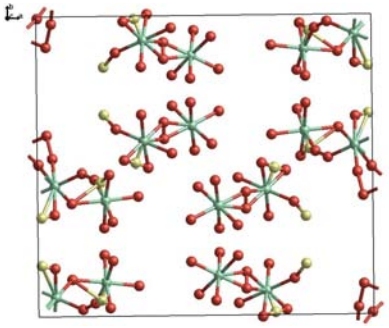	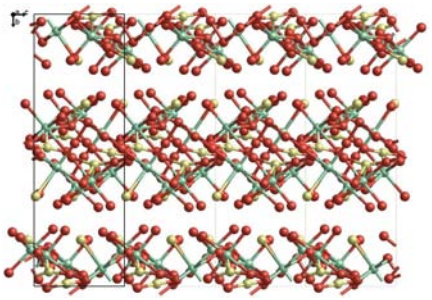
6542659	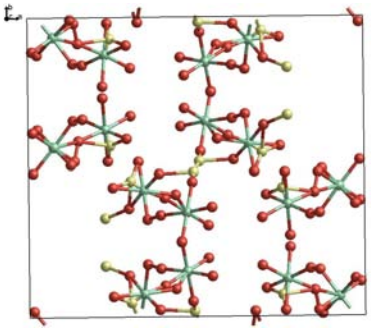	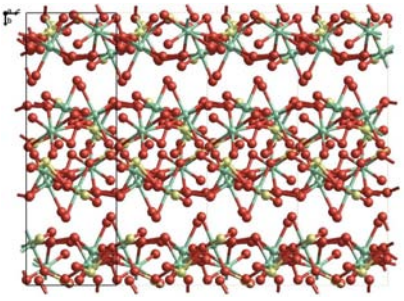

TABLE B.6: Images of the top ten results returned by FOX for a P 1 2_1/c 1 space group with 16 formula units of TiO_6 octahedra and SO_4 tetrahedra.

Cost value	**c-axis**	**a-axis**
3806545	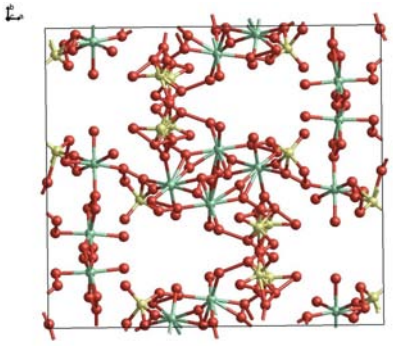	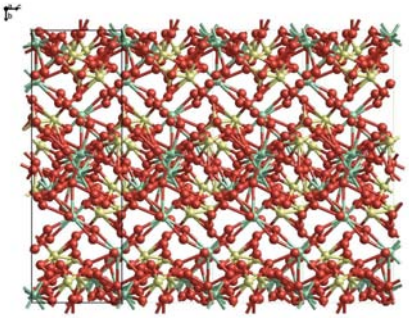
3855984	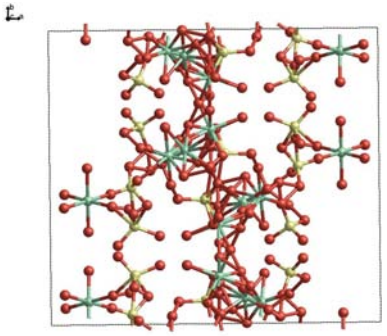	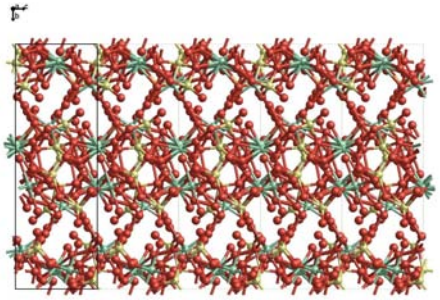
3977806	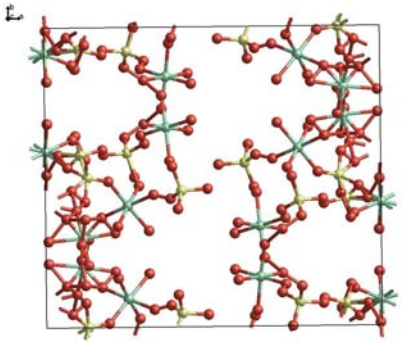	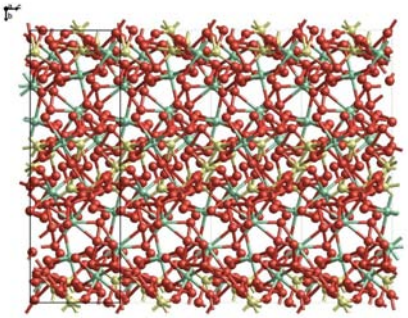
4002883	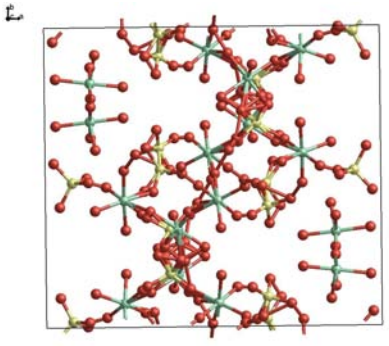	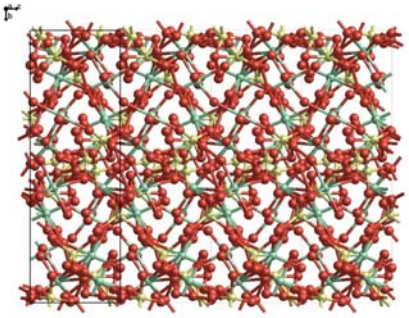

Continued on next page...

Table B.6 – Continued

Score	c-axis	a-axis
4004830	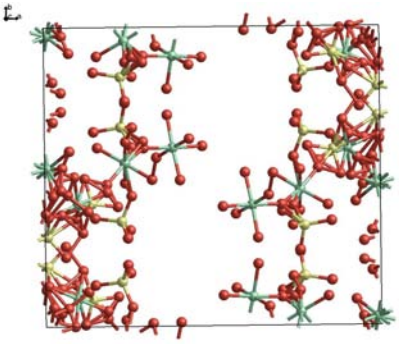	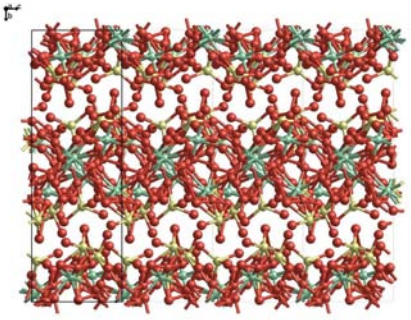
4091207	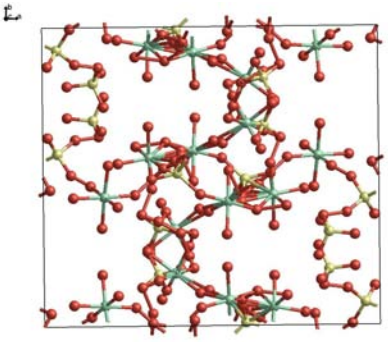	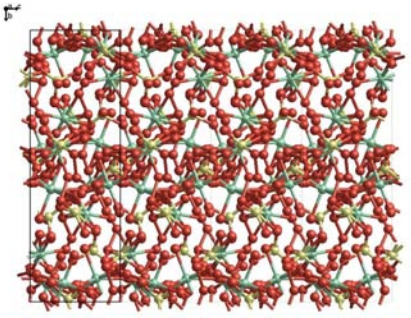
4091773	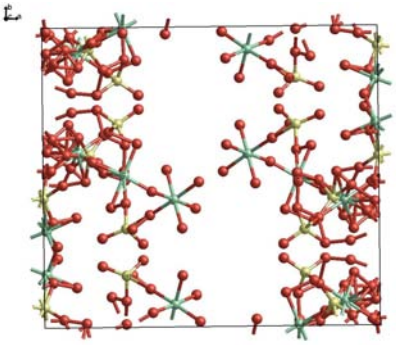	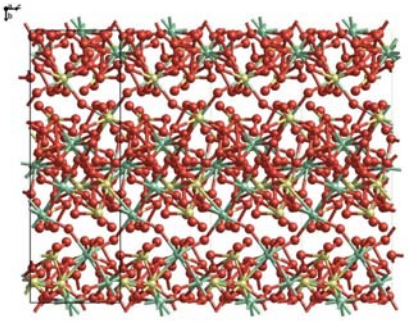
4116433	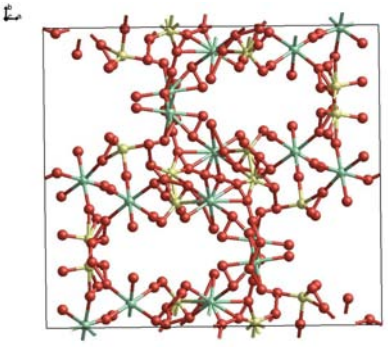	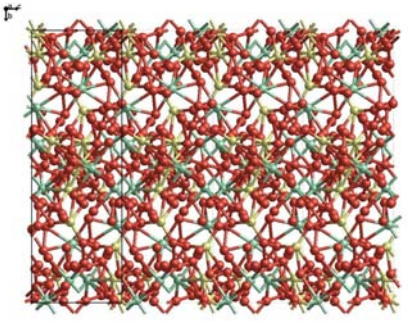

Continued on next page...

Table B.6 – Continued

Score	c-axis	a-axis
4131572	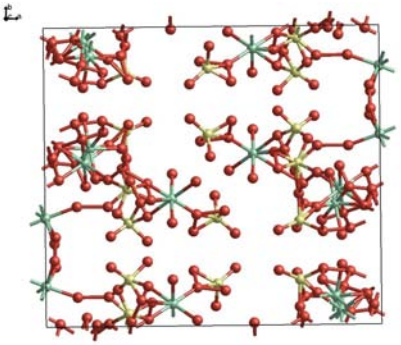	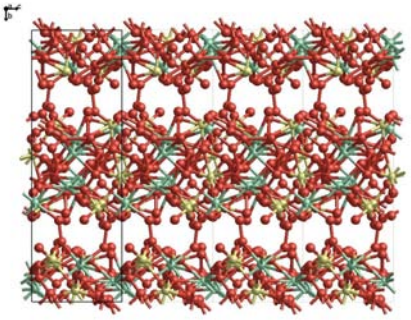
4146143	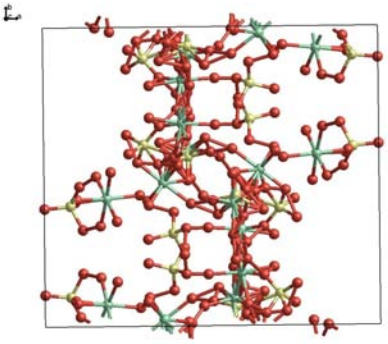	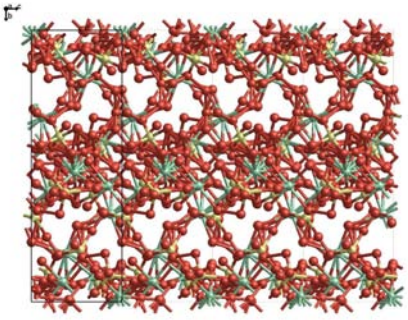

Bibliography

[1] *Year Book Australia*. Australian Bureau of Statistics, 2009-2010.

[2] A. Fujishima and K. Honda. Electrochemical Photolysis of Water at a Semiconductor Electrode. *Nature*, 238:37–38, 1972.

[3] B. O'Regan and M. Gratzel. A low-cost, high-efficiency solar cell based on dye-sensitized colloidal TiO2 films. *Nature*, 353:737–740, 1991.

[4] E. R. Force. *Geology of titanium-mineral deposits*. Geological Society of America, 1991.

[5] C. Noubactep. Metallic iron for environmental remediation: Learning from the Becher process. *Journal of Hazardous Materials*, 168:16091612, 2009.

[6] *Ullmann's Encyclopedia of Industrial Chemistry*. VCH, 2006.

[7] T. A. Lasheen. Sulfate digestion process for high purity TiO2 from titania slag. *Frontiers of Chemical Engineering in China*, 3:155–160, 2009.

[8] P. Doan. Sustainable Development in the TiO2 Industry: Challenges and Opportunites. In *TiO2 2003 Intertech Conference, February 5, 2003, Miami, Florida*, 2003.

[9] B. Richmond, F. Jones, and B. Pejcic. A Study of Titanyl Sulfate Precipitation from an Ilmenite Leach Solution (Part 1). Technical report, Nanotechnology Research Institute, 2005.

[10] B. Richmond, F. Jones, and B. Pejcic. A Study of Titanyl Sulfate Precipitation from an Ilmenite Leach Solution (Part 2). Technical report, Nanotechnology Research Institute, 2006.

[11] H. Peng. Determination of the Fudge Window for Synthetic Titanyl Sulfate Solutions (Parts 1,2, and 3). Technical report, BHP Billiton, 2007.

[12] S. Naka, K. Tanaka, Y. Suwa, and Y. Takeda. Single-crystal of titanyl sulfate anhydrate grown under hydrothermal condition. *Journal of Inorganic and Nuclear Chemistry*, 39:1239–1240, 1977.

[13] B. M. Gatehouse, S. N. Platts, and T. B. Williams. Structure of anhydrous titanyl sulfate, titanyl sulfate monohydrate and prediction of a new structure. *Acta Crystallographica Section B-Structural Science*, 49:428–435, 1993.

[14] S. L. Wang, C. C. Wang, and K. H. Lii. Crystal structure of WPO5, the second member of the monophosphate tungsten bronze series (WO3)2m(PO2)4. *Journal of Solid State Chemistry*, 82(2):298–302, October 1989. ISSN 00224596.

[15] M. A. K. Ahmed, H. Fjellvag, and A. Kjekshus. Syntheses and Crystal Structures of Titanium Oxide Sulfates. *Acta Chemica Scandinavica*, 50:275–283, 1996.

[16] G. Lundgren. On the crystal structure of TiOSO4H2O. *Arkiv. Kemi.*, 10:397–413, 1950.

[17] K. Jinriki, K. Kubo, and S. Kato. Research into rutile-type titania (2): Formation of titanyl sulphate. *Kyogo Kagaku Zasshi*, 56:832–834, 1953.

[18] M. L. Reynolds and T. J. Wiseman. Some observations on the structure of titanyl sulphate dihydrate. *Journal of Inorganic and Nuclear Chemistry*, 29:1381–1389, 1967.

[19] M. Johnsson, P. Pettersson, and M. Nygren. Thermal decomposition of fibrous TiOSO4.2H2O to TiO2. *Thermochimica Acta*, 298(1-):47–54, 1997.

[20] E. S. Hanrahan. The thermal decomposition of titanyl sulphate hydrates. *Journal of Inorganic and Nuclear Chemistry*, 26:1757–1758, 1964.

[21] R. G. Denning. Electronic Structure and Bonding in Actinyl Ions and their Analogs. *Journal of Physical Chemistry A*, 111:4125–4143, 2007.

[22] C. J. Ballhausen and H. B. Gray. The Electronic Structure of the Vanadyl Ion. *Inorganic Chemistry*, 1:111–122, 1962.

[23] P. Comba and A. Merbach. The Titanyl Question Revisited. *Inorganic Chemistry*, 26:1315–1323, 1987.

[24] P. N. Dwyer, L. Puppe, J. W. Buchler, and W. R. Scheidt. Molecular stereochemistry of (alpha-gamma-dimethyl-alpha-gamma-dihydrooctaethylporphinato)oxotitanium(iv). *Inorganic Chemistry*, 14:1782, 1975.

[25] B. P. Block and E. G. Meloni. The Chemistry of Dichloro[phthalocyaninato(2-)]titanium(IV). *Inorganic Chemistry*, 4:111, 1965.

[26] G. M. H. van de Velde. The oxalato complexes of titanium(IV)I : Mononuclear Ti(OH)2(C2O4)22 in solution. *Journal of Inorganic and Nuclear Chemistry*, 39: 1357–1362, 1977.

[27] J. Beukenkamp and K. D. Herrington. Ion-Exchange Investigation of the Nature of Titanium(IV) in Sulfuric Acid and Perchloric Acid. *Journal of the American Chemical Society*, 82:3025–3031, 1960.

[28] M. Pourbaix. *Atlas of electrochemical equilibria in aqueous solutions*. Pergamon Press, 1966.

[29] J. D. Ellis, A. K. Thompson, and A. G. Sykes. The Cr2+ Reduction of Titanium(IV). Comparisons with the Cr2+ Reduction of VO2+ and Evidence for a TiO2+ Structure in Aqueous Solutions, pH =¡ 1. *Inorganic Chemistry*, 15: 3172–3174, 1976.

[30] G. A. K. Thompson, R. S. Taylor, and A. G. Sykes. Kinetic Studies on the Complexing of Aquo TiO2+ with Thiocyanate, Pryrophosphate, and Hydrogen Fluoride. *Inorganic Chemistry*, 16:2880–2884, 1977.

[31] M. Gratzel and F. P. Rotzinger. Raman Spectroscopic Evidence for the Existence of TiO2+ in Acidic Aqueous Solutions. *Inorganic Chemistry*, 24:2320–2321, 1985.

[32] S. Sivakumar, P. K. Pillai, P. Mukundan, and K. G. K. Warrier. Sol-gel synthesis of nanosized anatase from titanyl sulfate. *Materials Letters*, 57:330–335, 2002.

[33] V. A. Yasir, P. N. MohanDas, and K. K. M. Yusuff. Preparation of high surface area TiO2 (anatase) by thermal hydrolysis of titanyl sulphate solution. *International Journal of Inorganic Materials*, 3:593–596, 2001.

[34] M. Iwasaki, M. Hara, and S. Ito. Facile synthesis of nanocrystalline anatase particles from titanyl sulfate. *Journal of Materials Science Letters*, 17:1769–1771, 1998.

[35] Y. V. Kolenko, A. A. Burukhin, B. R. Churagulov, and N. N. Oleinikov. Phase composition of nanocrystalline titania synthesized under hydrothermal conditions from different titanyl compounds. *Inorganic Materials*, 40:822–828, 2004.

[36] S. Sathyamoorthy, M. J. Hounslow, and G. D. Moggridge. Influence of stirrer speed on the precipitation of anatase particles from titanyl sulphate solution. *Journal of Crystal Growth*, 223:225–234, 2001.

[37] S. Sathyamoorthy, G. D. Moggridge, and M. J. Hounslow. Particle formation during anatase precipitation of seeded titanyl sulfate solution. *Crystal Growth and Design*, 1:123–129, 2001.

[38] G. Parkinson, B. Richmond, and B. Pejcic. A Study of Titanyl Sulfate Precipitation from an Ilmenite Leach Solution. Technical report, Nanotechnology Research Institute, 2005.

[39] M. Elbrahimi, J. Durand, and L. Cot. Crystal Structure of Basic Zirconium Sulfate Zr(OH)2SO4. *European Journal of Solid State and Inorganic Chemistry*, 25:185–189, 1988.

[40] M. Hansson. The crystal structure of Zr(OH)2SO4H2O. *Acta Chemica Scandinavica*, 27:2614–2622, 1973.

[41] D. Gascoigne, S. E. Tarling, P. Barnes, C. F. Pygall, P. Benard, and D. Louer. Ab initio structure determination of Zr(OH)2SO4.3H2O using the conventional monochromatic X-ray powder diffraction. *Journal of Applied Crystallography*, 27 (3):399–405, June 1994. ISSN 0021-8898.

[42] D. B. McWhan and G. Lundgren. The Crystal Structure of Zr2(OH)2(SO4)3(H2O)4. *Inorganic Chemistry*, 5:284–289, 1965.

[43] C. Hammond. *The Basics of Crystallography and Diffraction (2nd Ed)*. Oxford University Press, 2001.

[44] M. von Laue. Concerning the detection of x-ray interferences. *Nobel Lecture*, 1915.

[45] W. L. Bragg. The Diffraction of Short Electromagnetic Waves by a Crystal. *Proceedings of the Cambridge Philosophical Society*, 17:43, 1912.

[46] W. L. Bragg. The Specular Reflection of X-rays. *Nature*, 90:410, 1912.

[47] P. P. Ewald. Introduction to the Dynamical Theory of X-Ray Diffraction. *Acta Crystallographica A*, 25:103, 1969.

[48] B. K. Vainshtein. *Modern Crystallography*. Springer, 1996.

[49] J. I. Langford, D. Louer, and P. Scardi. Effect of a crystallite size distribution on x-ray diffraction line profiles and whole-powder-pattern fitting. *Journal of Applied Crystallography*, 33:964–974, 2000.

[50] Schematic of 4-circle diffractometer; the angles between the incident ray, the detector and the sample., March 2007. URL `http://serc.carleton.edu/details/images/8400.html`. Used under Stanford's 'Fair Use' policy.

[51] J. Apostolakis, C. Buchsbaum, S. Hohler-Schlimm, S. Rehme, K. Rajan, D. W. M. Hofmann, H. Cheng, T. Z. Sen, R. L. Jernigan, and A. Kloczkowski. *Data Mining in Crystallography.* Springer, 2010.

[52] D. W. M. Hofmann and L. N. Kuleshova. *Data Mining in Crystallography.* Springer, 2010.

[53] J. D. Hanawalt and H. W. Rinn. Identification of Crystalline Materials Classification and Use of X-ray Diffraction Patterns. *Industrial and Engineering Chemistry*, 8:244–250, 1936.

[54] P. Scardi, M. Leoni, and R. Delhez. Line broadening analysis using integral breadth methods: a critical review. *Journal of Applied Crystallography*, 37:381–390, 2004.

[55] R. C. Reynolds, R. Jenkins, D. L. Bish, R. L. Snyder, D. K. Smith, S. A. Howard, K. D. Preston, J. E. Post, L. W. Finger, and R. B. Von Dreele. *Modern Powder Diffraction.* Mineralogical Society of America, 1989.

[56] R. Jenkins and R. L. Snyder. *Introduction to X-ray Powder Diffractometry.* John Wiley & Sons, 1996.

[57] W. I. F. David, K. Shankland, L. B. McCusker, and Ch. Baerlocher. *Structure Determination from Powder Diffraction Data.* International Union of Crystallography, 2006.

[58] A. Le Bail, L. M. D. Cranswick, K. Adil, A. Altomare, M. Avdeev, C. Cuocci, C. Giacovazzo, I. Halasz, S.H. Lapidus, J. N. Louwen, A. Moliterni, L. Palatinus, R. Rizzi, E. C. Schilder, P. W. Stephens, K. H. Stone, and J. van Mechelen. Third structure determination by powder diffractometry round robin. *Powder Diffraction*, 24:254–262, 2009.

[59] V. V. Chernyshev. Structure determination from powder diffraction. *Russian Chemical Bulletin, International Edition*, 50:2273–2292, 2001.

[60] J. I. Langford and D. Louer. Powder diffraction. *Reports on Progress in Physics*, 59:131234, 1996.

[61] J. W. Visser. A fully automatic program for finding the unit cell from powder data. *Journal of Applied Crystallography*, 2:89–95, 1969.

[62] M. Louer and D. Louer. Methode d'Essais et Erreurs pour l'Indexation Automatique des Diagrammes de Poudre. *Journal of Applied Crystallography*, 5:271, 1972.

[63] A. Boultif and D. Louer. Powder pattern indexing with the dichotomy method. *Journal of Applied Crystallography*, 37:724–731, 2004.

[64] P. M. de Wolff. A simplified criterion for the reliability of a powder pattern indexing. *Journal of Applied Crystallography*, 1:108, 1968.

[65] A. D. Mighell and A. Santaro. Geometrical Ambiguities in the Indexing of Powder Patterns. *Journal of Applied Crystallography*, 8:372–374, 1975.

[66] H. Rietveld. A profile refinement method for nuclear and magnetic structures. *Journal of Applied Crystallography*, 2:65–71, 1969.

[67] C. Giacovazzo. *Direct Phasing In Crystallography.* Oxford University Press, 1998.

[68] A. K. Cheetham, B. E. F. Fender, and R. I. Taylor. High Temperature Neutron Diffraction Study of Fe1-xO. *Journal of Physics C*, 4:2160–2165, 1971.

[69] A. Le Bail, H. Duroy, and J. L. Fourquet. Ab-initio structure determination of LiSbWO6 by X-ray powder diffraction. *Materials Research Bulletin*, 23:447–452, 1988.

[70] G. S. Pawley. Unit-cell refinement from powder diffraction scans. *Journal of Applied Crystallography*, 14:357–361, 1981.

[71] M. F. C. Ladd and R. A. Palmer, editors. *Theory and Practice of Direct Methods in Crystallography.* Plenum Press, 1980.

[72] I. Uson and G.M. Sheldrick. Advances in direct methods for protein crystallography. *Current Opinion in Structural Biology*, 9:643–648, 1999.

[73] A. L. Patterson. A Fourier Series Method for the Determination of the Components of Interatomic Distances in Crystals. *Physical Review*, 46:372–376, 1934.

[74] K. D. M. Harris. Crystal Structure Determination from Powder Diffraction Data. *Chemistry of Materials*, 8:2554–2570, 1996.

[75] B. M. Kariuki, H. Serrano-Gonzalez, R. L. Johnston, and K. D. M. Harris. The application of a genetic algorithm for solving crystal structures from powder diffraction data. *Chemical Physics Letters*, 280:189–195, 1997.

[76] K. Shankland, W. I. F. David, and T. Csoka. Crystal structure determination from powder diffraction data by the application of a genetic algorithm. *Zeitschrift fur Kristallographie*, 212:550–552, 1997.

[77] H. Putz, J.C. Schon, and M. Jansen. Combined method for ab initio structure solution from powder diffraction data. *Journal of Applied Crystallography*, 32: 864870, 1999.

[78] G. W. Turner, E. Tedesco, K. D. M. Harris, R. L. Johnston, and B. M. Kariuki. Implementation of Lamarckian concepts in a Genetic Algorithm for structure solution from powder diffraction data. *Chemical Physics Letters*, 321:183–190, 2000.

[79] A. A. Coelho. Whole-profile structure solution from powder diffraction data using simulated annealing. *Journal of Applied Crystallography*, 33:899908, 2000.

[80] A. Le Bail. Espoir: A program for solving structures by monte carlo analysis of powder diffraction data. *Materials Science Forum*, 378-381:65–70, 2001.

[81] V. Favre-Nicolin and R. Cerny. FOX, 'free objects for crystallography': a modular approach to ab initio structure determination from powder diffraction. *Journal of Applied Crystallography*, 35:734–743, 2002.

[82] R. W. Grosse-Kunstleve, L. B. McCusker, and Ch. Baerlocher. Zeolite structure determination from powder diffraction data: applications of the FOCUS method. *Journal of Applied Crystallography*, 32:536–542, 1999.

[83] J. Rius and H. Hies. A Tangent Formula Derived From Patterson-Function Arguments. 3. Structure Determination of Zeolitic And Layered Materials From Low-Resolution Powder Diffraction Data. *Acta Crystallographica A*, 51:840–845, 1995.

[84] J. P. Attfield, A. W. Sleight, and A. K. Cheetham. Structure determination of alpha-CrPO4 from powder synchrotron X-ray data. *Nature*, 322:620–622, 1986.

[85] A. Le Bail. Whole Powder Pattern Decomposition Methods and Applications: A Retrospection. *Powder Diffraction*, 20:316–326, 2005.

[86] J. Rodriguez-Carvajal. Recent advances in magnetic structure determination by neutron powder diffraction. *Physica B*, 192:55–69, 1993.

[87] H. J. Toraya. Whole-powder-pattern fitting without reference to a structural model: application to X-ray powder diffraction data. *Journal of Applied Crystallography*, 19:440447, 1986.

[88] F. Izumi. RIETAN: A Software Package for the Rietveld Analysis and Simulation of X-ray and Neutron Diffraction Patterns. *The Rigaku Journal*, 6:10–20, 1989.

[89] A. Altomare, M.C. Burla, G. Cascarano, C. Giacovazzo, A. Guagliardi, A.G.G. Moliterni, and G. Polidori. EXTRA: a program for extracting structure-factor amplitudes from powder diffraction data. *Journal of Applied Crystallography*, 28: 842–846, 1995.

[90] M. Altomare, M.C. Burla, M. Camalli, B. Carrozzini, G.L. Cascarano, C. Giacovazzo, A. Guagliardi, A.G.G. Moliterni, G. Polidori, and R. Rizzi. EXPO: a program for full powder pattern decomposition and crystal structure solution. *Journal of Applied Crystallography*, 32:339–340, 1999.

[91] P. Lightfoot, A. K. Cheetham, and A. W. Sleight. Structure of Manganese(3+) Phosphate Monohydrate by Synchrotron X-ray Powder Diffraction. *Inorganic Chemistry*, 26:3544–3547, 1987.

[92] P. Lightfoot, J. A. Hriljac, S. Pei, Y. Zheng, A. W. Mitchell, D. R. Richards, B. Dabrowski, J. D. Jorgensen, and D. G. Hinks. BaBiO2.5, a New Bismuth oxide with a Layered Structure. *Journal of Solid State Chemistry*, 92:473–479, 1991.

[93] D. Louer, M. Louer, and M. Touboul. Crystal Structure Determination of Lithium Diborate Hydrate, LiB2O3(OH).H2O, from X-ray powder diffraction data collected with a curved position-sensitive detector. *Journal of Applied Crystallography*, 25:617–623, 1992.

[94] P. J. Knowles and N. C. Handy. A new determinant-based full configuration interaction method. *Chemical Physics Letters*, 111:315, 1984.

[95] E. Schrodinger. An Undulatory Theory of the Mechanics of Atoms and Molecules. *Physical Review*, 28:10491070, 1926.

[96] M. Born and J. R. Oppenheimer. On the Quantum Theory of Molecules. *Ann. Physik*, 84:457, 1927. (translated by S.M. Blinder).

[97] D. R. Hartree. The Wave Mechanics of an Atom with a Non-Coulomb Central Field. Part I. Theory and Methods. *Proceedings of the Cambridge Philosophical Society*, 24:89, 1928.

[98] V. Fock. Näherungsmethode zur lösung des quantenmechanischen mehrkörperproblems. *Zeitschrift fur Physik*, 61:126, 1930.

[99] D. Young. *Computational Chemistry: A Practical Guide for Applying Techniques to Real World Problems*. Wiley Interscience, 2001.

[100] R. J. Bartlett and J. F. Stanton. *Applications of Post-Hartree-Fock Methods: A Tutorial*, volume 5 of *Reviews in Computational Chemistry*, chapter 3, pages 65–169. VCH Publishers, 1994.

[101] L. H. Thomas. The calculation of atomic fields. *Proceedings of the Cambridge Philosophical Society*, 23:542–548, 1927.

[102] P. Hohenberg and W. Kohn. Inhomogeneous electron gas. *Physical Review*, 136 (3B):B864–B871, 1964.

[103] W. Koch and M. Holthausen. *A Chemist's Guide to Density Functional Theory*. Wiley-VCH, 2000.

[104] W. Kohn and L. J. Sham. Self-consistent equations including exchange and correlation effects. *Physical Review*, 140(4A):A1133–A1138, 1965.

[105] R. Armiento and A. E. Mattsson. Functional designed to include surface effects in self-consistent density functional theory. *Physical Review B*, 72(8):1–5, August 2005. ISSN 1098-0121.

[106] J. P. Perdew and Y. Wang. Accurate and simple analytic representation of the electron-gas correlation energy. 45(23):13244–13249, June 1992. ISSN 0163-1829.

[107] L. A. Cole and J. P. Perdew. Calculated electron affinities of the elements. *Physical Review A*, 25(3):1265–1271, 1982.

[108] J. P. Perdew and A. Zunger. Self-interaction correction to density-functional approximations for many-electron systems. *Physical Review B*, 1981.

[109] P. A. M. Dirac. Note on exchange phenomena in the thomas-fermi atom. *Proceedings of the Cambridge Philosophical Royal Society*, 26:376385, 1930.

[110] R. G. Parr, S. R. Gadre, and L. J. Bartolotti. Local density functional theory of atoms and molecules. *Proceedings of the National Academy of Science USA*, 76: 2522–2526, 1979.

[111] D. M. Ceperley and B. J. Alder. Ground State of the Electron Gas by a Stoichastic Method. *Physical Review Letters*, 45:566–569, 1980.

[112] S.H. Vosko, L. Wilk, and M. Nusair. Accurate spin-dependent electron liquid correlation energies for local spin density calculations: a critical analysis. *Canadian Journal of Physics*, 58:1200–1211, 1980.

[113] J. P. Perdew, K. Burke, and M. Ernzerhof. Generalized Gradient Approximation Made Simple. *Physical Review Letters*, 77(18):3865–3868, October 1996. ISSN 1079-7114.

[114] J. P. Perdew, A. Ruzsinszky, G. I. Csonka, L. A. Constantin, and J. Sun. Workhorse Semilocal Density Functional for Condensed Matter Physics and Quantum Chemistry. *Physical Review Letters*, 103:026403, 2009.

[115] A. D. Becke. Density-functional exchange-energy approximation with correct asymptotic behavior. *Physical Review A*, 38:3098–3100, 1988.

[116] C. Lee, W. Yang, and R. G. Parr. Development of the Colle-Salvetti correlation-energy formula into a functional of the electron density. *Physical Review B*, 37:785–789, 1988.

[117] A. D. Becke. A new mixing of Hartree Fock and local density functional theories. *Journal of Chemical Physics*, 98:1372–1377, 1993.

[118] J. C. Slater. Theory of complex spectra. *Physical Review*, 34:1293–1322, 1929.

[119] S.F. Boys. Electronic Wave Functions. I. A General Method of Calculation for the Stationary States of Any Molecular System. *Proceedings of the Royal Society A*, 200, 1950.

[120] R. Stewart. Small Guassian Expansions of Atomic Orbitals. *Journal of Chemical Physics*, 50:2485–2495, 1969.

[121] W. J. Hehre, R.F. Stewart, and J. A. Pople. Self-Consistent Molecular-Orbital Methods. I. Use of Guassian Expansions of Slater-Type Atomic Orbitals. *Journal of Chemical Physics*, 51:2657–2664, 1969.

[122] M. Dickson and A. D. Becke. Basis set free local density functional calculations of geometries of polyatomic molecules. *Journal of Chemical Physics*, 99:3898–3905, 1993.

[123] A. Leach. *Molecular Modelling Principles and Applications*. Pearson, 2001.

[124] F. Bloch. Uber die quantenmechanik der elektronen in kristallgittern. *Zeitschrift fur Physik*, 52:555–600, 1928.

[125] H. J. Monkhorst and J. D. Pack. Special points for Brillouin-zone integrations. *Physical Review B*, 13:5188–5192, 1976.

[126] P. E. Blochl, O. Jepsen, and O. K. Andersen. Improved tetrahedron method for brillouin-zone integrations. *Physical Review B*, 49:1622316233, 1994.

[127] URL `http://commons.wikimedia.org/wiki/File:Brillouin_Zone_%281st,_FCC%29.svg`. Public Domain Image, Wikimedia Commons.

[128] B. J. Lynch, Y. Zhao, and D. G. Truhlar. The Effectiveness of Diffuse Basis Functions for Calculating Relative Energies by Density Functional Theory. *Journal of Physical Chemistry A*, 107:13841388, 2003.

[129] Jan K. Labanowski. Simplified introduction to ab initio basis sets: terms and notation, December 1996. URL `http://www.ccl.net/cca/documents/basis-sets/basis.html`.

[130] R. M. Balabin. Enthalpy difference between conformations of normal alkanes: Intramolecular basis set superposition error (BSSE) in the case of n-butane and n-hexane. *The Journal of Chemical Physics*, 129(16):164101, October 2008. ISSN 1089-7690.

[131] I. Mayer. The chemical Hamiltonian approach for treating the BSSE problem of intermolecular interactions. *International Journal of Quantum Chemistry*, 70(1): 41–63, 1998. ISSN 0020-7608.

[132] S. F. Boys and F. Bernardi. The calculation of small molecular interactions by the differences of separate total energies. Some procedures with reduced errors. *Molecular Physics*, 100(1):65–73, January 2002. ISSN 0026-8976.

[133] J. A. Sordo, S. Chin, and T. L. Sordo. On the counterpoise correction for the basis set superposition error in large systems. *Theoretica Chimica Acta*, 74(2):101–110, August 1988. ISSN 0040-5744.

[134] H. Hellman. A New Approximation Method in the Problem of Many Electrons. *Journal of Chemical Physics*, 3:61, 1935.

[135] S. G. Louie, S. Froyen, and M. L. Cohen. Nonlinear ionic pseudopotentials in spin-density-functional calculations. *Physical Review B*, 26(4):1738–1742, 1982.

[136] D. R. Hamann, M. Schluter, and C. Chiang. Norm-conserving pseudopotentials. *Physical Review Letters*, 43(20):1494–1497, 1979.

[137] G. B. Bachelet and M. Schluter. Relativistic norm-conserving pseudopotentials. *Physical Review B*, 25(4):2103–2108, 1982.

[138] D. Vanderbilt. Soft self-consistent pseudopotentials in a generalized eigenvalue formalism. *Physical Review B*, 41(11):7892–7895, 1990.

[139] H. Jahn and E. Teller. Stability of Polyatomic Molecules in Degenerate Electronic States. I. Orbital Degeneracy. *Proceedings of the Royal Society of London. Series A*, 161:220235, 1937.

[140] M. Born. Atomtheorie des festen Zustandes (Dynamik der Kristallgitter). *Monatshefte fur Mathematik*, 1923.

[141] P. P. Ewald. Die Berechnung optischer und elektrostatischer Gitterpotentiale. *Ann. Phys.*, 369:253287, 1921.

[142] J. Lennard-Jones. On the Determination of Molecular Fields. *Proceedings of the Royal Society of London A*, 106:463477, 1924.

[143] R. A. Aziz. A highly accurate interatomic potential for argon. *Journal of Chemical Physics*, 99:4518, 1993.

[144] R. A. Buckingham. The Classical Equation of State of Gaseous Helium, Neon and Argon. *Proceedings of the Royal Society of London A*, 168:264–283, 1938.

[145] P. Morse. Diatomic Molecules According to the Wave Mechanics. II. Vibrational Levels. *Physical Review*, 34:57–64, 1929.

[146] A Warshal and S. Lifson. Consistent Force Field Calculations. II. Crystal Structures, Sublimation Energies, Molecular and Lattice Vibrations, Molecular Conformations, and Enthalpies of Alkanes. *Journal of Chemical Physics*, 53: 582–594, 1970.

[147] S. Fleming and A. Rohl. GDIS: a visualization program for molecular and periodic systems. *Zeitschrift fur Kristallographie*, 220:580–584, 2005.

[148] V. Pervushin. *Journal of Inorganic Chemistry*, 34:615, 1989.

[149] G. Samoilova. *Journal of Inorganic Chemistry*, 31:801, 1986.

[150] J. W. Mullin. *Crystallization*. Reed Educational and Professional Publishing Ltd., 1997.

[151] Top-up mode project, 2009. URL `http://www.synchrotron.org.au/index.php/about-us/australian-synchrotron-development-plan/projects/major-facility-upgrades/top-up-mode-project`.

[152] Sheldrick's rule.

[153] R. Shirley. The crysfire system for automatic powder indexing, 1999. URL `http://www.ccp14.ac.uk/tutorial/crys/`. CRYSFIRE Software Suite.

[154] N. Dragoe. Powder4 program for windows, 2002. URL `http://pcb4122.univ-lemans.fr/du-sdpd/nexus/ccp14/web/tutorial/powder/index.htm`.

[155] E. J. Sonneveld and J. W. Visser. Automatic collection of powder data from photographs. *Journal of Applied Crystallography*, 8(1):1–7, February 1975. ISSN 0021-8898.

[156] K. Chapman. Personal communication, 2009.

[157] A. Munter. Neutron scattering lengths and cross-sections, 1999. URL `http://www.ncnr.nist.gov/resources/n-lengths/elements/h.html`.

[158] J. M. Soler, E. Artacho, J. D. Gale, A. Garcia, J. Junquera, P. Ordejon, and D. Sanchez-Portal. The SIESTA method for ab initio order-N materials simulation. *Journal of Physics: Condensed Matter*, 14:2745–2779, 2002.

[159] E. Artacho, E. Anglada, O. Dieguez, J. D. Gale, A. Garcia, J. Junquera, R. M. Martin, P. Ordejon, J. M. Pruneda, D. Sanchez-Portal, and J. M. Soler. The Siesta method; developments and applicability. *Journal of Physics: Condensed Matter*, 20:064208, 2008.

[160] P. Ordejon, D. A. Drabold, R. M. Martin, and M. P. Grumbach. Linear system-size scaling methods for electronic-structure calculations. *Physical Review B*, 51: 1456–1476, 1995.

[161] D. D. Johnson. Modified Broydens method for accelerating convergence in self-consistent calculations. *Physical Review B*, 37:12807–12813, 1988.

[162] A. Garcia. Simple general-purpose optimization system, 2007. Included in SIESTA software package.

[163] J. A. Nelder and R. Mead. A simplex method for function minimization. *Computer Journal*, 7:308–313, 1965.

[164] J. Kennedy and R. Eberhart. Particle Swarm Optimization. *Proceedings of IEEE International Conference on Neural Networks*, IV:1942–1948, 1995.

[165] E. Artacho, J.-M. Cela, J. D. Gale, A. Garcia, J. Junquera, R. M. Martin, P. Ordejon, D. Sanchez-Portal, and J. M. Soler. Siesta 3.0-beta-15 user's guide, March 2010. URL `http://www.icmab.es/siesta/Documentation`.

[166] J. Moreno and J. M. Soler. Optimal meshes for integrals in real- and reciprocal-space unit cells. *Physical Review B*, 45:13891–13898, 1992.

[167] Siesta pseudopotentials and basis sets repository, May 2011. URL `http://www.icmab.es/siesta/Pseudos-Bases`. Requires registration.

[168] J. Junquera and P. Ghosez. Critical thickness for ferroelectricity in perovskite ultrathin films. *Nature*, 422:506–509, 2003.

[169] D. Spagnoli, K. Refson, K. Wright, and J. D. Gale. Density functional theory study of the relative stability of the iron disulfide polymorphs pyrite and marcasite. *Physical Review B*, 81:094106, 2010.

[170] A. E. Mattsson and T. R. Mattsson. AM05 Density Functional Applied to the Water Molecule, Dimer, and Bulk Liquid. *Journal of Chemical Theory and Computation*, 5:887–894, 2009.

[171] J. K. Burdett, T. Hughbanks, G. J. Miller, J. W. Richardson, and J. V. Smith. Structural-electronic relationships in inorganic solids: powder neutron diffraction studies of the rutile and anatase polymorphs of titanium dioxide at 15 and 295 k. *Journal of the American Chemical Society*, 109:3639–3646, 1987.

[172] F. Labat, P. Baranek, and C. Adamo. Structural and Electronic Properties of Selected Rutile and Anatase TiO2 Surfaces: An ab initio Investigation. *Journal of Chemical Theory and Computation*, 4(2):341–352, February 2008. ISSN 1549-9618.

[173] J Muscat, V. Swamy, and N. Harrison. First-principles calculations of the phase stability of TiO2. *Physical Review B*, 65(22):1–15, June 2002. ISSN 0163-1829.

[174] M. R. Ranade, A. Navrotsky, H. Z. Zhang, J. F. Banfield, S. H. Elder, A. Zaban, P. H. Borse, S. K. Kulkarni, G. S. Doran, and H. J. Whitfield. Energetics of nanocrystalline TiO2. *Proceedings of the National Acadmey of Sciences of the United States of America*, 99:6476–6481, 2002.

[175] A. Fahmi, C. Minot, B. Silvi, and M. Causa. Theoretical analysis of the structures of titanium dioxide crystals. *Physical Review B*, 47:11717–11724, 1993.

[176] T. Mitsuhashi and O. J. Kleppa. Transformation Enthalpies of the TiO2 Polymorphs. *Journal of the American Ceramics Society*, 62:356, 1979.

[177] P. Giannozzi, S. Baroni, N. Bonini, and M. Calandra. QUANTUM ESPRESSO: a modular and open-source software project for quantum simulations of materials. *Journal of Physics: Condensed Matter*, 21:395502, 2009.

[178] L. Koci, D. Y. Kim, J. S. de Almeida, M. Mattesini, E. Isaev, and R. Ahuja. Mechanical stability of TiO 2 polymorphs under pressure: ab initio calculations. *Journal of Physics: Condensed Matter*, 20(34):345218, August 2008. ISSN 0953-8984.

[179] J. D. Gale. Empirical potential derivation for ionic materials. *Philosophical Magazine B*, 73:3–19, 1996.

[180] J. D. Gale. GULP : A computer program for the symmetry-adapted simulation of solids. *Journal of the Chemical Society, Faraday Transactions*, 93:629–637, 1997.

[181] J. D. Gale and A. L. Rohl. The General Utility Lattice Program (GULP). *Molecular Simulation*, 29:291–341, 2003.

[182] S. M. Woodley, P. D. Battle, J. D. Gale, and C. R. A. Catlow. The prediction of inorganic crystal structures using a genetic algorithm and energy minimisation. *Physical Chemistry Chemical Physics*, 1:2535–2542, 1999.

[183] V. Volis, C. Busco, and P. Ugliengo. Thermodynamic study of water adsorption in high-silica zeolites. *Journal of Physical Chemistry B.*, 110:14849–59, 2006.

[184] L. Glasser and F. Jones. Systematic thermodynamics of hydration (and of solvation) of inorganic solids. *Inorganic Chemistry*, 48:1661–1665, 2009.

[185] R. Shirley. *The CRYSFIRE System for Automatic Powder Indexing: Users Manual*. The Lattice Press, 41 Guildford Park Avenue, Guildford, Surrey GU2 5NL, England, 1999.

[186] Diffracplus TOPAS, 2011. URL `http://www.bruker-axs.com/topas.html`. Commerical computer software developed by Bruker.

[187] W. I. F. David, K. Shankland, J. van de Streek, E. Pidcock, W. D. S. Motherwell, and J. C. Cole. DASH: a program for Crystal Structure Determination from Powder Diffraction Data. *Journal of Applied Crystallography*, 39:910–915, 2006.

[188] F. Kohlbeck and E. M. Horl. Trial and error indexing program for powder patterns of monoclinic substances. *Journal of Applied Crystallography*, 11:60–61, 1978.

[189] Vincent Favre-Nicolin. Fox reference manual, March 2008. URL `http://vincefn.net/Fox/Manual`.

[190] R. Shirley. *NBS Spec. Publ.*, 567:361–82, 1980.

[191] Robin Shirley. Indexing problems (dominant zone), June 2004. URL `http://www.mail-archive.com/rietveld_l@ill.fr/msg02144.html`.

[192] W. I. F. David. Powder Diffraction: Least Squares and Beyond. *Journal of Research of the National Institute of Standards and Technology*, 109:107–123, 2004.

[193] A. C. Larson and R. B. Von Dreele. General Structure Analysis System (GSAS). *Los Alamos National Laboratory Report*, LAUR:86–748, 2000.

[194] A. Le Bail. SDPD Newsgroup, . URL `http://tech.groups.yahoo.com/group/sdpd/`.

[195] A. Le Bail. *Powder Diffraction*, 19:249–254, 2004.

[196] G.M. Sheldrick. A short history of SHELX. *Acta Crystallographica A*, 64:112–122, 2008.

[197] A. Le Bail. Personal communication. .

[198] J. Rodriguez-Carvajal. Recent Developments of the Program FULLPROF. *Commission on Powder Diffraction (IUCr) Newsletter*, 26:12–19, 2001.

[199] P. F. Henry, M. T. Weller, and C. C. Wilson. Structural Investigation of TS-1: Determination of the True Nonrandom Titanium Framework Substitution and Silicon Vacancy Distribution from Powder Neutron Diffraction Studies Using Isotopes. *Journal of Physical Chemistry B.*, 105:7452–7458, 2001.

[200] G. N. Vayssilov. Structural and Physicochemical Features of Titanium Silicalites'. *Catalysis Reviews*, 39:209–251, 1997.

[201] B. Gilbert, H. Zhang, F. Huang, J. Banfield, Y. Ren, D. Haskel, J. C. Lang, G. Srajer, A. Jurgensen, and G. A. Waychunas. Analysis and simulation of the structure of nanoparticles that undergo a surface-driven structural transformation. *Journal of Chemical Physics*, 120:11785–11795, 2004.

[202] C.W. Glass, A.R. Oganov, and N. Hansen. USPEX–Evolutionary crystal structure prediction. *Computer Physics Communications*, 175:713–720, 2006.

[203] A. R. Oganov, C. W. Glass, and S. Ono. High-pressure phases of CaCO3: Crystal structure prediction and experiment. *Earth and Planetary Science Letters*, 241: 95–103, 2006.

[204] A. R. Oganov, S. Ono, Y. Ma, C. W. Glass, and A. Garcia. Novel high-pressure structures of MgCO3, CaCO3 and CO2 and their role in the Earth's lower mantle. *Earth and Planetary Science Letters*, 273:38–47, 2008.

[205] M. G. Zhang, H. Wang, and H. B. Wang. First-Principles Prediction on the High-Pressure Structures of Transition Metal Diborides (TMB2, TM = Sc, Ti, Y, Zr). *Journal of Applied Physics*, 108:023507, 2010.